Seismic Performance and Design of Japanese Steel Chevron-Braced Moment-Resisting Frames

by

Ilanildo DIAS

A thesis submitted in partial fulfillment of the requirements for the degree of Doctor of Engineering

Examination Committee: Dr. Taichiro Okazaki
Dr. Masaru Kikuchi
Dr. Nobuo Takai

Doctoral Thesis No.:
Division of Architectural and Structural Design
Graduate School of Engineering, Hokkaido University
March 2023

ABSTRACT

Steel braced frames are widely used for buildings in high-seismicity regions due to their versatility in meeting stiffness and strength requirements. Japanese engineers often choose to place the braces in a "chevron" (or V or inversed-V) arrangement within a moment-resisting frame (MRF). In such systems, hereafter referred to as chevron-braced MRFs, the design of the beam intersected by braces poses a design challenge because this beam yields due to forces delivered by the tension and compression braces in combination with forces produced by moment-frame action. The energy dissipating mechanism of chevron-braced MRFs is dependent on the loading history, and therefore, might not be uniquely determined because the structural system is statically indeterminate, and the cyclic-loading response of steel braces is highly complex. Despite the very wide use, limited design guidance is provided by the Japanese design codes and standards on how to proportion the beams and the braces and how to detail the bracing connections. The lack of guidance has allowed engineers to choose a very wide variety of designs, and this situation is at least partly responsible for the damage observed in steel chevron-braced MRFs after even the most recent earthquakes. A computational study was conducted with the following objectives: (1) to further the understanding of the seismic performance of steel chevron-braced MRFs, and thereby identify design concerns; (2) to derive proportion rules for the beams and braces in steel chevron-braced MRFs; (3) to derive bracing requirements to control the beam intersected by braces against the severe transverse forces and torsional moment delivered by the braces, and bending moments arising from moment-frame action; and (4) to assess the seismic performance of Japanese steel buildings that employ steel chevron-braced MRFs.

The computational study comprised two schemes, using 3D nonlinear finite-element-method models to examine the interaction between chevron braces and MRF, and 2D nonlinear frame models with fiber elements to examine the time-history response of building systems under strong ground motions. Both schemes utilized general-purpose software, the former a commercial package ADINA and the latter an open-source platform OpenSEES. In both schemes, basic models were validated against data and observations from an experimental study on steel chevron-braced MRFs. The validated models were used to conduct a parametric study on key design parameters such as the torsional and translational restraint of the beam intersected by braces, the relative strength of the beam with respect to the braces, and the type of bracing connection. Minimum lateral bracing requirements for the beam was recommended and design equations to estimate the torsional demands on the beam intersecting braces were proposed. Furthermore, a design procedure for chevron-braced moment-resisting frames, that accounts for the dependency of the energy dissipation mechanism on the cyclic loading history was proposed. The numerical study on the single-story single-bay chevron-braced moment-resisting frames was supplemented with an extensive number of numerical simulations to study the performance of low- and mid-rise chevron-braced frames designed using different design philosophies often used in Japan. The seismic performance of the chevron-braced-frame systems was assessed through monotonic pushover and nonlinear time history analysis. Finally, recommendations for analysis and design of

chevron-braced MRFs are provided aimed at ensuring an acceptable performance of the system.

ACKNOWLEDGMENTS

This thesis is a result of experimental and computational work conducted by many students at the laboratory of Structural Engineering, Department of Architecture and Structural Design, from which I was able to gather data and knowledge regarding the research topic and pursue the research.

I would like to, firstly, express my deeply and sincere gratitude and thankfulness to my advisor Dr. Taichiro Okazaki for his guidance, support and patience over the past years. I know, with no doubt that, without him I would not be able to finish this research. Over the past years, for so many times I was lost, not knowing how to proceed and he could easily put me back on track and for that I am truly thankful. I am deeply in debt to him for granting me the opportunity to come pursue my masters and later the doctoral course under his supervision.

I would also like to thank Associate Professor Dr. Matsui Ryota for his valuable input, guidance and help whenever requested. His guidance and advice were fundamental to complete this thesis.

I would like to acknowledge the collaboration of my colleagues from the research group, in particular Uesugi Shuhei, Akiri Seki, Yang Shaoqi, Yi Qie, Akshay Somkuwar, Kelvin Ikogba, Raheem Ibrahim, Rafiqul, Yuka, and so many others that have passed come and go over the past years.

I would like to express my sincere gratitude to my laboratory colleagues for their friendships, help and support in both research and/or academic related matters during the duration of my stay in Japan making my student live at Hokkaido University memorable in so many different levels.

Most of all, I would like to thank my family: My mother Maria Lopes, my father Sergio Dias, for their love and support for without them I wouldn't be here. Special thanks also to my brothers and sisters for their unconditional love, support when I most definitely needed it.

Special thanks also to my girlfriend Aleida Mota, whose support was a fundamental source of strength and motivation over the past years.

I am truly grateful to the Japanese government and the MEXT - Ministry of Education, Culture, Sports, Science and Technology – for the financial support and the opportunity to study in Japan for the past two years.

TABLE OF CONTENTS

TABLE OF FIGURES

LIST OF TABLES

1. INTRODUCTION

1.1 General

Concentrically Braced Frames (CBF) shown in Figure 1.1 has been over the past few decades, widely used as lateral loading resisting systems in regions of high seismicity such as United States, Japan, New Zealand, and other seismically active countries. The system in popular due to high elastic stiffness and strength, its aesthetic appeal, architectural advantages.

This lateral-load resisting system is composed of framing elements, shown in Figure 1.1(a), braces, beams, and columns. In CBFs, the braces are often considered as the "fuses", where lateral-load resistance relies solely on the braces.

The inelastic cyclic behavior of chevron CBFs is often characterized by deterioration of the lateral strength, a tendency to form soft stories and fracture due to excessive deformation demand [Khatib et al. [1]]. The seismic performance of braced frames designed according to the *U.S* provisions has been examined by full -scale, multistory tests, and clear design guidelines are provided.

In Japanese steel construction, braces are often placed in a "chevron" (or V or inversed-V) arrangement, within a moment-resisting frame (MRF), herein referred as chevron-braced MRFs. Despite being widely used in various building types including commercial offices, shopping centers, factories, and parking ramps, there is to date, limited information provided by the standards or regulations on how to proper design and detail steel chevron-braced MRFs. Although reconnaissance from past earthquakes suggests that braced frames are prone to seismic damage [1,2], engineers have employed a wide range of members proportions and bracing connections.

The Japanese codes and provisions [2]–[4] warn against the yielding of the beam intersecting the b races in chevron-braced MRFs but fall short of providing specific proportioning and detailing rules.

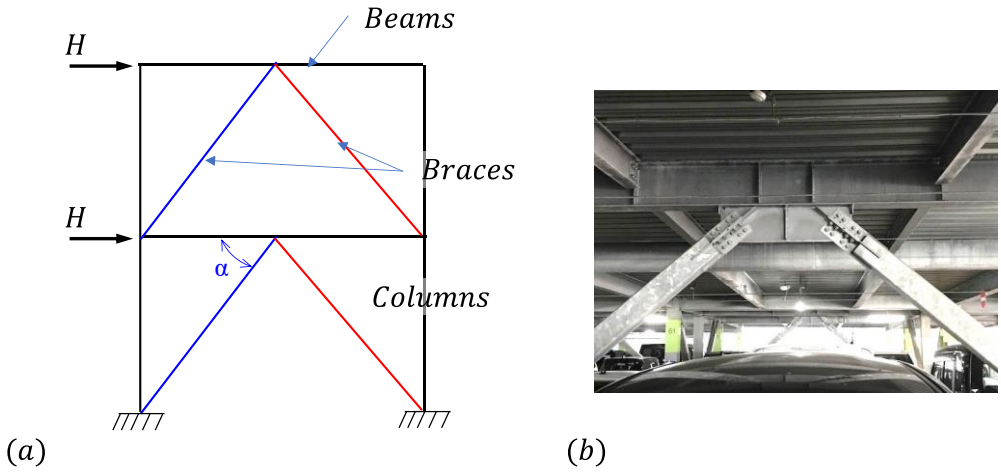

Figure 1.1: Brace Frame Configuration

This situation has allowed Japanese engineers to design a wide variety of chevron-braced MRFs with different member proportions, bracing connections, and lateral bracing. Design and detailing of chevron-braced MRFs are left to the judgment of the structural designer in the designer, hence, numerous questions still exist performance of chevron-braced MRFs built in Japan. CBF's. It is therefore suspected that there may be many underconservative and overconservative designs in existence, caused by the lack inconsistency of design rule or consensus in the Japanese practice.

1.2 Objectives

This dissertation aims at investigating the performance of low- to mid-rise chevron-braced frames in Japan. The behavior of the system, the effect of the design approach used in proportioning the members and the effect of the bracing connection on the dynamic response of the low- and mid-rise steel chevron braced MRFs is thoroughly investigated. The main goal is to investigate and understand the performance of chevron-braced MRFs, to further extend the knowledge and close the knowledge gap by complementing and extending observations obtained from a series of experimental studies on a single-story single-bay chevron-braced MRF.

The specific objectives are:

1. To investigate the seismic performance of Japanese Steel Chevron-Braced MRF.
2. Understand the torsional demands on the beam intersecting the braces.
3. Consolidate the design information for Japanese Steel chevron-brace MRFs, to provide a streamlined design procedure that can be used by engineers in Japan;
4. Propose design guidelines to enhance the seismic performance of chevron-braced MRFs.
5. Understand the performance of low- and mid-rise Japanese braced frames.
6. Access the performance of existing chevron-braced MRFs to provide recommendations for the analysis, design and construction of chevron-braced MRFs.

1.3 Outline

To achieve the goals, this dissertation is composed of 7 chapters.

Chapter 1 discusses the background and scope of the research, research gaps to be addressed, and the primary objectives.

Chapter 2 presents the current state of knowledge through analysis of the literature and code provisions. Chapter 3 introduces the Experimental program conducted at the Laboratory of Structural Engineering Hokkaido University. Details of the Finite element Model is also introduced.

Chapter 4 reports on the lateral bracing requirements of the beam intersected by braces. The validated nonlinear finite-element model built in chapter 3 was used to investigate the torsional and translational demands delivered by the braces on the beam intersected by braces. The study considered three different chevron-braced MRFs, employing two different bracing connection, and with the braces oriented to buckle in different direction (in-plane and out-of-plane). Five different combinations of translational and rotational bracing were considered. The results showed that lateral bracing of the beam is as concern, especially when the bracing connection is rigid and the braces are oriented to buckle out of plane, but it may not affect the lateral resistance of the braced frame. As such, minimum lateral bracing requirements for the beam was recommended and design equations to estimate the torsional demands on the beam intersecting braces were proposed.

Chapter 5 discusses the design equations developed to predict the energy-dissipation mechanism of chevron-braced MRFs, and the lateral resistance of the brace and MRF. Nonlinear finite-element-method models were built using the Adina analysis software and validated against data and observations from previously tested chevron-braced MRF specimens. The validated models were used to conduct a parametric study on the performance of sixteen chevron-braced MRFs with different members proportions. The relative horizontal strength of the beam with respect to the braces ranged from 1.3 to 11.3. The braced frames employed six different bracing connections (rigid and flexible connections) and were subjected to three different loading protocols (Monotonic pushover, symmetric cyclic-loading and non-symmetric cyclic-loading).

Chapter 6 describes a straightforward design procedure proposed for design of steel chevron-braced MRFs. In the sequence, a total of 21 low- and mid-rise chevron-braced MRFs were designed using the procedure introduced. The braced frames were designed according to three different design philosophies. Two of the design philosophies are often used in Japan. The third design procedure used the structural system used in the US and was used for comparison with the Japanese systems.

Finally in chapter 7, a two-dimensional finite-element model was built using the OpenSees Framework, to evaluate the seismic performance of the low- and mid-rise chevron-braced MRFs designed using the procedure introduced in Chapter 6. The performance of the braced-frame systems was studied through nonlinear monotonic pushover analysis and nonlinear time history analysis using a ground motion suite comprised of 28 earthquake records. The results show that, all the braced-frame systems had good seismic performance with the median story drift demands within the 2% rad drift which suggests that all systems meet the design requirements stipulated by the Japanese code specified for buildings in Japan. Between all the design philosophies, the braced frame systems designed using the American configuration had better performance although it uses considerable larger amount of steel. Low-rise chevron-braced frames are subjected to larger deformation demands than the mid-rise braced frames.

Chapter 8 provides a discussion on the design and performance of Japanese Low- and Mid-rise steel chevron braced concentrically braced frames and Chapter 9 provides the main conclusion for this research.

2. LITERATURE REVIEW

2.1 General

Over the years, numerous research has been conducted to study the seismic behavior of concentrically braced frames, its components specially the braces and its bracing connections. To date, most of the research has been conducted in North America studies on the performance of concentrically braced frames has also been conducted in Japan, but in a much smaller scale.

The main focus of the research has been on understanding the behavior of the individual components such as the braces, the bracing connections, etc., and more recently, the study of concentric-braced frames subassemblages. Some of the most relevant works is summarized in this chapter. The review of the literature presented in this chapter is divided in to three categories, first examining the body of literature on the performance of brace-frame structures during major earthquakes. In the sequence, the most relevant research studies on experimental programs and lastly numerical modeling of CBFs.

2.2 Performance of Steel Chevron-Braced Frames in Past earthquakes

Post-earthquake investigations on the performance of steel structures following the 1994 Northridge earthquake, showed extensive damage to steel braced frames [5], [6]. Damage to a four-story commercial office structure constructed in 1986 according to the 1980 Los Angeles Building Code or the 1982 UBC code was observed and reported by Tremblay et al. [5] and Kelly et al. [6]. The structure consists of a steel braced frames for gravity loads ad a steel braced frame for wind and seismic force [6]. According to Tremblay et al. [5] the building experienced extreme bracing related fracture and deformations which is attributed to strong motion shaking. Tremblay et al. [5] observed crack and tearing at the center of the brace was observed (as shown in Figure 2.1) but the damage was limited to the braced bays at the second floor. Most of the failures observed were attributed to local buckling of the section which can be attributed to the high width-to-thickness ratios of the walls of the steel braces [5]. Fracture of the braces was observed as reported by Tremblay et al. [5] they were caused by low cycle fatigue and subsequent formation of crack at the location where local bulking had occurred. Tremblay et al. [5] and Kelly et al.[6] reported on damage to the beam intersecting the braces, namely in-plane bending and torsion due to brace buckling. According to Kelly et al.[6], the braced frames at every second level lost all or most of its capacity. Light damage was reported in the other stories, but Tremblay et al. [5] inferred that the second story drift was around 5mm. Although the frame retained its

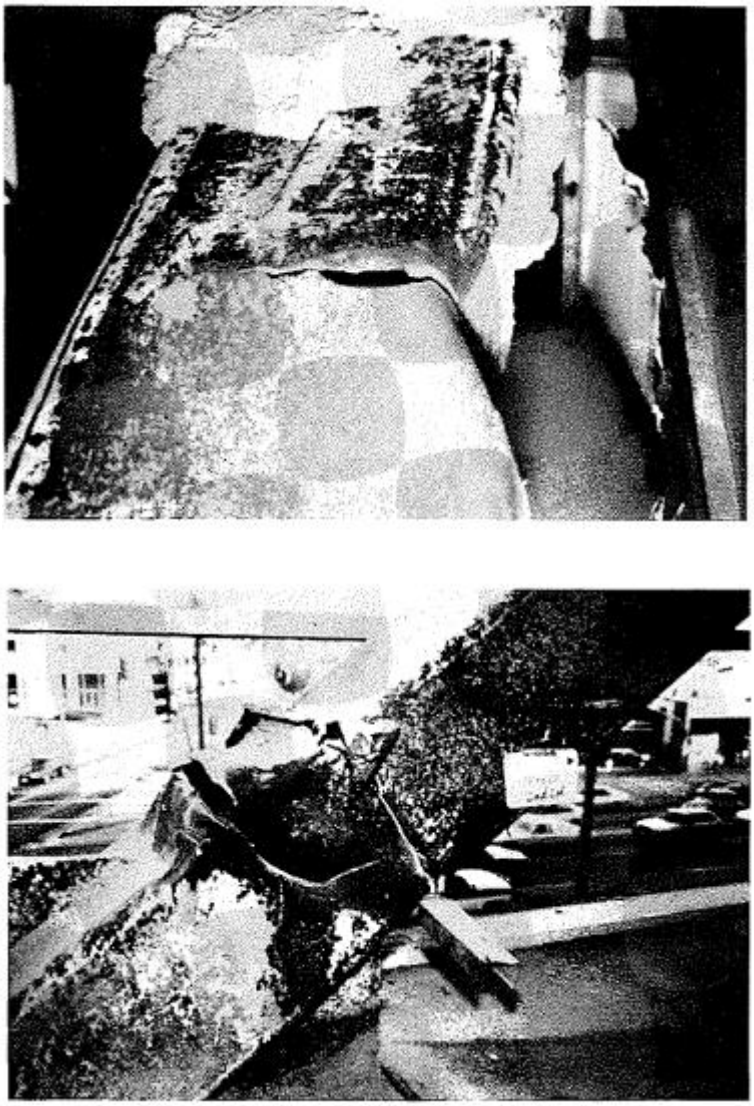

Figure 2.1: Fracture of hollow structural steel brace of a four-story commercial structure (source: Tremblay et al [5])

vertical loading resistance, after inspection, entry to the building was limited due to the extent of damage to the braces [5].

Damage to buildings using concentric-braced frames as the main lateral loading resistance system was also observed in the Oviatt Library at the California State University [5] and at the penthouse level of a 19-story office building [7].

Damage to braced-frame systems was also observed after the 1995 Hyogoken-Nanbu (Kobe) earthquake. In the past, braced frame systems were very common in the Hanshin area. According to the report by NIST [8], a variety of fractures was observed in steel structures. For braced frame structures, the most commonly observed damage was fracture of diagonal braces. Fracture of the braced frame

systems were generally observed in garage buildings or low- to mid-rise office buildings [8].

A seven-story braced frame building with lightweight concrete panels for cladding was heavily damaged as shown in Figure 2.2. The building which had a one bay in the east-west direction and two bays in the north-south direction, drifted severely in the north direction due to fracture of numerous braces. Fracture was observed at the bolted connections to gusset plates. Block shear failure of the tension braces was observed at the upper floor levels.

Figure 2.2: Heavily damaged seven-story braced frame building (source: NIST [8]).

Following the 2011 Tohoku-oki earthquake, a reconnaissance was conducted and reported by Okazaki et al ([9]). Damages to CBF structures were observed. Much of the damage reported concerned damage to the bracing connections.

Damage was observed in an office building, with eight-span X-configuration CBF in the north-south direction and a single-span MRF in the east-west direction. In the north-south direction, lateral-load resistance was nearly fully resisted by the braces. Fracture of the end gusset plate (Figure 2.3 (c)), and large bending deformation of the middle gusset plate was observed.

Damage was also observed in a two-story seven-bay parking garage using chevron CBFs (shown in Figure 2.4). Severe damage was observed at the bracing connections, with the braces failing by failure at the ends of the braces. Plastic hinge formed at the center of the beam due to the force unbalance between the braces [9].

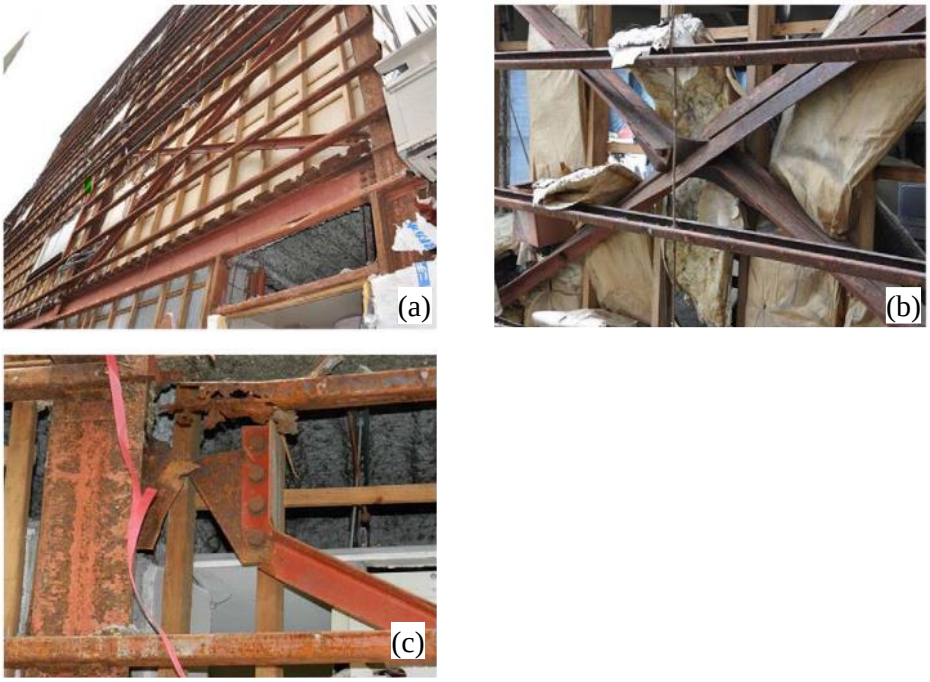

Figure 2.3:Damage to a CBF: (a) Exterior View; (b)Middle gusset plate deformation; and (c) Fracture Gusset Plate; (Source: Okazaki et al. [7]).

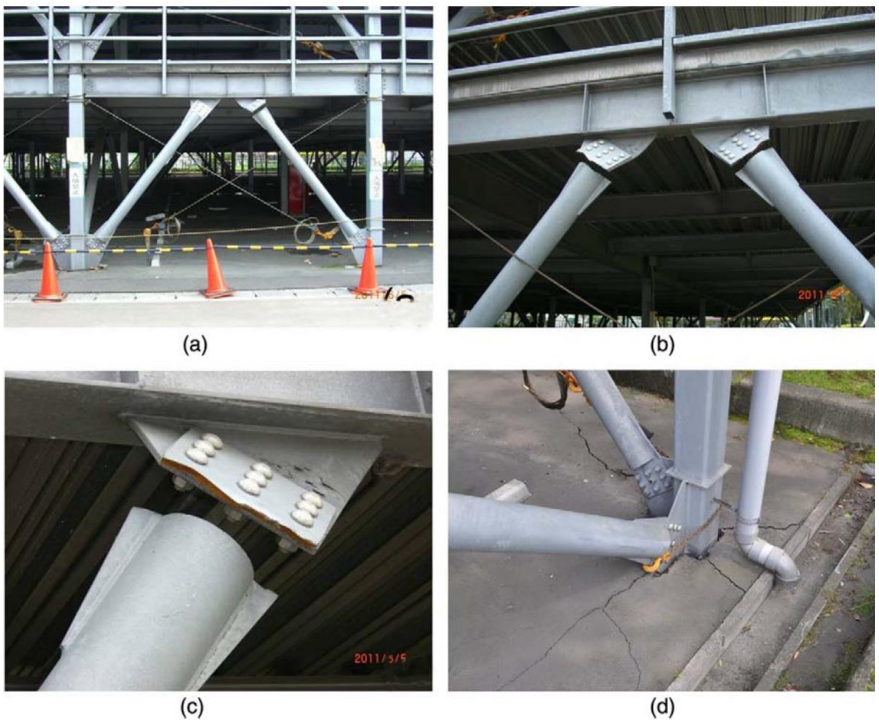

Figure 2.4:Damage to Parking Garage using Chevron braced frame (source: Okazaki et al. [7])

Summary

Damage to chevron-braced MRFs have been observed after the recent earthquakes in Japan. Although it cannot be clearly stated, it is believed that the damages to chevron-braced MRFs can be partly associated with the proportioning and detailing and of the system; Okazaki et al. [7] concluded that, the CBF structures were not properly detailed to ensure ductile behavior. Hence, further studies through experiments and numerical simulation are warranted to properly understand the performance of the systems. Proper proportioning and detailing rules and required to ensure ductile response under even larger earthquake ground motions.

2.3 Experimental Studies

Because of the damages observed in the braces and bracing connection in the past earthquakes, experimental works have been conducted with the goal to improve our understanding of the performance of braced frames during earthquakes. Some of the most relevant works conducted to study the performance of braced frames are summarized next.

The performance of Japanese steel chevron-braced MRFs has been studied in Japan since the 1970s [e.g., Yamanouchi et al. [10], Shibata and Wakabayashi [11], Fukuta et al. [12] etc.].

Fukuta et al. [12] studied the seismic behavior of six inverted V-braced frames with braces of intermediate slenderness (λ=70-120) at Building research institute as part of the U.S-Japan cooperative earthquake research program. The main goal of this study was to analyze the elastic-plastic behavior of the lower stories of the chevron-braced frame and to determine the post-buckling behavior of the braces.

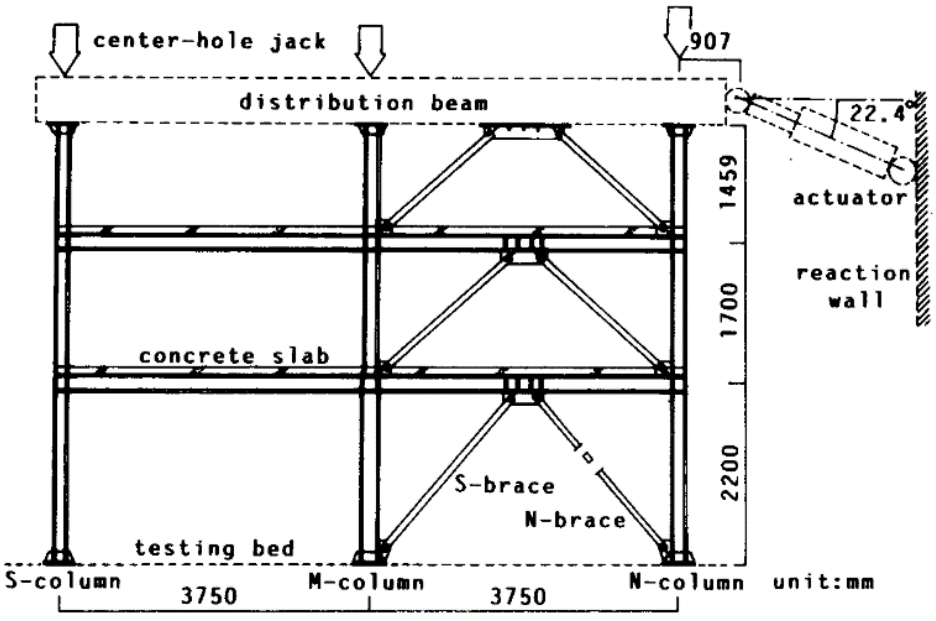

Figure 2.5: 3-story CBF configuration (source: Fukuta et al. [10]).

The interaction between the braces and the beam intersecting braces was also studied. The hysteretic response of the braced frame system was decomposed into the contribution of the two lateral loading resisting systems, the moment-resisting frame and the braces. The study showed that the braces contributed to roughly 80% of the lateral strength in the elastic range, but in the post-buckling range the contribution decreased to 50%. For chevon braced frame configuration unless a very strong beam is used, the braces were not able to elongate enough in tension to reach their yield strength. The authors proposed a simple hysteresis model to predict the hysteretic response of the inverted V braced frame. Fukuta et al. provided equations to compute the lateral strength (Q_{ry}), of the braced frame at the limit state.

The performance of Japanese chevron-braced frames was further studied by Shibata and Wakabayashi [11]. The performance of five braced frame specimens were tested. The results showed that the hysteretic response of the frame is highly dependent on the inelastic response of the beam. The relative strength of the beam with respect to the braces was partially discussed. The research showed that if a stubby brace is used, the restoring force is large but the beam is severely damaged, and the hysteretic response of the braced frame deteriorates. In contrast if a slender brace is used, the hysteretic response of the braced frame is stable, and little plastification occurs on the beam.

Yamanouchi et al.[10] studied the performance of a full scale six-story, 2 by 2 bay, steel chevron-braced frame structure. The importance of the interaction between the bracing members and the Moment-Resisting Frame was highlighted. It was noted that the braces developed large inelastic deformation in compression but did not develop its yielding tensile strength, due to vertical deflection at the mid-span of the beam due to the force unbalance between the braces. Fukuta and Yamanouchi [13] proposed a method to compute the ultimate lateral capacity of chevron-braced MRF, and a design rule to proportion the beam intersected by braces.

The performance of CBFs have been widely studied in the US. Roeder et al. [14] and Sen et al. [15] demonstrated by extensive experiments and numerical simulations that chevron CBFs can exhibit ductile performance even if beam yielding due to unbalanced vertical force occur. In fact, Roeder et al. [14] showed that the performance of chevron CBFs improves by proportioning the beam intersected by braces for 30% of the requirement by the AISC *Seismic Provisions* at that time. These previous studies suggest that limited beam yielding should have no adverse effect on the structural performance of chevron CBFs.

Following the reconnaissance by Okazaki et al ([9]), Seki et al. [16] conducted an experimental study on a total of six large-scale chevron-braced MRF specimens to tested to examine the performance of chevron-braced MRF designed and constructed according to the practice in Japan at that time. The

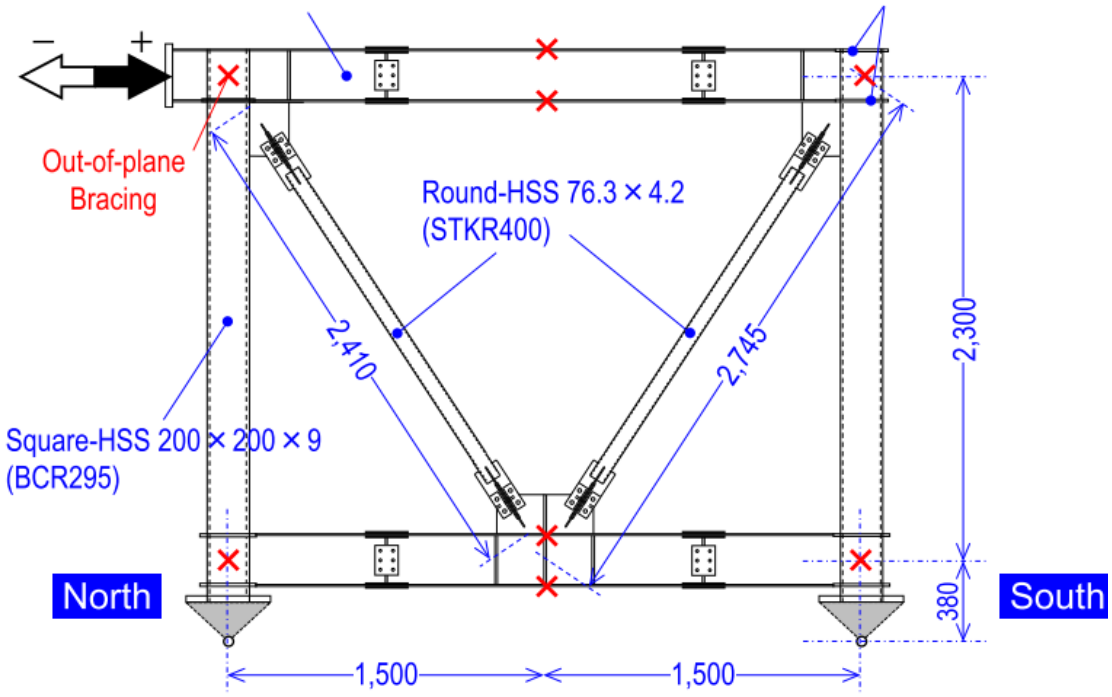

Figure 2.6: Chevron-Braced MRF Configuration (source: Seki et al. 2021 [16])

specimens differed in design and type of bracing connections. Four specimens adopted bolted bracing connections widely used in Japan and two specimens adopted a bracing connection detail according to US recommendations [16]. The braced frames were loaded according to the standard loading protocol provided in the AISC. More details about this work can be found in [16] and will be discussed in chapters 3 and 4.

The study showed that chevron-braced MRF system combining a compact chevron brace and a moment-resisting frame can safely develop large story drifts larger than 0.03 rad without failure to the brace or bracing connections. Severe yielding and torsion of the beam accompanied by substantial strength reduction in the lateral resistance of the moment-resisting frame occurred due to the force unbalance between the tension and compression braces.

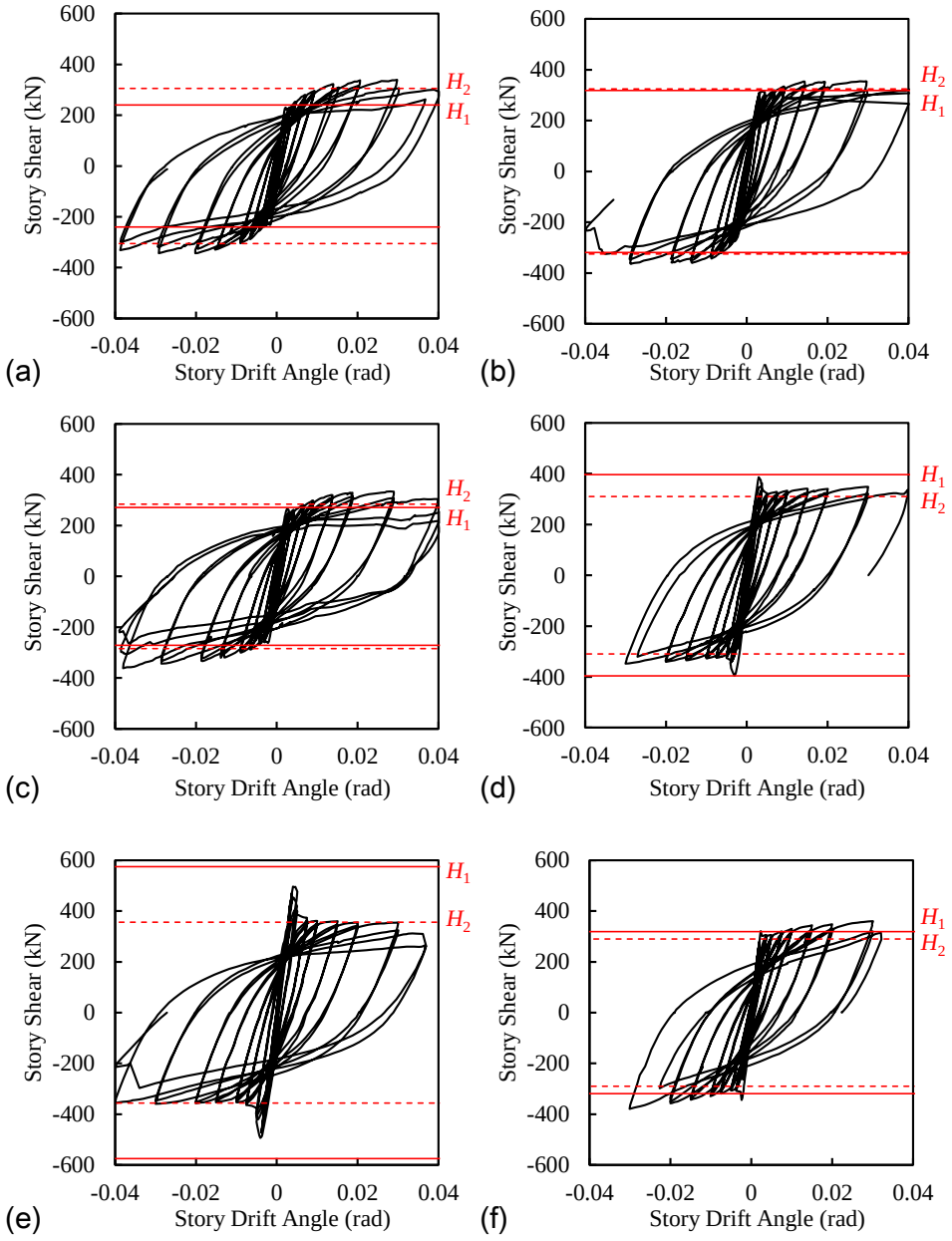

Figure 2.7: Hysteretic Response of braced frame by Seki et al. [16];

2.4 Analytical Studies

Substantial research had been conducted over the past years to study the performance of isolated braces and braced-frame subassemblages [Uriz and Mahin[17] , Huang and Mahin [18] , Hsiao et al.[19], [20], Sen et al. [21], [22], Karamanchi and Lignos[23] , Asada et al. [24], Tremblay and Roberts [25], Richards [26], etc.]. Models such as physical theory models, phenomenological models, fiber element models and finite element models (FEM) are often employed to simulate the performance of braces and

braced frames. Limited computational studies have been conducted on the performance of low- and mid-rise chevron-braced MRFs. Therefore, this section will discuss the computational studies on the performance of CBFs.

In a more recent study conducted by Uriz and Mahin [17], illustrated potential issues with conventional modelling of CBFs and validated numerical models able to model the global buckling of braces and low-cycle fatigue using *OpenSees*. Karamanchi et al. [23] further extend the work by Uriz and Mahin, and using a significantly larger brace database on brace tests, provided empirical equations to compute the fracture parameters for the most commonly used brace cross sections.

Hsiao et al. [19] conducted a research to develop a numerical model approach to simulate the performance of CBFs more accurately. Hsiao et al. [19] proposed a proposed an approach to simulate the behavior of the gusset plates. The models use a moment versus out-of-plane rotation relationship to account for the resistance provided by the gusset plates. The model will be discussed later. More recently, Sen et al. [21] numerically studied the performance of CBFs designed prior to the adoption of the capacity-based design principles. The older CBFs have complex yielding and failure mechanism and as per the authors, diverge from Special CBFs. The goal was to provide guidance for modelling non-ductile CBFs, including the effect of fracture of the braces for different slenderness ratio, different loading histories, etc.

Research to assess the seismic performance of multistory braced frames have been conducted. Khatib et al. [1] conducted a numerical investigation to study the inelastic response of multistory chevron-braced frames. The study investigated the used of stocky braces, stiff versus flexible beams, and the effect of frame participation. The research concluded that the inelastic response of chevron frames is highly sensitive to beam stiffness, brace slenderness and the characteristics of the ground excitation. Moreover, the use of stiff beams in multistory chevron CBFs may be counterproductive due to the build-up of large column compressive forces. Tremblay and Roberts [25] conducted a numerical study to investigate the performance of CBFs built according to Canadian standards, with 2-, 4-, 8-, and 12 story braced frame buildings. Different design approach for the beam was considered to assess the need to further relax the unbalance force required to proportion CBF beams (100%, 80%, and 60%). The results suggested that the unbalanced force required to proportion the beam can be relaxed up to 60% for buildings up to 4-story, but that 100% should be used for braced frames up to 12-story height. The work by Tremblay and Roberts suggested that for 12-story braced frames, chevron-braced frames can be used so long the gravity loads applied on the beams are small.

Following the experiments by Roeder et al. [14] and Sen et al. [15], Asada et al. [24] investigated the performance of CBFs where the beam was designed using conventional design approach (AISC

provisions at that time and "X" configuration (X CBFs)) and a proposed design method. The performance of 3- and 9- story braced frames designed with the different methods subjected to different ground motion hazards was investigated. The results suggested that the performance of the braced frames designed using the method proposed by the authors, where yielding of the beam was permitted, was comparable to the braced frames designed the AISC provisions. Paul Richards [26] conducted a numerical study on the performance a series buckling-restrained braced frames (BRBs), special concentrically braced frames (SCBFs), and eccentrically braced frames (EBFs) with 3, 9, and 18 story. The goal was to investigate the column demands on ductile braced frames. The results suggest that, for the 9- and 18-story frames, the demands were between 55 to 70% of the demands commonly used in design, but for the 3- story braced frames, the column demands were up to 100% greater than the demands used in design.

2.5 Design of Braced frames in Japan

The building standard Law of Japan requires a two-phase design for structures in Japan. The Level-2 is required for structures of 31 m < h < 60 m where h is the height of the building. The second phase design targets severe earthquake motions expected to occur one in the lifetime of the structure [27]. In the second-phase design, the capacity and the ductility of the structure must be computed to ensure the structure can sustain the earthquake load without major structural damages. As will be discussed later, for Japanese Concentrically braced frames, CBFs, the plastic lateral strength of the braced frames can be evaluated as a sum of the strength of the pair of braces and the Moment resisting frame.

The main design concern are:

1. The plastic strength of the system depends on the strength of the braces at the ultimate state, however, because no design provision is provided by the Japanese code and provisions, engineers use their engineering judgement to compute the strength of the braces;
2. No proportioning and detailing rules for the beams is provided, and there is no consensus among the structural engineering community on how to proportion the beams;

Because of this, there is uncertainty regarding the lateral strength capacity of braced frames built in Japan. It is believed that some braced frames may have overconservative designs at the same time that some other structures may not be able to sustain such earthquake demands.

3. EXPERIMENTAL PROGRAM AND FINITE-ELEMENT-MODEL

Figure 3.1 shows a chevron-braced MRF specimen reported by Seki et al.[16]. The figure illustrates the braced frame configuration and the different bracing connections examined, designated Types I to VI .

All specimens used braces that qualify as highly ductile according to the AISC *Seismic Provisions* [28]: Specimens 1 to 3 used round-HSS braces with D/t =18.2, and Specimens 4 to 6 used I-section braces with $b_f/2t_f = 4.2$ and $d/t_w = 9.5$. The different bracing connections controlled the buckling direction of the braces and rotational restraints: Specimen 5 oriented the braces to buckle in plane (IP) and the other specimens forced the braces to buckle out-of-plane (OOP). Bracing connections type III and VI were designed according to the suggestion by Roeder et al. [29] that asks for an elliptical clearance of 8 times the gusset-plate-thickness to accommodate out-of-plane buckling of the braces.

The specimens may be represented by the structural model illustrated in Figure 5.1 (b). As recommended by the AISC *Seismic Provisions* [28], the beam intersected by braces was braced at the brace-to-beam intersection. In Japan, sensible engineers would brace the beam at this section even though the code provisions [2], [3] do not require such bracing. The unbraced length of L_b =1,500 mm, measured between the braced point and beam-to-column node, was less than the lateral bracing requirement specified Special CBFs, computed as 3,660 mm, and the more stringent requirement for beams in Special MRFs, computed as 1,830 mm. The specimens were loaded cyclically using the loading sequence specified for prequalification tests of MRFs (AISC *Seismic Provisions* [28]) but abbreviating the smaller drift cycles. Three cycles were repeated for story-drift angles ±0.002, ±0.00375, ±0.005, ±0.0075 and ±0.01 rad, and two cycles were repeated for ±0.015, ±0.02, ±0.03 and ±0.04 rad. The performance of all the braced frame specimens was dictated by yielding of the beams. The forces transferred by the braces caused large vertical deflection and lateral-torsional deformation of the beam intersected by braces.

The vertical deflection of the beam forced the braces to deform more in compression than in tension, and thereby, prevented the braces from developing their tensile yield strength. Despite the severe deformation of the braces and beam, the specimens completed at least one cycle at ±0.03 rad prior to brace fracture or load termination. At the end of the test, no discerning damage had occurred at the bracing connections.

Lateral-torsional deformation of the beam was more severe in specimens whose braces buckled out-of-plane, and that had the braces rigidly connected to the beam (Figure 3.2). It was suspected that, for such brace orientation and bracing connections, improved performance might be achieved by

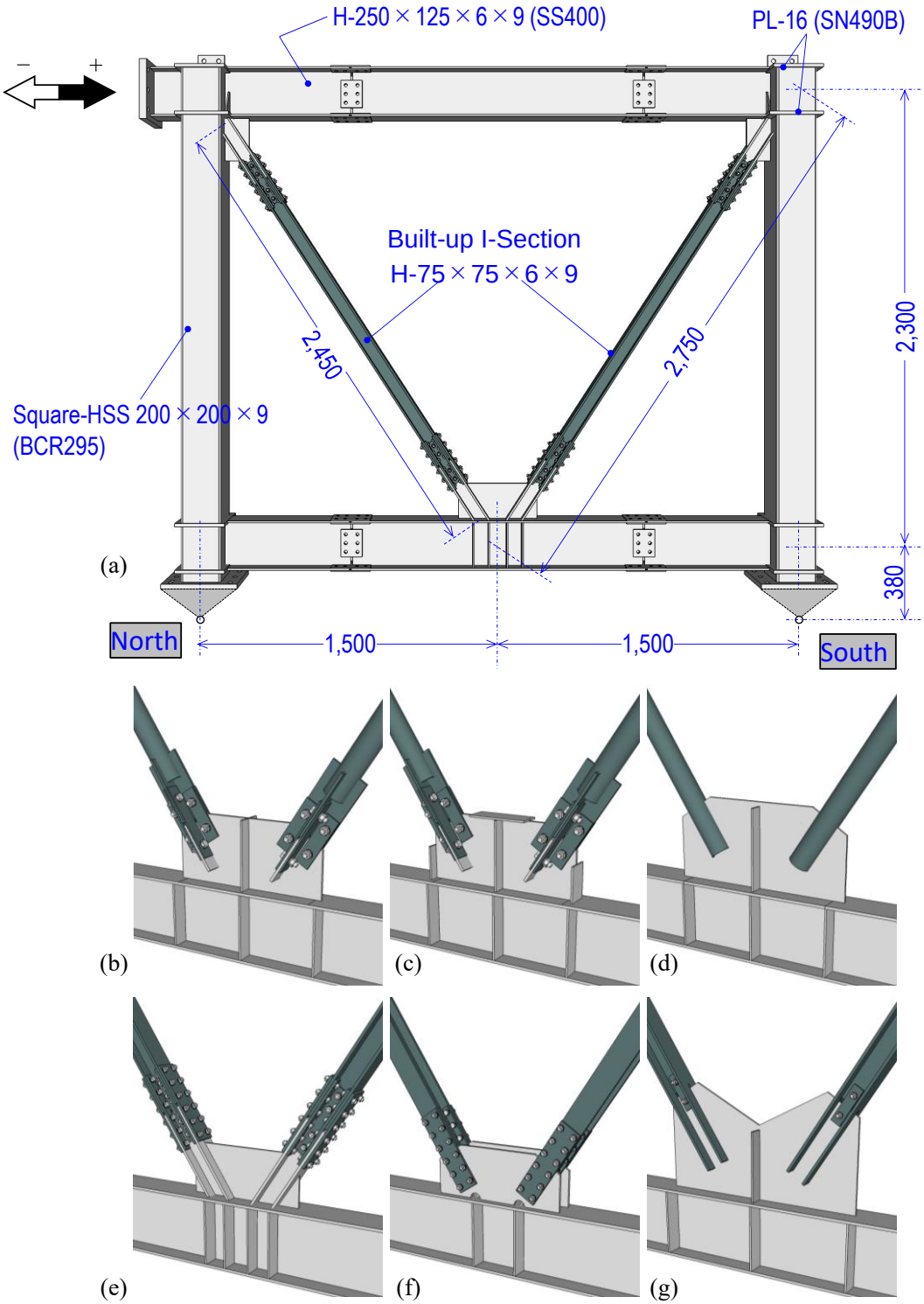

Figure 3.1: Chevron-braced MRF specimens tested by Seki et al [8]: (a) Specimen 4; and connections (b) type I from Specimen 1; (c) type II from Specimen 2; (d) type III from Specimen 3; (e) type IV from Specimen 4; (f) type V from Specimen 5; (g) type VI from Specimen 6 [Unit: mm].

enhancing lateral bracing of the beam intersected by braces, either by reducing the unbraced length of the beam or by increasing the bracing stiffness and strength.

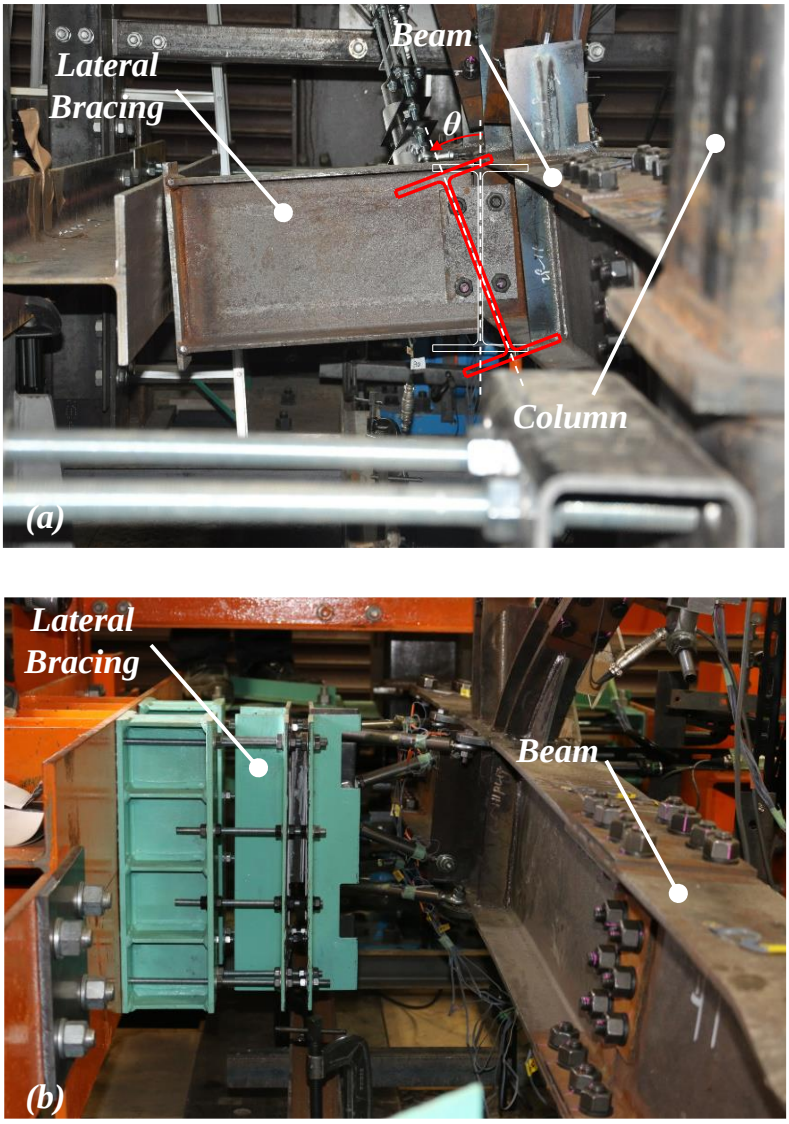

Figure 3.2: Rotation of the beam intersected by braces: (a) Specimen 3, and (b) Specimen 4 reported by Seki et al.[16].

The general-purpose finite element model (FEM) analysis software ADINA(2021) [30] was used to carry out the numerical analysis with the goal to reproduce and expand on the tests by Seki et al. [16]. Figure 3.3 outlines a typical three-dimensional FEM model used in this study. Load was applied at the top of the North column quasi-statically to produce the same story-drift history as in the tests. The models were pinned at the column bases and braced out-of-plane at midspan of the beams and at the column panels. The vertical rollers at the column base were not present in the tests and were not used for model validation. Under this condition, the eccentricity between the beam and pin support produces concentrated moments at the beam-to-column nodes. The vertical rollers at the column base were not used for a parametric study to examine bracing requirements for the beam intersected by the braces but were used for a parametric study to examine behavior over a range of different beam and brace proportions. By placing the vertical rollers, the mentioned eccentricity is eliminated. Bracing at the brace-to-beam joint was achieved by connecting a rotational spring of stiffness K_R and a translational spring of stiffness K_H to the centroid of the beam cross section.

The model comprised 4-node quadrilateral shell elements with 6 degrees-of-freedom per node, 2×2 integration points in plane and 5 integration points across the thickness. The welds were modelled by merging the elements. The bolted connections, which were designed as slip critical, and in fact did not slip during the experiments, except for the bracing connections of Specimen 4 that eventually fractured, were merged at the faying surface without explicitly modeling the bolts and bolt holes. Cracking and fracture were not modeled. Mesh refinement studies were conducted to determine the meshing scheme. The finest mesh size of 15×6 mm was adopted in the middle and ends of the braces. Fine meshing was also adopted in regions of the beams and columns and bracing connections where inelastic deformation was expected based on observations from the tests. The remaining regions that were expected to remain elastic were modeled by either a coarse mesh or by beam elements.

The first buckling mode obtained by eigenvalue analysis was used to specify initial imperfection with maximum out of straightness of $L/1000$ at the center of the braces. The magnitude of $L/1000$ was found to be adequate based on validation study that is partly presented in the next chapter.

Table 3.1: Material Calibration Parameters

Isotropic Hardening	Kinematic Hardening	
σ_{y0}=270Mpa	C_1=30000	γ_1=300
E_p=100	C_2=2000	γ_2=15

Material nonlinearity was incorporated in the model using the Von Mises yield condition and an associated flow rule. A combined nonlinear isotropic and kinematic hardening (Armstrong-Frederick kinematic hardening) rule was defined to account for cyclic hardening. The plasticity parameters are listed in table 1. The isotropic and kinematic hardening parameters were partly taken from Huang et al. [18] and calibrated to material tests on Japanese SN 400 and SM 490 steel by Yamada et al. [31].

The two pairs of kinematic hardening parameters (C_i and γ_i) are listed in Table 3.1. As shown in Figure 3.4 for SN 400 steel, the material model was calibrated to capture the coupon response on the tension side. The discrepancy between model and coupon response on the compression side was due to higher strength in the coupon test caused by contact between the coupon and buckling-restraining system. In the simulations of the braced frames, the parameters were adjusted to the yield and tensile strength reported by Seki et al. [16].

The accuracy and reliability of the FE modeling scheme were validated against the six CBF specimens tested by Seki et al. [16]. Figure 3.5 compares the numerical simulation against the experimental response, plotting the relationship between story shear and story-drift angle for three different specimens. In these simulations, the spring stiffness of the braces at the brace-to-beam joint matched the value measured during the tests: $K_R = 1.1K_{R0}$ and $K_H = 1.0K_{H0}$, where K_{R0} = 72.0 kN·m/rad and K_{H0} = 4,275 kN/m are the rotational and translational stiffness of the beam derived from fundamental mechanics assuming the beam fixed at the beam-to-column nodes against a concentrated torque or lateral load, respectively, in the middle. The numerical simulation reproduced the stiffness, strength, and gradual strength degradation of all specimens. Figure 3.6 compares the overall deformation of Specimen 6 from numerical simulation and experiment. The numerical simulation reproduced the experimental behavior quite adequately, from brace buckling, formation of a weak-beam mechanism, deformation of the beam intersected by braces, and local flange deformation of the beam at plastic hinges.

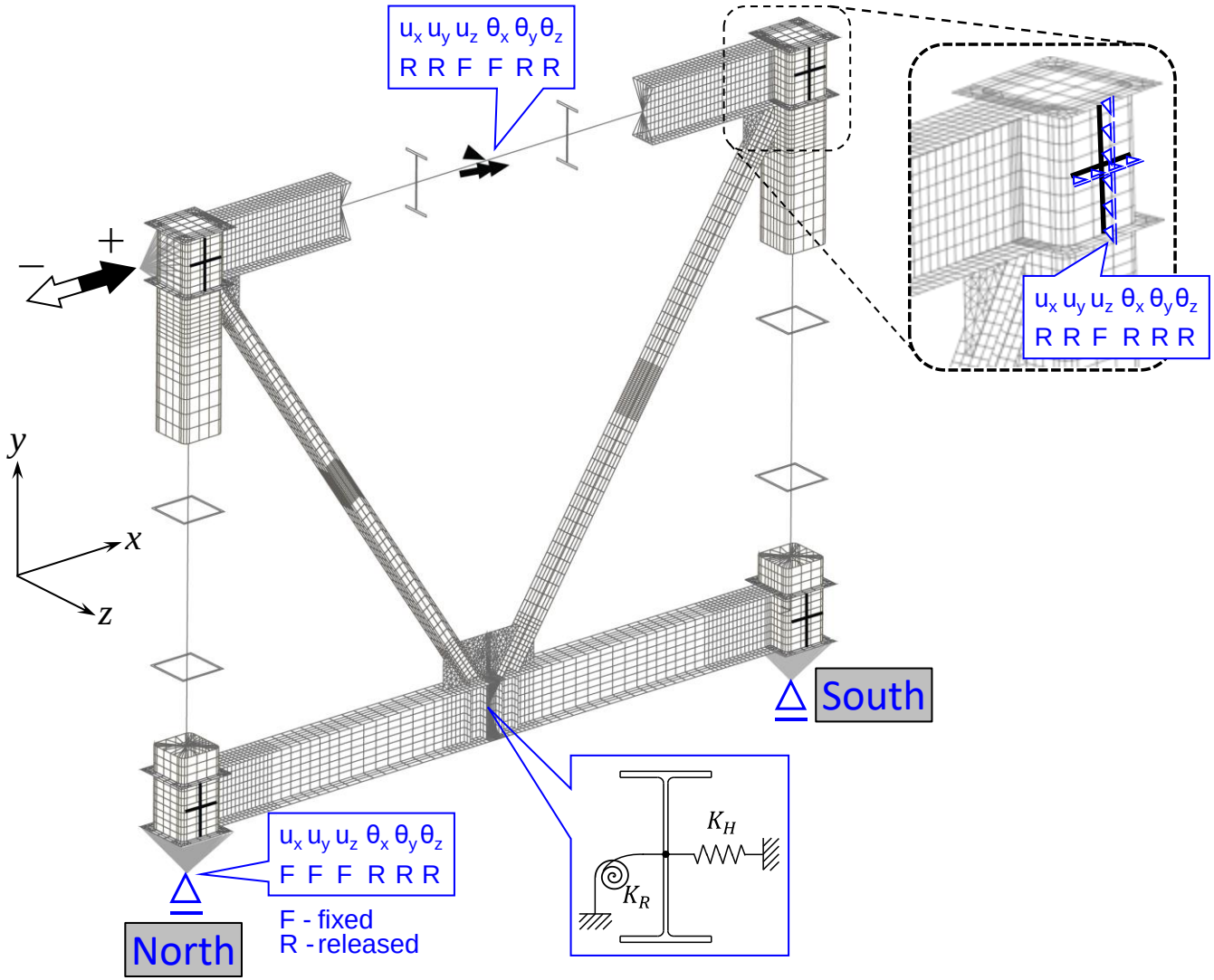

Figure 3.3 - Overview of Chevron-braced MRF Finite Element Model.

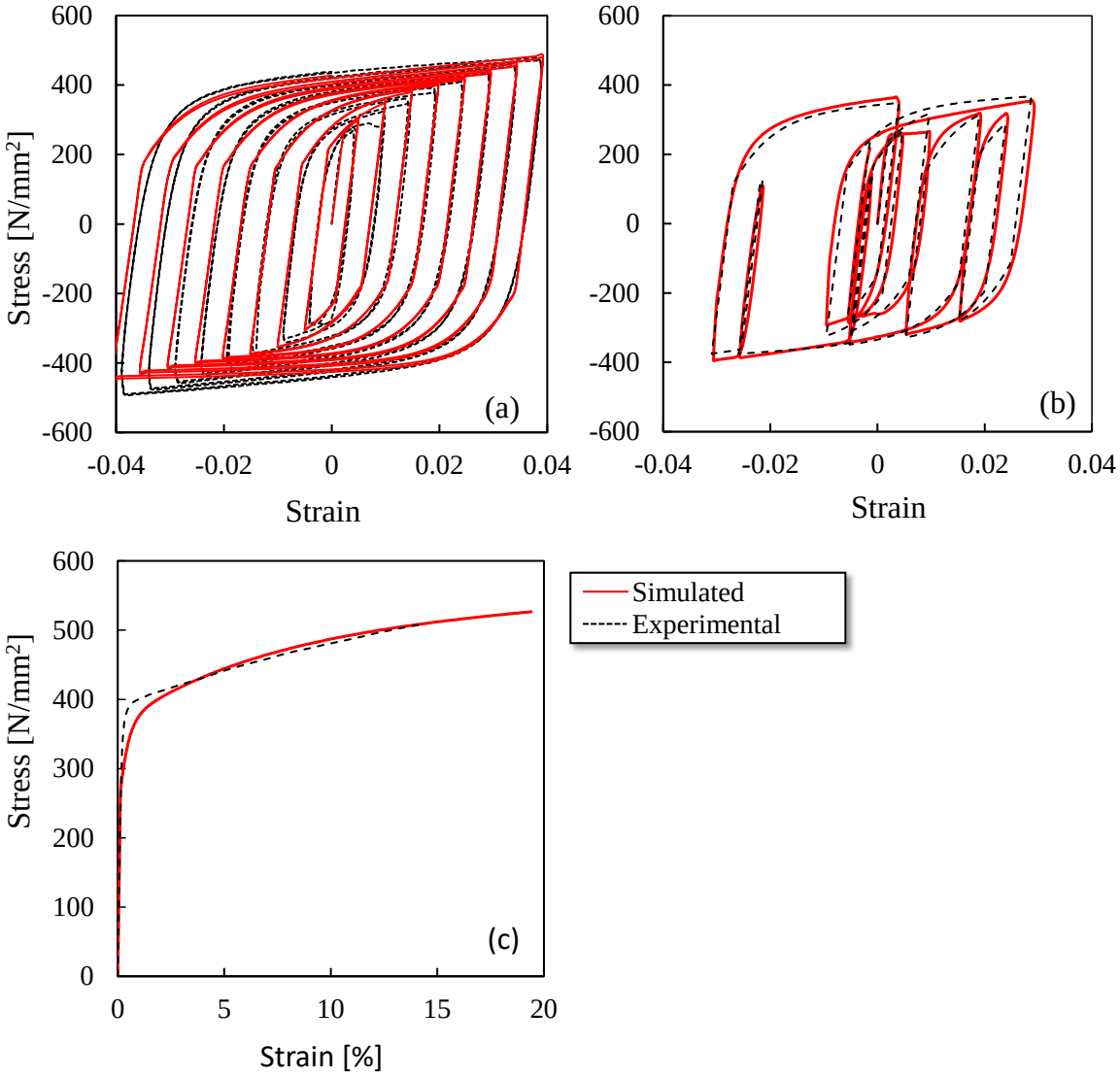

Figure 3.4: Simulated vs. experimental cyclic stress-strain curves: (a) Symmetric cyclic loading; (b) non-symmetric cyclic loading; and (c) monotonic tension.

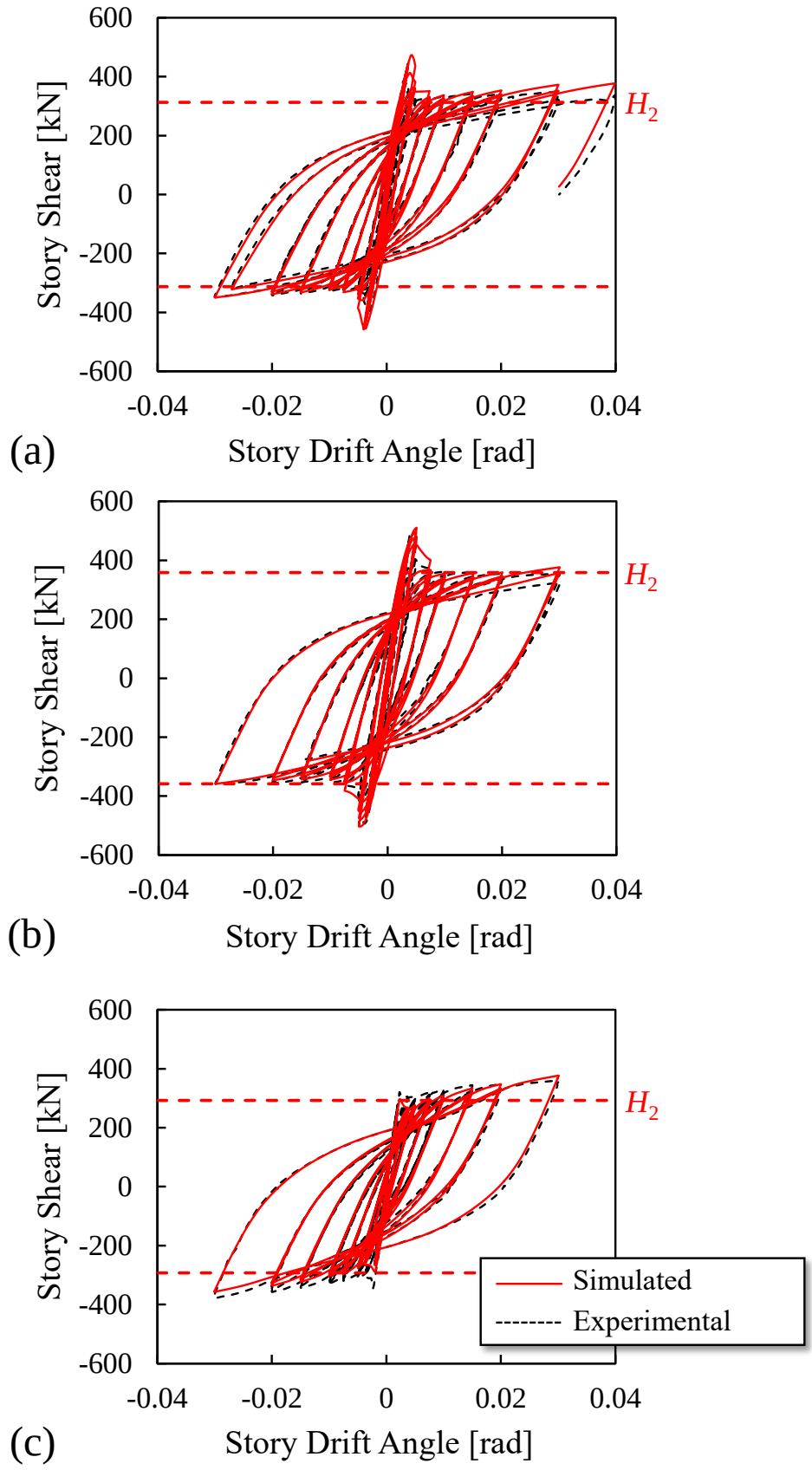

Figure 3.5 – Experimental versus simulated response for: (a) Specimen 4; (b) Specimen 5 and (c) Specimen

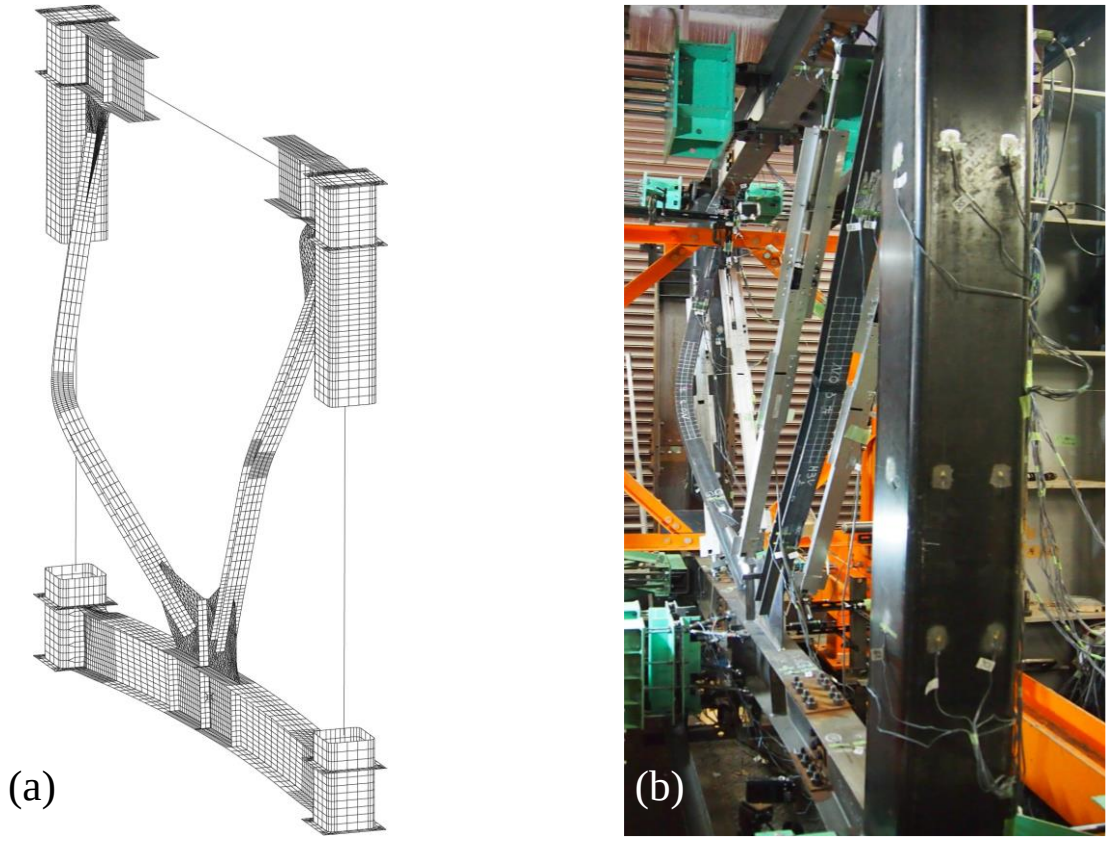

Figure 3.6 - Deformed of Specimen 6 at end of test: (a) Experiment; (b) FE Model.

Figure 3.7 decomposes the relationship between the story shear and story-drift angle, for Specimen 4, obtained from simulation and experiment, into the contribution of the MRF and the pair of braces for Model 4. Good agreement was obtained between simulation and experiment. In the figure, key strength values defined in Seki et al. [16] are shown in the figure: H_{1b} is the lateral strength of the pair of braces at the onset of brace buckling, where, for this specimen, brace length was taken as the distance between the face of the column or beam, and the effective buckling length factor was taken as 0.75; H_{2b} and H_{2f} are the resistance of the braces and the MRF when an energy-dissipation mechanism is formed, computed for κ = 1.25 and 1.5. It is noted that $H_2 = H_{2b} + H_{2f}$, indicated in Figure 3.5, is mathematically independent of κ. In both simulation and experiment, the combined strength of braces was largest when first brace buckling occurred, but the simulated strength exceeded the measured strength and H_{1b} by 22% and 17%, respectively; at ±0.02 rad, the simulated strength of the braces nearly equaled the measured strength and H_{2b}.

The simulated strength of the MRF nearly equaled the measured strength but exceeded H_{2f}. The large exceedance of the simulated MRF strength over H_{2f} assuming κ =1.5 suggested a need to further examine κ. As observed in the experiments, the weak-beam mechanism controlled for all the models.

The validated FEM modelling and analysis scheme was used to conduct a parametric study on the effect of key design parameters beyond the range examined in the experimental program. The design parameters included: (1) torsional and translational restraint of the beam intersected by braces discussed in Chapter 4; (2) the relative lateral strength of the beam with respect to the braces, expressed by r_0; and (3) the type of bracing connection.

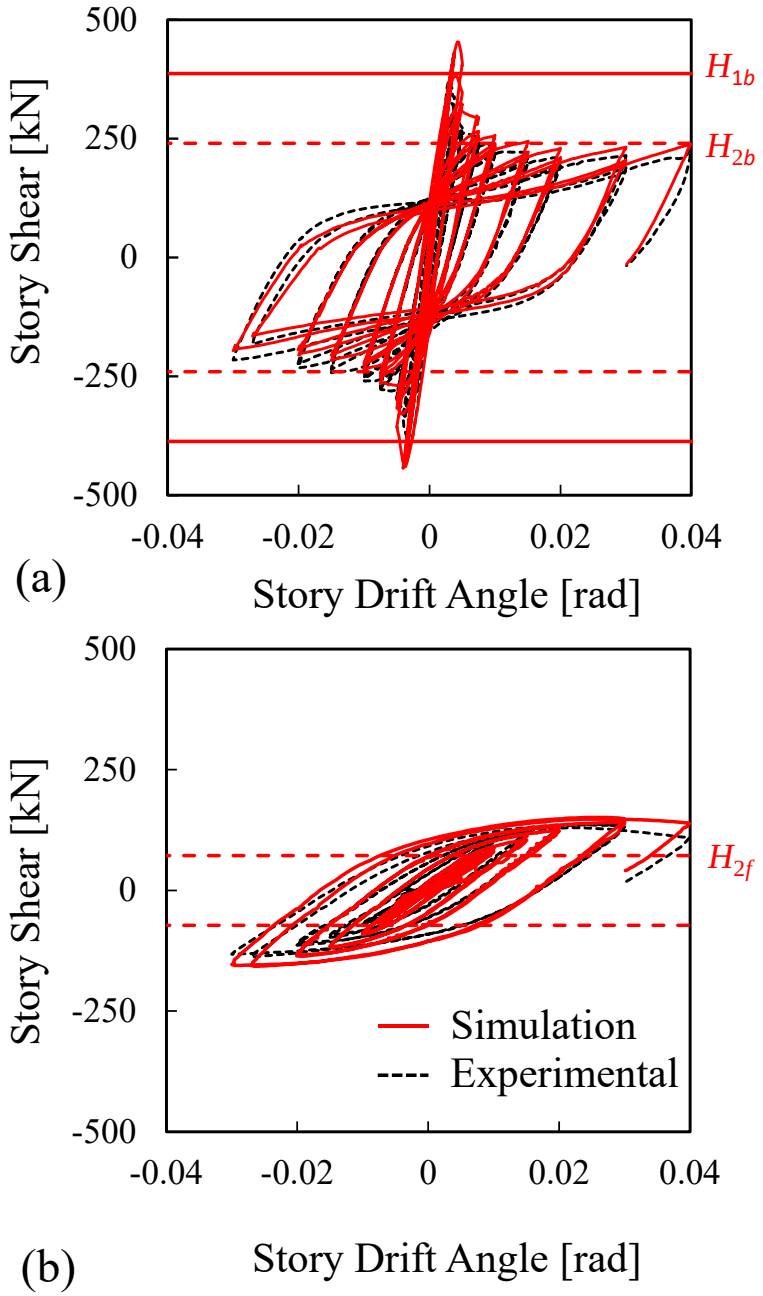

Figure 3.7:Decomposed simulated and experimental response of Specimen 4: (a) Braces; and (b) Moment frame.

4. BRACING REQUIREMENTS FOR BEAM INTERSECTED BY BRACES

A parametric study was conducted to examine the lateral bracing requirements for the beam intersecting the braces. The cyclic loading behavior of Models 4, 5 and 6, by Seki et al. [16] which corresponds to Specimens 4, 5 and 6 in the experimental program, were varied with different spring stiffnesses K_R and K_H at the brace-to-beam joint.

As listed in Table 4.1, the stiffness of the spring was varied as the previously mentioned reference values K_{R0} or K_{H0} times zero, unity or infinity. The braces in Specimens 4 and 6 were oriented to buckle out of plane (OOP) whereas in Specimen 5 the braces were oriented to buckle in plane (IP). For Specimen 4, an additional case was examined where the beam was braced at two quarter points in addition to middle at the brace-to-beam joint.

The main goal of this parametric study is to understand the magnitude of the torsional moment demands on the beam intersecting the braces and provide guidelines on the bracing of this beam.

Table 4.1: Simulated cases to examine bracing requirements.

Model	**Braces**		**Lateral Bracing**		
	Bracing connection	Buckling direction	K_R	K_H	Location
4a	IV	OOP	0	0	middle
4b			K_{R0}	0	
4c			0	K_{H0}	
4d			K_{R0}	K_{H0}	
4e			∞	∞	
4f			K_{R0}	K_{H0}	quarter points
5a	V	IP	0	0	middle
5b			K_{R0}	0	
5c			0	K_{H0}	
5d			K_{R0}	K_{H0}	
5e			∞	∞	
6a	VI	OOP	0	0	middle
6b			K_{R0}	0	
6c			0	K_{H0}	
6d			K_{R0}	K_{H0}	
6e			∞	∞	

4.1. Torsion Demands on the Beam Intersecting the Braces

The torsional moment delivered by the braces on the beam cannot be evaluated straightforwardly from the numerical simulation. Instead, the components of the torsional moment had to be sampled at a key location (in this case the connection between the braces and the gusset plates). The loading history of the braces axial force (F_y), out-of-plane force component (F_Z) and bending moment (M) illustrated in Figure 4.1 were sampled from the numerical simulation model. The torsional moment delivered by the braces, T, can be computed as follows:

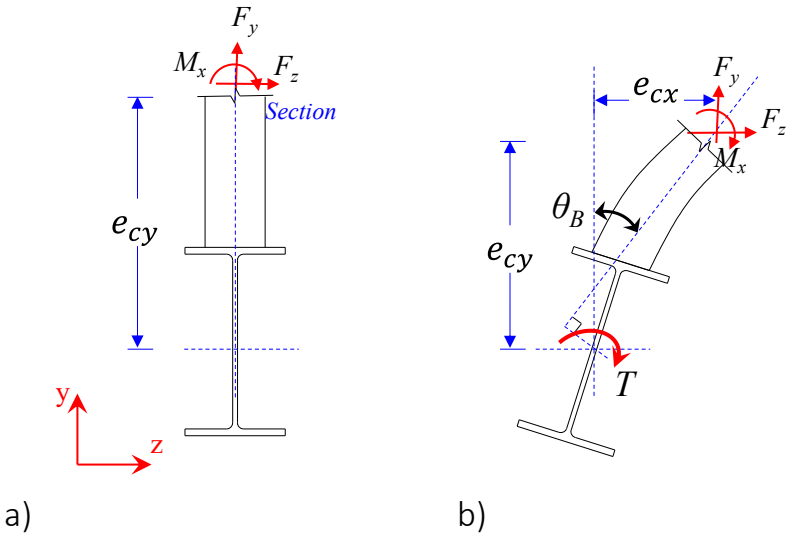

Figure 4.1: Structural model to compute torsional demands from FEM Model: (a) before deformation (b) after deformation of the beam

$$T = (-F_z \times e_{cy} + F_y \times e_{cx} - M_x)_{NB} + (-F_z \times e_{cy} + F_y \times e_{cx} + M_x)_{SB} \quad (4.1)$$

In the above equation, the balance between the torsional moment delivered by each brace is quantified. The two components of the equation compute the moment delivered by the opposing braces. For both Models 4 and 6, the braces were oriented to buckle out-of-plane, with both braces buckling in the same direction. Therefore, the torsional moment tends to cancel between the two braces.

Figure 4.2 plots the history of force components sampled for Model 4a for the two braces. As observed in the figure, the out-of-plane component of the brace force is close to zero and can therefore be neglected.

The eccentricities of the brace forces components are depicted in Figure 4.3. The figure shows that the transverse displacement of the braces starts to grow after buckling of the braces and grows larger with further loading cycle. In Model 4a, the beam is unbraced, and thus can rotate freely. The eccentricity of the tension and compression brace grows large compared to Model 4e, where the beam is fully braced.

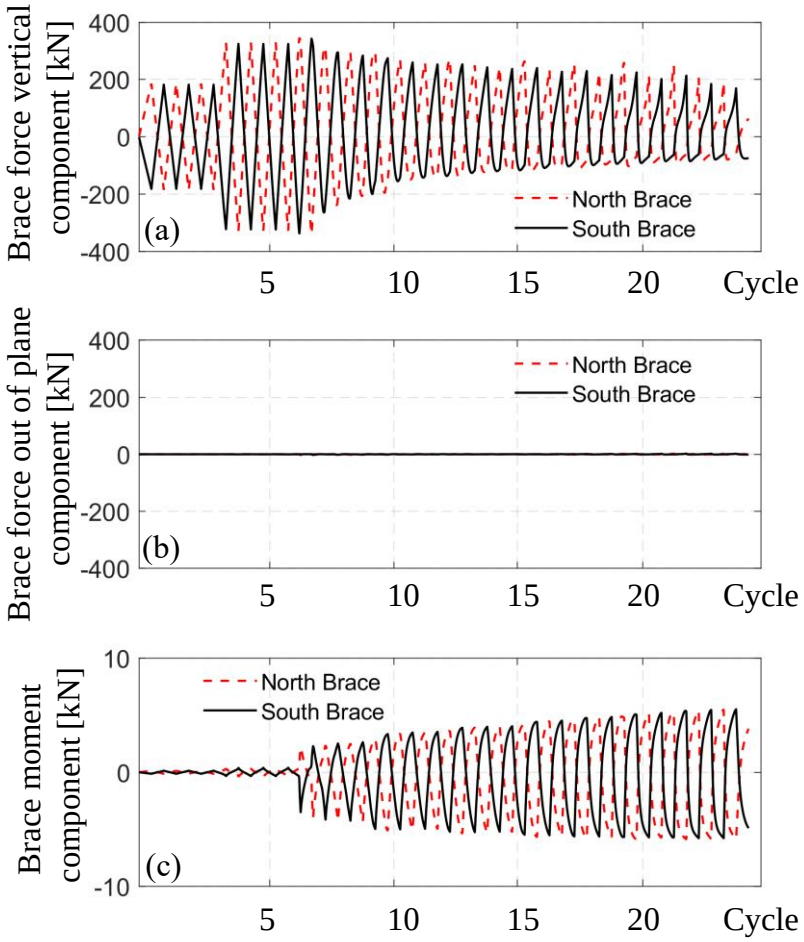

Figure 4.2: Brace force components for Model 4a: (a) Vertical component, (b) horizontal out-of-plane component, and (c) Bending moment.

In the cycle after buckling of the brace, the rotation of the brace in tension was small but increase with further loading amplitude.

The torsional moment delivered by each component of the brace force is shown in Figure 4.4 to Figure 4.6, for Model 4a, 4d and 4e, respectively. For Model 4a, the torsional moment delivered by the tension and compression brace after buckling of the braces seems to be nearly symmetric, but the

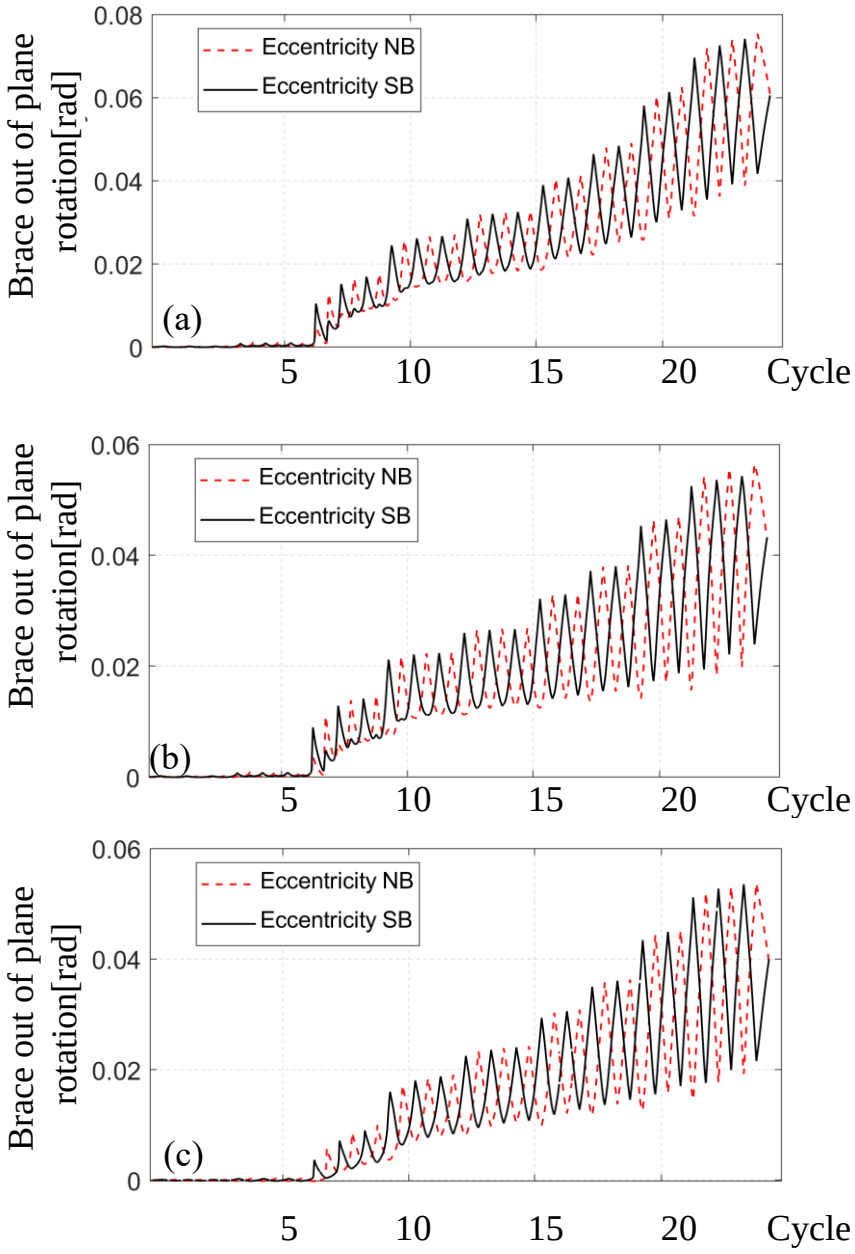

Figure 4.3: Brace out-of-plane rotation angle: (a) Model 4a, (b) Model 4d, and (c) (b) Model 4e.

moment delivered by the brace when in tension grows larger with increasing loading amplitude due to the rotation of the beam.

In Model 4d and 4e, the torsional moment delivered by the vertical force component of the brace when in tension is smaller than the compression brace.

For Model 4e, the torsional moment delivered by the tension brace was small at the onset of brace buckling but grew large with increasing loading cycle. In contrast the moment delivered by the compression brace was large after buckling of the braces. At the end of the loading protocol, the magnitude of the torsional moment delivered by the tension and compression brace was nearly the same.

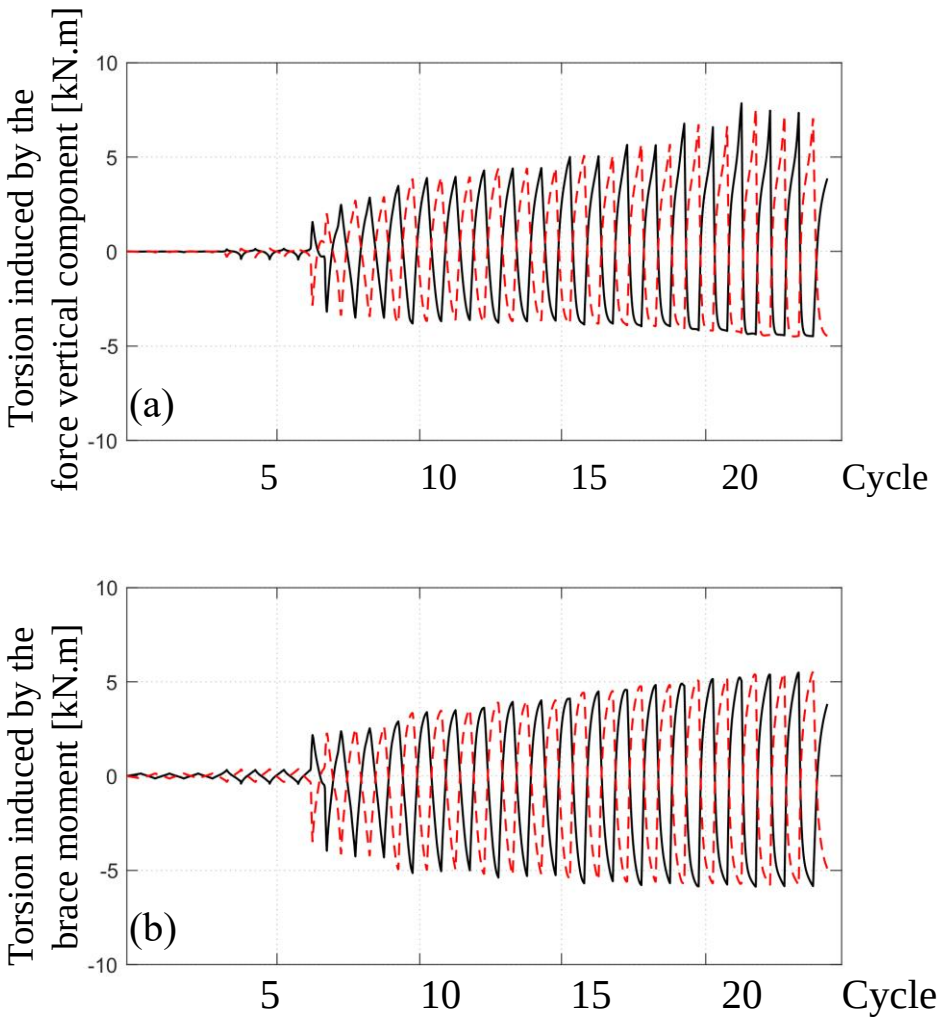

Figure 4.4: Decomposition of the Brace Induced torsional Moment for Model 4a: (a) Torsion due to brace axial force, and (b) torsional moment due to brace moment.

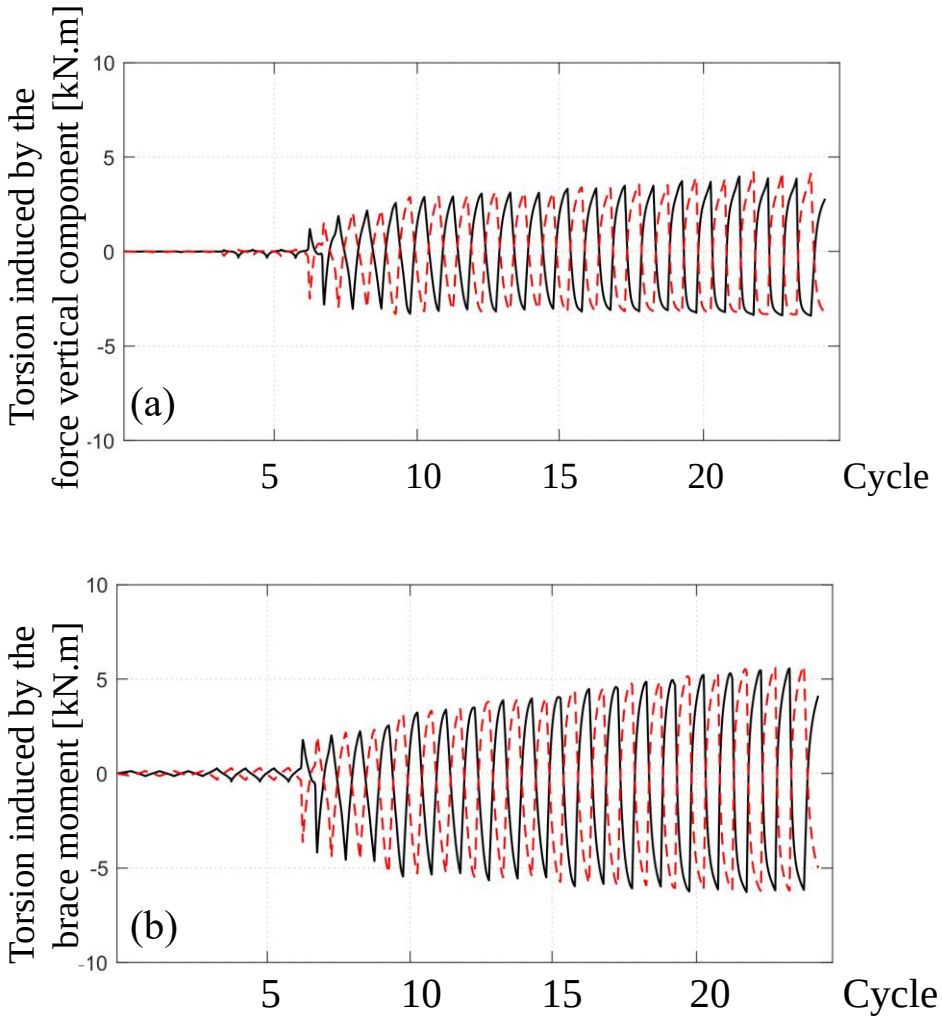

Figure 4.5: Decomposition of the Brace Induced torsional Moment for Model 4d: (a) Torsion due to brace axial force, and (b) torsional moment due to brace moment.

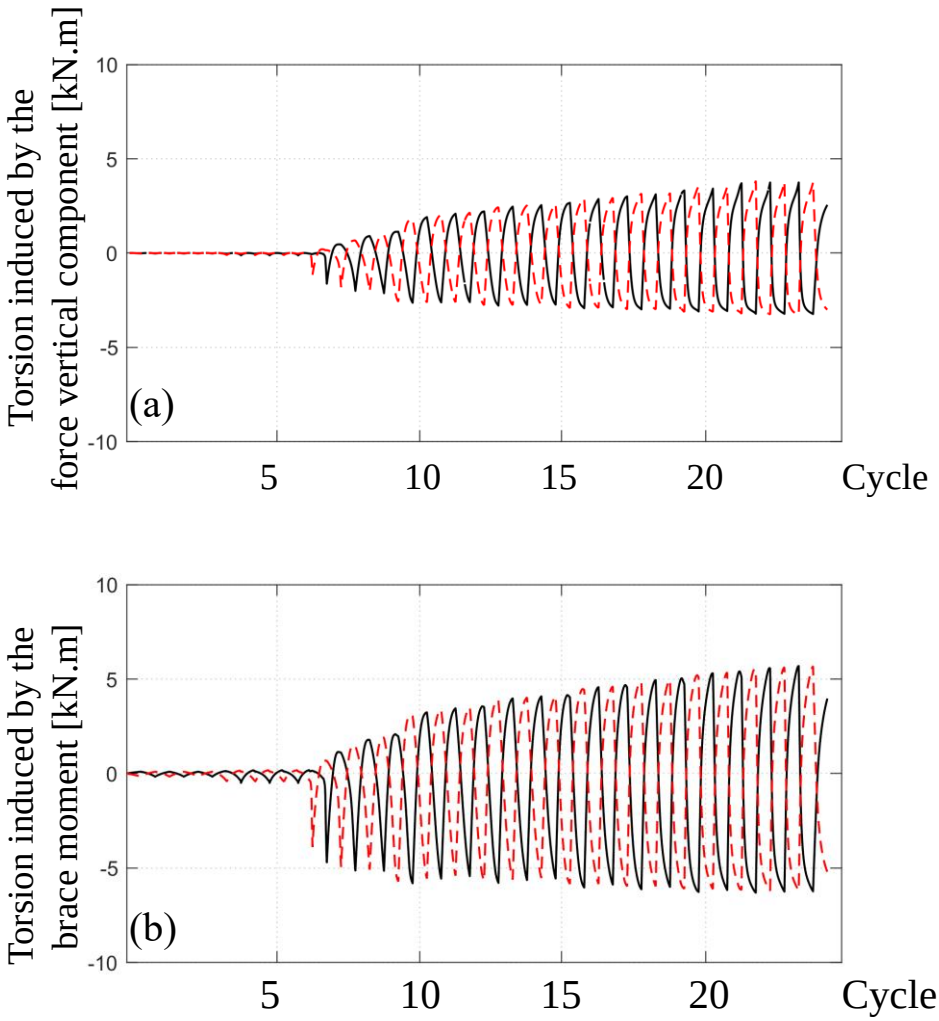

Figure 4.6: Decomposition of the Brace Induced torsional Moment for Model 4e: (a) Torsion due to brace axial force, and (b) torsional moment due to brace moment.

4.1.1. Torsional Moment delivered by the braces

For both Models 4 and 6, the braces were oriented to buckle out-of-plane (OOP), with both braces buckling in the same direction. but the bracing connections were rigid for Model 4 and flexible for Model 6.

Figure 4.7 and Figure 4.8 plots for Models 4a and 6a, which adopted $K_R = K_H = 0$, and Models 4e and 6e, which adopted $K_R = K_H = \infty$, the torsional moment delivered to the beam by each brace over the loading history. In all the braced frame models, the torsional moment was negligible until buckling of the braces, after which the moments grew larger with increasing loading amplitude. The compression and tension braces delivered moment in the opposing direction because the two braces were forced by the rigid bracing connections, which induced plastic deformation of themselves, to buckle in the same out-of-plane orientation. In Model 6a and 6e, the torsional moment delivered by both braces remained small even after brace buckling and was one order smaller than in Model 4e.

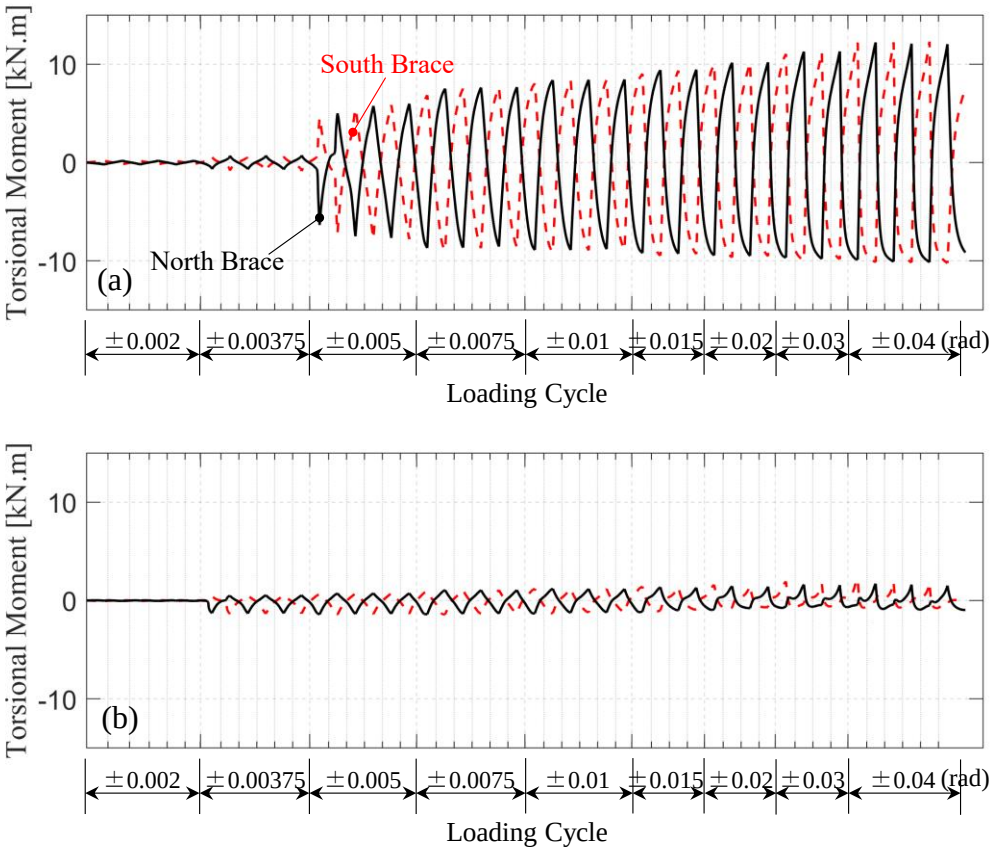

Figure 4.7-Torsional Moment induced by each brace: (a) Model 4a and (b) Model 6a.

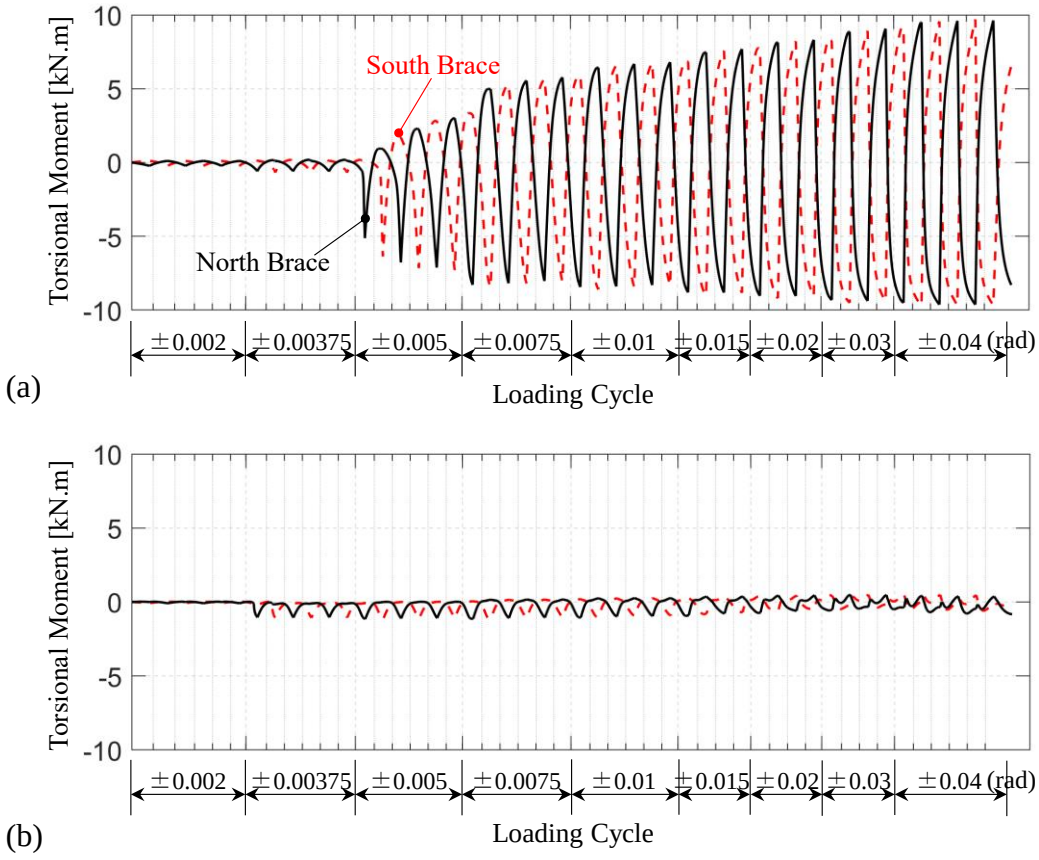

Figure 4.8-Torsional Moment induced by each brace: (a) Model 4e and (b) Model 6e.

Figure 4.9 plots the torsional moment delivered by the braces, T, i.e., the sum of contributions of the two braces, against the story drift angle for both Models 4 and 6 with different cases of lateral bracing. The yielding torsional moment, T_y of the beam, assuming the beam fixed at the beam-to-column nodes and subjected to a concentrated torque at mid span, is shown for reference. Between these two models, the induced torsional moment was expected to be larger in Model 4, given that the bracing connection provided larger fixity to brace out-of-plane displacement, than in Model 6.

Models 4a and 6a, which adopted $K_R = K_H = 0$, and hence resisted the torsional moment solely by the beam, drew a large moment of $1.04T_y$ and $0.63T_y$, respectively. Models 4d and 6d, which adopted $K_R = K_{R0}$ and $K_H = K_{H0}$, drew substantial moment of $0.61T_y$ and $0.20T_y$, respectively, but the moment resisted by the rotational spring was roughly half of the delivered moment at, $0.37T_y$ and $0.1T_y$, respectively. Models 4e and 6e, which adopted $K_R = K_H = \infty$, drew $1.24T_y$ and $0.26T_y$, respectively, but the moment was nearly fully resisted by the

springs. Among the different cases of lateral bracing, case $K_R = K_H = \infty$ drew the largest moment from the braces.

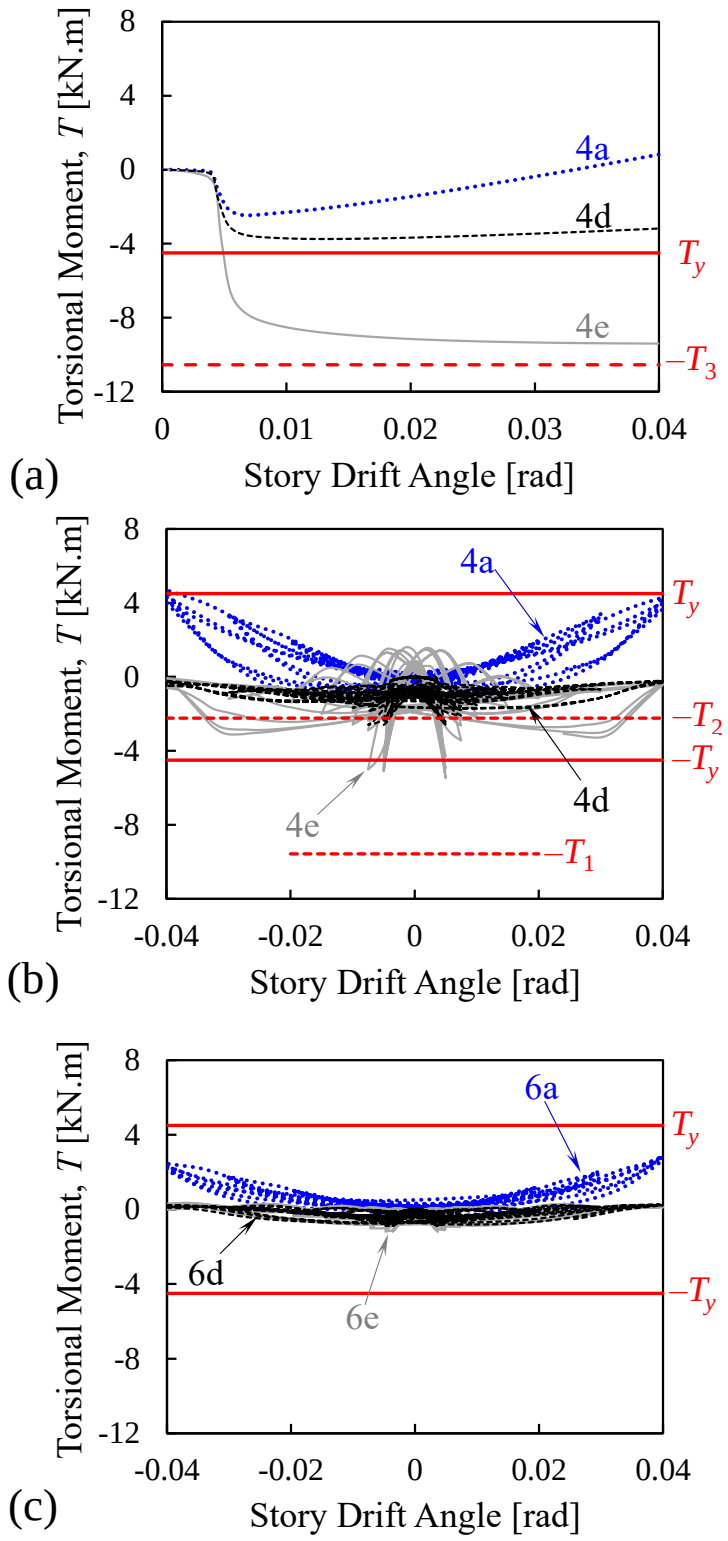

Figure 4.9: Torsional moment delivered by the braces: (a) Model 4 under Monotonic; (b) Model 4; and (b) Model 6.

Except for case $K_R = K_H = 0$, all cases developed the maximum torsional moment after buckling of the second brace. The moment reduced after brace buckling, and subsequently grew with story drift, but remained smaller than the value recorded at second brace buckling.

It is noted that that torsional moment depends on loading history. Figure 4.9(a) shows the monotonic loading response of Model 4, which is quite different from the cyclic loading response of the same model shown in Figure 4.9(b).

Models 4e, which adopted $K_R = K_H = \infty$, drew torsional moment greater than T_y because the tension brace remained completely straight and did not cancel the moment delivered by the compression brace. Models 4a and 4d drew much smaller moment as the beam twisted and thereby allowed the tension brace to produce a cancelling moment. At 0.02-rad drift, the rotational spring of Model 4d resisted $0.53T_y$. Although not included in the figure, Models 5a to 5e, which had the braces oriented to buckle in plane (IP), drew negligible torsional moment from the braces for all lateral bracing cases.

The torsional demands on the beam were evaluated for the three bracing connections shown in Figure 4.10. The figure shows that the torsional moment demands delivered by the braces in Model 4 was significantly larger than Model 5 and 6.

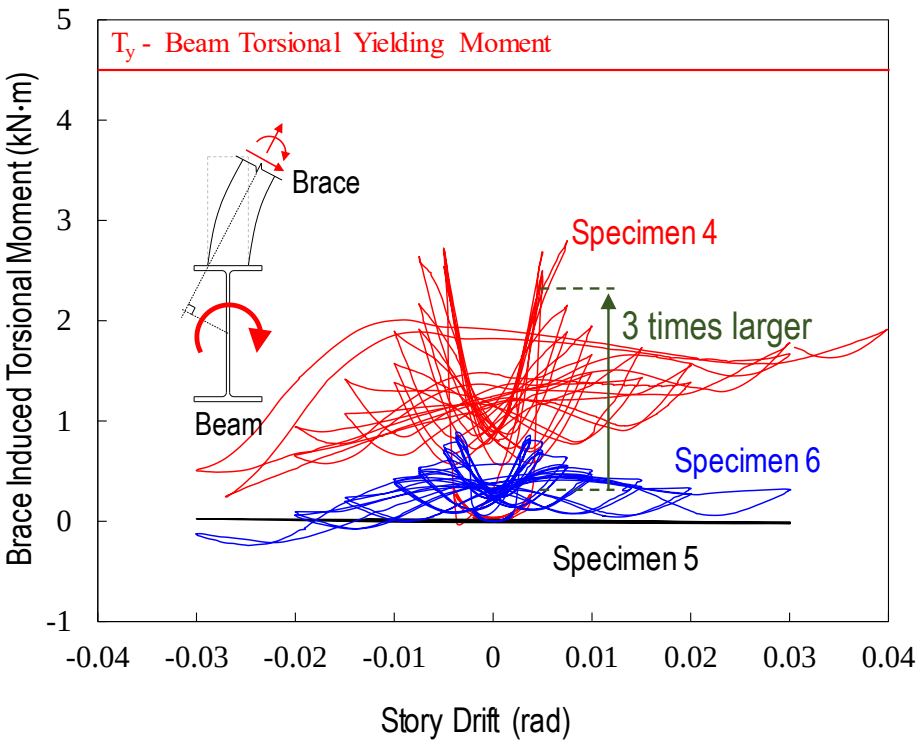

Figure 4.10: Comparison of the torsional moment delivered by the different bracing connections.

4.1.2. Beam Response

The beam twist angle, φ, and the lateral deflection of beam at mid-span, δ shown in was accessed for all the models. Figure 4.12 to Figure 4.13 plots for Models 4 and 6, respectively, with different cases of lateral bracing, the relationship between the torsional moment delivered by the braces, *T*, and twist angle, φ, and the relationship between out-of-plane deflection of the brace-to-beam joint, δ, and story-drift ratio. The reference line in the figure, indicates the twist angle at first yield, φ_y, computed assuming the beam as torsionally fixed at the ends, subjected to a concentrated torque at the midspan. Computed deformation sampled at +0.04 rad is depicted for reference. Models 4a and 6a, which adopted $K_R = K_H = 0$, allowed twisting and out-of-plane deflection to start immediately after brace buckling and grow larger during each subsequent cycle. The torsional moment and twist angle was twice as large in Model 4a than in Model 6a. Models 4d and 6d, which adopted $K_R = K_{R0}$ and $K_H = K_{H0}$, developed small twist angle, $0.39\varphi_y$ in Model 4d and $0.11\varphi_y$ in Model 6d, and negligible out-of-plane deflection. Models 4e and 6e, which adopted $K_R = K_H = \infty$ developed no twist angle and no out-of-plane deflection. Model 4f, which braced the beam at the quarter points (3 sections), was more effective than Model 4d, which braced the beam only at the middle (1 section), in restraining the twist and out-of-plane displacement of the beam.

Two bracing cases, $K_R = K_{R0}$ and $K_H = 0$ (Models 4b and 6b), and $K_R = 0$ and $K_H = K_{H0}$ (Models 4c and 6c), may be used to examine whether rotational or translational bracing alone is sufficient. Models 4b and 6b restrained beam twisting to within $0.48\varphi_y$ and $0.26\varphi_y$ but allowed large out-of-plane deflection of 26 mm and 13.5 mm, respectively. Models 4c and 6c allowed beam twisting

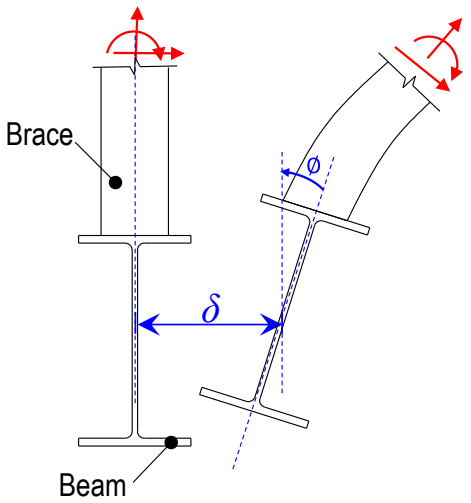

Figure 4.11: Beam intersected by braces out-of -plane displacement and rotation.

of $0.96\varphi_y$ and $0.27\varphi_y$ but restrained out-of-plane deflection to within 2 mm for both Models. Therefore, both rotational and translational bracing should be provided to effectively restrain deformation of the beam intersected by braces in Model 4.

For case $K_R = 0$ & $K_H = K_{H_0}$, where only the translational spring was provided, the twist angle of the beam was allowed to grow to large size, close to 0.037 rad and 0.013 rad in Model 4 and 6, respectively. Beam lateral deflection was effectively restrained with the out of plane deflection of the beam growing close to 5 mm and 1.5 mm for Model 4 and 6, respectively.

The results suggest that a lateral bracing system that provides $K_R = K_{R0}$ and $K_H = K_{H0}$ at the brace-to-beam node can effectively restrain twisting and out-of-plane deflection of the beam. It is noted that, in real applications, the composite floor slab if present restrains rotational and translational motion of the beam. Although no supporting data is provided in this research, the presence of floor slab may reduce beam deformation, but the floor slab may experience substantial damage due to forces delivered by the braces. Further study is warranted to understand how the floor slab and the beam interact in chevron-braced MRFs. Rigid bracing connections such as Connection IV (Figure 3.1 (e)) provides large rotational restraint to the braces and thereby induces large torsional demands on the beam. The torsional demand is much smaller if the braces are oriented to buckle in plane as per Connection V (Figure 3.1 (f)) or if the bracing connection supplies minimal rotational restraint as per Connection VI (Figure 3.1 (g)).

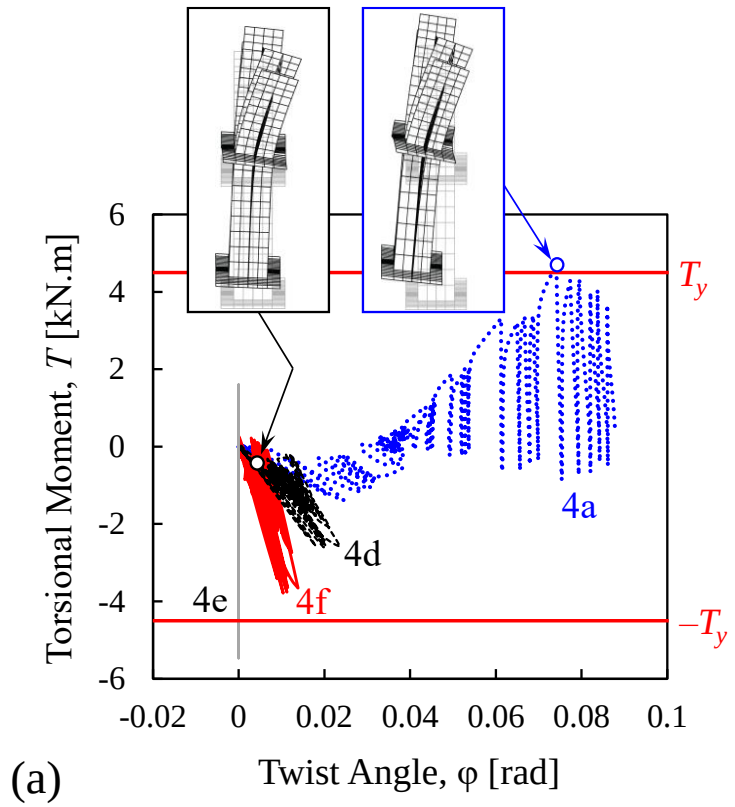

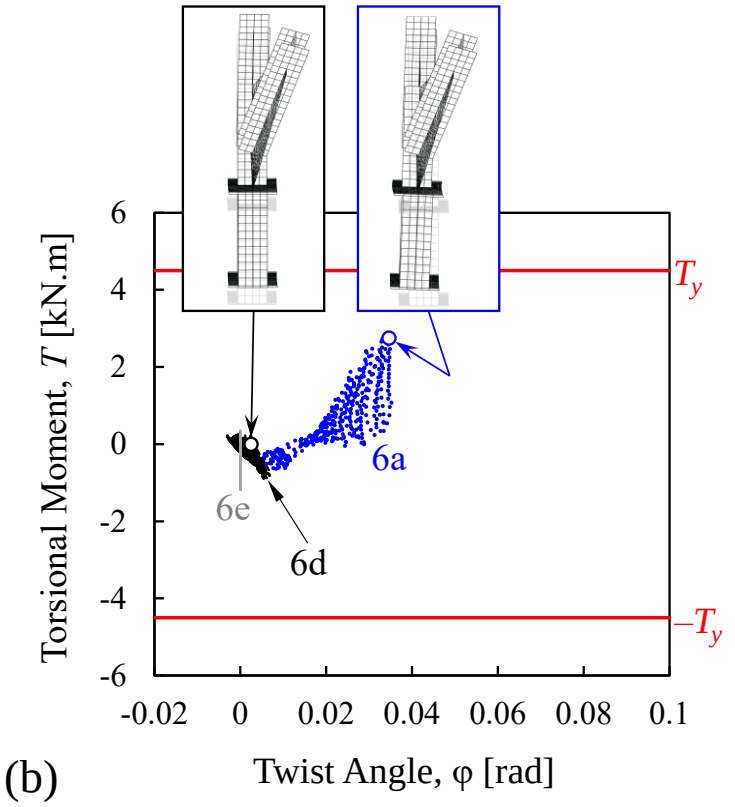

Figure 4.12: Torsional response of the lower beam: (a) Model 4; and (b) Model 6.

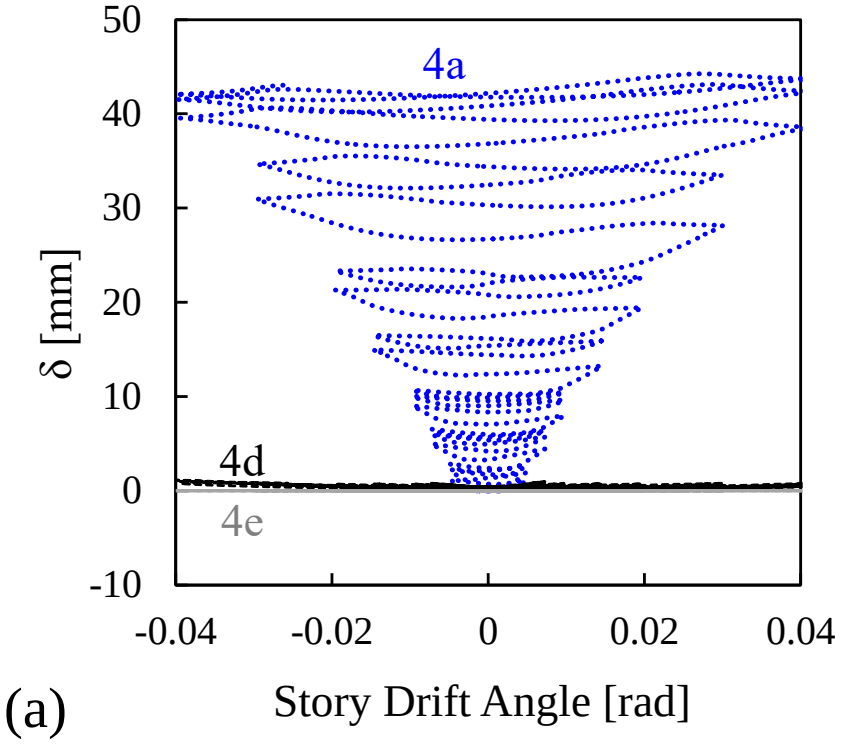

(a)

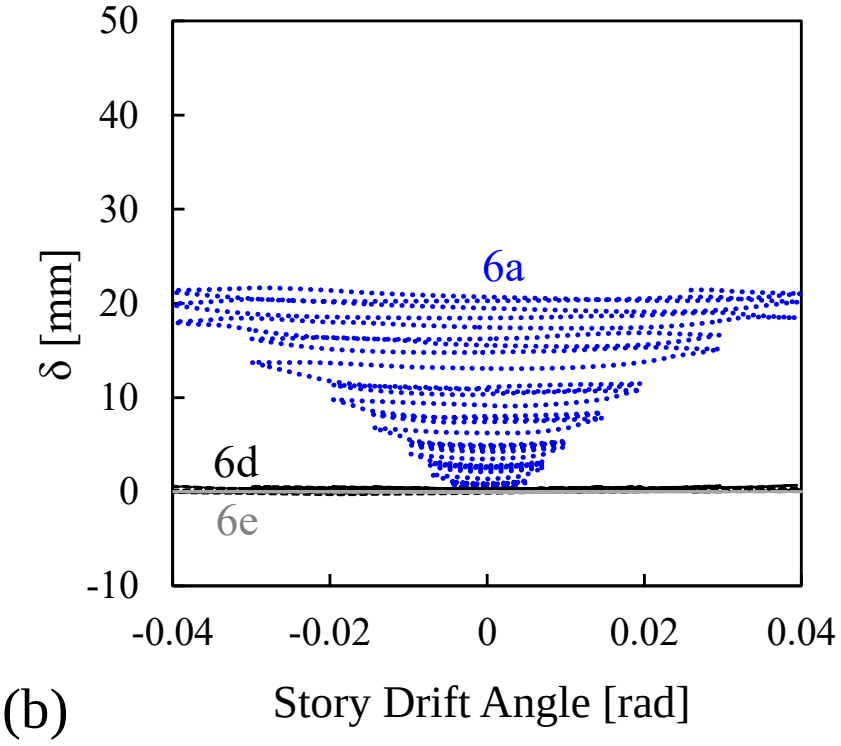

(b)

Figure 4.13: Effect of lateral bracing stiffness on the beam lateral deflection: (a) Model 4; and (b) Model 6.

4.1.3. Brace Response

Figure 4.14 plots the simulated response of the braces of Model 4 and 6 with different cases of lateral bracing. The figure shows that for all the braced frame models, the effect of the lateral bracing on the performance of the braces was negligible.

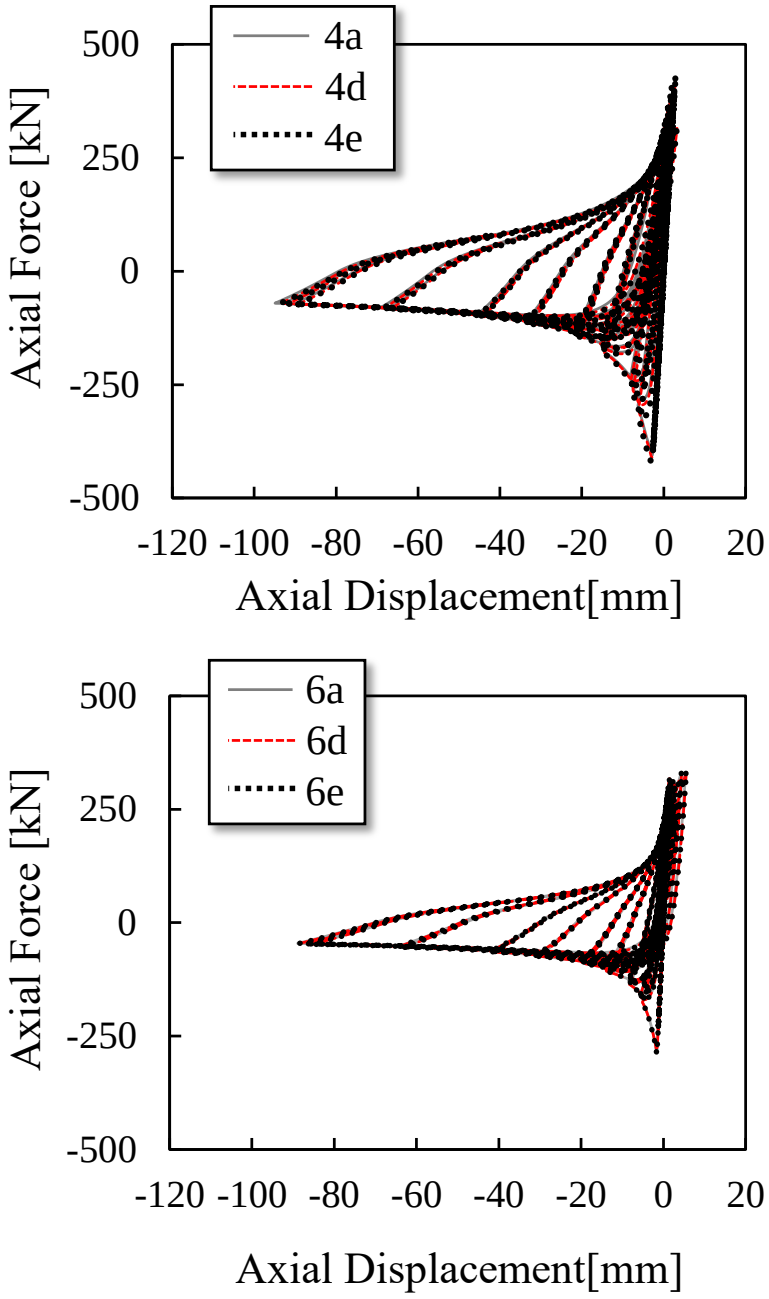

Figure 4.14: Effect of lateral bracing stiffness on the performance of the braces: (a) Model 4; and (b) Model 6.

4.1.4. Global Response

Fig. 4.12 compares the simulated response of Model 4 and 6 with different cases of lateral bracing. Interestingly, although the analysis results showed that the lateral bracing cases lead to substantial difference in twisting and out-of-plane deformation of the beam intersected by braces, the bracing cases had negligible effect on the overall cyclic performance of the chevron-braced MRFs.

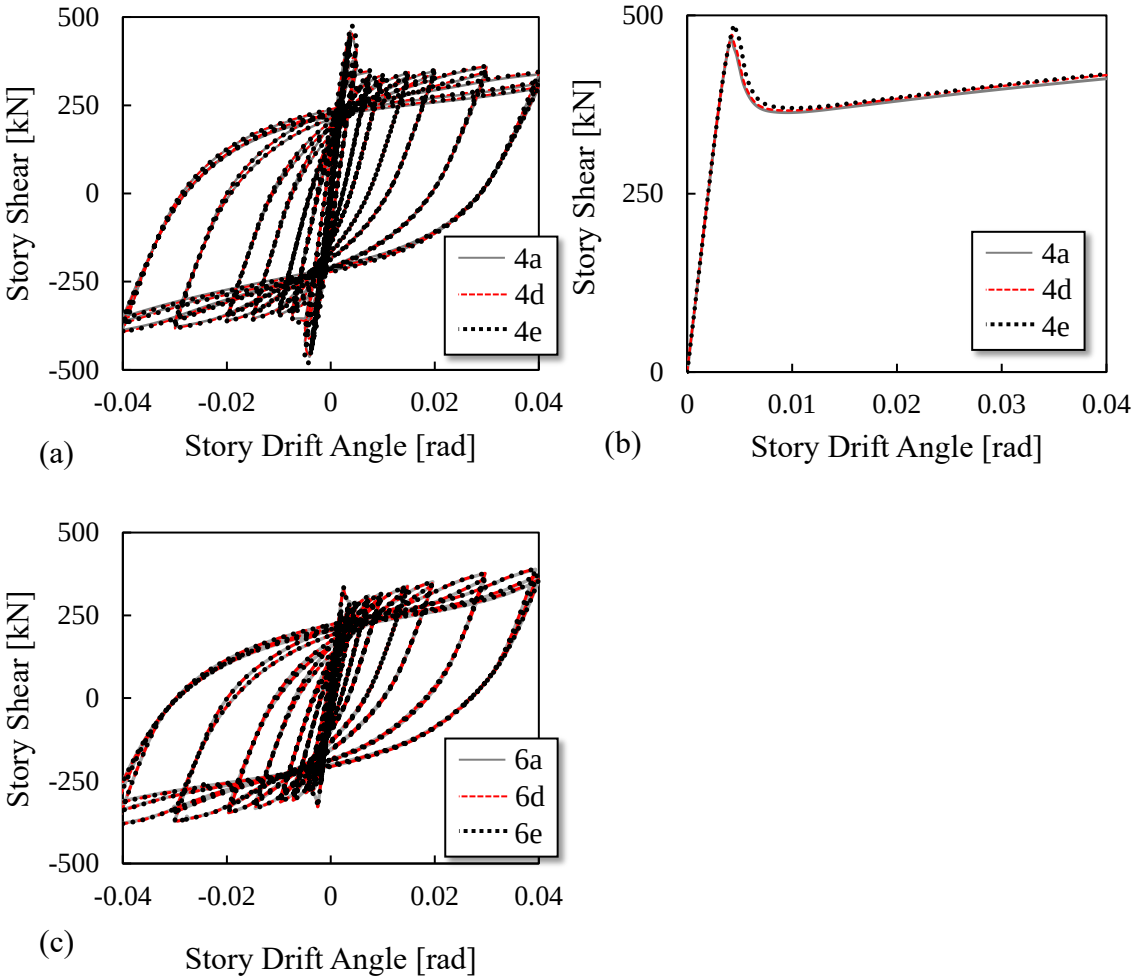

Figure 4.15: Effect of lateral bracing stiffness on the performance of the chevron brace MRF: (a) Model 4 under cyclic loading; (b) Model 4 under cyclic monotonic loading; and (b) Model 6.

4.2. Design Equation for Torsional Moment Delivered by the Braces

From the equilibrium equation in 4.1, and recognizing that the out-of-plane component of the brace force (F_Z) has negligible contribution to the torsional moment delivered by the braces, equation 4.1 can be rewritten as:

$$T = (-Fy \times e_{cx} - Mx)_{NB} + (-Fy \times e_{cx} + Mx)_{SB} \quad (4.2)$$

where F_y can be computed from the braces tensile and compressive strength, and M_x the bending moment at the end of the braces. The vertical component of the brace for is capped by the brace yielding strength when the brace is in tension and compressive strength when the brace is in compression.

As illustrated in Figure 4.16, the torsional moment delivered by the braces may be decomposed into the four components, two from each brace: The product of brace axial force and eccentricity between the line of action of the deformed brace and the beam centroid, and moment at the bracing connection. Noting that the torsional moment from the compression brace always exceeds the moment from the tension brace, and that the latter always act in the orientation to cancel the former, the sum of four components may be expressed as follows:

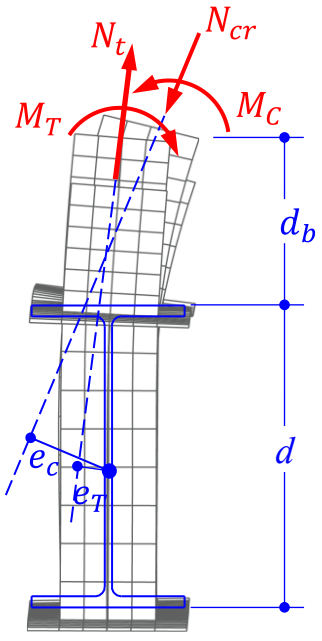

Figure 4.16: Structural Model for evaluation of the brace induced torsional moment.

$$T_1 = N_{cr} \times e_{C1} + M_{C1} \tag{4.3}$$

$$T_2 = 0.3N_{cr} \times e_{C2} + M_{C2} - N_{t,\max} \times e_{T2} - M_{T2} \tag{4.4}$$

$$T_3 = 0.3N_{cr} \times e_{C2} + M_{C2} \tag{4.5}$$

$$N_{t,\max} = \min.\left\{\left(\kappa\frac{4M_p}{l}\cdot\frac{1}{\sin\alpha} + 0.3N_{cr}\right),\ \ N_y\right\} \tag{4.6}$$

In the above equations, M_T and M_C are the out-of-plane bending moment at the end of the tension and compression brace, respectively, computed from the flexure-and-axial force interaction equation in AISC[28]; $N_{t,\max}$ is the force in the tensile brace consistent with the assumed plastic mechanism in Figs. 1(b) or (c) and with Seki et al.[16]; and e_C and e_T are the eccentricity of the compression and tension braces, respectively. The subscripts 1 to 3 corresponds to the aforementioned conditions. To be specific, T_1 assumes that, after brace buckling, the compression brace maintains a relatively large force of N_{cr} while the tension brace remains straight and therefore delivers zero torsional moment; T_2 assumes a condition where the tension brace is deformed out-of-plane, and therefore, delivers cancelling torsional moment; T_3 assumes a condition where the tension brace has never buckled, and therefore, delivers zero torsional moment; T_2 and T_3 samples the respective values at a story drift of ±0.02 rad, and assumes that the force in the compressive braces has reduced to $0.3N_{cr}$.

The brace eccentricities are computed using the proposed relationship between story drift and brace out-of-plane displacement and observation that brace with fixed ends tend to develop plastic hinges one cross-sectional depth away from the brace ends, both by Tremblay et al.[32]:

$$e = \frac{2\cdot\Delta}{L_H}(d_b + d/2) \tag{4.7}$$

In the above equation, d_b is depth of the brace section; d is depth of the beam; L_H is distance between plastic hinges formed at the brace ends; and Δ is the out-of-plane displacement of the brace, respectively.

A relationship between Δ and L_H was obtained from analysis of chevron-braced MRFs with different proportions but the same bracing connection Type IV as Model 4 (Models 4, 9, 12, 15 and 16 discussed in the chapter 3) subjected to the same cyclic loading procedure. For condition (1) $\Delta = 0.033L_H$ for compression braces as shown in Figure 4.17(a); for conditions (2) $\Delta = 0.091L_H$ for the

compression brace (Figure 4.17(b)) and $\Delta = 0.023L_H$ for the tension brace shown in (Figure 4.17 (c)); and for condition (3), $\Delta = 0.091L_H$ for the compression brace (Figure 4.17(b)).

Figure 4.9 indicates the torsional moments computed from Eqs. (4.3) to (4.6) for Model 4. For cyclic loading, T_1 and T_2 provided conservative estimates of the torsional moment delivered by the braces after brace buckling, and at large story drifts. Under monotonic loading, T_3 provided a conservative estimate by 15%.

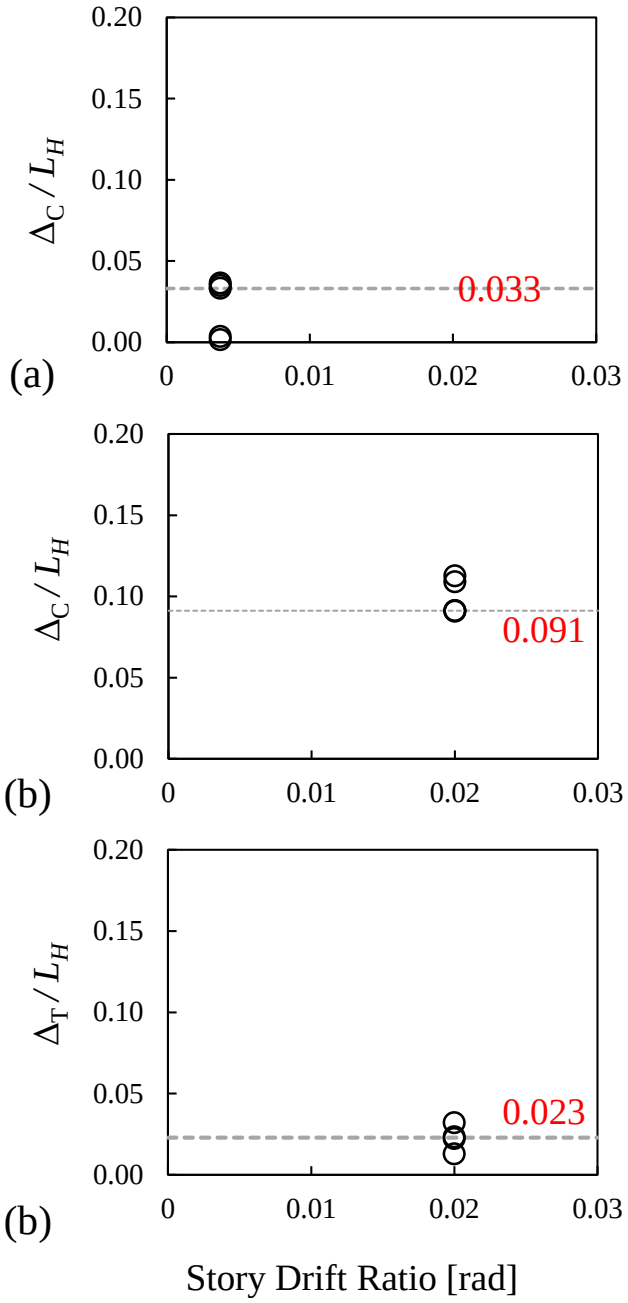

Figure 4.17: Derivation of brace eccentricities: (a) condition (1); (b) condition (2); and (c) condition (3);

4.3. Summary

The effect of beam bracing on the seismic performance of chevron braced frames was analyzed through a parametric study to examine the bracing requirement for the beam intersected brace. Different rotational and translational spring stiffness combinations was examined.

The following main findings can be drawn for the analysis:

i) Lack of lateral bracing of the beam intersected by braces can lead to severe twist and out-of-plane deflection of the beam but may not affect the lateral-load resistance of chevron-braced MRF system. In order to control lateral-torsional deformation of the beam, lateral bracing at the brace-to-beam joint should be accompanied by adequate rotational bracing.

1) If the bracing connection is rigid and the braces are oriented to buckle out-of-plane, the braces deliver large torsional moment to the beam intersected by braces. In such bracing connections, both braces are forced to buckle in the same orientation, and therefore, the tensile brace counters the torsional moment delivered by the compression brace. An unfavorable condition is realized by large monotonic pulses that allow only one of the chevron braces to buckle, in which case the tension brace remains straight, and thereby produces zero countering moment.

2) The torsional moment delivered by the braces may be estimated conservatively as the sum of four components: the moment produced through eccentricity of the action line of the deformed brace and out-of-plane bending moment at the brace ends, each from the compression and tension braces.

5. STRENGTH DEMANDS ON THE BEAM INTERSECTED BY BRACES

5.1 Introduction

This chapter discuss a series of computational study conducted to examine the seismic performance of chevron-braced MRFs designed and constructed according to the current practice in Japan. The objective was to further the understanding obtained from the experimental observations conducted by [16] and to examine how the seismic performance of chevron-braced MRFs may be affected by primary design parameters, such as the proportion of lateral strength carried by the braces, the relative horizontal strength of the beam intersecting braces with respect to the braces, the bracing connections and the loading protocol.

5.2 Design Equations

When chevron braces are placed in an MRF, the required beam strength cannot be evaluated as simply as in the AISC-341-16[28] design rules because the beam comprises a statically indeterminate system. The design issue may be illustrated by a conceptual analytical model shown in Figure 5.1.

The proportion of the plastic lateral strength of the CBF derived from chevron braces, β_0, may be expressed as a function of the relative horizontal strength of the brace with respect to the beam, r_0.

The factor β_0 is an important design parameter that dictates the ductility category of CBFs in the Japanese building code (AIJ 2010 [2]). As depicted in Figure 5.2, Japanese chevron braced MRFs may be decomposed into a pair of braces, placed in an angle α, and a moment-resisting frame. In this

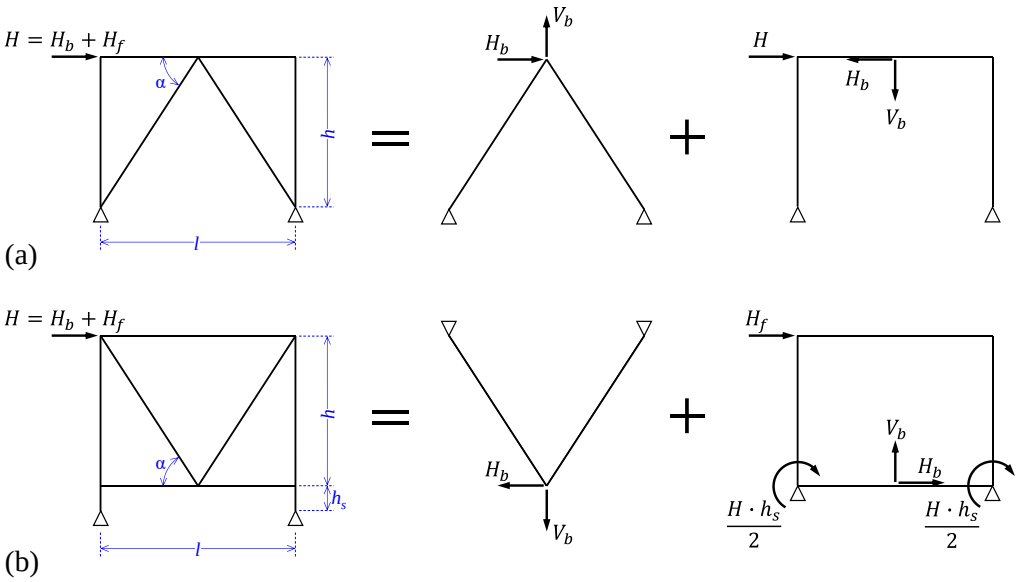

Figure 5.1: Strength Evaluation of chevron-braced MRFs: (a) Strength decomposition for General Case; (b) Strength decomposition for chevron-braced MRFs tested by Seki et al.[16]

study, the columns and the column panel zones are assumed to be substantially stronger than the beam. The plastic strength of the combined system, H_u, may be evaluated as the sum of the contributions of the MRF, H_f, and that of the braces, H_b, and thereby $\beta_0 = H_b/H_u$.

Depending on the relative strength of the braces with respect to the beam, the tension brace may develop its yield strength N_y to form a "strong-beam" mechanism (Figure 5.2 (a)), or else the beam may yield under the action of reverse end moments and force unbalance between the braces to form a "weak-beam" mechanism (Figure 5.2(b)). In the latter case, the force carried by the tension brace is limited by the strength of the beam and will not reach N_y.

The ultimate strength of the brace in tension and compression is computed as $N_y = A_{gs} \cdot F_y$ and $N_c = 0.3 \times N_{cr}$.

Introduce x, the brace compressive to tensile strength ratio, computed as:

$$x \equiv \frac{N_u}{N_y} \tag{5.1}$$

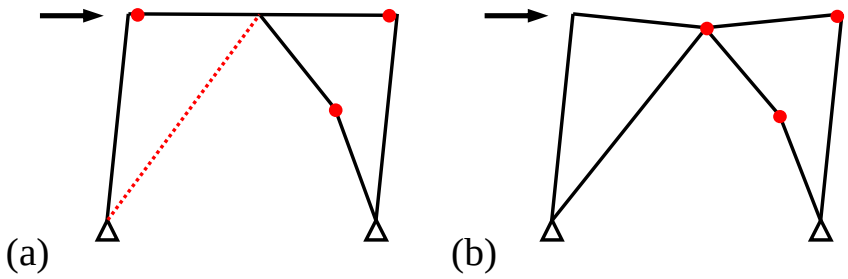

Figure 5.2: Mechanical behavior of CBFs: (a) Strong-Beam Mechanism, and (b) Weak-Beam Mechanism

The vertical (V_b) and horizontal (H_b) unbalance force produced by the force unbalance between the braces is computed as in equation (2) and (3), respectively:

$$V_b = (N_t - N_c) \sin \alpha \tag{5.2}$$

$$H_b = (N_t + N_c) \cos \alpha \tag{5.3}$$

Alternatively, the force on the tension and compression brace is computed as in eq. (4) and (5) respectively:

$$N_t = \frac{H_b}{2 \cdot cos\alpha} + \frac{V_b}{2 \cdot sin\alpha} \tag{5.4}$$

$$N_c = \frac{H_b}{2 \cdot cos\alpha} - \frac{V_b}{2 \cdot sin\alpha} \tag{5.5}$$

The relationship between β_0 and r_0 can be computed as follows for the two possible collapse mechanisms:

1. **Case 1 – Strong Beam Mechanism**:

   The strong beam mechanism will control the mechanism of the brace frame, under the following condition:

$$0 \leq (N_y - N_c) sin\alpha \leq V_{pl} \equiv \frac{4M_p}{l} \tag{5.6}$$

In the above equation V_{pl} is the unbalance load required to yield the beam, computed as:

$$V_{pl} \equiv \frac{4M_p}{l} \tag{5.7}$$

The condition under which the strong beam mechanism controls can be rewritten as follows, by diving eq. (6) by N_y:

$$(1 - x) N_y sin\alpha \leq V_{pl} \text{ or } x \geq 1 - \frac{V_{pl}}{N_y sin\alpha} \tag{5.8}$$

Under this condition, the brace develops its yield strength, and therefore the tension brace will develop its yield strength and $N_t = N_y$.

From the energy dissipating mechanism of the frame under horizontal load, the lateral strength carried

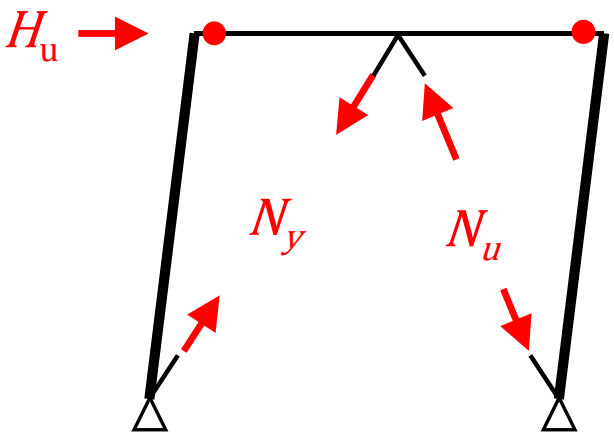

Figure 5.3: Strong beam mechanism

by the MRF, H_f, is computed as: $H_f = H - H_b$. The plastic strength of the MRF, considering that plastic hinge forms only at the ends of the beam is computed as:

$$H_f = \frac{2M_p}{h} \tag{5.9}$$

where h is the height of the frame, and M_p is the plastic strength of the beam.

The lateral strength of the chevron-braced MRF, is computed by combining the contribution of the pair of braces, H_b, computed as $H_b = (N_y + N_c)\cos\alpha$ and the MRF. The braced frame strength is therefore:

$$H = H_f + H_b = \frac{2M_p}{h} + (N_y + N_c)\, cos\alpha \tag{5.10}$$

Introducing β_0, the proportion of the lateral strength carried by the pair of braces, computed as the ratio $\beta_0 = \frac{H_b}{H}$, is computed as:

$$\begin{aligned}\beta_0 = \frac{H_b}{H_b + H_f} &= \frac{(N_y + N_c)\, cos\alpha}{\frac{2M_p}{h} + (N_y + N_c)\, cos\alpha} = \frac{(1+x)\, N_y\, cos\alpha}{\frac{2M_p}{h} + (1+x)\, N_y\, cos\alpha} \\ &= \frac{\frac{(1+x)\, N_y h\, cos\alpha}{2M_p}}{1 + \frac{(1+x)\, N_y h\, cos\alpha}{2M_p}}\end{aligned} \tag{5.11}$$

Thus β_0 can be written as:

$$\beta_0 = \frac{(1+x)\frac{N_y}{2M_p} h \cdot cos\alpha}{1 + \left\{(1+x)\frac{N_y}{2M_p} h \cdot cos\alpha\right\}} \tag{5.12}$$

Introduce the ratio r_0, the relative horizontal strength of the brace with respect to the beam. Assuming that

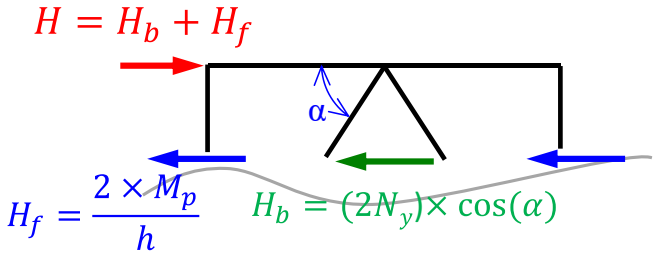

Figure 5.4: Derivation of r_0 relationship

the, in the limit state, following mechanism occurs:

The relative horizontal strength of the braces with respect to the braces can be computed as $r_0 = \frac{H_b}{Hf}$. Replacing the lateral strength derived from the pair of the braces, assuming that both braces develop their yielding strength $H_b = (2N_y) \times \cos(\alpha)$, and the lateral strength derived from underlying MRF, $H_f = \frac{2 \times M_p}{h}$, the relative horizontal strength with respect to the braces can be computed as:

$$r_0 = {}^{N_y \cdot h \cdot cos\alpha.}/_{M_p} \tag{5.13}$$

Replacing r_0 in Eq.12, yields:

$$\beta_0 = \frac{(1+x) \cdot {}^{r_0}/_2}{1 + (1+x) \cdot {}^{r_0}/_2} \tag{5.14}$$

2. Case 2: Weak-Beam Mechanism

The weak-beam mechanism controls the inelastic behavior of the chevron-braced MRF, for the condition where the unbalance load induced on the beam exceeds the vertical load required to yield the beam, or: This condition can be simplified and written as:

$$(N_y - N_c) sin\alpha \geq V_{pl} \equiv \frac{4M_p}{l} \tag{5.15}$$

$$(1-x) N_y sin\alpha \geq V_{pl} \text{ or } x \leq 1 - \frac{V_{pl}}{N_y sin\alpha} \tag{5.16}$$

Recognizing that the magnitude of the unbalance load and hence κ varies with the loading protocol, the

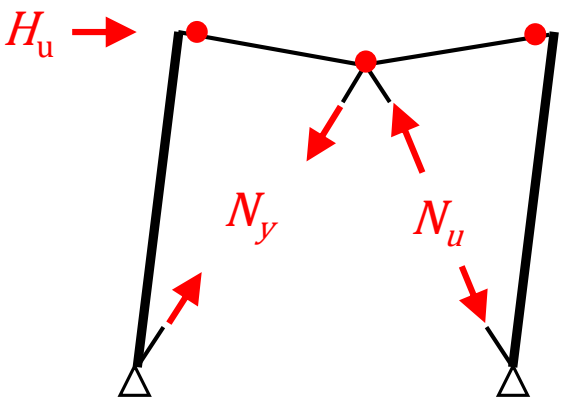

Figure 5.5: Weak-Beam Mechanism

unbalance load can be computed as:

$$V_b = \kappa\, V_{pl} \tag{5.17}$$

The limiting value for κ, $1 \le \kappa \le 2$ is the assumed limit for the maximum possible unbalance vertical force over the plastic resistance of the beam, $V_{b0} = 4M_p/l$, when subject to reverse end moments M_p. The factor κ addresses the beam end moments that act in combination with the unbalanced vertical force [13], [16] [33]. The maximum value $\kappa = 2.0$ gives the plastic resistance of the beam when the end moments M_p both act in the direction to oppose the force unbalance. Fukuta et al. [13] recommended $\kappa = 1.0$ to avoid yielding of the beam intersected by braces.

The bending moment distribution of chevron-braced MRFs for different κ values is shown in the Figure

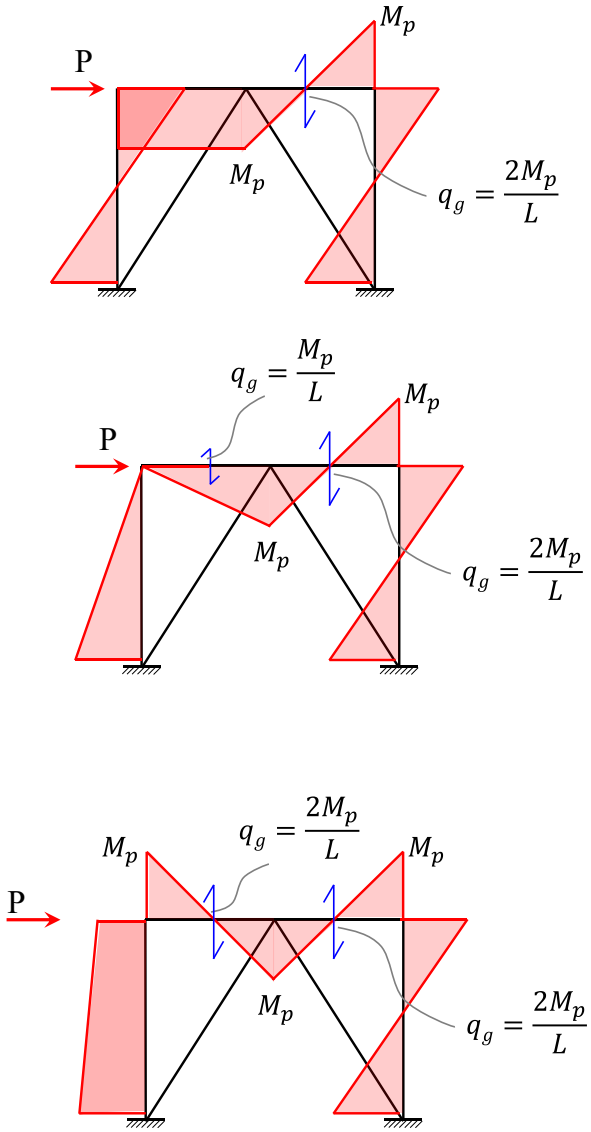

Figure 5.6: Moment distribution patterns for chevron braced frames: (a) κ=1; (b) κ=1.5 and (c) κ=2.

5.6.

From the energy-dissipating mechanism of the frame under lateral load, the strength derived from the brace can be computed as $H_f = H - H_b$. The virtual work done by the force is computed as:

$$H_f h + V_b \frac{l}{2} = 4M_p \tag{5.18}$$

The lateral strength of the MRF is therefore computed as:

$$H_f = \frac{4M_p}{h} - V_b \frac{l}{2h} \tag{5.19}$$

where h is the height, and l the span of the brace frame. The energy dissipated by the pair of braces is computed as:

$$H_b h - V_b \frac{l}{2} = (N_t + N_c)h\, cos\alpha - (N_t - N_c)\frac{l}{2}\, sin\alpha \tag{5.20}$$

$$H_b = \frac{(N_t + N_c)h\, cos\alpha}{h} - (N_t - N_c)\frac{l}{2h}\, sin\alpha + V_b \frac{l}{2h} \tag{5.21}$$

$$H_b = (N_t + N_c)\, cos\alpha - (N_t - N_c)\frac{l}{2h}\, sin\alpha + V_b \frac{l}{2h} \tag{5.22}$$

Combining the contribution of the pair of braces $H_b = (N_y + N_c)\, cos\alpha$ and the MRF, yields.

$$H = H_f + H_b = \frac{4M_p}{h} - V_b \frac{l}{2h} + (N_t + N_c)\, cos\alpha - (N_t - N_c)\frac{l}{2h}\, sin\alpha + V_b \frac{l}{2h} \tag{5.23}$$

Simplifying the equation yields:

$$H = \frac{4M_p}{h} + (N_t + N_c)\, cos\alpha - (N_t - N_c)\frac{l}{2h}\, sin\alpha \tag{5.24}$$

Note that: $\tan\alpha = \frac{2h}{l}$ thus:

$$H = \frac{4M_p}{h} + (N_t + N_c)\, cos\alpha - (N_t - N_c) \times \frac{1}{tan\alpha} \cdot sin\alpha \tag{5.25}$$

The ultimate lateral strength is computed as:

$$H = \frac{4M_p}{h} + 2N_c\, cos\alpha \tag{5.26}$$

When the weak-beam mechanism controls, κ is very important. When $\kappa = 1.5$, there is a range of r_0 where both the brace and the beam might yield. Therefore, the mechanism can be divided into two, as follows:

2.1. Case 2A: The tension brace develops its yield strength under the condition

$$(N_y - N_c)sin\alpha \leq \kappa \cdot V_{pl} \tag{5.27}$$

The condition can be rewritten as:

$$x \geq 1 - \frac{\kappa \cdot V_{pl}}{N_y cos\alpha} \tag{5.28}$$

Assuming that the brace develops its tensile strength:

$$N_t = N_y$$

The lateral strength derived from the pair of braces and the force unbalance is therefore computed as:

$$H_b = (N_y + N_c)\, cos\alpha \tag{5.29}$$

$$V_b = (N_y - N_c)\, sin\alpha \tag{5.30}$$

The lateral strength derived from the MRF can be computed as:

$$H_f = \frac{4M_p}{h} - V_b \frac{l}{2h} \tag{5.31}$$

This equation can be rewritten as:

$$H_f = \frac{4M_p}{h} - (N_y - N_c)sin\alpha \frac{l}{2h} \tag{5.32}$$

The lateral strength of the braced frame, $H = H_f + H_b$ is computed as:

$$H = \frac{4M_p}{h} - \left(N_y - N_c\right)sin\alpha\,\frac{l}{2h} + \left(N_y + N_c\right)cos\alpha \tag{5.33}$$

From the geometry of the braced frame,

$$\tan\alpha = {}^{2h}/_{l} \tag{5.34}$$

Replacing eq. 33 into eq. 32, yields:

$$H = \frac{4M_p}{h} - \left(N_y - N_c\right)\frac{sin\alpha}{\tan\alpha} + \left(N_y + N_c\right)cos\alpha \tag{5.35}$$

The ultimate lateral strength of the chevron-braced MRF can be rewritten:

$$H = \frac{4M_p}{h} - \left(N_y - N_c\right)cos\alpha + \left(N_y + N_c\right)cos\alpha \tag{5.36}$$

Cancelling the parameters:

$$H = \frac{4M_p}{h} + 2N_c cos\alpha \tag{5.37}$$

The proportion of the lateral strength carried by the braces, β_0 can be written as:

$$\beta_0 = \frac{H_b}{H} = \frac{\left(N_y + N_c\right)cos\alpha}{\frac{4M_p}{h} + 2N_c\,cos\alpha} = \frac{(1+x)\frac{N_y}{2M_p}h \cdot cos\alpha}{2 + (2x)\frac{N_y}{2M_p} \cdot cos\alpha} \tag{5.38}$$

or:

$$\beta_0 = \frac{(1+x)\cdot {}^{r_0}/_{2}}{3 + 2x \cdot {}^{r_0}/_{2}} = \frac{(1+x)\cdot {}^{r_0}/_{2}}{3 + r_0 \cdot x} \tag{5.39}$$

2.2. Case 2B – The tension brace cannot develop its yield strength under the following condition:

$$\left(N_y - N_c\right)sin\alpha \;\geq \kappa \cdot V_{pl} \tag{5.40}$$

or:

$$x \leq 1 - \frac{\kappa \cdot V_{pl}}{N_y sin\alpha} \tag{5.41}$$

Under this condition, the maximum tensile strength reached by the tension brace is:

$$N_t = \kappa \cdot \frac{V_{pl}}{\sin \alpha} + N_c < N_y \tag{5.42}$$

The lateral strength derived from the braces is computed as:

$$H_b = (N_t + N_c)\, cos\alpha \tag{5.43}$$

Replacing eq. 41 into eq. 42, yields:

$$H_b = \left(\kappa \cdot \frac{4M_p}{l \sin \alpha} + 2N_c\right) cos\alpha \tag{5.44}$$

or

$$H_b = \kappa \cdot \frac{4M_p}{l \sin \alpha} cos\alpha + 2N_c\, cos\alpha = \kappa \cdot \frac{4M_p}{l \tan \alpha} + 2N_c\, cos\alpha \tag{5.45}$$

Further simplifying the equation, the lateral strength derived from the pair of braces is computed as:

$$H_b = \kappa \cdot \frac{4M_p}{2h} + 2N_c\, cos\alpha = \kappa \cdot \frac{2M_p}{h} + 2N_c\, cos\alpha \tag{5.46}$$

The lateral strength derived from the MRF is computed as:

$$H_f = \frac{4M_p}{h} - V_b \frac{l}{2h} \tag{5.47}$$

Recognizing that for this case, $V_b = \kappa\, V_{pl}$, the equation can be rewritten as:

$$H_f = \frac{4M_p}{h} - \kappa \cdot \frac{2M_p}{h} \tag{5.48}$$

The lateral strength of the braced frame is therefore computed as:

$$H = \frac{4M_p}{h} - \kappa \cdot \frac{2M_p}{h} + \kappa \cdot \frac{2M_p}{h} + 2N_c\, cos\alpha \tag{5.49}$$

Or simplified as:

$$H = \frac{4M_p}{h} + 2N_c\, cos\alpha \tag{5.50}$$

Thus, the proportion of the lateral strength carried by the braces, β_0, can be written as:

$$\beta_0 = \frac{H_b}{H} = \frac{\kappa \cdot \frac{2M_p}{h} + 2N_c\, cos\alpha}{\frac{4M_p}{h} + 2N_c\, cos\alpha} = \frac{\kappa + 2x\frac{N_y}{2M_p}h \cdot cos\alpha}{2 + (2x)\frac{N_y}{2M_p} \cdot cos\ \alpha} \tag{5.51}$$

or:

$$\beta_0 = \frac{\kappa + x \cdot r_0}{2 + x \cdot r_0} \tag{5.52}$$

In summary, for the two cases, the proportion of the lateral strength carried by the braces, β_0 is expressed as follows:

Strong beam mechanism: $$\beta_0 = \frac{(1+x)r_0}{2 + (1+x)r_0} \tag{5.53}$$

Weak beam mechanism: $$\beta_0 = \frac{\kappa + x \cdot r_0}{2 + x \cdot r_0} \tag{5.54}$$

The strong-beam mechanism controls when $r_0 \leq 2\,\kappa/(1-x)$ and the weak beam mechanism controls otherwise. When $2/(1-x) \leq r_0 \leq 2\kappa/(1-x)$, the collapse mechanism of the braced frame is

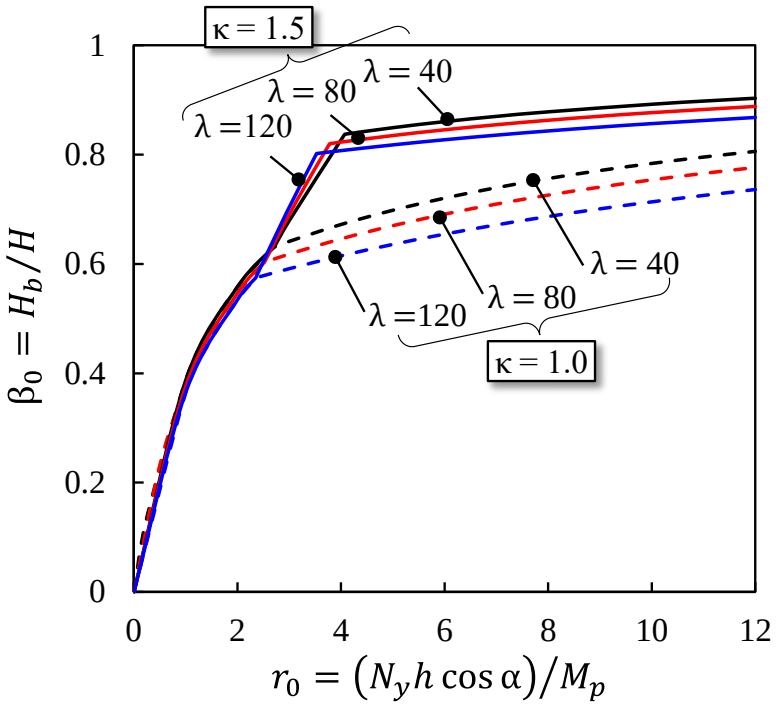

Figure 5.7-Relationship between β_0 and $\boldsymbol{r_0}$

sensitive to $\boldsymbol{\kappa}$, and both the braces and the beam might yield.

The relationship between β_0 and r_0 provides a useful design guide for engineers. Figure 5.7 shows, for $\kappa = 1.0$ and 1.5, the relationship between β_0 and r_0 computed for three different values of brace slenderness ratios, $\lambda =$ 40, 80 and 120.

The results show that, regardless of λ, β_0 is a monotonically increasing function of r_0. The difference in λ has little effect on β_0 because the provisions define a small $x = N_u/N_y$ regardless of λ. Within $2/(1-x) \leq r_0 \leq 2\kappa/(1-x)$, greater κ gives a larger range of r_0 over which the strong-beam mechanism controls. Consequently, β_0 can reach a larger value when κ is greater. In the range of r_0 where the strong-beam mechanism controls, β_0 is nearly proportional to r_0, and thus stronger braces lead to larger β_0. In the range of r_0 where the weak beam-mechanism controls, beyond $r_0 = 2.5$ for $\kappa = 1.0$ and beyond $r_0 = 4$ for $\kappa = 1.5$, the increase of β_0 with r_0 is small, but larger κ leads to larger β_0.

A key design issue for chevron-braced MRFs is that κ should reflect the cyclic loading history experienced by the system, and therefore, the plastic mechanism by pushover monotonic loading analysis represented in Figure 5.1 may not necessarily represent the behavior realized by real earthquake demands.

5.3 Relative strength of the Beam with Respect to the Braces

Sixteen models listed in Table 5.1 were used to examine the cyclic-loading performance of steel chevron-braced MRFs over various proportions and bracing connections. Models 1 to 6 were according to Specimens 1 to 6 reported by Seki et al. [16], but with the eccentricity at the column supports eliminated. Figure 5.8 illustrates how the difference in column base support affects the mechanical conditions of the braced frame system by comparing the bending moment distribution of Model 4, sampled at the end of the first positive excursion of ±0.02 rad, for two cases: the standard model that used the vertical rollers at the column bases and a varied model that did not (i.e., the latter was the model used in Figure 3.5(a)). In both cases, the beam intersected by braces yielded one half in double-curvature bending and the other one half in uniform bending. The eccentricity at the column base affected the bending moment in the columns (as observed by Seki et al. [16], the concentrated moment at the column base acts in the opposite direction to the bending moment produced by moment frame action) but had limited effect on the bending moment distribution in the beam.

The 16 models differed in column span, beam section, brace section, and bracing connection. The centroidal distance between the beams was kept constant at h = 2,300 mm, but the centroidal distance between the columns was l = 3,000, 4,600 or 6,570 mm, to produce a brace placement angle of

α = 57°, 45° or 35°. Either an H-250×125×6×9 or H-300×150×6.5×9, which differed by 1.4 in plastic strength, was used for the beams. One of six sections, a round-HSS with D/t of 18.2 or 27.3 or an I-shape with $b_f/2t_f$ in the range between 4.2 and 7.8, and d/t_w in the range between 8.4 and 23.4, was used for the braces.

The bracing connections were adopted from Types I to VI by Seki et al. [16] and shown in Figure 3.1 (b) to (g). The brace slenderness ratio λ ranged from 70 to 131 for the round-HSS braces and from 62 to 145 for the I-section braces. In this calculation, the brace length was taken differently depending on the bracing connection: the clear distance between the face of column or beam for connections I, II, IV or V; the distance between fold lines in the gusset plate for connections III and VI. The effective brace buckling length was taken as 1.0 for connections I, III and VI; 0.75 for connection II and IV; 0.5 for connection V. The relative lateral strength of the braces with respect to the beam, r_0, based on the material properties reported by Seki et al.[16], ranged from 1.3 to 11.3 to cover a wide range of possible mechanisms. The listed plastic mechanism and β_0 values assumed $\kappa = 1.5$. Except for Models 8, 10 and 11, the weak-beam mechanism was expected to control. The adequacy of $\kappa = 1.5$ is examined later.

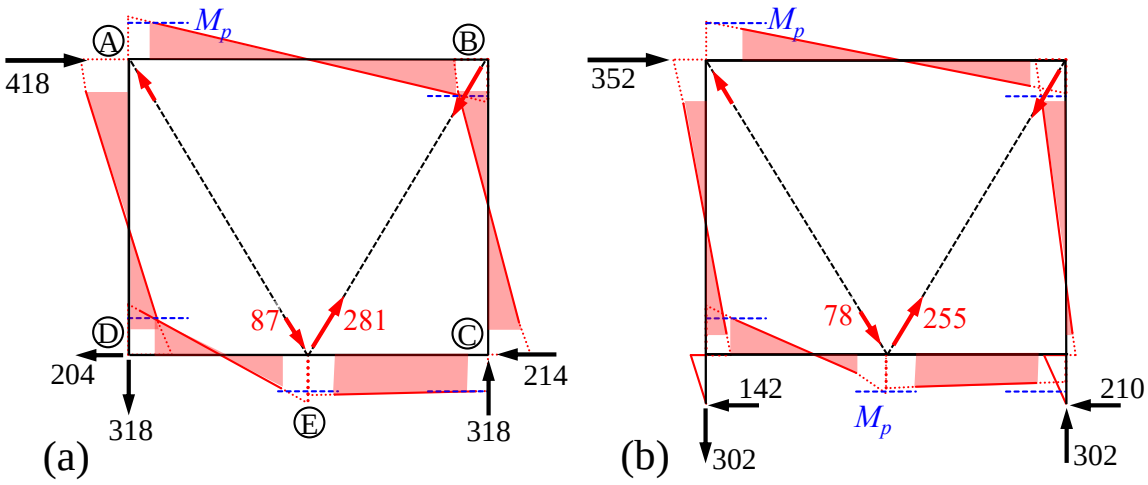

Figure 5.8: Forces in Model 4 sampled at the end of the 0.02 rad cycle: (a) Model with no eccentricity at column base; and (b) Model with eccentricity at column base (same as in Seki et al. [16]). (Unit: Forces in kN).

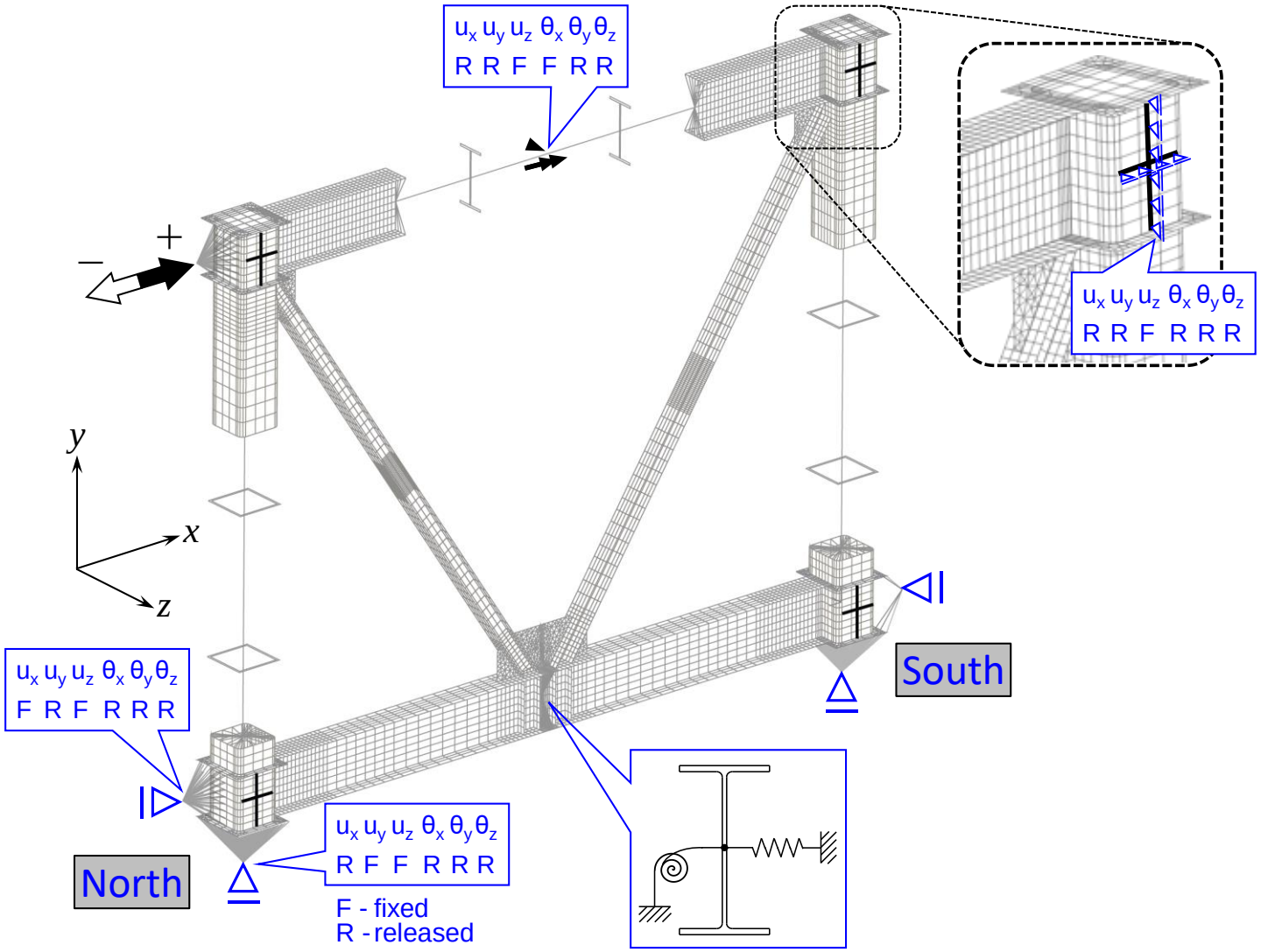

Figure 5.9 - Overview of Chevron-braced MRF Finite Element Model.

Table 5.1: Chevron-Braced MRF properties

Model	Geometric features				Brace properties				Bracing Connection	Design Values		
	l [mm]	α [°]	Beam	Brace	λ	N_y	N_{cr}	$V_{b,\max}$		r_0	β_0 (κ =1.5)	Mechanism
1	3000	57	H-250×125×6×9	HSS-76.3×4.2	95	356	203	199	I	4.1	0.81	W
2					71	356	275	270	II	4.1	0.82	W
3					85	356	231	226	III	4.1	0.81	W
4				H-75×75×6×9	94	570	353	347	IV	7.5	0.84	W
5					62	604	517	486	V	8.0	0.86	W
6					110	604	283	276	VI	8.0	0.83	W
7				H-50×50×4.5×6	141	260	80	76	IV	3.4	0.78	W
8				HSS-76.3×2.8	84	242	188	189	III	2.8	0.66	S
9				H-75×75×3.2×4.5	95	299	183	176	IV	4.0	0.81	W
10			H-300×150×6×9	H-50×50×2.5×3.2	145	145	42	41	IV	1.3	0.42	S
11				HSS-76.3×2.8	84	242	162	158	III	2.0	0.54	S
12				H-75×75×6×9	94	570	359	351	IV	5.3	0.83	W
13	6570	35	H-250×125×6×9	HSS-76.3×4.2	131	356	112	110	III	6.2	0.80	W
14	4600	45			105	356	172	169	III	5.3	0.81	W
15	6570	35		H-75×75×6×9	138	570	171	167	IV	11.3	0.83	W
16	4600	45			112	570	270	264	IV	9.8	0.84	W

Note: Bracing connection types are according to Figure 3.1.

Abbreviations: S: Strong-beam mechanism; W: Weak-beam mechanism

Each model was subjected to monotonic or cyclic loading controlled by story-drift ratio: Monotonic, Cyclic-1 and Cyclic-2. Cyclic-1 (Figure 5.10 (a)) was the same as in the experiments, while Cyclic- 2 (Figure 5.10 (b)) was based on the near-fault loading protocol by Gupta and Krawinkler [34] but scaled to two-third of the original amplitude to set the maximum story drift to 0.04 rad. (Note: the original near-fault loading protocol produces very similar results to monotonic loading.)

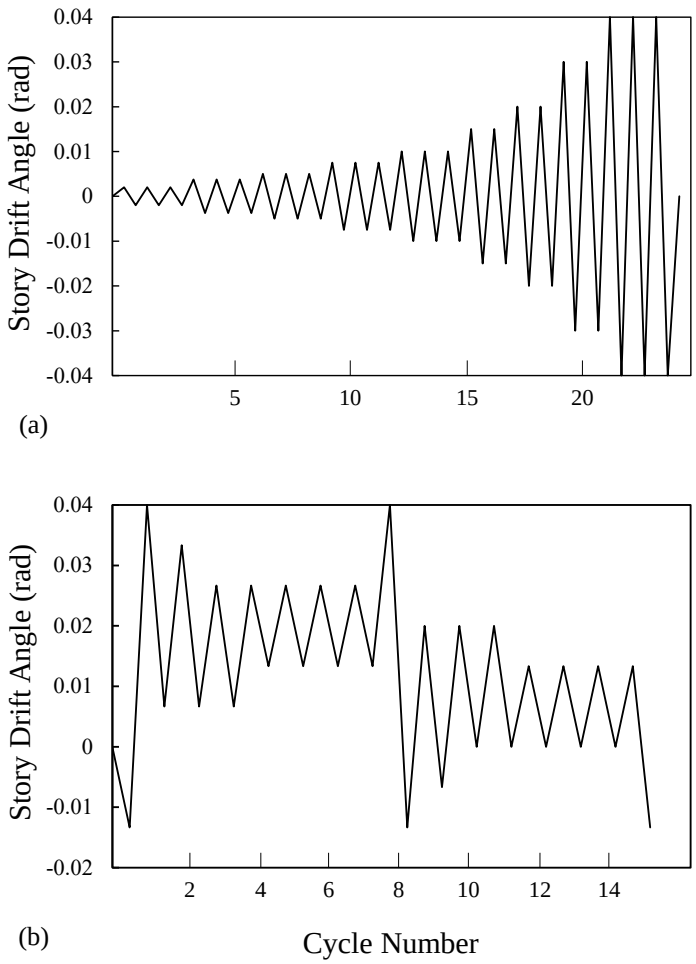

Figure 5.10: Loading Protocols: a) Cyclic-1, and b) Cyclic-2

Figure 5.11 to Figure 5.15 plots the simulated response of Models 1, 4, 5, 8, and 12 subjected to the three loading cases. Recognizing the difference in condition from Figure 3.5(a), the lateral-load resistance of the MRF is represented by $H_f = M_{DA}/h + M_{CB}/h$, where M_{DA} and M_{CB} are the beam-end moments based on the notations in Figure 5.8(a). The horizontal lines indicate the lateral strength of the chevron-braced MRF at the onset of buckling H_1, and the predicted lateral strength at the formation of the mechanism, H_2.

For all the models, with the exception of model 8, the simulated strength of the braced frames at brace buckling, exceeded H_1. The strength at ± 0.02 rad was smaller for Cyclic-1 than for the other loading cases, but H_2 assuming κ =1.5 was exceeded for all loading cases. The story shear carried by the braces was larger for Monotonic and Cylic-2 than for Cyclic-1, but the story shear carried by the MRF was larger for Cyclic-1.

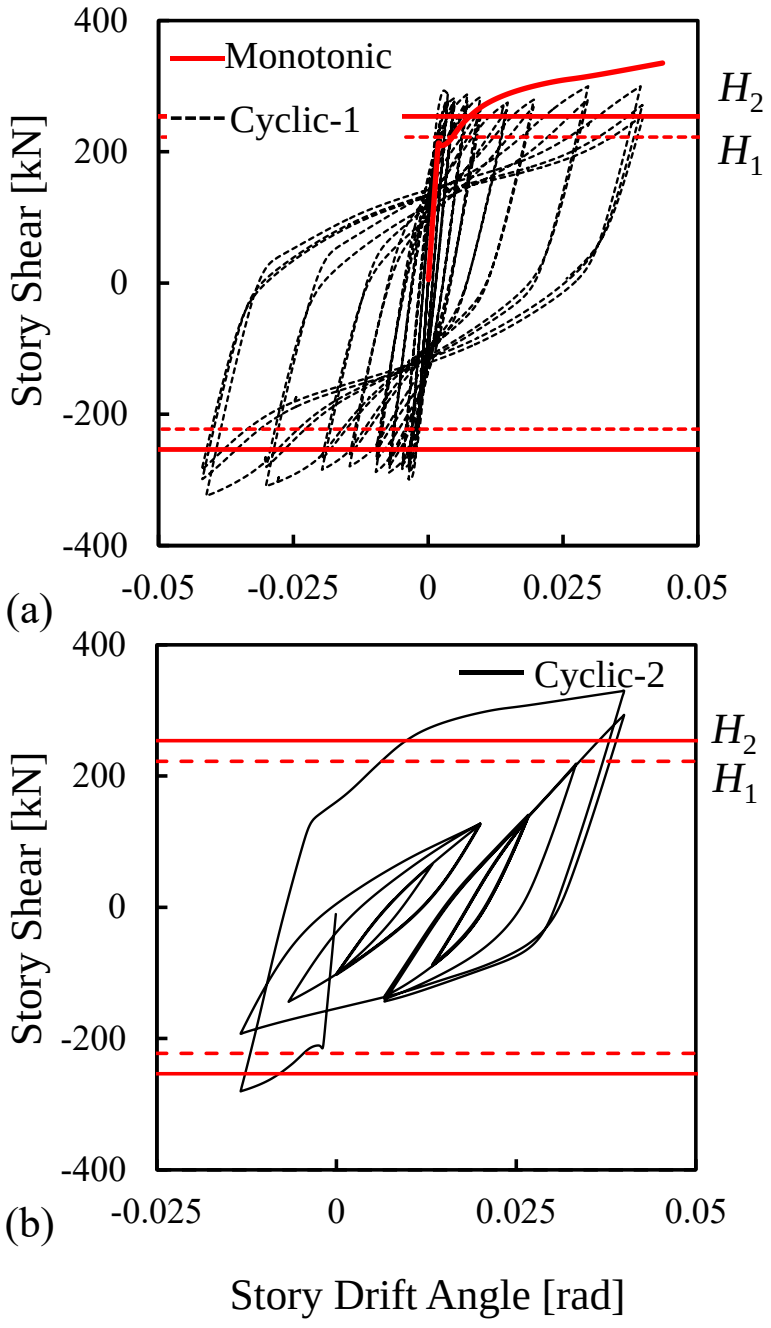

Figure 5.11: Global Response of Model 1: (a) Monotonic and Cyclic-1, and (b) Cyclic-2;

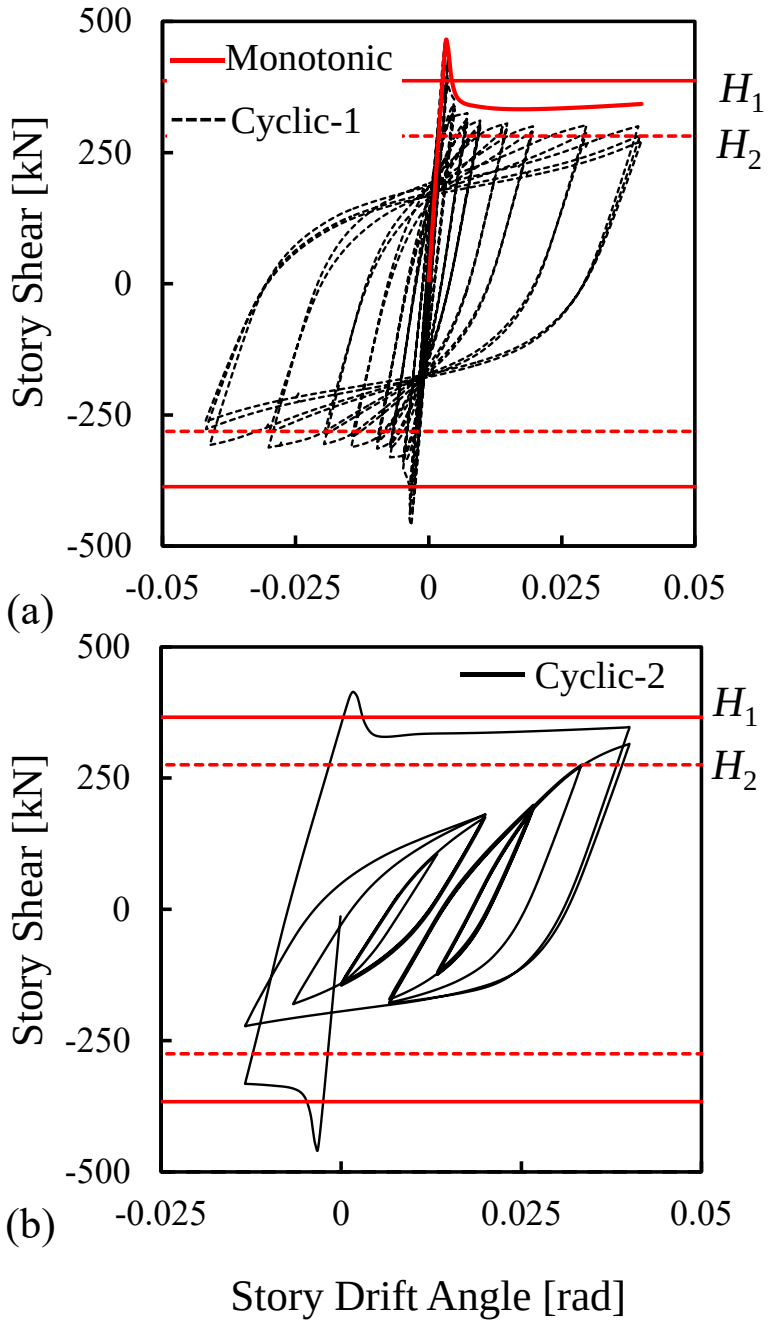

Figure 5.12: Global Response of Model 4: (a) Monotonic and Cyclic-1, and (b) Cyclic-2;

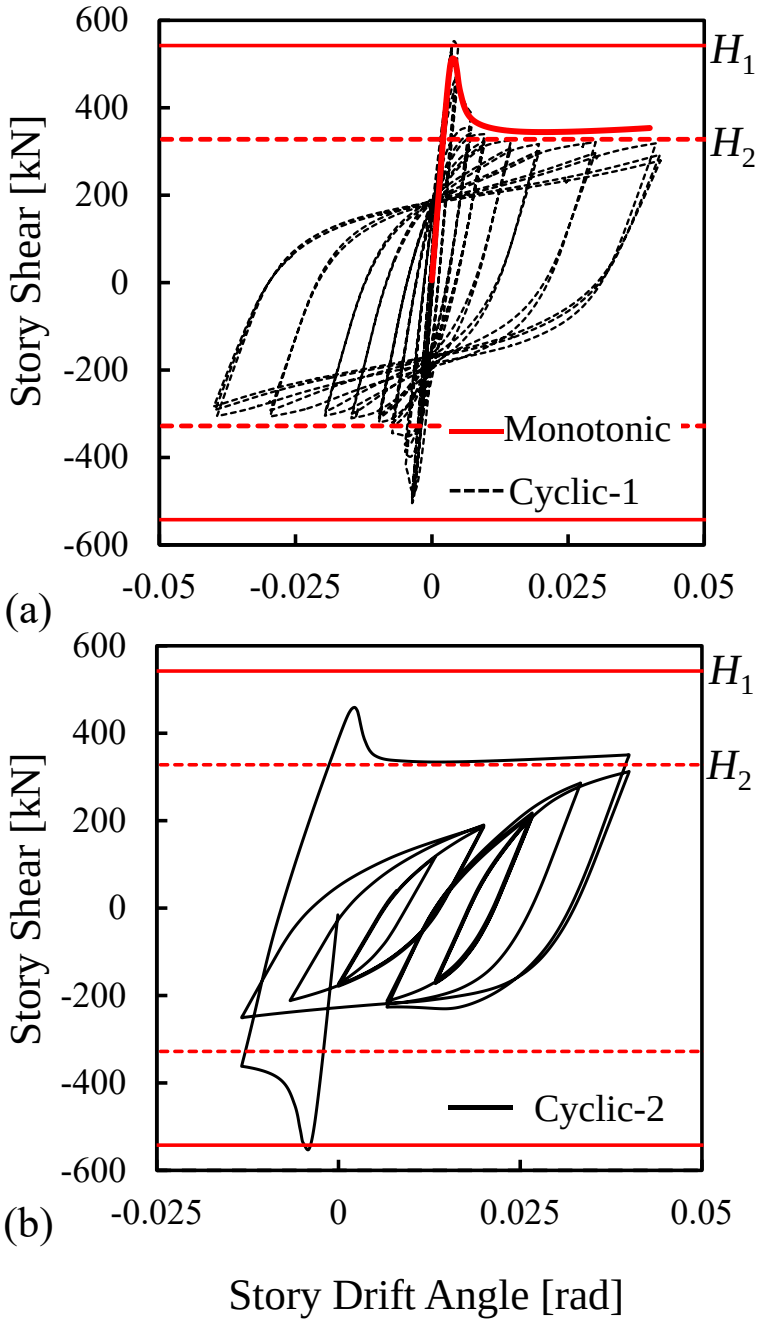

Figure 5.13: Global Response of Model 5: (a) Monotonic and Cyclic-1, and (b) Cyclic-2;

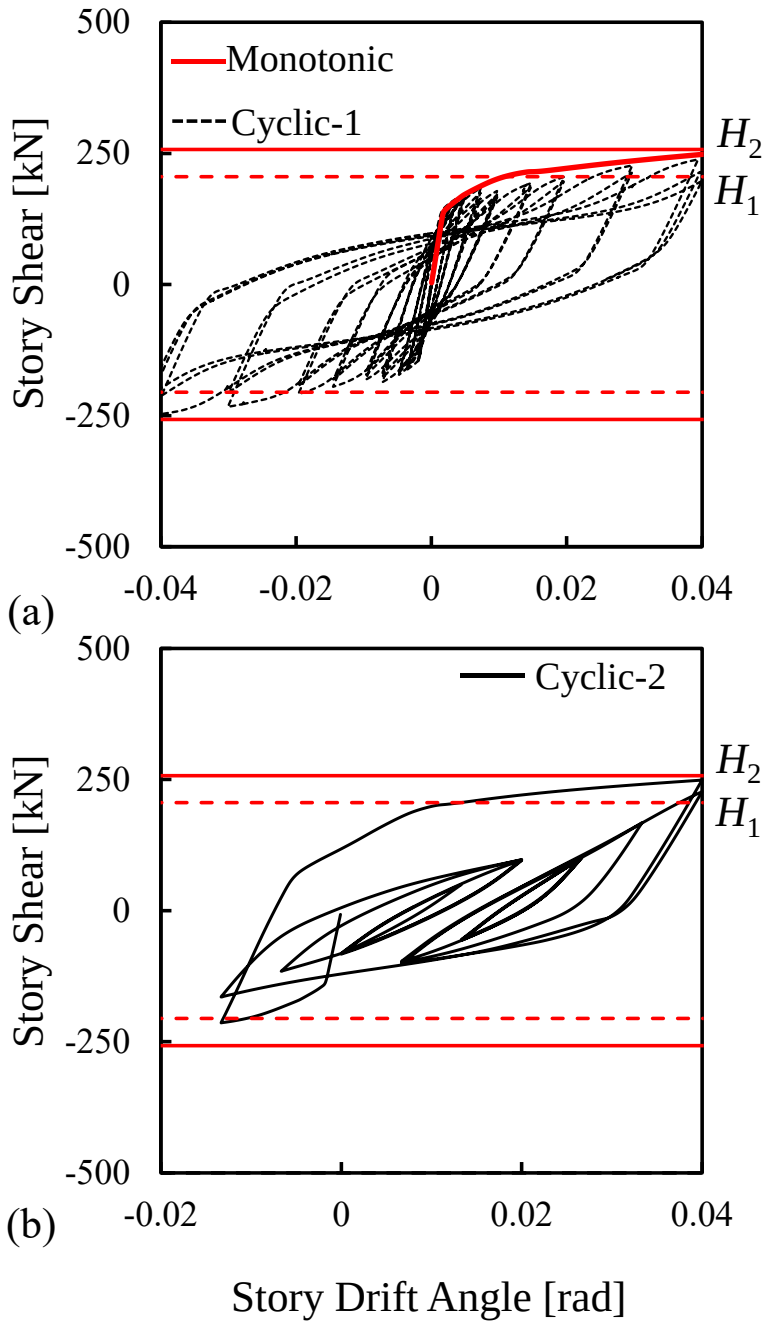

Figure 5.14: Global Response of Model 8: (a) Monotonic and Cyclic-1, and (b) Cyclic-2;

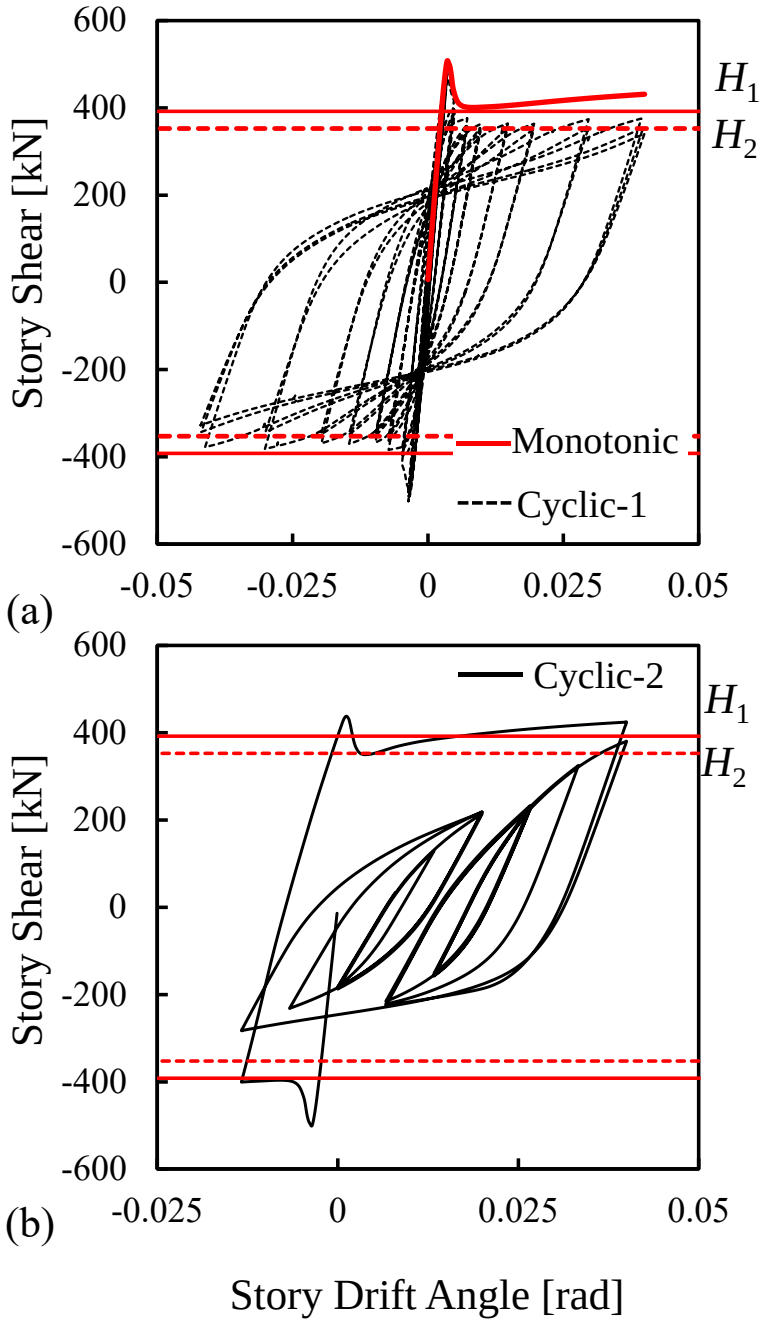

Figure 5.15: Global Response of Model 12: (a) Monotonic and Cyclic-1, and (b) Cyclic-2;

5.3.1 Strength Decomposition: Braces and MRF

One of the main goals of the numerical simulation is to compute the proportion of the lateral strength carried by the braces, H_b/H. Therefore, the lateral strength of the braces (H_b) and the MRF (H_f) were sampled at a fixed loading stage: the end of the first positive excursion at ± 0.02 rad for Monotonic and Cyclic-1 and at the end of the first positive excursion at +0.04 rad for the Cyclic-2 loading protocol.

Figure 5.16 to Figure 5.19 decomposes the hysteretic response of the chevron-braced frames for Models 1, 4, 5, 8, and 12, into the strength carried by the braces and the MRF for all the three loading cases. The key strength values previously introduced, defined in Seki et al.[16], are shown in the figure.

As observed in the figures, the simulated strength of the braces and the MRF exceeded H_{2b} and H_{2f}, for Monotonic respectively, for nearly all the braced frames simulated. Under cyclic-1, the strength of the MRF tended to exceed H_{2f} but the strength of the braces slightly underestimated H_{2f} , for all the cases studied.

During pushover analysis, the simulated strength of the braces exceeded the prediction, for nearly all the cases, with exception of Model 8 and 11. The contribution of the MRF slightly exceeded the predicted strength, except models 13 to 16, where the contribution of the MRF was significantly overpredicted. During Cyclic-1 analysis, the contribution of the pair of braces was overpredicted by the design equations, whereas the contribution of the MRF was exceeded the predictions for nearly all the cases. During cyclic-2 loading protocol, both the H_f and H_b exceeded the predicted strength for nearly all the cases.

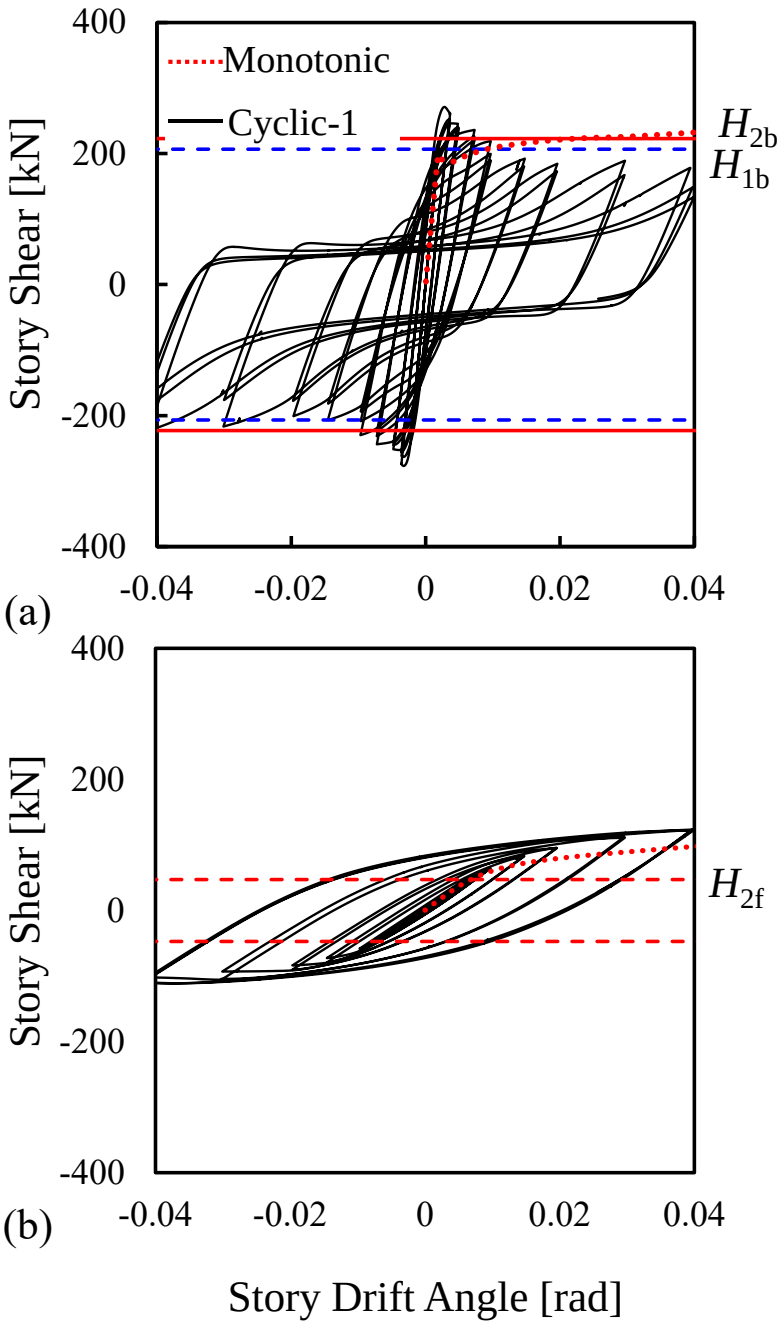

Figure 5.16:Decomposed simulated and experimental response of Model 1: (a) Braces; and (b) Moment

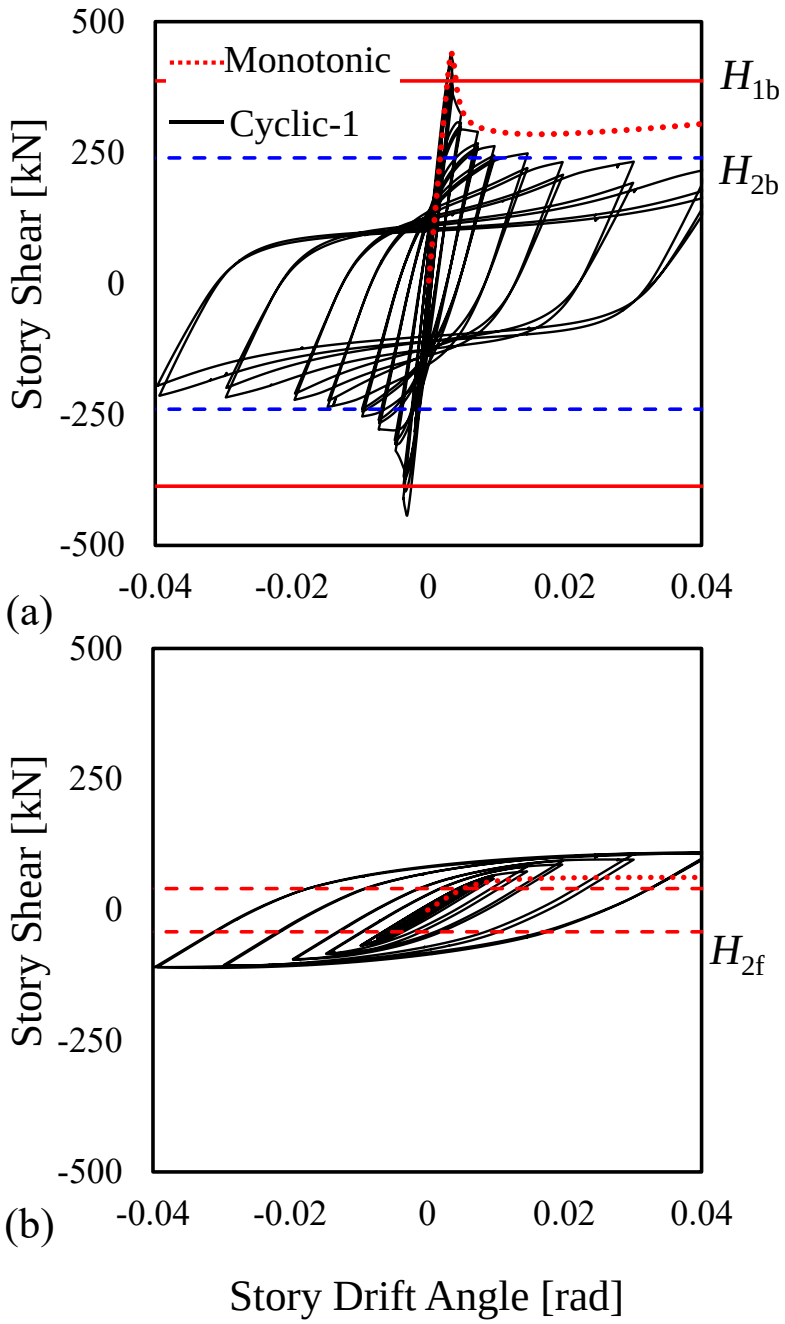

Figure 5.17:Decomposed simulated and experimental response of Model 4: (a) Braces; and (b) Moment frame.

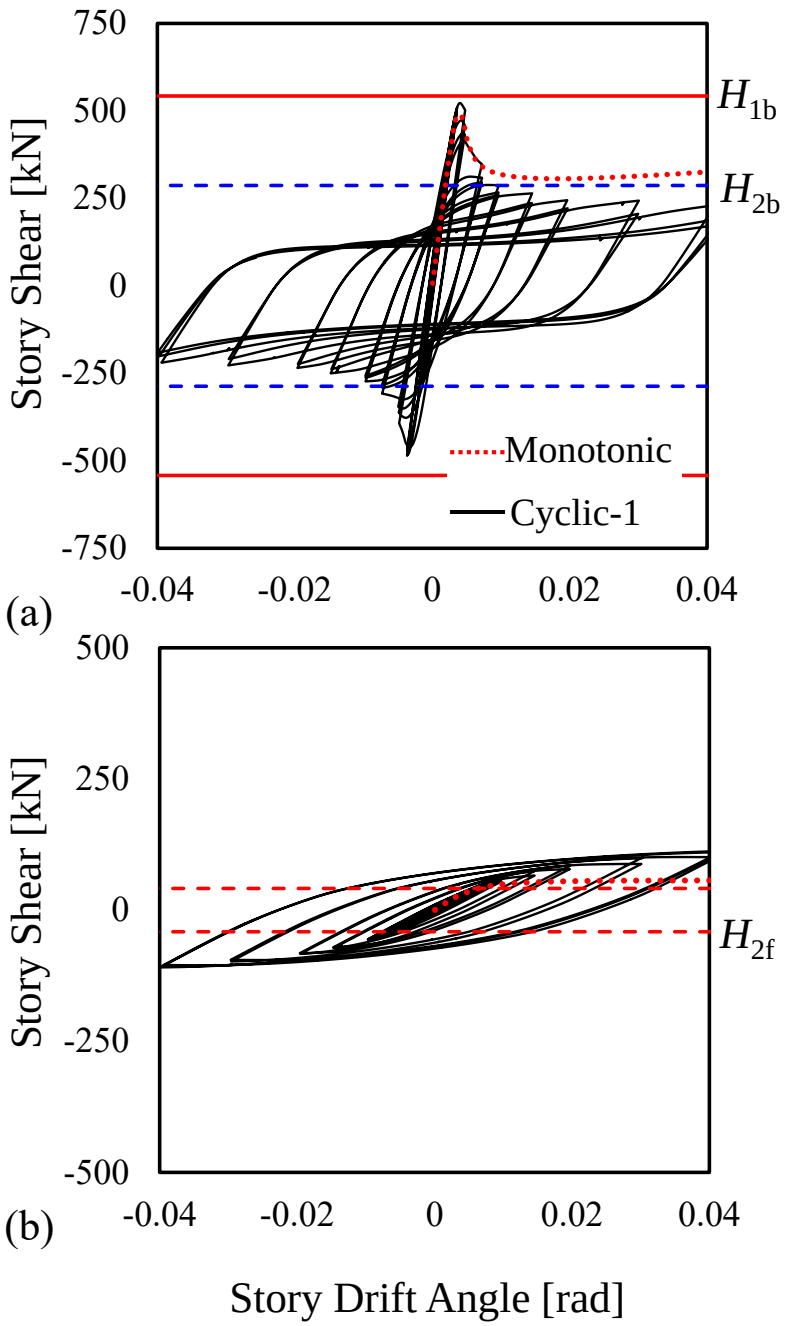

Figure 5.18:Decomposed simulated and experimental response of Model 5: (a) Braces; and (b) Moment frame.

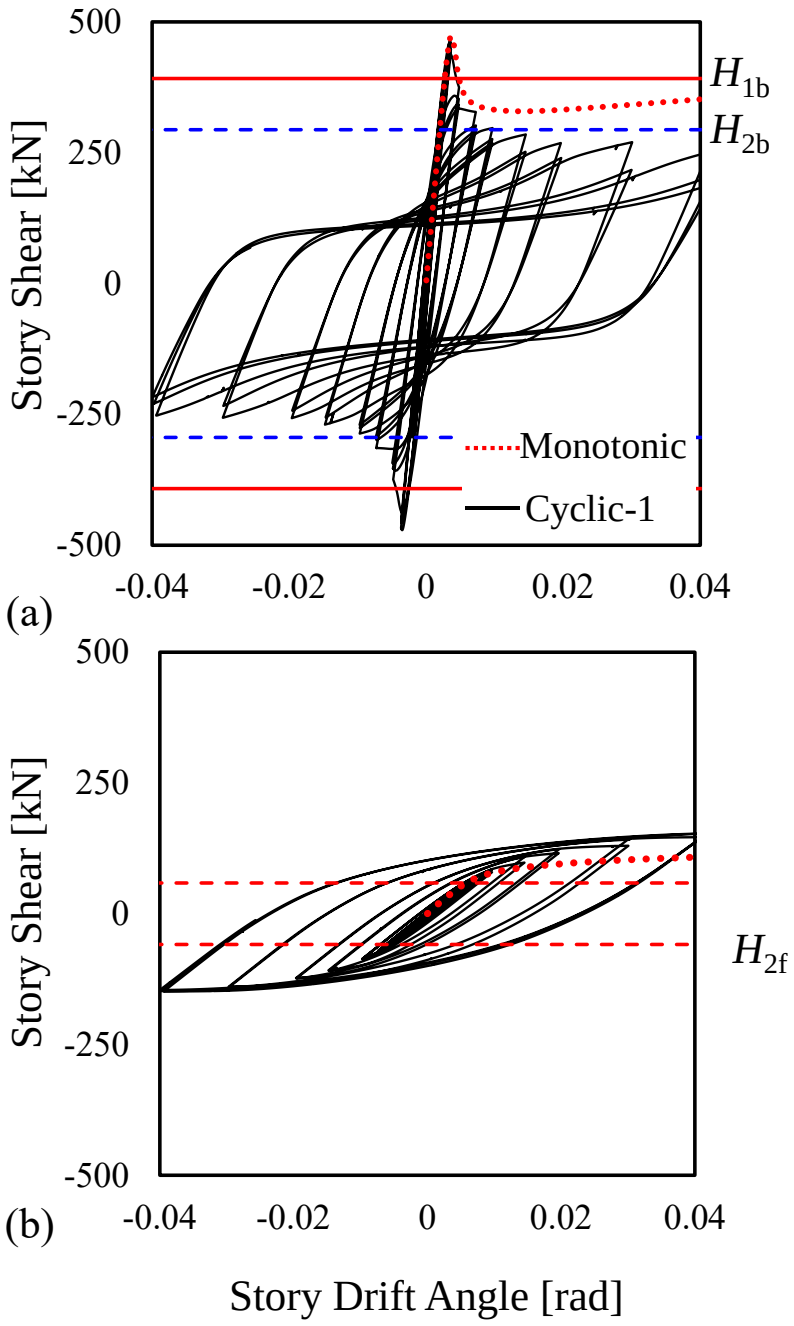

Figure 5.19:Decomposed simulated and experimental response of Model 12: (a) Braces; and (b) Moment frame.

5.3.2 Brace Response

The hysteretic response of the braces is next here. As discussed before, there was significant difference in the hysteretic response of the braces from Monotonic, Cyclic-1, and Cyclic-2, as observed in Figure 5.20 through Figure 5.23.

For all braced-frame models, the braces developed larger tensile strength during Monotonic and Cyclic-2 analysis. In general, Monotonic and Cyclic-2 tended to force the braces do develop larger tensile strength compared to the Cyclic-1 analysis. Because Cyclic-2 analysis is representative of a near-field loading protocol, it tends to force the brace to develop large tensile force. In contrast, Cyclic-1, which is the standard loading protocol, induces large accumulated vertical deflection on the beam. The beam strength deteriorates with repeated loading cycles and thus, the braces develop smaller tensile strength. This response leads to some braces yielding when they were subjected to the Cylic-2 and Monotonic while remaining elastic when subjected to Cyclic-1 loading protocol. For the cases where the strong-beam mechanism controls, the braces yielded, and developed a maximum tensile strength of $1.22N_y$, $1.15N_y$, and $1.20N_y$ Monotonic, Cyclic-1 and Cyclic-2 analysis, respectively. Where the weak-beam mechanism controlled the braces developed a maximum tensile strength of $0.97N_y$, $0.96N_y$, and $0.96N_y$ Monotonic, Cyclic-1 and Cyclic-2 analysis, respectively.

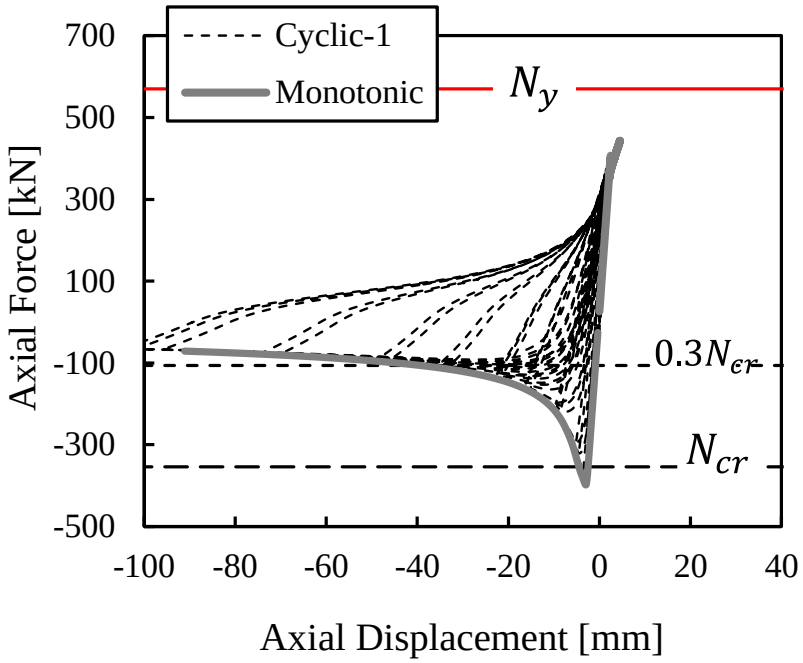

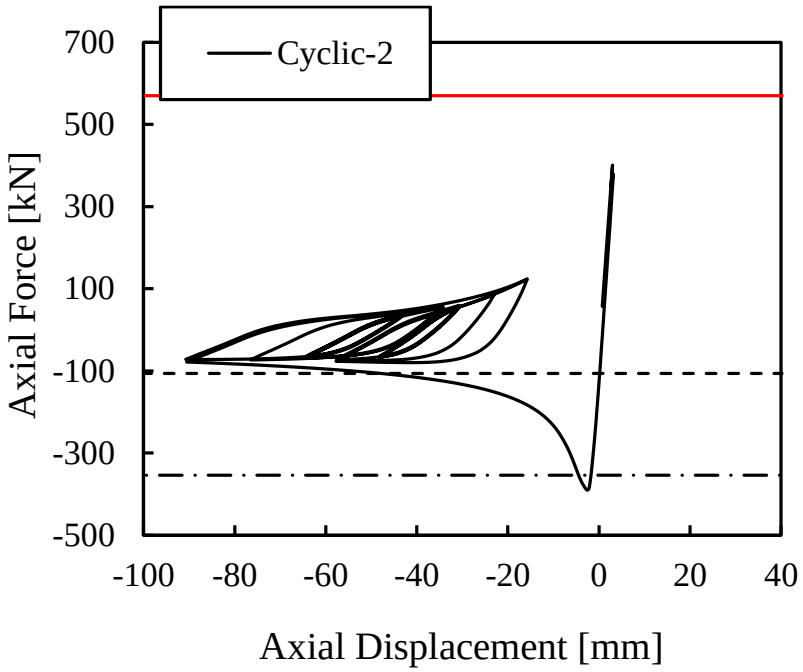

Figure 5.20: Hysteretic response of braces Model 4

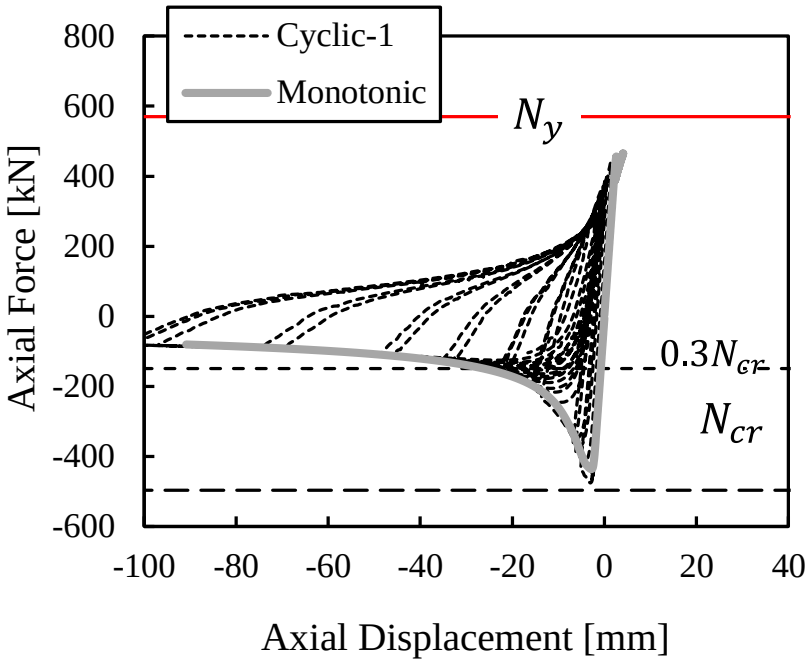

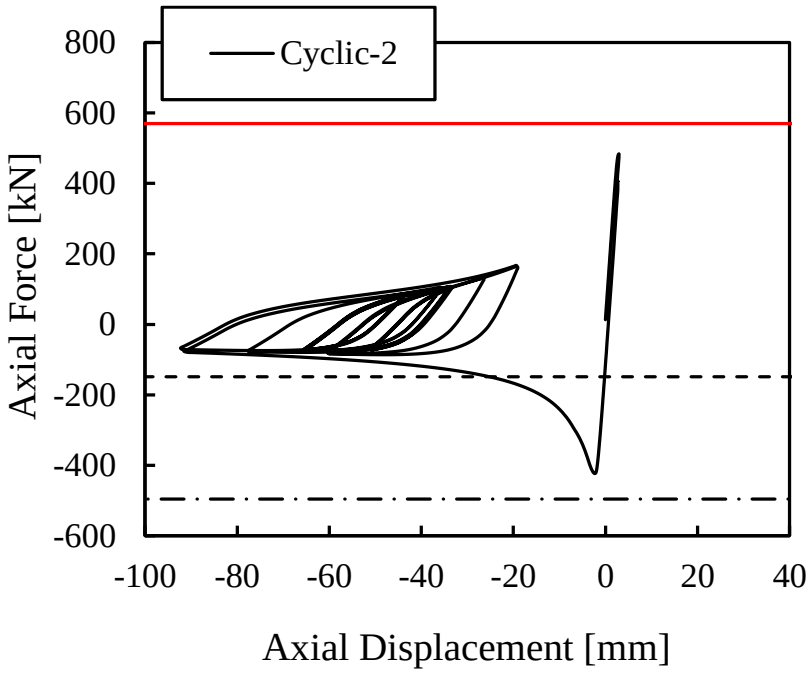

Figure 5.21: Hysteretic response of the North brace for Model 5;

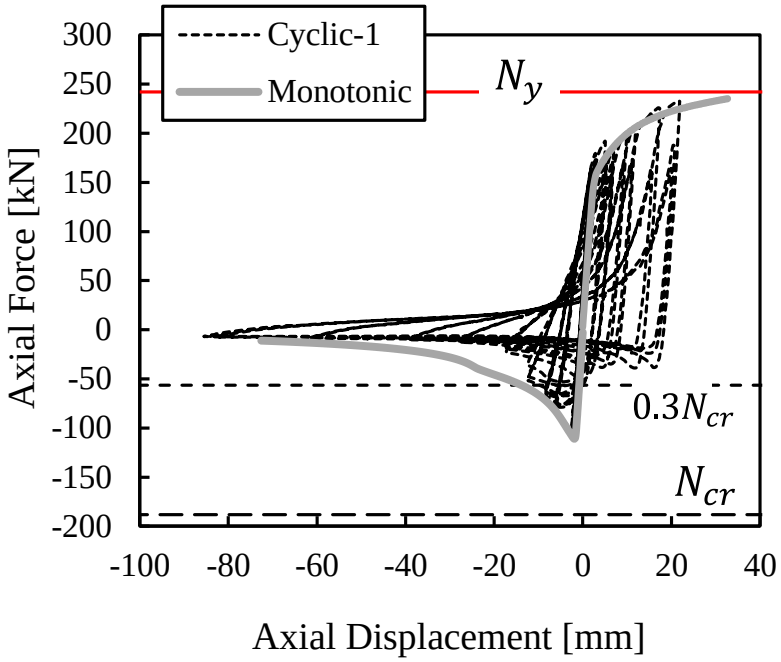

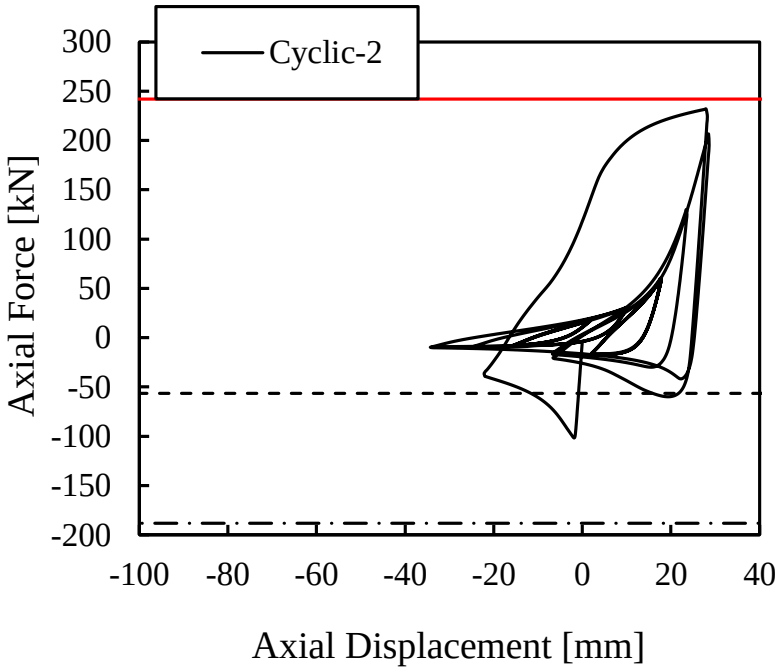

Figure 5.22: Hysteretic response of the North brace for Model 8;

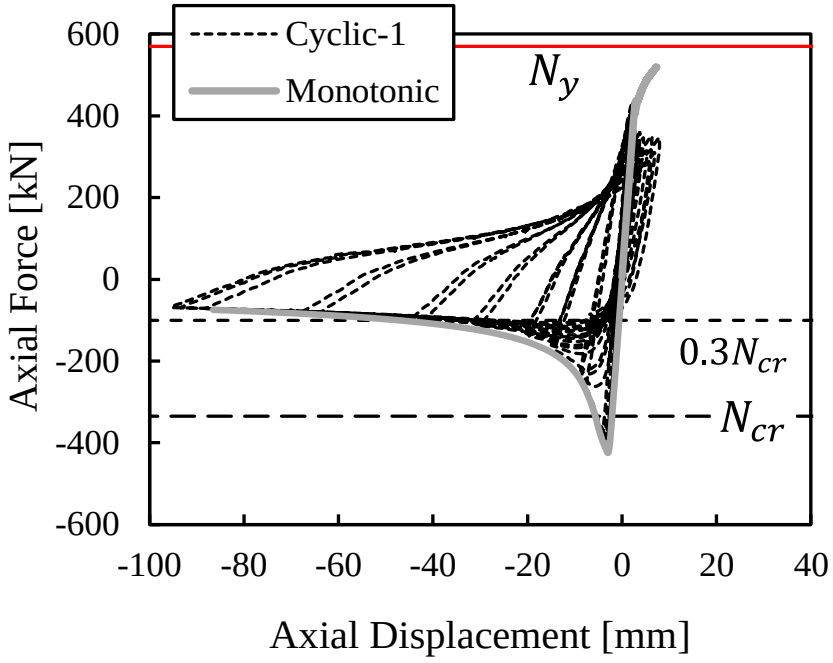

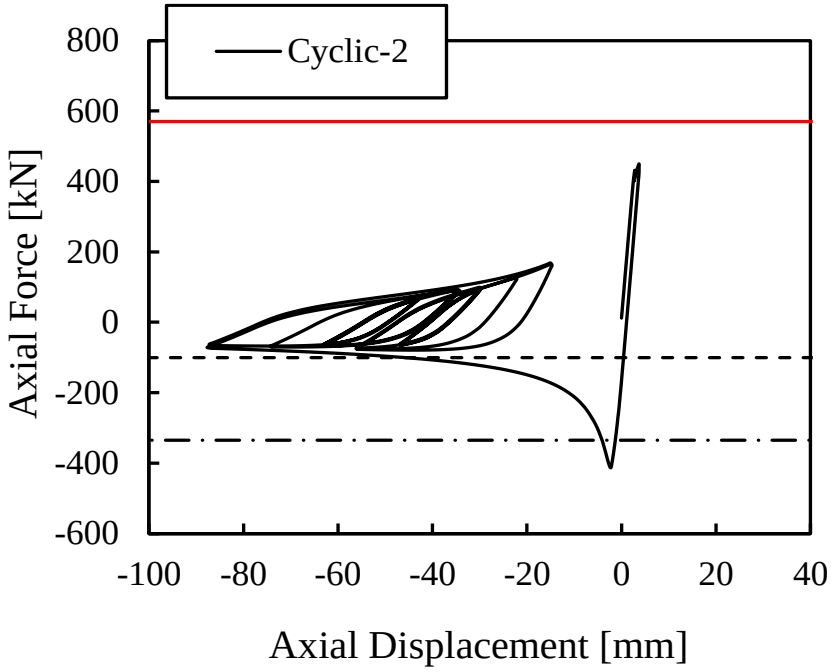

Figure 5.23: Hysteretic response of the North brace for Model 12;

5.3.3 Variation of Beam Capacity with the Loading History

During design a single value of κ is used, however, it is known that the capacity of the beam is a function of the loading history experienced by the braces and the beam end-moments. The capacity of the beam to resist the unbalance load was evaluated. In this discussion, V_{bm} is a variable defined as the maximum force unbalance that the beam can sustain, given the end moments sampled at that instant, without developing M_p in the unstiffened portions of the beam (e.g., outside of the connection elements such as gusset plates). The capacity of the beam, V_{bm} was computed from the bending moments M_{BC} and M_{DC}, sampled at the ends of the beam, as shown in Figure 5.24.

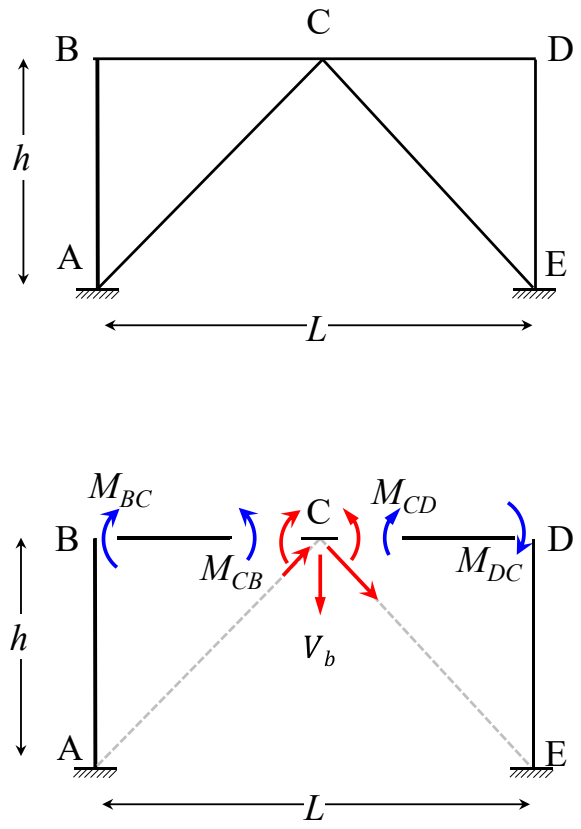

Figure 5.24: Computation of beam capacity

The unbalance load required to yield the beam, when subjected to end moments M_{BC} and M_{DC}, can be computed from equilibrium as follows:

$$-M_{BC} + 2M_C + M_{DC} = {}^{V_b L}/_{2} \tag{43}$$

Since we are interested in the value of V_{bm} required to yield the beam at the center such that (M_{CB} or $M_{CD} \geq M_p$), the unbalance load required to yield the beam can be computed as follows:

$$V_{bm} = \left(-M_{BC} + 2M_p + M_{DC}\right) \times \frac{2}{L} \tag{44}$$

Figure 5.25 to Figure 5.29 plots for Models 1, 4, 5, 8, and 12, subjected to the three loading protocol, the instantaneous unbalance force, V_b/V_{b0}, and the available resistance of the beam, V_{bm}/V_{b0}, over the loading procedure, where V_{bm} is the maximum unbalance force that the beam, can sustain, given the end moments at that instant, without developing M_p in the unstiffened portions of the beam (outside the connection elements such as gusset plates).

When V_b/V_{b0} exceeded V_{bm}/V_{b0}, it was judged that the beam yielded due to the unbalanced force. The figures highlight the statement made in the beginning that κ should reflect the cyclic loading history experienced by the system. Under cyclic loading, κ fluctuated two cycles within each story drift cycle, fell below unity during unloading, and took a maximum value at peak amplitude. For Model 4, the beam yielded over a long process beyond 0.007 rad under Monotonic, at each peak amplitude under Cyclic-1, and during a few large story drift strokes under Cyclic-2. Monotonic was bound to produce larger κ than Cyclic-1. The sampled κ reached a maximum of 1.59, 1.46, and 1.49, and at the reference states of 0.02 rad, first positive 0.02 rad and first positive 0.04 rad, 1.50, 1.20 and 1.48, for Monotonic, Cyclic-1 and Cyclic-2, respectively.

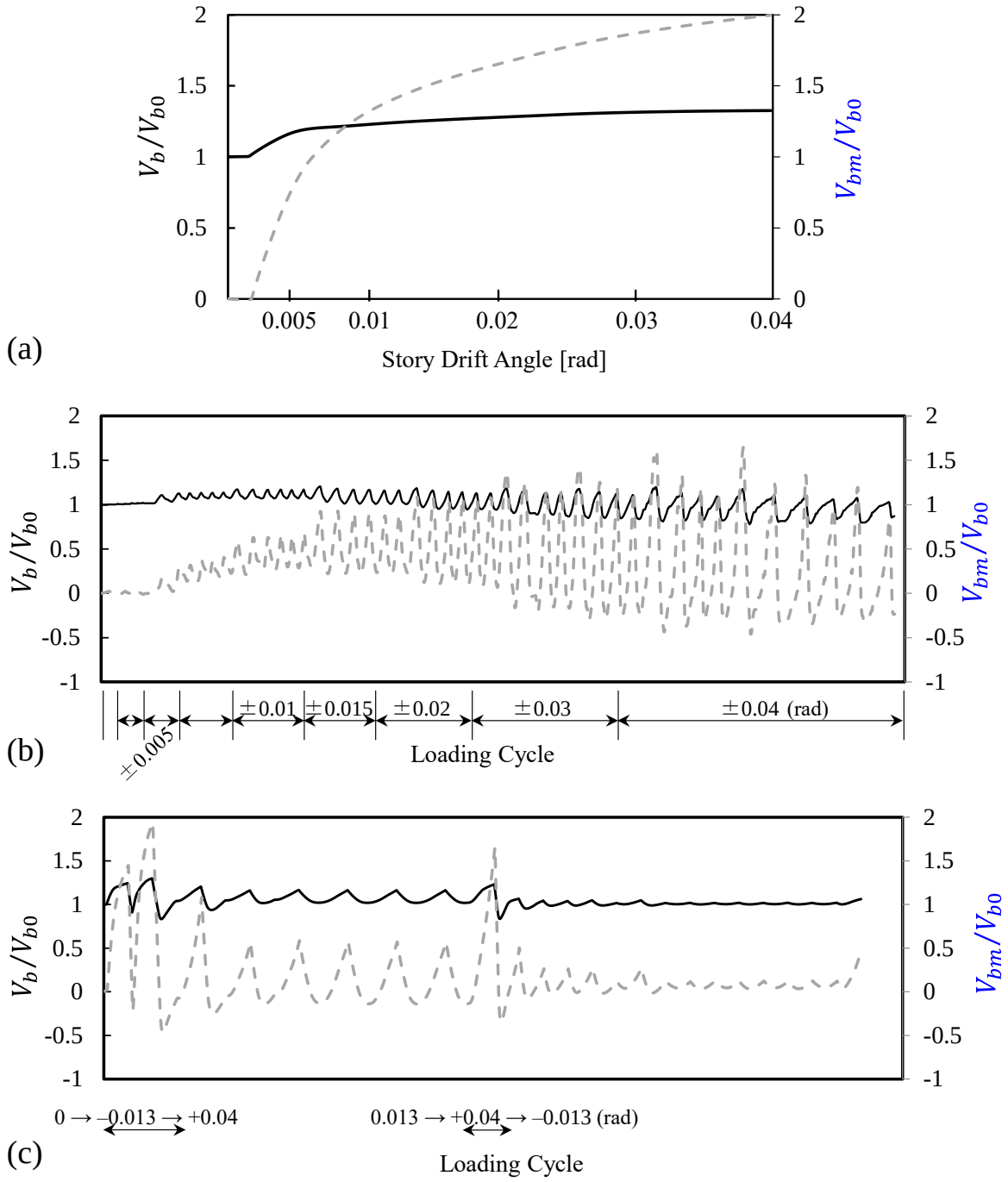

Figure 5.25: Change in $\mathbf{V_{bm}/V_{b0}}$ and κ over loading history for Model 1: (a) Monotonic; (b) Cyclic-1; and (c) Cyclic-2.

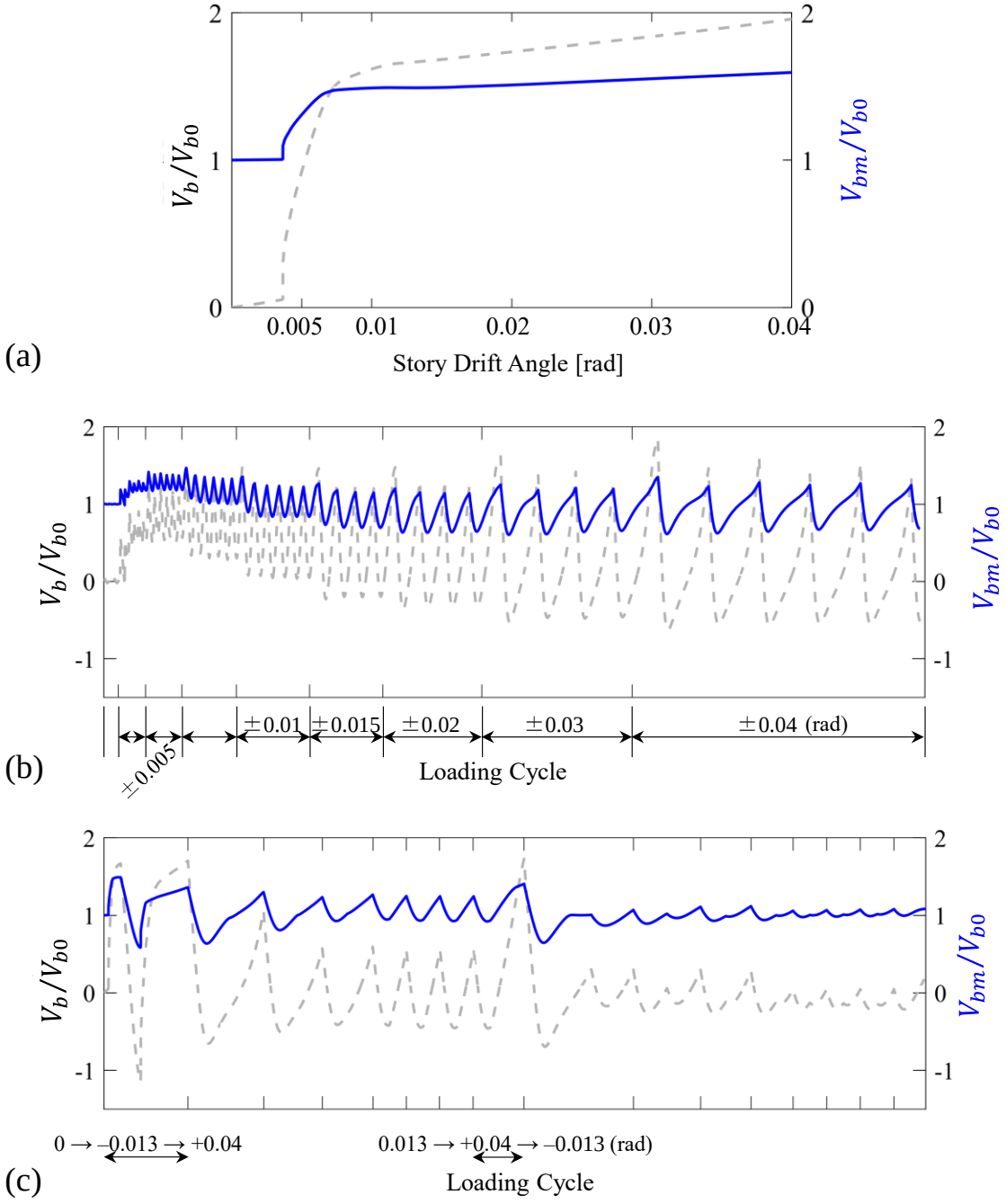

Figure 5.26:Change in $\boldsymbol{V_{bm}/V_{b0}}$ and κ over loading history for Model 4: (a) Monotonic; (b) Cyclic-1; and (c) Cyclic-2.

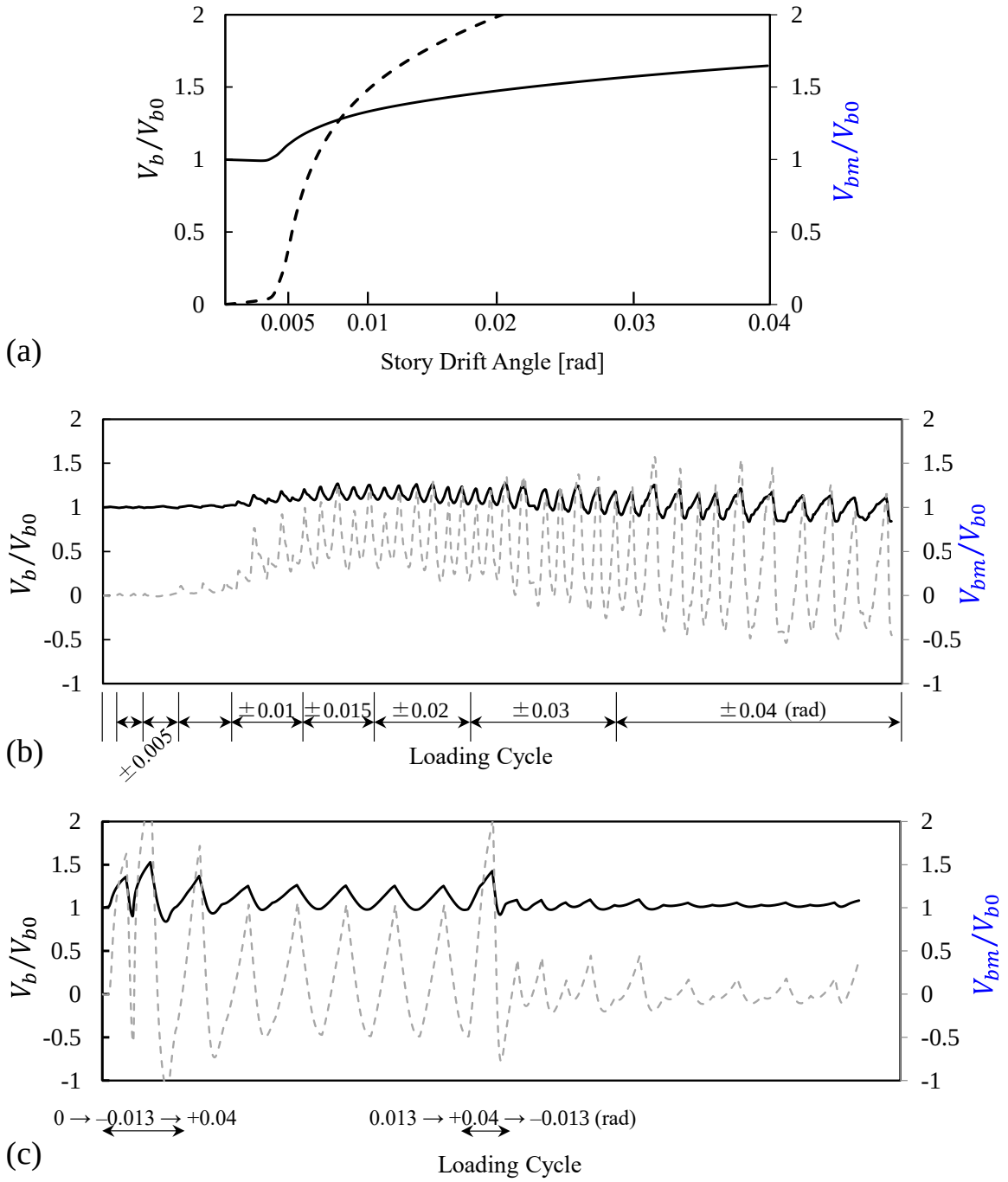

Figure 5.27:Change in $\boldsymbol{V_{bm}/V_{b0}}$ and κ over loading history for Model 5: (a) Monotonic; (b) Cyclic-1; and (c) Cyclic-2.

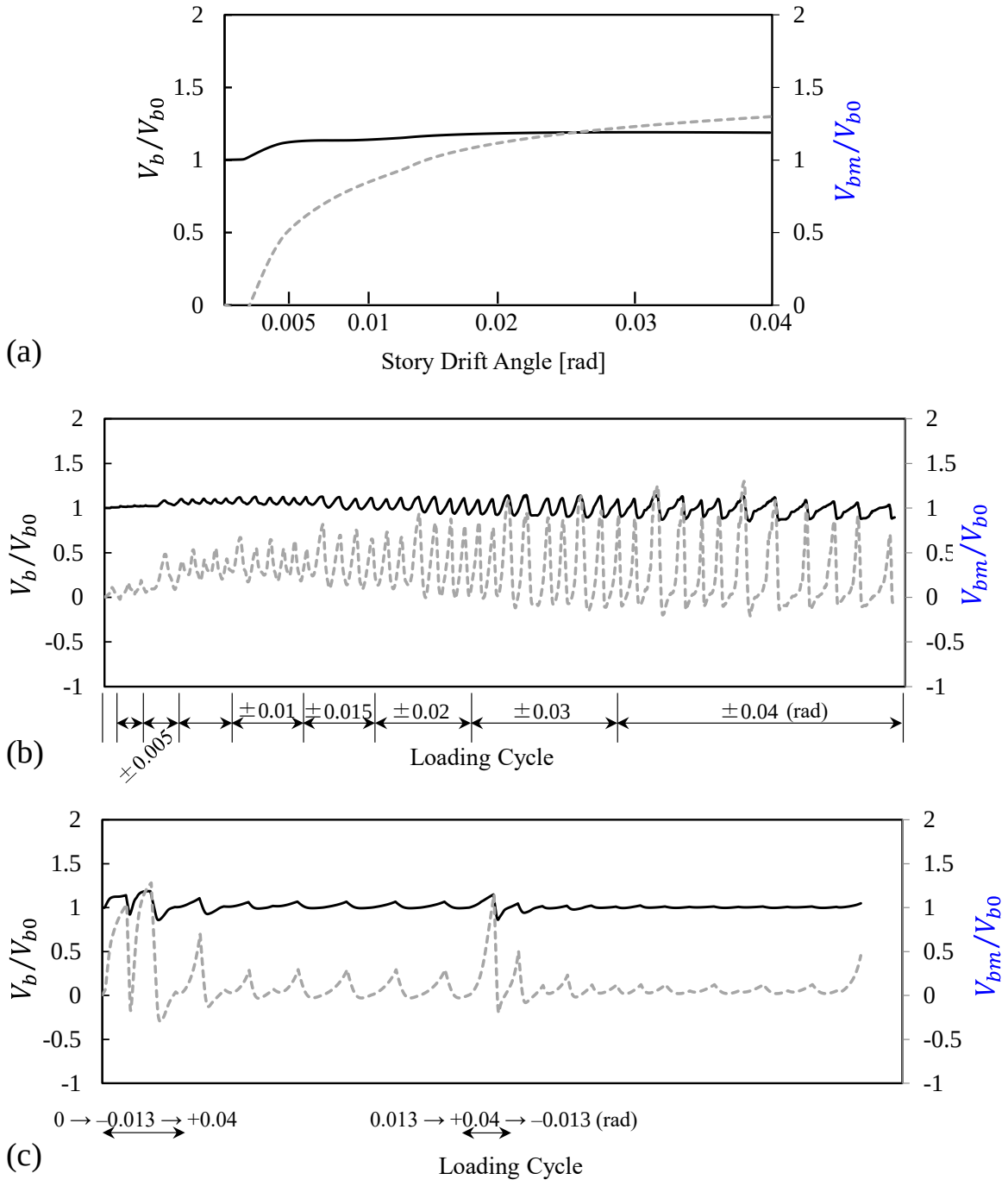

Figure 5.28:Change in $\boldsymbol{V_{bm}/V_{b0}}$ and κ over loading history for Model 8: (a) Monotonic; (b) Cyclic-1; and (c) Cyclic-2.

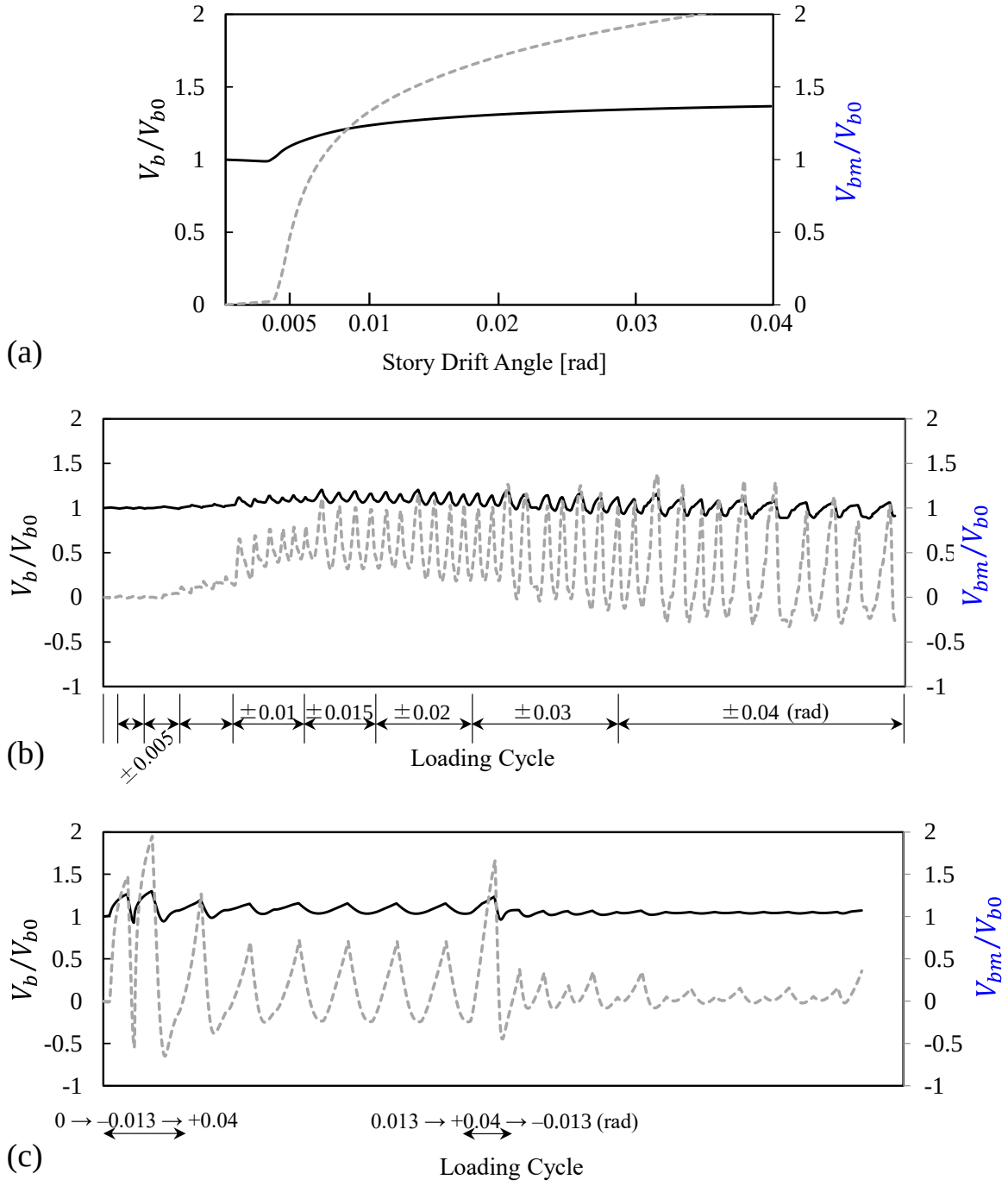

Figure 5.29:Change in V_{bm}/V_{b0} and κ over loading history for Model 12: (a) Monotonic; (b) Cyclic-1; and (c) Cyclic-2.

5.3.4 Correlation between the Sampled H_b/H and r_0.

Figure 5.30 plots the proportion of the lateral strength carried by the brace, H_b/H, against the r_0 listed in Table 2. Table 3 also summarizes key results obtained from each numerical model, the collapse mechanism, β_0 , the unbalanced force and the vertical displacement of the beam. The table lists the energy-dissipation mechanism, either strong-beam, weak-beam or combined mechanism, identified based on whether the brace tensile force reached N_y, the ratio V_b/V_{b0}, discussed in the next section, exceeded the instantaneous κ, or both occurred.

The values H_b/H were sampled at 0.02 rad for Monotonic, the end of the first positive excursion at 0.02 rad for Cyclic-1, and at 0.04 rad for Cyclic-2. The figure indicates the energy-dissipation mechanism, either strong-beam, weak-beam, or combined mechanism, identified based on whether the brace tensile force reached N_y, the ratio V_b/V_{b0} exceeded V_{bm}/V_{b0}, or both occurred. The β_0 from Eqs. (5.48) and (5.49) assuming κ = 1.0 or 1.5 are plotted for reference. Figure 5.30 shows that the sampled H_b/H lied between β_0 assuming κ = 1.0 and 1.5: close to $\beta_0$assuming κ = 1.5 for Monotonic, but somewhat smaller than β_0 assuming κ = 1.0 for Cyclic-1. With no exception, the sampled H_b/H was largest for Monotonic and smallest for Cyclic-1. When the strong-beam mechanism controlled, the sampled H_b/H was close to β_0, but when the weak-beam mechanism controlled, the sampled H_b/H was between 0.89 and 1.06β_0, 0.74 and 0.92β_0, and 0.85 and 1.02β_0 assuming κ = 1.5 for Monotonic, Cyclic-1 and Cyclic-2, respectively. Monotonic and Cyclic-2 tended to stretch the tension braces more than Cyclic-1, and thereby develop larger unbalance force to force a weak-beam mechanism. Cyclic-1 tended to produce smaller unbalance force than predicted, and thereby, allow the MRF to develop larger lateral strength than predicted.

Models 1 to 3 and 7 to 9, with 2.8≤ r_0 ≤4.1, did not necessarily develop the predicted mechanism. Cyclic-1 produced the same mechanism as predicted, except for Model 8, which was predicted to form a strong-beam mechanism but instead nearly formed a combined mechanism where, after beam yielding, brace tension reached 0.96N_y. Monotonic and Cyclic-2 caused disagreement in more models: Models 1, 2, 3, 7 and 9, which were predicted to develop a weak-beam mechanism instead developed a combined mechanism, yielding first in the beams and subsequently in the tension brace; Model 8 formed a weak-beam mechanism, again, close to a combined mechanism.

The figure also highlights the fact that H_b/H is affected primarily by the loading protocol while brace slenderness ratio (62 to 145), relative strength of the braces with respect to the beam (r_0 between 4 and 11), and bracing connection have a smaller effect.

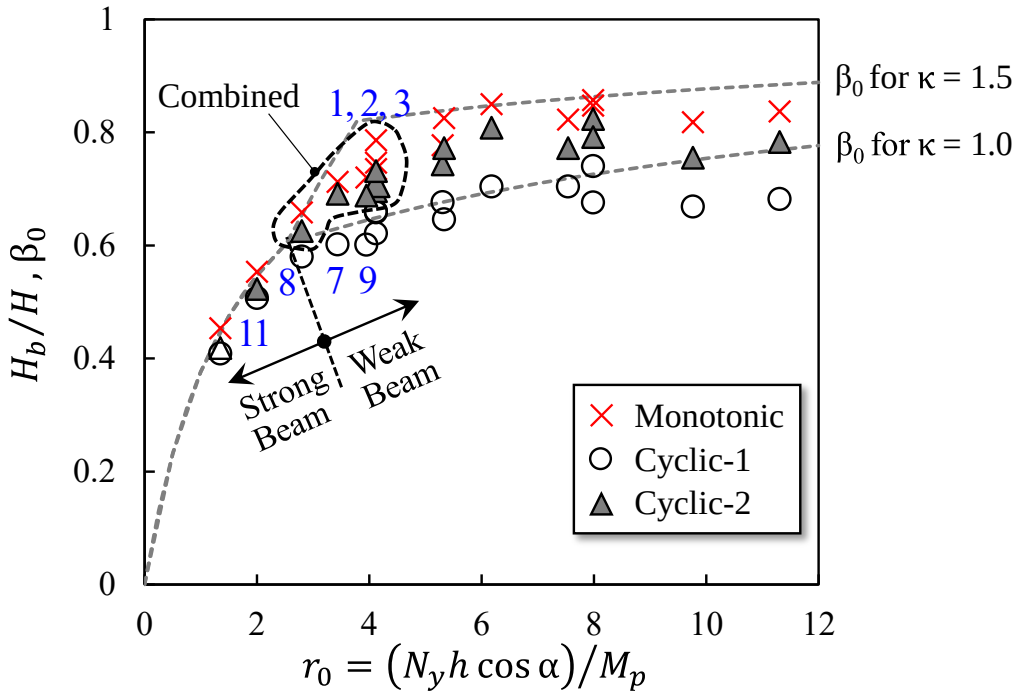

Figure 5.30: Sampled H_b/H versus r_0.

To explore an appropriate design value for κ, the correlation between the predicted β_0 and the sampled H_b/H from all the loading cases for different values of κ: 1.5, 1.25, and 1.0. Figure 5.31 plots the correlation between the predicted β_0 and the sampled H_b/H form all the three loading protocols. As recognized in the figure, larger κ gives larger β_0. κ = 1.5 matched Monotonic but substantially overpredicted Cyclic-1; κ = 1.0 matched Cyclic-1 on average but underpredicted Monotonic and Cyclic-2 for most models. In comparison, κ = 1.25 matched Monotonic and Cyclic-2 but overpredicted Cyclic-1 for most models. Between the 3 cases, the best match over the 16 models and 3 loading protocols was obtained with κ = 1.25: the simulated H_b/H was between 0.84 and $1.01\beta_0$ for Monotonic, between 1.01 and $1.2\beta_0$ for Cyclic-1, and between 0.88 and $1.05\beta_0$ for Cyclic-2. For all the braced frames, larger κ predicts larger H_{2b} and smaller H_{2f}, but $H_2 = H_{2b} + H_{2f}$ is mathematically independent of κ, as shown in Figure 5.32. Between the two choices, κ = 1.25 provided a better estimate of the MRF resistance.

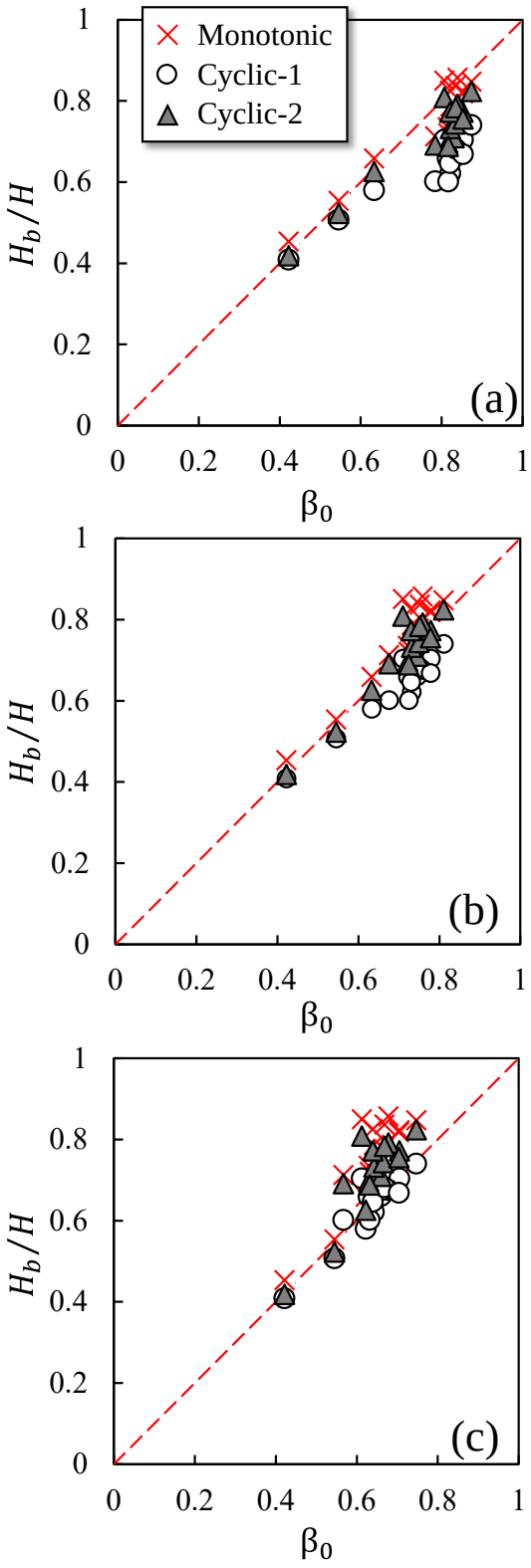

Figure 5.31: Correlation between the computed and simulated β_0: (a) κ=1.5, (b) κ=1.25, and (c) κ=1.0.

Table 5.2: Comparison of the Analytical predictions and Numerical Analysis response

		Analytical Prediction			Monotonic-Pushover				Cyclic-1					Cyclic-2				
Models	r_0	Mechanism	β0 (κ =1.5)	Mechanism	H_b/H	V_b/V_{b0}	N/N_y	v/l	Mechanism	β_0	V_b/V_{b0}	N/N_y	v/l	Mechanism	β_0	V_b/V_{b0}	N/N_y	v/l
1	4.12	WB	0.81	CM	0.74	2.00	1.03	0.012	WB	0.66	1.65	0.91	0.016	CM	0.70	1.94	0.89	0.012
2	4.12	WB	0.82	CM	0.75	1.91	1.05	0.011	WB	0.66	1.65	0.91	0.017	CM	0.71	1.88	0.92	0.011
3	4.12	WB	0.81	CM	0.79	1.88	0.99	0.013	WB	0.62	1.55	0.79	0.016	CM	0.73	1.91	0.92	0.013
4	7.54	WB	0.84	WB	0.82	2.46	0.78	0.019	WB	0.70	1.59	0.72	0.021	WB	0.77	2.25	0.73	0.018
5	7.98	WB	0.86	WB	0.85	2.55	0.82	0.019	WB	0.74	1.57	0.85	0.022	WB	0.82	2.40	0.78	0.018
6	7.98	WB	0.83	WB	0.86	2.80	0.83	0.017	WB	0.68	1.98	0.60	0.019	WB	0.79	2.51	0.65	0.016
7	3.43	WB	0.78	CM	0.71	1.84	1.10	0.013	WB	0.60	1.22	0.75	0.016	CM	0.69	1.77	1.05	0.013
8	2.80	SB	0.66	WB	0.66	1.30	0.97	0.007	WB	0.58	1.30	0.96	0.014	WB	0.63	1.28	0.90	0.008
9	3.95	WB	0.81	CM	0.72	1.93	1.08	0.015	WB	0.60	1.37	0.80	0.018	CM	0.69	1.83	1.03	0.014
10	1.34	SB	0.42	SB	0.45	0.78	1.22	0.003	SB	0.41	0.75	1.15	0.005	SB	0.42	0.78	1.06	0.003
11	2.00	SB	0.54	SB	0.55	0.99	1.05	0.005	WB	0.51	0.97	1.00	0.009	WB	0.52	1.00	0.92	0.005
12	5.30	WB	0.83	WB	0.78	2.07	0.91	0.017	WB	0.68	1.39	0.77	0.017	WB	0.74	1.95	0.86	0.016
13	6.18	WB	0.80	WB	0.85	3.49	0.82	0.019	WB	0.70	2.53	0.59	0.019	WB	0.81	3.09	0.61	0.016
14	5.33	WB	0.81	WB	0.83	2.73	0.90	0.016	WB	0.65	1.87	0.62	0.016	WB	0.77	2.40	0.71	0.015
15	11.31	WB	0.83	WB	0.84	0.00	0.00	0.021	WB	0.68	0.00	0.00	0.024	WB	0.78	0.00	0.00	0.018
16	9.76	WB	0.84	WB	0.82	0.00	0.00	0.021	WB	0.67	0.00	0.00	0.024	WB	0.76	0.00	0.00	0.018

Note: SW: Strong-beam mechanism; WB: Weak -beam mechanism

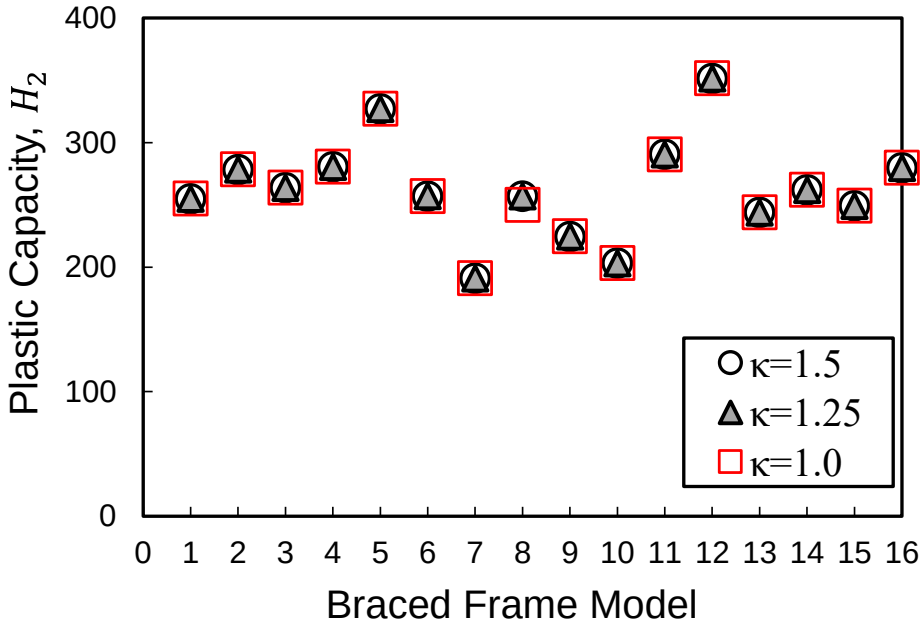

Figure 5.32: Plastic strength for all the chevron-braced frames for κ=1.5, κ=1.25, and κ=1.0.

5.3.5 Beam Deflection

Figure 5.33 to Figure 5.38 shows the deflection of the beam for the three loading protocols for models 1, 4, 5, 8, 10 and 12. In general, cyclic-1 loading protocol led to larger vertical deflection of the beams for all the braced frame specimens. Cyclis-2 and Monotonic induce similar vertical deflection demands on the beam. All the cases where the weak-beam mechanism controlled the energy dissipation mechanism of the chevron-braced MRF, the beam was subjected to larger vertical deflections.

Figure 5.39 plots the correlation between the peak beam vertical deflection, normalized by the span, and the relative lateral strength of the beam with respect to the braces, r_0, for all the braced frame models simulated. Where the strong-beam mechanism controlled, the normalized peak beam deflection was 0.007, 0.014, and 0.008 for Monotonic, Cyclic-1, and Cyclic-2 analysis, respectively. Where the weak-beam mechanism controlled, the normalized peak beam deflection grew large, reaching a maximum of 0.021, 0.024, and 0.018 for Monotonic, Cyclic-1, and Cyclic-2, respectively.

The simulated vertical deflection of the beam in all the braced frames specimens is summarized in table 2. Although recent research (Roeder et al.[14], Sen et al. [15]) has shown that yielding of the beam is not necessarily detrimental to the performance of the chevron-braced MRF, and in fact may lead to improved performance, it is important to limit the vertical deflection of beam as it may induce cracks in the concrete floor slab.

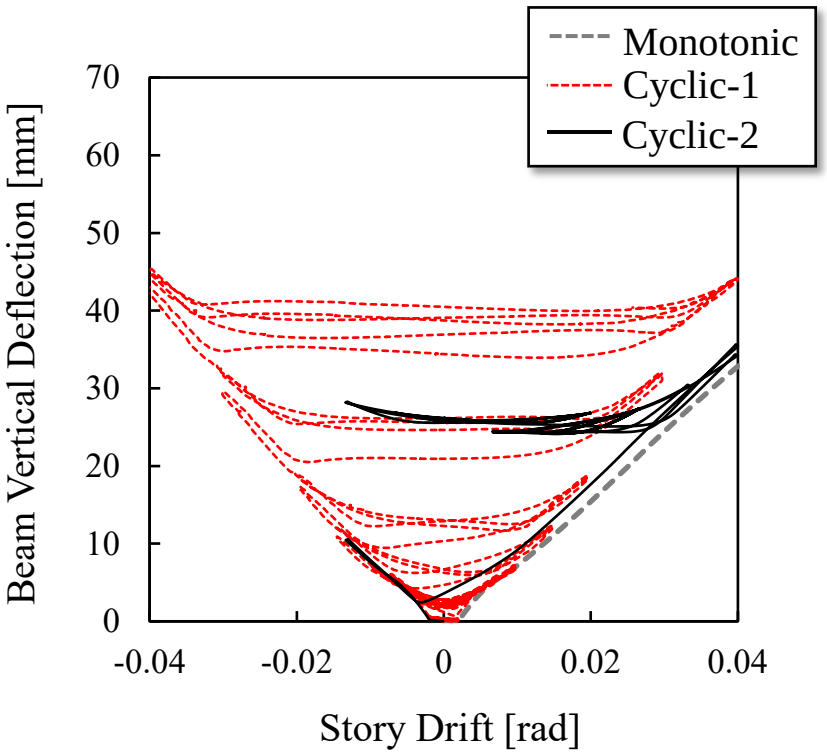

Figure 5.33: Beam Vertical Deflection Model 1

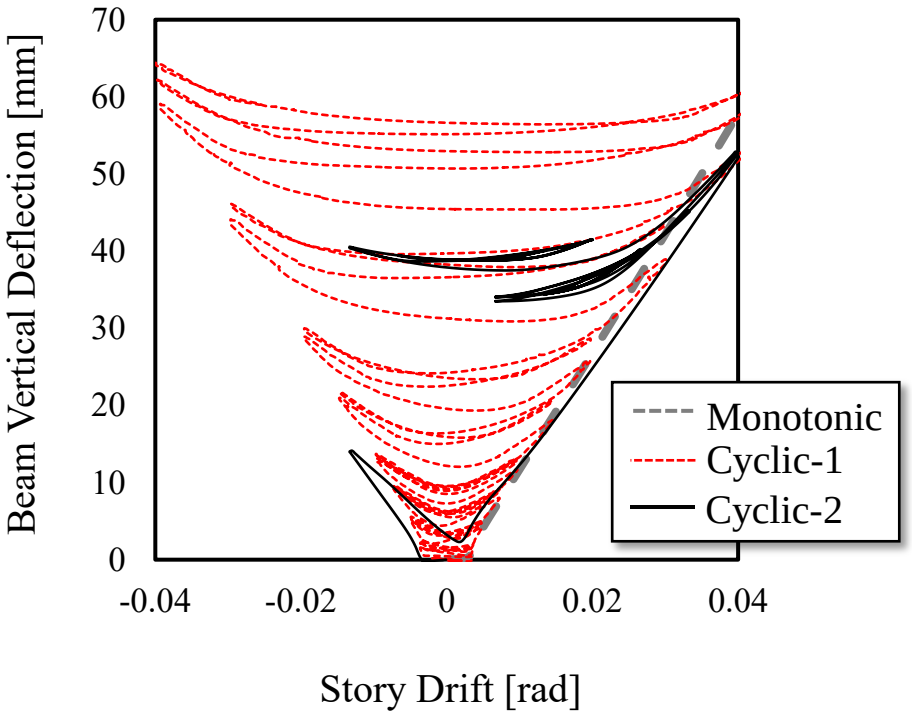

Figure 5.34: Beam Vertical Deflection Model 4

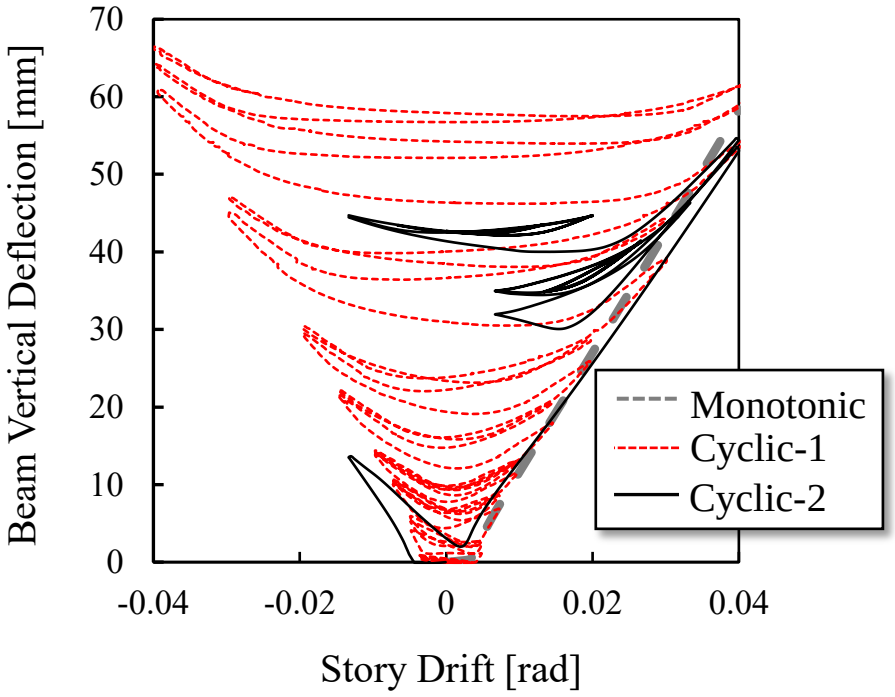

Figure 5.35: Beam Vertical Deflection Model 5

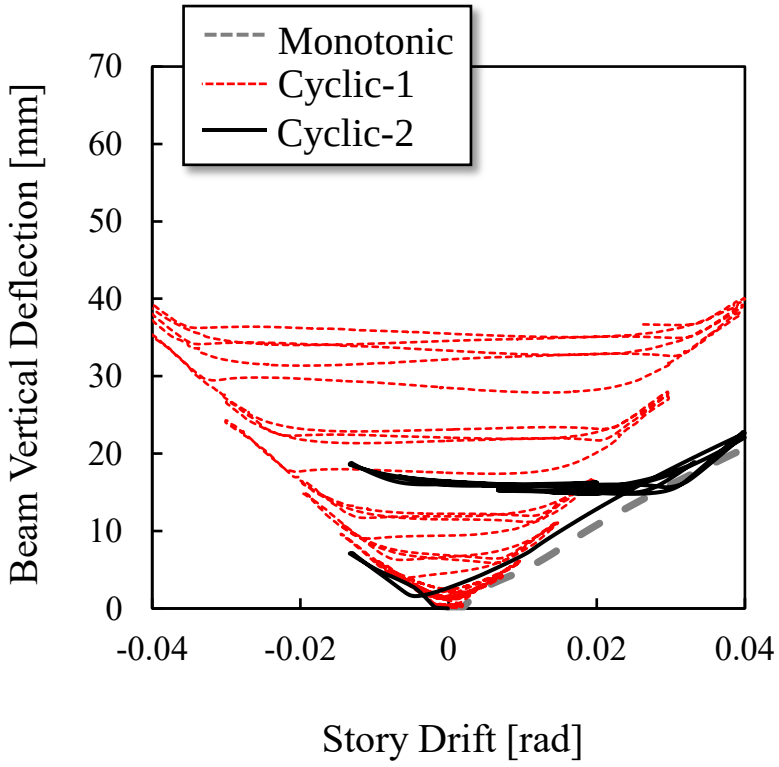

Figure 5.36: Beam Vertical Deflection Model 8

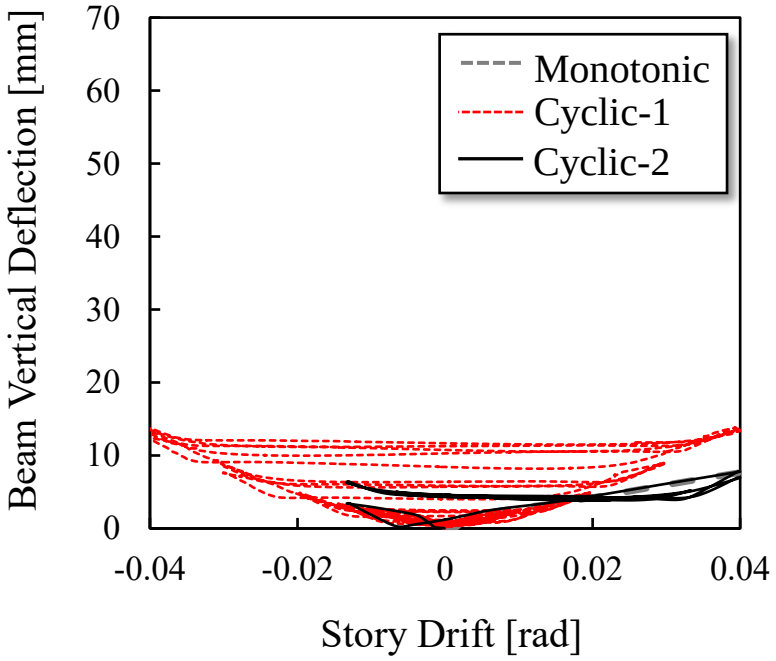

Figure 5.37: Beam Vertical Deflection Model 10

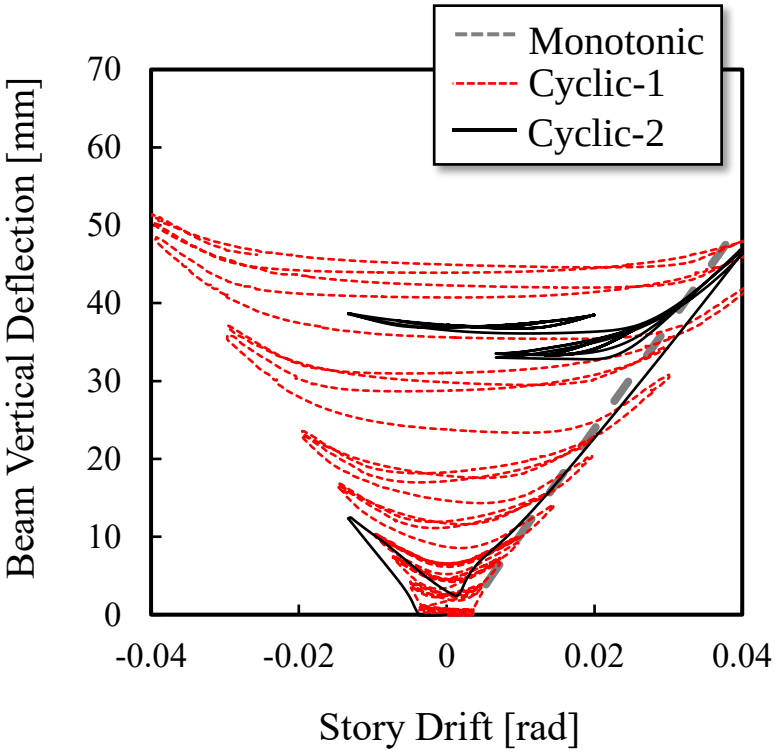

Figure 5.38: Beam Vertical Deflection Model 12

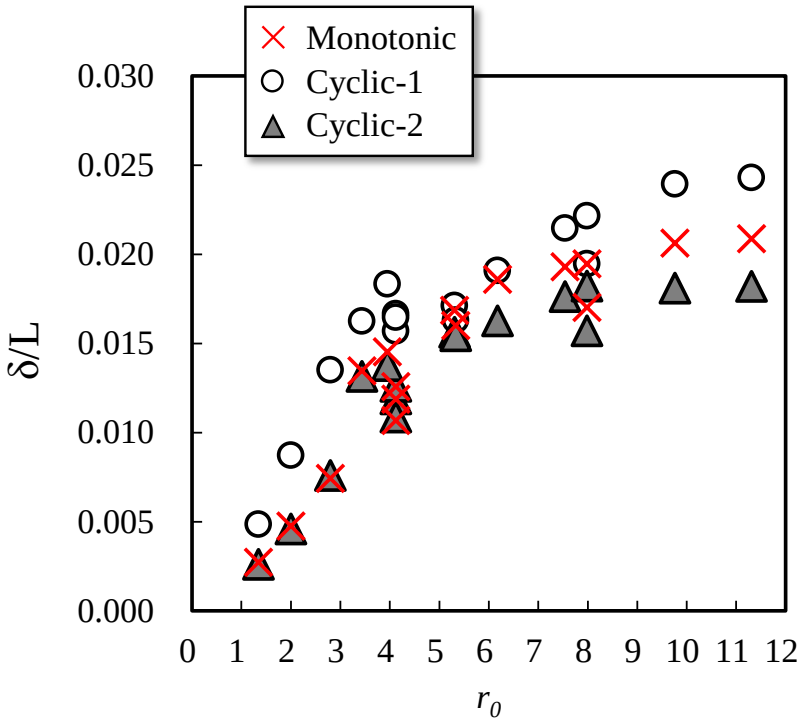

Figure 5.39: Beam vertical deflection

5.4 Summary

A computational parametric study was conducted to examine how the performance of Japanese chevron CBFs is affected by key design parameters such as: (*i*) the strength of the beam intersecting braces with respect to the braces; (*ii*) the effect of the bracing connection; (iii) the brace placement angle. A design equation that quantifies the correlation between the relative horizontal strength of the braces with respect to the beam, r_0 and the proportion of the lateral strength derived from the chevron braces, β_0 was proposed.

The main findings of the analyses can be summarized as follows:

3) The design equation can reliably predict the plastic mechanism using a fixed ratio κ of the maximum unbalanced load over the plastic strength of the beam of κ = 1.5, however it tends to overestimate the proportion of the lateral strength derived from the pair of braces.

4) A key design parameter to control the energy dissipating mechanism of chevron-braced MRFs is the factor κ to proportion the beam intersected by braces. The factor κ changes over the loading sequence, but generally reaches 1.5 under monotonic loading or large

monotonic pulses and develops a smaller value close to unity under gradually increasing cyclic loading. Rather than the value $\kappa = 1.5$ previously used by Seki et al. [16], $\kappa = 1.25$ was more representative over the examined proportions and loading sequences and better matched the test results by Seki et al. [16]. Although κ affects the predicted mechanism, it does not affect the predicted lateral plastic strength of the chevron-braced MRF.

5) The "weak-beam mechanism" provides a stable energy dissipation if the beam intersecting braces is provided with sufficient lateral bracing.

6. SEISMIC DESIGN OF LOW- AND MID-RISE BRACED FRAME SYSTEMS

6.1 Introduction

Steel chevron braced frames (CBFs) are widely used in Japan, however, to day, limited design guidance is provided in the Japanese design code and provisions to how to proper design and detail the beams and braces. This chapter aims at developing a straightforward and rational design procedure to design chevron-braced concentrically MRFs to meet Japanese design requirements. The β_0 versus r_0 relationship introduced in chapter 3, was used to proportion the chevron-braced MRFs. In the sequence, a series of low- and mid-rise chevron braced frames were designed to evaluate the performance of this structural system.

6.2 Design Procedure

The design procedure for design and detailing steel chevron braced frames is shown in Figure *6.1*. The first step is to define the desired or the target energy-dissipation mechanism of the brace frame and based on the members preliminary ductility, compute the force reduction factor, D_s, computed according to the Japanese provisions [35], based on the ductility of the braces and moment-resisting frame.

In step (2) depending on the target energy-dissipation mechanism, the target value for the relative horizontal strength of the brace with respect to the beam r_0, is defined and the proportion of the lateral strength carried by the pair of braces can be computed using the β_0 versus r_0 equations introduced chapter 3. The next step in the design process **(**step (3**)),** the story shear demand can be computed. Here the story shear, Q_n, was computed according to the level II design of the Japanese code [35].

In step (4), the demands on the brace, Q_{n_br} and the moment-resisting frame, Q_{n_MRF} can be computed as follows:

$$Q_{n\_br} = \beta_0 \times Q_n \tag{6.1}$$

$$Q_{n\_MRF} = (1 - \beta_0) \times Q_n \tag{6.2}$$

The proportion of the lateral strength carried by the pair of braces over the brace frame lateral strength, β_0 is computed as follows:

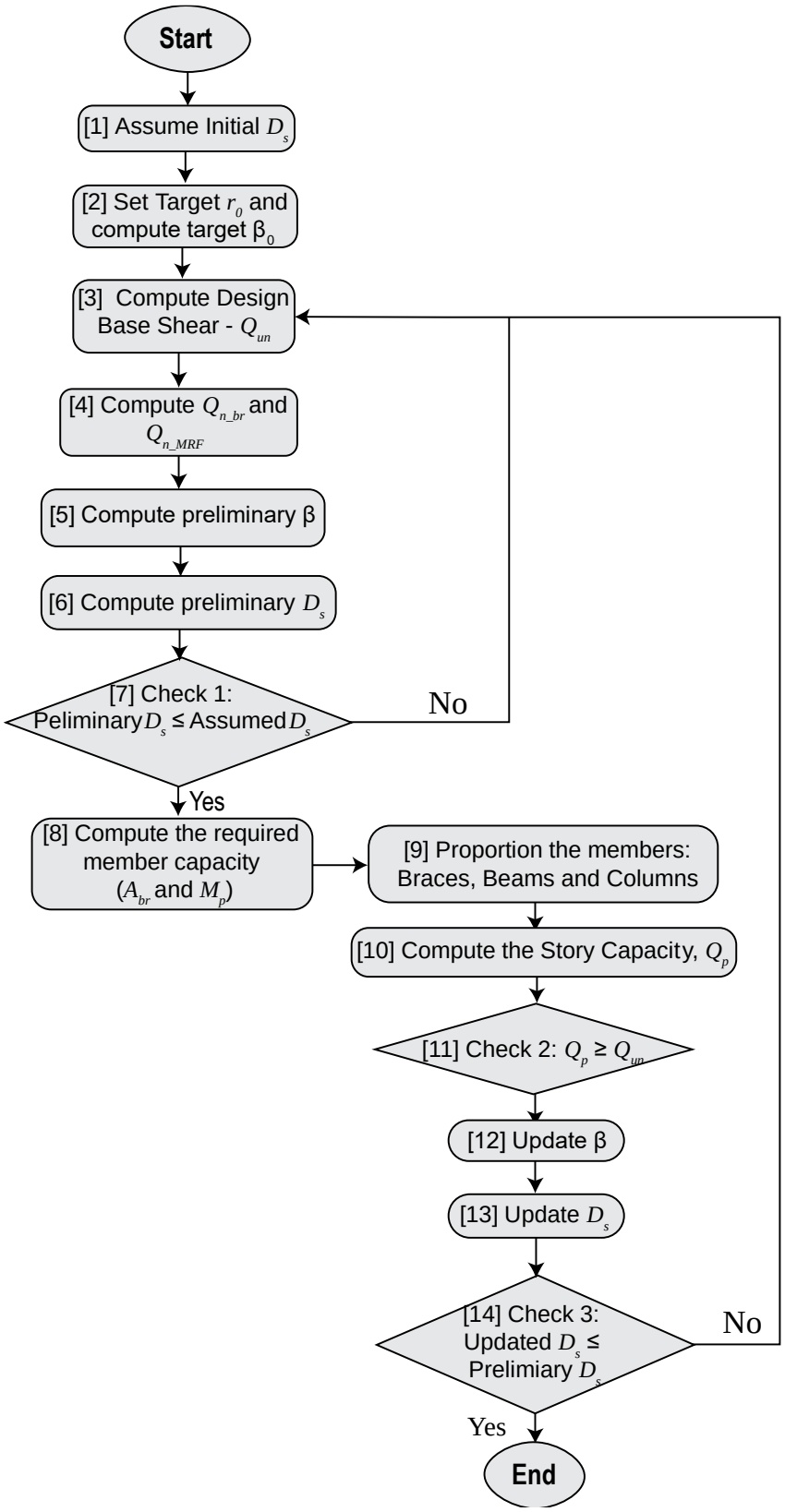

$$\beta_0 = \frac{Q_{n\_br}}{Q_n} \tag{6.3}$$

Because the D_s values depends on the proportion of the lateral strength carried by the braces for the entire story, β and the brace slenderness ratio, the preliminary D_s values should be computed (**step (6)).** In **step (8 and 9)**, the required member properties, brace area, ${}_{req}A_g$ and beam capacity, ${}_{req}M_p$ are computed. The plastic strength of each story, Q_p, should be computed (**step 10**). In the next step, the condition in (5.4) must be verified in any story:

$$Q_p \geq Q_n \tag{6.4}$$

This finalizes the design process. A final check must be done, to evaluate the need to adjust the force reduction factor, D_s. The proportion of the lateral strength carried by the braces, β should be updated and, β is the same as computed in (Step 5), D_s does not need to be updated, and the design is finalized. No additional check is required as all the requirements have been verified.

6.3 Design of Low- and Medium-Rise Chevron-Braced Frames

To study the reliability of the design procedure introduced, the seismic performance of a series of 4-, 8- and 12- story braced-frame systems is designed and will later be analyzed using the OpenSees framework.

6.3.1 Design Approach

The design of the braced frames was conducted using plastic design employing the design procedure discussed earlier. More details about the design method can be found in Inoue et al. [36].

The braced frame plan and elevation is depicted in Figure 6.2. The braced frame models comprised steel chevron-braced frames with heights (4-, 8- and 12- stories). The floor height was uniform and set to 4 *m*. It's assumed that the buildings are used as a general office, and the frame is continuous at intervals of 7.5 *m* in the depth direction. The seismic design code in Japan since 1981 [35], considers two levels of seismic forces (Level 1 or first phase for serviceability and Level 2 or second phase for safety). The braced frames were proportioned for Level-2 design requirements of the Japanese Building Standard. The gravity load was secured using the simplified design method proposed by Inoue et al.[36].

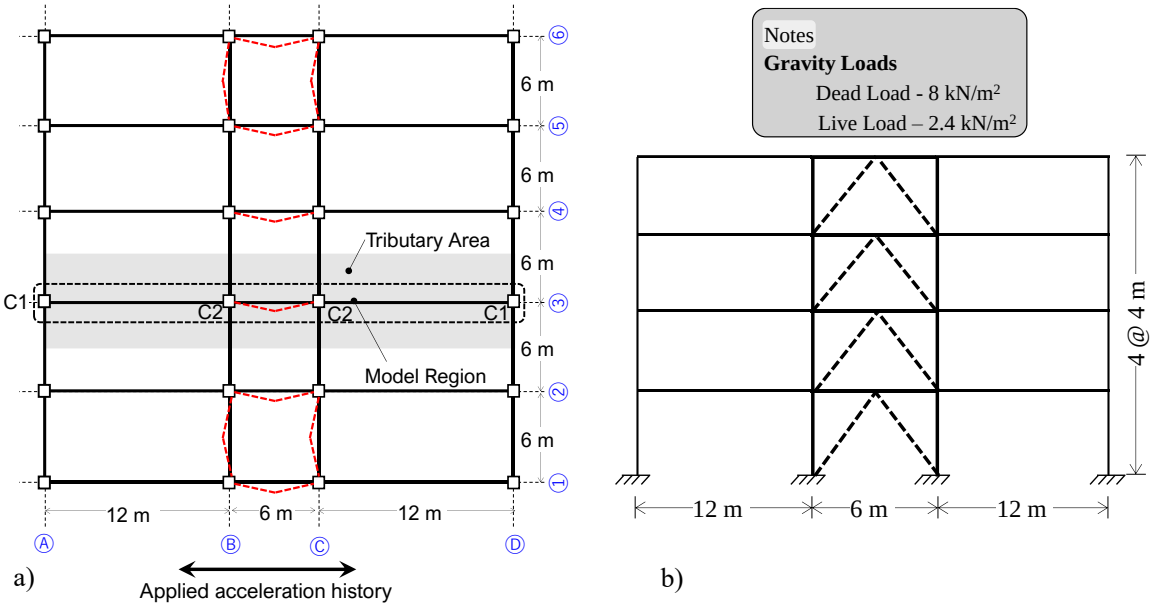

a) Building Plan b) Elevation

Figure 6.2: 4-Story chevron CBF building Configuration.

The braced frames models were proportioned according to three different design procedures illustrated in Figure 6.3. The design procedures are based on the assumed energy dissipation mechanism of the chevron-braced MRF.

i) Type A

Design approach Type A is a fictitious energy-dissipation mechanism, used in the design of chevron-braced MRFs in Japan until 2015. This energy-dissipation mechanism assumes that, at the ultimate stage, both braces will develop their expected buckling strength, N_{cr}. This assumption disregards the unbalance force between the tension and compression brace, thus neglecting the interaction between the pair of braces and the beam during proportioning of the members. For this

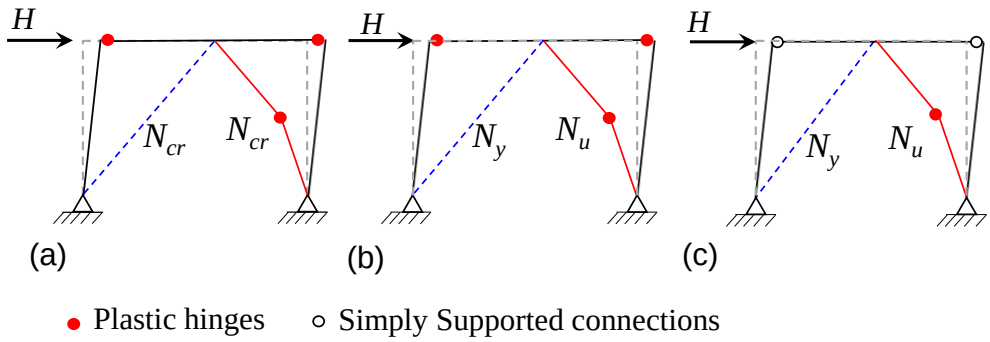

Figure 6.3:Design approaches: (a)Type A; (b)Type B; and (c)Type C.

design approach, it is expected that the beam may yield for large relative strength of the beams with respect to the braces .

ii) Type B

Design approach Type B is a realistic mechanism, that takes into account the interaction between the braces and the beam, as per observation from chapter 3. Here the beams and the braces are proportioned considering the force unbalance between the tension and compression brace.

iii) Type C

Type C refers to concentrically braced frames (CBFs) per definition in the US where lateral-load resistance relies solely on the chevron braces. The beam is simply supported and proportioned to remain elastic under brace tension N_y and brace compression N_u, according to the *US Provisions* [28].

For both design approach Types A and B, three different r_0 values, $r_0 =$ 2.0, 4.0, and 8.0 were considered. Design approach Type B requires the beam to remain elastic for r_0 =2.0. For $r_0 =$ 4.0, 8.0, design approach Type B permits yielding of the beam up to κ = 1.5, and therefore the weak-beam mechanism is expected to control the energy-dissipation mechanism of the chevron-braced frames.

For design approach Type A, the relationship between the proportion of the lateral strength carried by the braces β_0 and r_0 introduced in Chapter 3 in eq. 3.48 and 3.49 cannot be used. The equations were derived for the cases where the interaction between the braces and the beams is considered. Type A assumes that both braces developed their buckling strength, N_{cr}. This mechanism only occurs at the onset of brace buckling (H_1). Hence the relationship between β_0 versus r_0 must be adjusted.

Following the same procedure described in chapter 5, the proportion of the lateral strength carried by the pair of braces can be computed as:

$$\beta_0 = \frac{H_b}{H_b + H_f} = \frac{(N_{cr} + N_{cr})\, cos\alpha}{\frac{2M_p}{h} + (N_{cr} + N_{cr})\, cos\alpha} = \frac{3.33 \cdot x \cdot N_y\, cos\alpha}{\frac{2M_p}{h} + 3.33 \cdot x \cdot N_y\, cos\alpha} \tag{6.4}$$

From equation 5.13, the relative strength of the braces with respect to the beam is $r_0 = {N_y \cdot h \cdot cos\alpha.}/{M_p}$, thus equation 6.4 can be rewritten as:

$$\beta_0 = \begin{cases} \dfrac{3.33 \cdot x \cdot r_0}{1 + 3.33 \cdot x \cdot r_0} & for\ the\ upper\ stories \\ \dfrac{1.11 \cdot x \cdot r_0}{1 + 1.11 \cdot x \cdot r_0} & for\ the\ first\ floor \end{cases} \tag{6.5}$$

Note that, for this case yielding of the beam is not considered in design and hence the strong-beam mechanism is assumed to always control the energy-dissipation mechanism of the braced frame. The β_0 versus r_0 relationship for design approach Type A and β_0 versus r_0 relationship for design approach Type B is shown in Figure *6.4*.

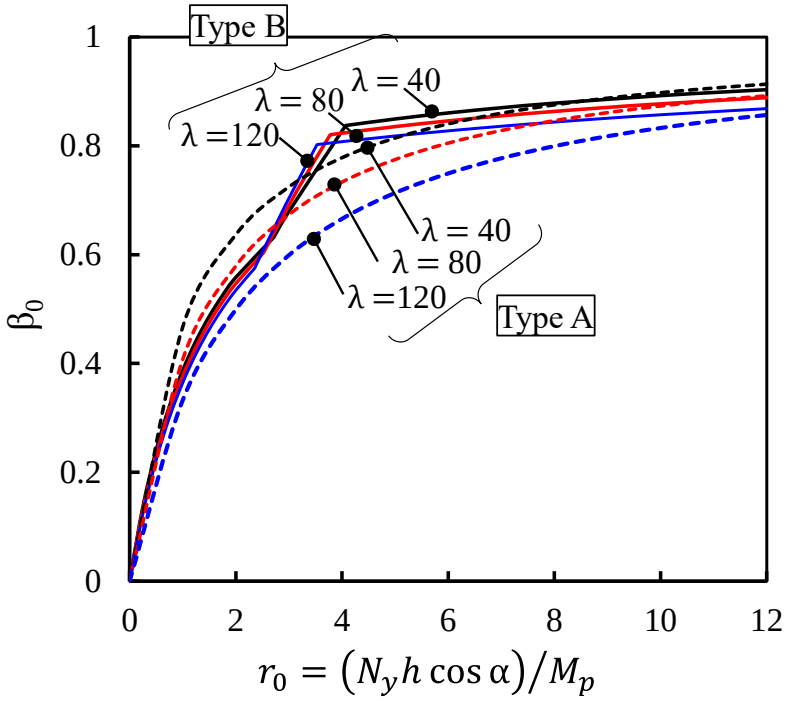

Figure 6.4: Relationship between β_0 and r_1 for design approach Type A and β_0 and r_0 for design approach Type B assuming κ=1.5.

6.3.2 Design Story Shear

The proportion of the story shear carried by the braces is computed according to the predicted brace tensile and compressive strength of the braces and whether or not the beam intersecting braces is allowed to yield under the action of the force unbalance. Three different combinations were used to compute the strength carried by the braces, as a function of the design philosophies and its assumptions:

Type A：It is assumed that both the tension and the compression brace will develop the expected compressive strength of the brace, N_{cr}.

Type B：The compression brace develops the post buckling strength N_u and the tensile brace developed it's the brace tensile strength, computed as *min* (N_y, N_t);

Type C：The compression brace develops the post buckling strength N_u and the tensile brace developed its yield tensile strength N_y.

6.3.3 Design Policies

For the design of the braced frames, the following policies to guide the design were defined:

[1] The column is a square-HSS section and the beam cross -section is wide-flange section. The braces were Round-HSS members (STK400);

[2] The panel zone was not explicitly designed, and as such, it is assumed the larger cross-section of the upper and lower column.

[3] The weight on the beam was computed as 48 kN / m [36]. The weight was distributed half to the center of the beam, and the other half to the supporting column nodes at both ends.

[4] The seismic shear force for design is targeted to Type II ground, the seismic zone factor, Z was set to 1.0 (applicable to large cities like Tokyo). The natural period is computed as 0.03 H where H is the building height.

[5] The material used in the beam and brace are SN 400 steel, with yield stress, F = 235 N / mm^2, and the columns are SN 490, with F=295 N/mm^2.

[6] The structural characteristic coefficient D_s (seismic force reduction coefficient) is stipulated according to the frame classification, brace classification and the proportion of the lateral strength carried by the braces β.

[7] The beams were designed with no consideration of the axial force from the braces. The columns were designed for a bending moment 1.5 times the bending moment distributed by plastic design, to ensure the strong-column weak-beam design principle.

[8] Except at the base of the building, the distribution of the story moment to the top and base of the column is 1: 1. For the first story, the distribution ratio between top and base of the column 1: 1.5 as per [36].

[9] The braced frame structure is assumed as a two-dimensional structure, thus, the shape factor F_s which is used to account for the torsional response of the structure was not considered.

To ensure ductile response of the braced frame systems, the column and beam was set to ductility category FA. Sections available in the Japanese market was always chosen unless the no section was able to provide the required strength, at which point an America section was adopted. For all the members, the cross-section was selected to achieve a least weight cross-section. For the beams, only deep sections with depth/width ≥ 2.0 are chosen. It is assumed that the beams are provided with full lateral support and thus no lateral nor overall buckling were considered.

The braces were predefined category of BB or BC. The structural characteristic coefficient, D_s was determined according to the procedure indicated in the *Japanese provisions* (BCJ).

6.4 Plastic Design of the Chevron-Braced MRFs

Plastic design of structures is a method of determining the cross-sectional dimensions of each member so that the capacity of the structures exceeds the demands that the structure is expected to withstand, and that the equilibrium condition of the frame is satisfied. Plastic design is commonly used for design of steel structures in Japan. This because the Japanese design code requires braced frame structures to: (1) remain within the allowable strength limits and serviceable drift limits under Level 1 design earthquake loads (0.02 rad); and (2) safely sustain (remain within the collapse limit) under Level 2 design earthquake loads, which is accomplished by plastic design. The plastic strength or lateral capacity is the lower bound of the collapse load resulting from an assumed collapse energy-dissipation mechanism developed in each member.

Because the position where the plastic hinge is formed and the total plastic moment of each member are left to the designer, the collapse mechanism can be freely determined. Here, aiming at an economical frame that resists seismic lateral forces by framing structure, the full collapse mechanism was set the target collapse mechanism.

6.4.1 Design Base Shear

The seismic force was computed according to the Japanese design code [35]. The natural period T, for design was computed as $T = 0.03H$ *(commonly used for steel structures)*, where H is the building height. The natural period was 0.48, 0.96, and 1.44 for the 4-, 8- and 12-story structures, respectively. For the 4- story systems, the natural period T_c is smaller than 0.6, hence the vibration characteristic coefficient, R_t is 1.0. For the 8- and 12-story structures, the natural period is larger than 0.6, thus, the vibration characteristic coefficient, R_t is equal to 0.93 and 0.61 for the 8- and 12-story structures, as per Japanese Building Standard. As previously mentioned, the structural characteristic coefficient, D_s, was

Table 6.1: Level II Design Parameters

Z - Seismic Zone factor	1
R_t - Vibration characteristic factor (4-story)	1.0
R_t - Vibration characteristic factor (8-story)	0.93
R_t - Vibration characteristic factor (12-story)	0.67
T_c : Ground characteristic coefficient (double ground)	0.6
T : Building Period – 4-Story Structures	0.48
T : Building Period – 8-Story Structures	0.96
T : Building Period – 12-Story Structures	1.44
C_0 : Standard shear coefficient	1
Initial D_s : Structural characteristic coefficient (Minimum D_S)	0.3
C_r : Base Shear coefficient (Level II)	1.0

computed based on proportion of the lateral strength carried by the braces, β and varied from system to system.

The main design coefficients used in the design of all the structural systems are listed in Table 6.1. The floor weight was computed assuming the general weight of the steel structures (8 kN / m^2). The frame was assumed to be continuous at intervals of 7.5 m in the depth direction. Thus, the tributary weight of each story was computed as:

$$8\ kN/mm^2 \cdot 7.5\ m \cdot 30\ m = 1800 \text{ kN/floor}$$

The A_i distribution can be computed using the following equation:

$$A_i = 1 + \left(\frac{1}{\sqrt{\alpha_i}} - \alpha_i\right)\frac{2T}{1+3T} \quad , \ \alpha_i = \frac{W_i}{W_T} \tag{6.6}$$

where W_i is the weight up to the i-*th* story and W_T is the total weight of the building.

From the above coefficients**,** the story shear force coefficient C_i is computed as follows:

$$C_i = Z \cdot R_t \cdot A_i \cdot C_0 \tag{6.7}$$

The seismic zone factor, Z, the vibration characteristic coefficient R_t, and the standard shear force coefficient C_0 are set to 1.0, therefore, the story shear coefficient depends on the A_i distribution only. The shear force Q_i is obtained as the product of the total weight of the building above that story and the story shear coefficient C_i.

$$Q_i = C_i \cdot \sum W \tag{6.8}$$

The design story shear, Q_{un} is computed as the product between the story shear force Q_i and the structural characteristic coefficient D_s, as follows.

$$Q_{un} = D_s \cdot Q_i \tag{6.9}$$

The D_s values are listed in Table 6.2. For all the braced frame designs, D_s was assumed constant over the height of the frames, although some stories would qualify for smaller D_s.

For design approach A and B, the story shear is distributed to the braces and the MRF according to the β_0 value.

An example of the procedure design discussed above is shown in Table 6.3 to Table 6.4 below for the 4-, 8- and 12-story systems designed using design approach Type A, with $r_0 = 2.0$.

Table 6.2: Structure Characteristics factors, D_s

4-story			
r_0=2.0	r_0=4.0	r_0=8.0	β=1.0
β=0.21~0.28	β=0.35~0.44	β=0.41~0.50	
0.3	0.35	0.35	0.4
8-story			
r_0=2.0	r_0=4.0	r_0=8.0	β=1.0
β=0.22~0.40	β=0.39~0.62	β=0.44~0.72	
0.3	0.4	0.4	0.4
12-story			
r_0=2.0	r_0=4.0	*r_0=8.0*	β=1.0
β=0.20~0.45	β=0.37~0.70	*β=0.39~0.73*	
0.35	0.4	0.4	0.4

6.4.2 Plastic Design of the Structures

This section discusses the plastic design of the 4-, 8-, and 12 story braced frames depicted in Figure 6.2. The distribution of the design story shear to the braces and the MRF, as specified in the design procedure, is shown in Table 6.6 to Table *6.8* for the 4-, 8-, and 12- story systems designed according to design approach Type A, for $r_0 = 2.0$. In the table, ${}_sQ_i^D$ is the required lateral strength derived from the braces, and ${}_sQ_i^F$ is the required lateral strength required from the underlying MRF.

Table 6.3 : 4-story system: Model A with r_0=2.0 (β_0 =0.57 and D_s = 0.3)

Floor	**Height [m]**	**Weight [kN]**	α_i	**A_i distribution**	C_i	Q_i **[kN]**	Q_{un} **[kN]**
4	4	1800	0.25	1.69	1.69	3039	912
3	4	1800	0.50	1.36	1.36	4895	1468
2	4	1800	0.75	1.16	1.16	6260	1878
1	4	1800	1.00	1.00	1.00	7200	2160
Total	16	7200				21394	6418

Table 6.5: 8-story system: Model A with r_0 = 2.0 (β_0 = 0.57 and D_s = 0.35)

Floor	Height [m]	Weight [kN]	α_i	A_i distribution	C_i	Q_i [kN]	Q_{un} [kN]
8	4	1800	0.13	2.34	2.17	3913	1370
7	4	1800	0.25	1.87	1.74	6247	2187
6	4	1800	0.38	1.62	1.51	8148	2852
5	4	1800	0.50	1.45	1.35	9725	3404
4	4	1800	0.63	1.32	1.22	11020	3857
3	4	1800	0.75	1.20	1.12	12055	4219
2	4	1800	0.88	1.10	1.02	12843	4495
1	4	1800	1.00	1.00	0.93	13392	4687
Total	32	14,400	-	-	-	77345	27071

Table 6.4: 12-story system: Model A with $r_0 = 2.0$ (β_0 = 0.57 and D_s = 0.35)

Floor	Height [m]	Weight [kN]	α_i	A_i distribution	C_i	Q_i [kN]	Q_{un} [kN]
12	4	1800	0.08	2.83	1.89	3396	1,189
11	4	1800	0.17	2.24	1.49	5366	1,878
10	4	1800	0.25	1.95	1.30	7011	2,454
9	4	1800	0.33	1.76	1.17	8435	2,952
8	4	1800	0.42	1.61	1.08	9679	3,388
7	4	1800	0.50	1.49	1.00	10763	3,767
6	4	1800	0.58	1.39	0.93	11701	4,095
5	4	1800	0.67	1.30	0.87	12500	4,375
4	4	1800	0.75	1.22	0.81	13166	4,608
3	4	1800	0.83	1.14	0.76	13703	4,796
2	4	1800	0.92	1.07	0.71	14113	4,940
1	4	1800	1.00	1.00	0.67	14400	5,040
Total	48	21,600	-	-	-	-	-

Table 6.6: *Distribution of the story shear to the braces and MRF for design approach Type A with* r_0= 2.0

Story	h [m]	Q_{un} [kN]	${}_sM_i$ [kN·m]	${}_sQ_i^D$ [kN]	${}_sQ_i^F$ [kN]	β_0	β	${}_sM_i^F$ [kN·m]
4	4	912	3647	16	14	0.50	-	3582
3	4	1468	5874	311	276	0.50	0.21	4629
2	4	1878	7512	528	468	0.50	0.28	5399
1	4	2160	8640	-	-	-	-	8640

Table 6.7: *Distribution of the story shear to the braces and MRF for design approach Type A with* r_0=2.0

Story	***h*** **[m]**	***Q**un* **[kN]**	***sMi*** **[kN·m]**	**sQiD [kN]**	**sQiF [kN]**	**β0**	**β**	**sMiF [kN·m]**
8	4	1370	5479	309	309	0.50	0.23	4243
7	4	2187	8746	653	653	0.50	0.3	6136
6	4	2852	11408	985	985	0.50	0.35	7466
5	4	3404	13615	1261	1261	0.50	0.37	8570
4	4	3857	15429	1488	1488	0.50	0.39	9477
3	4	4219	16878	1669	1669	0.50	0.4	10201
2	4	4495	17980	1807	1807	0.50	0.4	10753
1	4	4687	18749	-	-	-	-	18749

Table 6.8: Distribution of the story shear to the braces and MRF for design approach Type A with r_0=2.0

Floor	h[m]	Q_{un} [kN]	${}_sM_i$ [kN·m]	${}_sQ_i^D$ [kN]	${}_sQ_i^F$ [kN]	β_0	β	${}_sM_i^F$
12	4	1189	4755	218	218	0.50	0.184	3881
11	4	1878	7512	498	498	0.50	0.265	5519
10	4	2454	9815	786	786	0.50	0.320	6670
9	4	2952	11808	1035	1035	0.50	0.351	7667
8	4	3388	13550	1253	1253	0.50	0.370	8538
7	4	3767	15069	1443	1443	0.50	0.383	9297
6	4	4095	16382	1607	1607	0.50	0.392	9953
5	4	4375	17500	1747	1747	0.50	0.399	10513
4	4	4608	18433	1863	1863	0.50	0.404	10979
3	4	4796	19184	1957	1957	0.50	0.408	11354
2	4	4940	19759	2029	2029	0.50	0.411	11642
1	4	5040	20160	-	-	0.37	0.253	15053

6.4.2.1 Brace Design

The cross-section dimensions of the braces were determined according to the design approach and the target value of r_0, and hence the target β_0. The capacity of the braces can be computed as follows:

Type A $$Q_{br} \geq (N_{cr} + N_{cr}) \cos\theta \quad (6.10)$$

Type B (SB) and Type C $$Q_{br} \geq (N_y + N_u) \cos\theta \quad (6.11)$$

Type B (WB) $$Q_{br} \geq (N_t + N_u) \cos\theta \quad (6.12)$$

In the above equation, N_t is the maximum tensile strength developed in the braces. Seki et al [16] suggested the following equation to compute N_t:

$$N_t = min\left\{\left(\kappa\frac{4M_p}{l} + N_u sin\theta\right)\frac{1}{sin\theta}, N_y\right\} \quad (6.13)$$

The required brace cross-section (A_{br}) can be computed as:

*D*esign approach type A $$A_{br} \geq \frac{H_b}{2 \cdot cos\alpha \cdot F_{cr}} \quad (6.14)$$

For Strong-beam mechanism: $$A_{br} \geq \frac{H_b}{(F_y+0.3\cdot F_{cr})\cdot cos\alpha} \quad (6.15)$$

For Weak-beam mechanism: $$A_{br} \geq \frac{H_b}{0.6\times F_{cr}\times cos\alpha} - \frac{4\kappa M_p}{0.6\times F_{cr}\times l\times sin\alpha} \quad (6.16)$$

The design of the braces is an interactive process. One must choose a random section and compute the lateral strength provided by the selected cross-section. In the cases where the weak-beam mechanism controls, both the beam and the braces must be designed simultaneously since the beam section affects the braces strength.

6.4.2.2 Distribution of the Story Moments

To design the beams of the MRF, the story moment required to be provided by the MRF must be computed. The story moment provided by the brace is obtained as follows:

$$M_i^{br} = {}_sQ_i^D \cdot h_i \quad (6.17)$$

where ${}_sQ_i^D$ is the story shear derived from the braces of the i^{th} floor and h_i the floor height. The story moment provided by the MRF is computed as:

$$M_i^F = {}_sM_iF - M_i^{br} \quad (6.18)$$

where ${}_sM_iF$ is the total required story moment and $\boldsymbol{M_i^{br}}$ the moment provided by the braces. The procedure to distribute the story moment to the MRF is summarized in Table 6.6 to Table *6.8*.

The story moment is distributed half to the top and base of the column. Figure 6.5 illustrates the distribution procedure of the story moment. In the figure M_i^T and M_i^B are the distributed components of the story moment ${}_sM^i$ of the i^{th} -story to the top and base of the column, respectively.

The floor moment ${}_GM^i$ is therefore, the sum of the column end moments of the i^{th} and i^{th} *+1* story. The equilibrium condition on the i^{th} story and the i^{th} floor is expressed by the following equation.

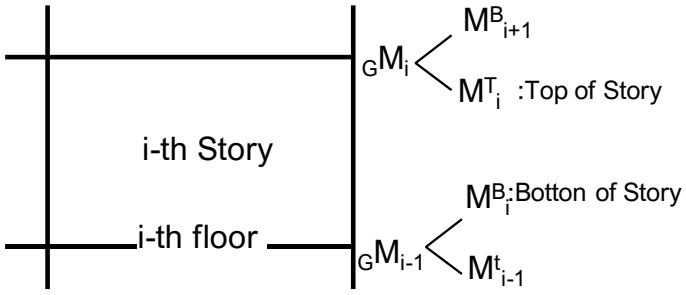

Figure 6.5: Distribution of Story moments

$$ {}_sM_i = M_i^T + M_i^B, \quad {}_GM_i = M_i^T + M_{i+1}^B \tag{6.19} $$

The distribution of the story moment into the top and bottom side of the column was based on the design policy [8]. For the bottom story, the distribution ratio of the story moment is 1: 1.5.

The distribution of the story moment, ${}_sM_iF$ for the 4-, 8- and 12- story models are listed in Table *6.9* to Table *6.11*. The bending moment distribution are depicted in Figure *6.6*.

Table 6.9: Distribution of Story Moments: 4-Story System for design approach Type A with r_0=2.0

Story	${}_sM_i^F$	M_i^T M_i^B	${}_GM_i$	$B_{i,1}$	$B_{i,2}$
4	3582	1791 1791	1791	300	881
3	4629	2314 2314	4106	559	881
2	5399	2699 2699	5014	915	881
1	8640	3456 5184	6155	915	881

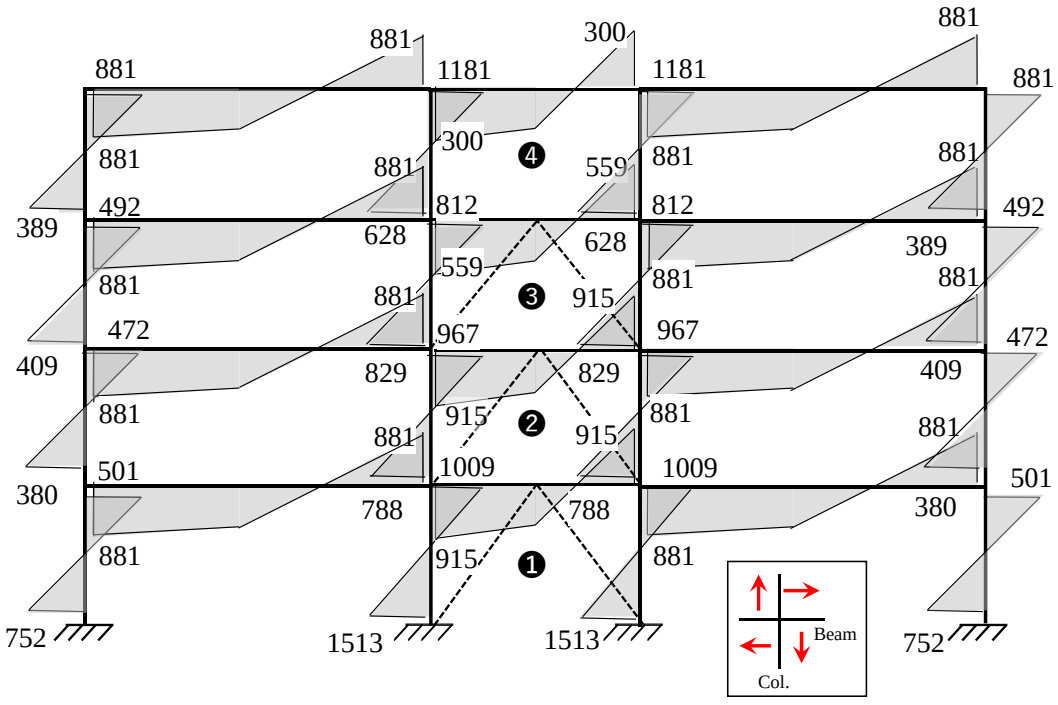

Figure 6.6: Bending Moment Distribution for design approach Type A with r_0 =2.0.

Table 6.10:Distribution of Story Moments: 8-Story System for design approach Type A with r_0=2.0

Floor	${}_sM_i^F$	M_i^T M_i^B	${}_GM_i$	$B_{i,1}$	$B_{i,2}$
8	4243	2035	2035	528	752
		2035	4920		
7	6136	2885		1130	881
		2885	6342		
6	7466	3457		1669	881
		3457	7389		
5	8570	3932		2260	881
		3932	8254		
4	9477	4322		2570	881
		4322	8955		
3	1021	4633		2780	881
		4633	9504		
2	10753	4870		3130	881
		4870	12370		
1	18749	7500		3130	881
		8574			

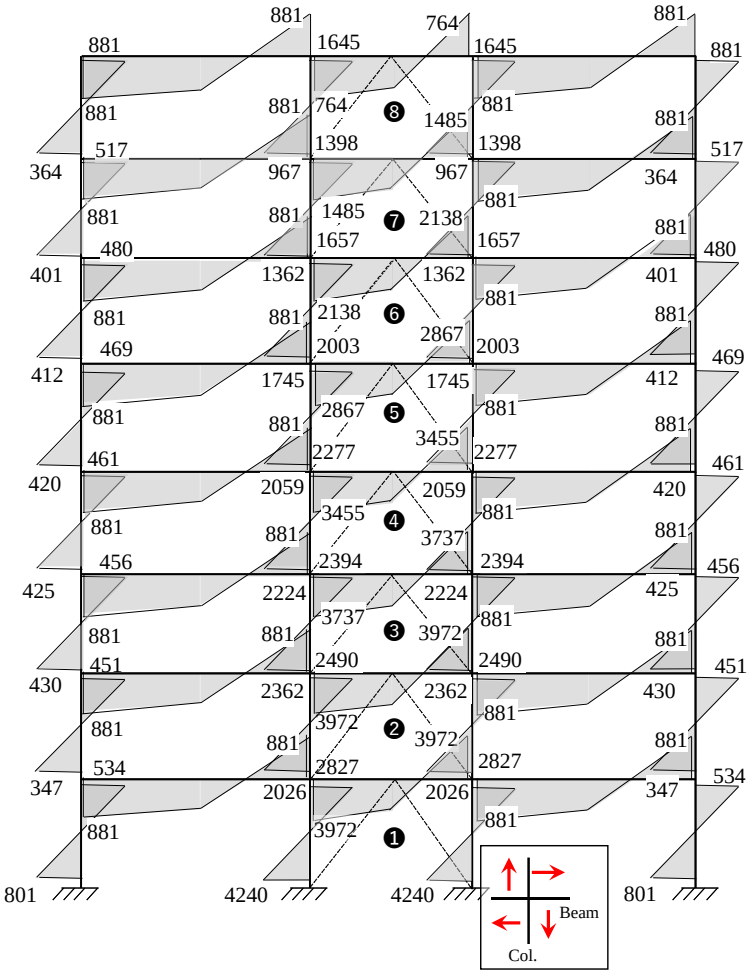

Figure 6.7: Bending moment distribution: 8-Story CBF designed using design approach Type A with r_0 = 2.0

Table 6.11:Distribution of Story Moments for the 12-Story System designed using design approach Type A with r_0=2.0.

Floor	$_sM_i^F$	M_i^T / M_i^B	$_GM_i$	$B_{i,1}$	$B_{i,2}$
12	3881	1941	1941	477	752
		1941	4700		
11	5519	2759		1069	881
		2759	6094		
10	6670	3335		1596	881
		3335	7168		
9	7667	3833		2156	881
		3833	8102		
8	8538	4269		2586	881
		4269	8917		
7	9297	4648		2706	881
		4648	9625		
6	9953	4977		3268	881
		4977	10233		
5	10513	5256		3588	881
		5256	10746		
4	10979	5489		3912	881
		5489	11167		
3	11354	5677		3912	881
		5677	11498		
2	11642	5821		3912	881
		5821	11842		
1	15053	6021		3912	881
		9032			

6.4.2.3 Beam Design

The design of the beam intersected by the braces is discussed next. For Type A the beam was proportioned to resist the end moments plus vertical force due to the gravity loads. For design approach type B the beam was designed to resist the combinations of the end moments, the unbalance load induced by the braces and the gravity loads. For this design approach, two fundamental conditions must be considered, depending on the target collapse energy-dissipation mechanism: (*i*) if the strong-beam mechanism is the target collapse energy-dissipation mechanism, plastic hinges forms at both ends of the beam as shown in Figure 6.9 (a), (*ii*) if the weak-beam mechanism is the target energy-dissipation mechanism, yielding of the beam occurs prior to yielding of the braces, and a plastic hinge forms at the center of the beam as shown in Figure 6.9(b).

For design approach Type C, the beam is pinned at the ends, and hence it is proportioned to support the vertical force at the center due to gravity and th unbalance force as shown in Figure *6.10*.

Therefore, for design approach Type B with $r_0 = 2.0$ and Type C, the following condition must be satisfied:

$$M_p \geq M_c = \frac{1}{4}VL \tag{6.20}$$

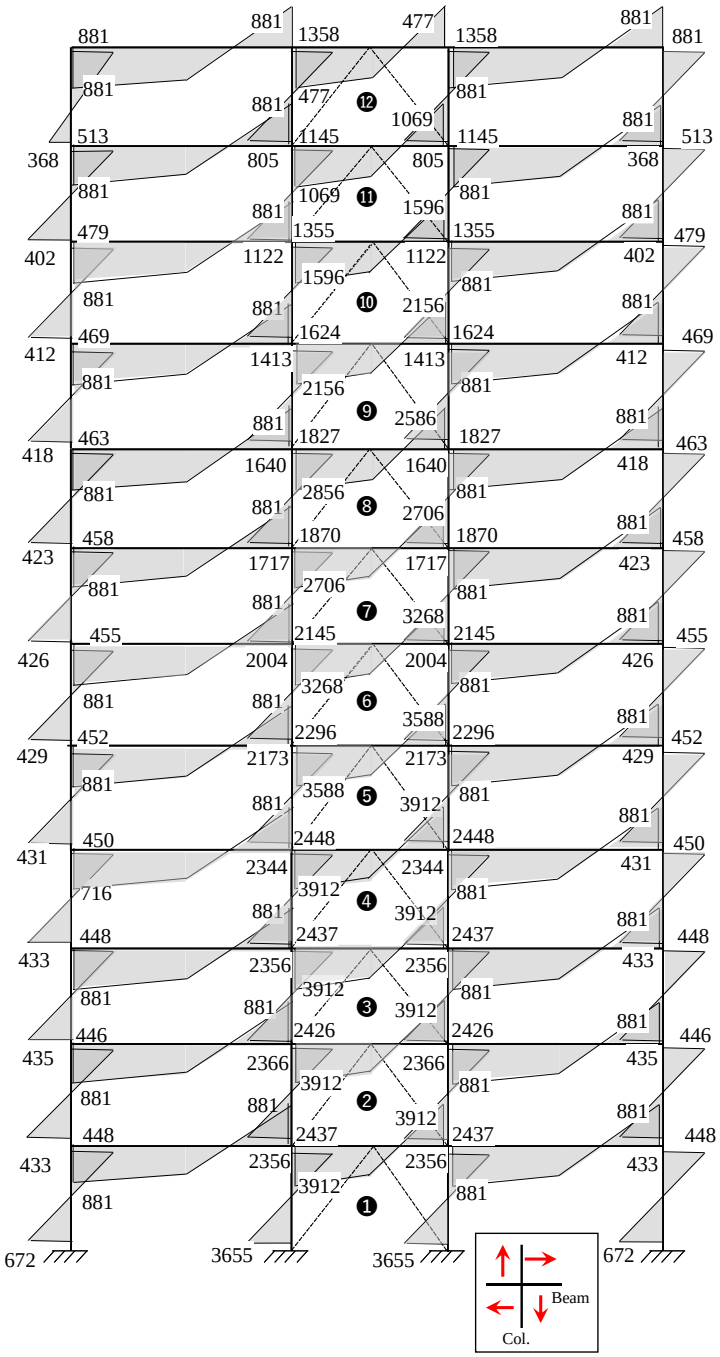

Figure 6.8: Bending moment distribution 12-Story CBF Model A with $r_0 = 2.0$.

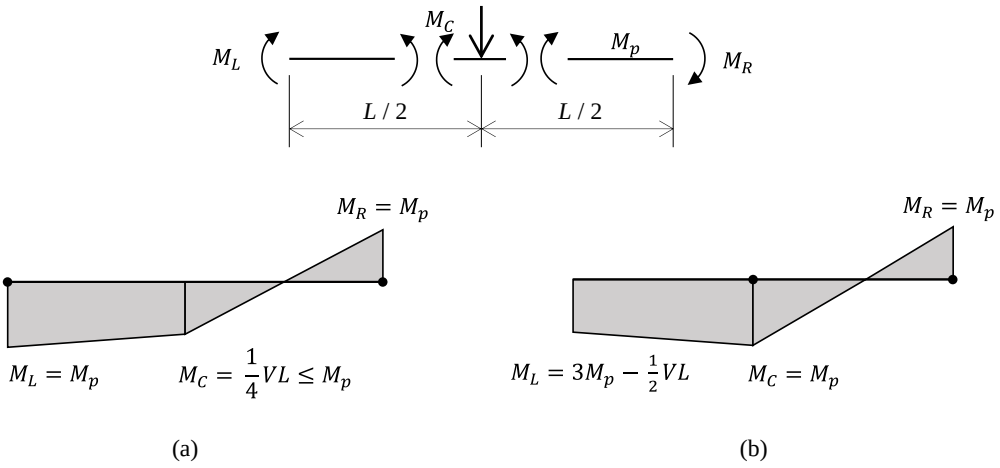

Figure 6.9: Bending moment distribution of the beams in Types B

For design approach Type B with $r_0 = 4.0$ and $r_0 = 8.0$, the above condition does not have to be satisfied since the beam is allowed to yield up to $\kappa = 1.5$.

For design approach Type C, the beam was expected to remain elastic and therefore, the beam should satisfy the condition:

$$\frac{Mp}{Mc} \geq 1.0 \tag{6.21}$$

The procedure to design the cross- section of the chevron braced bent beam is exemplified next. The example is for the 2nd story beam of the 4-story chevron braced frame designed according to design type B with r_0=2.0 and type B with r_0= 8.0. This highlights the two conditions previously mentioned. In Model B_2.0, the chosen brace cross-section was Round-HSS-139.8.2 × 6.0. The expected yielding tensile strength of the brace is N_y = 829.7 *kN*, and a post buckling strength, N_u = 139.9 kN.

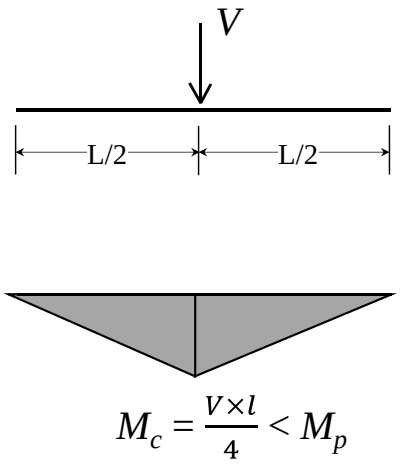

Figure 6.10: Bending moment distribution of beams in type C design approach

In Model B_8.0, the selected brace cross-section is a Round-HSS-267.4 × 8 with the expected yielding tensile strength of $N_y = 2140\ kN$, and post buckling strength, N_u = 599 kN. The beam is expected to yield, and hence the maxim tensile strength $N_t = 1360\ kN$. The unbalanced load delivered on the beam is therefore, 557 kN and 614 kN for Model B_2.0 and Model B_8.0, respectively.

Therefore, the required beam plastic strength is computed as:

For Model B_2.0:

$$M_c = \frac{1}{4}\left\{(N_y - N_u)\ \sin\theta + V\right\} \cdot L$$

$$M_c = \frac{1}{4}\{\ (829.7 - 139.9\ ) \cdot 0.8\ +\ 160\ \text{kN}\} \cdot\ 6$$

$$M_c = 1068\ [\text{kN} \cdot \text{m}]$$

Thus, the beam required plastic strength must be larger than M_c. The selected beam cross section was an H - 500×250×12×25 with a plastic strength, M_p = 1200 k*N*·m. This beam section does fulfill the condition of $M_p \geq M_c$, and provides the required lateral strength required from the MRF.

For Model B_8.0:

$$M_c = \frac{1}{4}\left\{(\min(N_t, N_y) - N_u)\ \sin\theta + V'\right\} \cdot L$$

$$M_c = \frac{1}{4}\{\ (1360\ -\ 599) \cdot 0.8\ +\ 160\} \cdot\ 6$$

$$M_c = 1153.2\ [\text{kN} \cdot \text{m}]$$

However, for design approach Type B, since the beam is allowed to yield, a beam with a smaller plastic strength can be chosen as long as the selected section satisfies the strength requirements. The selected beam cross-section was an H - 450×200×12×22 with a plastic strength, M_p = 615 k*N*·m.

For Type C, the braces adopted at the first floor were HSS 406.4 x 9.0. The brace has an expected yielding tensile strength of $N_y = 3690\ kN$, a post buckling strength, N_u = 1100 kN, and an unbalance force V_b=2070 kN. Hence the beam was required to resist the combined action between the force unbalance and the gravity loading computed as:

$$M_c = \frac{1}{4}\left\{(N_y - N_u)\ \sin\theta + V\right\} \cdot L$$

$$M_c = \frac{1}{4}\{\ (3690\ -\ 1100\ ) \cdot 0.8\ +\ 160\} \cdot\ 66$$

M_c = 3348 [kN · m]

The adopted beam is an H-850 x 350 x 19 x 40 with a plastic strength, Mp= 3650 kN.m. Therefore, the beam can sustain the induced loading and remain elastic.

6.4.2.4 Column Design

The design philosophy used assumed that the columns should survive the design ground motion and thus it must be able to resist the maximum axial loads that will develop in the structure before and after buckling of the braces.

The column axial loads were computed assuming that the braces reach their ultimate compressive capacity simultaneously over the height of the structure, as follows:

1. for design approach Type A:

$$N_{col\ i} = Ncol_{G\ i} + \sum_{x=i+1}^{n} (N_{cr} sin\theta) + \sum_{x=i+1}^{n} (N_{e,G2} - N_{e,G1}) \quad (6.22)$$

2. for design approach Type B:

$$N_{col\ i} = Ncol_{G\ i} + \sum_{x=i+1}^{n} (N_{u} sin\theta) + \sum_{x=i+1}^{n} (N_{e,G2} - N_{e,G1}) \quad (6.23)$$

3. for design approach Type C:

$$N_{col\ i} = Ncol_{G\ i} + \sum_{x=i+1}^{n} (N_{u} sin\theta) + \sum_{x=i+1}^{n} \frac{(N_y - N_u) sin\theta}{2} \quad (6.24)$$

where $N_{col,G,i}$ is the gravity loads induced on the columns, $N_{cr}sin\theta$ and $N_u sin\theta$ is the vertical component of brace compression strength, and $(N_{e,G2} - N_{e,G1})$ is the difference between the shear force induced by the interior chevron-braced MRF and adjacent MRF beams, and N_y is the brace tensile yielding strength.

For design approach Type A and B, the column is subjected to combined bending moment and axial force *N*, and thus the reduced total plastic moment of the column, M_{pnX} is computed using the interaction equation (H1-1) provided in [28]:

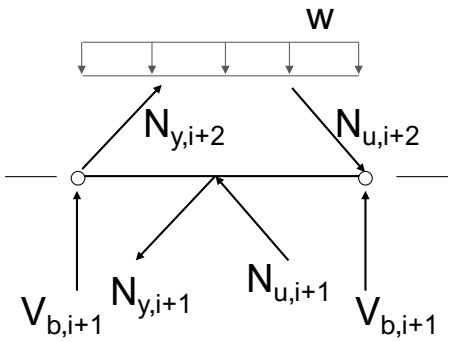

Figure 6.12. Column Axial Force for the 4-story system: Design approach Type C

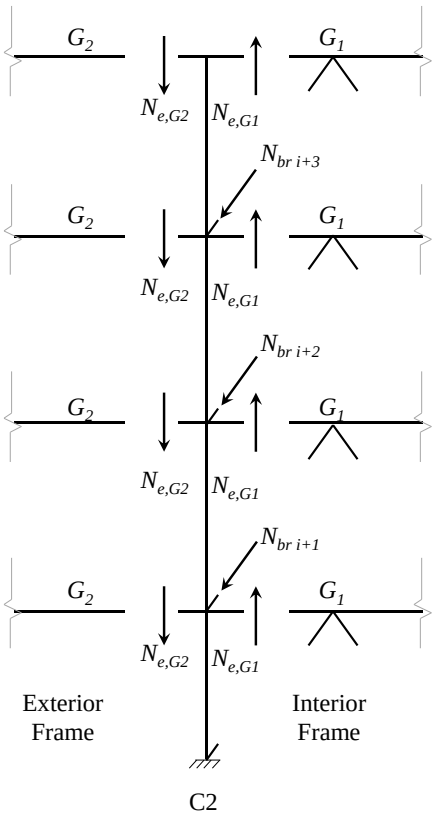

Figure 6.11: Column Axial Force for the 4-story system

$$\frac{P_r}{P_c} + \frac{8}{9}\left(\frac{M_{rx}}{M_{cx}}\right) = 1 \text{ for } \frac{P_r}{P_c} \geq 0.2 \quad (6.25)$$

$$\frac{P_r}{2P_c} + \left(\frac{M_{rx}}{M_{cx}}\right) = 1 \text{ for } \frac{P_r}{P_c} < 0.2 \quad (6.26)$$

where M_{rx} is the required flexural strength, M_{cx} is the available flexural strength, P_r is the column required axial strength, Pc is the available axial strength, and x is the subscript related to the strong axis bending.

For design approach Type C, the beam-to-column connection is pinned and thus no bending moment is considered to be induced on the column. An example of the column design is discussed next for three of the models: A_2.0, B_8.0 and C, for the 4-, 8-, and 12- story systems.

Table 6.12 to Table *6.14* summarizes the axial forces transferred induced on to the columns at each story for the 4-, 8- and 12-story systems under design approach Type A with r_0=2.0. In the table, ${}_bQ$, is the shear force induced on the column by the beam, N_L is the gravity loads, N^D is the vertical component of the brace axial force. N_E is the accumulated earthquake axial force on the column computed as the sum of the shear force delivered by the beam, and the brace axial force.

For design approach type A and B, the columns were designed to resist the bending moment delivered due to moment frame actions. For design approach type C, the columns are subjected to only vertical axial loads.

Table *6.15* and Table 6.18, shows the design of the columns for the 4-, 8- and 12- story systems designed using Type A with r_0=2.0. The table lists the required axial force and the bending moment demands, computed from equilibrium of the bending moments delivered by the beams, as shown in Figure 6.6 to *Figure 6.8*. The columns moments were amplified by 1.5 to ensure the weak-beam- strong- column philosophy. The beam-to-column strength ratio ($\Sigma MpC/\Sigma MpB$) is listed in Table 6.15 to Table 6.18.

Table 6.12: Column Axial Force for the 4- story CBF Model designed with design approach type A with r_0=2.0

	N_L [kN]		${}_bQ$ [kN]		N^D	N_E [kN]		$N_L + N_E$ [kN]	
Floor level	C1	C2	G1	G2	C2	C1	C2	C1	C2
4	468	702	200	147	0	200	53	668	755
3	936	1404	373	147	246	573	279	1509	1683
2	1404	2106	610	147	546	1183	1007	2587	3112
1	1872	2808	610	147	546	1793	2017	3665	4825

Table 6.13: Column Axial Force for the 8- story CBF Model designed with design approach type A with r_0=2.0

Floor	N_L [kN]		${}_bQ$ [kN]		N^D	N_E [kN]		$N_L + N_E$ [kN]	
level	C1	C2	C1	C2	C2	C1	C2	C1	C2
8	468	702	125	255	245	125	129	593	831
7	936	1404	147	495	663	272	771	1208	2175
6	1404	2106	147	713	840	419	1829	1823	3935
5	1872	2808	147	956	1012	566	3441	2438	6249
4	2340	3510	147	1152	1208	713	5449	3053	8959
3	2808	4212	147	1246	1328	860	7696	3668	11908
2	3276	4914	147	1324	1406	1006	10200	4282	15114
1	3744	5616	147	1324	1406	1153	12703	4897	18319

Table 6.14: Column Axial Force 12 - story CBF Model designed with design approach type A with r_0=2.0.

Floor	N_L **[kN]**		${}_bQ$ **[kN]**		N^D	N_E **[kN]**		$N_L + N_E$ **[kN]**	
Level	C1	C2	C1	C2	C2	C1	C2	C1	C2
12	468	702	125	159	172	125	34	593	736
11	936	1404	147	356	324	272	414	1208	1818
10	1404	2106	147	532	570	419	1124	1823	3230
9	1872	2808	147	719	660	566	2265	2438	5073
8	2340	3510	147	862	933	713	3641	3053	7151
7	2808	4212	147	902	1061	860	5329	3668	9541
6	3276	4914	147	1089	1061	1006	7332	4282	12246
5	3744	5616	147	1196	1187	1153	9442	4897	15058
4	4212	6318	147	1304	1225	1300	11786	5512	18104
3	4680	7020	147	1304	1326	1447	14169	6127	21189
2	5148	7722	147	1304	1486	1594	16652	6742	24374
1	5616	8424	147	1304	1486	1741	19295	7357	27719

Table 6.15: Column design – Model A with r_0=2.0

Floor	N	$_{req}M_{pn}X$	C2	N/N_y	$M_{pn}X$	ΣMpC/ΣMpB
4	755	1181	□ - 400×400×25	0.07	1505	1.3
3	1683	1244	□ - 400×400×25	0.15	1439	2.0
2	3113	1451	□ - 450×450×25	0.25	1692	1.7
1	4825	1513	□ - 450×450×25	0.38	1284	1.7

Table 6.16: Column design – Model A with r_0=2.0

Floor	N	$_{req}M_{pn}X$	C2	N/N_y	$M_{pn}X$	ΣMpC/ΣMpB
8	831	1645	□ - 500×500×25	0.06	2424	1.60
7	2175	2098	□ - 500×500×25	0.15	2311	2.00
6	3935	2618	□ - 550×550×36	0.18	3836	2.04
5	6249	3089	□ - 550×550×36	0.29	3385	1.93
4	8959	3415	□ - 650×650×36	0.34	4441	1.80
3	11908	3591	□ - 650×650×36	0.46	3676	1.76
2	15114	3736	□ - 700×700×40	0.45	5517	1.89
1	18319	4240	□ - 700×700×40	0.55	4556	2.08

Table 6.17: Column design – Model A with r_0=2.0

Floor	N	$^{req}M_{pn}X$	C2	N/N_y	$M_{pn}X$	ΣMpC/ΣMpB
12	736	1358	□-450×450×25	0.06	1942	1.6
11	1818	1717	□-450×450×25	0.15	1855	1.9
10	3230	2119	□-500×500×25	0.18	2822	1.9
9	5073	2461	□-500×500×25	0.29	2491	1.7
8	7151	2740	□-600×600×36	0.30	4005	1.9
7	9541	3006	□-600×600×36	0.40	3435	2.1
6	12246	3260	□-650×650×40	0.43	4264	1.9
5	15058	3517	□-650×650×40	0.52	3539	1.7
4	18104	3672	□-750×750×40	0.54	4620	1.7
3	21189	3655	□-750×750×40	0.63	3695	1.7
2	24374	3639	□-850×850×40	0.64	4739	1.8
1	27719	3655	□-850×850×40	0.73	3595	1.7

Table 6.18: Column design – Model A with r_0=2.0

Floor	N	$_{req}M_{pn}X$	C2	N/N_y	$M_{pn}X$	ΣMpC/ΣMpB
12	736	1358	□-450×450×25	0.06	1942	1.6
11	1818	1717	□-450×450×25	0.15	1855	1.9
10	3230	2119	□-500×500×25	0.18	2822	1.9
9	5073	2461	□-500×500×25	0.29	2491	1.7
8	7151	2740	□-600×600×36	0.30	4005	1.9
7	9541	3006	□-600×600×36	0.40	3435	2.1
6	12246	3260	□-650×650×40	0.43	4264	1.9
5	15058	3517	□-650×650×40	0.52	3539	1.7
4	18104	3672	□-750×750×40	0.54	4620	1.7
3	21189	3655	□-750×750×40	0.63	3695	1.7
2	24374	3639	□-850×850×40	0.64	4739	1.8
1	27719	3655	□-850×850×40	0.73	3595	1.7

The column design for design approach B is identical to design approach A, and is therefore not shown here. The column design for design approach Type B is identical to design approach Type A, hence not shown here. The member cross-sections dimensions are listed in Appendix B.

The design of the columns for design approach Type C is discussed next, and summarized in Table 6.19 to Table 6.21. Here the columns are subjected to only axial force and hence the design of the columns was different. For design approach Type C, the N/N_y *and* N/N_{cr} was constrained to a maximum of 0.69 and 0.70, respectively.

Table 6.19: Column design for the 4-story using design approach Type C

Floor	N	$_{req}M_{pn}X$	C2	N/N_y	N/N_{cr}
4	1217	0	□ 350×350×19	0.16	0.15
3	2983	0	□ 350×350×19	0.41	0.39
2	5215	0	□ 450×450×25	0.49	0.47
1	7730	0	□ 450×450×25	0.63	0.61

Table 6.20: Column design for the 8-story using design approach Type C

Floor	N	M_{pnX}^{req}	C2	N/N_y	N/Ncr
8	1320	0	□ 350×350×19	0.14	0.15
7	3404	0	□ 350×350×19	0.37	0.39
6	6073	0	□ 500×500×22	0.39	0.40
5	9245	0	□ 500×500×22	0.60	0.62
4	12821	0	□ 500×500×36	0.52	0.54
3	16744	0	□ 500×500×36	0.68	0.70
2	21008	0	□ 700×700×40	0.54	0.55
1	25427	0	□ 700×700×40	0.68	0.69

Table 6.21: Column design for the 12-story using design approach Type C

Floor	N	$_{req}\ M_{pnX}$	C2	N/N_y	N/Ncr
12	1245	0	□ 350×350×19	0.13	0.14
11	3163	0	□ 350×350×19	0.34	0.36
10	5582	0	□ 400×400×25	0.40	0.43
9	8541	0	□ 400×400×25	0.62	0.65
8	11864	0	□ 500×500×36	0.48	0.50
7	15352	0	□ 500×500×36	0.62	0.64
6	19074	0	□ 600×600×40	0.58	0.59
5	23019	0	□ 600×600×40	0.70	0.71
4	27258	0	□ 800×800×40	0.61	0.62
3	31677	0	□ 800×800×40	0.71	0.72
2	36096	0	□ 850×850×50	0.61	0.62
1	40555	0	□ 850×850×50	0.69	0.70

For each braced frame model, the lateral plastic capacity of each story was computed and compared to the design base shear. The lateral resistance of the braced frames was computed for all the braced frame models based on the target collapse mechanism. Table 6.22 and Table 6.23 illustrates the computation of the lateral strength of the braced frame designed using Type A with r_0=2.0 and Type C.

As observed, the plastic strength of the braced frames exceeded the design base shear at all the story levels. For both design approaches type A and B, the plastic strength of the bottom story was significantly larger than the design base shear. This is because the design procedure tended to design the bottom story with significant overstrength compared to the upper stories.

The detailed calculation of the plastic lateral strength of the braced frames is provided in Appendix C.

Table 6.22: Plastic capacity of Model 4A_2.0

Floors	$H_{Ext.MRF}$	H_{CBF}			Q_i	Q_i/Q_{un}
		$H_{Int.MRF}$	H_{braces}	H_{CBF}		
4	881	150	0	150	1031	1.1
3	881	279	317	597	1478	1.0
2	881	458	656	1114	1995	1.1
1	1486	1150	656	1806	3292	1.5

Table 6.23: Plastic capacity of Model 4C

Floors	$H_{Ext.MRF}$	H_{CBF}			Q_i	Q_i/Q_{un}
		$H_{Int.MRF}$	H_{braces}	H_{CBF}		
4	0	0	1240	1240	1240	1.0
3	0	0	1892	1892	1892	1.0
2	0	0	2521	2521	2521	1.0
1	0	0	2908	2908	2908	1.0

6.4.3 Comparison between the Design Approaches

The selected cross-section for design approach A and B with $r_0 = 2.0$ and 8.0, and C are shown Appendix B, for the 4-, 8- and 12-story systems. The steel tonnage required for the different design approaches is also provided in Table 6.24 and compared in Figure 6.13.

For the 4-story systems, there was little difference between the required brace and beam size for $r_0 = 2.0$ for the braced frame systems designed using design approach Type A and B. There is minimal difference in the required steel weight for all the members. For $r_0 = 4.0$, and 8.0, Type B

required bigger braces and beams. This is because the lateral strength derived from $(N_{cr} + N_{cr})\cos\alpha$ is larger than $(N_y + N_u)\cos\alpha$, and hence larger brace cross sections is required to provide the required minimum lateral strength from the braces; Type B also required larger beams. This because yielding of the beams was permitted for $k = 1.5$. In general, the braces frames designed using design approach Type B required between 17% to 19 % larger steel tonnage compared to Type A.

Type C required both bigger braces, beams, and columns. There is a significant increase in steel tonnage compared to the braced frames designed using Type A or B. Compared to the braced frame designed using design approach Type B with $r_0 = 8.0$, which used larger braces, there is an increase of 130% in the steel weight.

The brace slenderness ratio, assuming an effective length factor of 1, ranged from 36 to 45 for the 4-story systems, 24 to 41 for the 8-story systems and 24 to 43 for the 12-story systems.

In terms of column demands, larger column axial force demand was induced on the columns in order of Type C, A and B due to larger axial forces induced on the column by the braces. In general, for Type A and B, larger r_0 values lead to larger column axial force demands.

For the taller frames, Type B with $r_0 = 2.0$ required bigger braces than Type A. There is an increase of 29% on the steel tonnage for the braces. However, for the beams and columns, the difference is negligible. For $r_0 = 4.0$, and 8.0, Type B required bigger braces and beams. The total steel tonnage used by the braces frames in Type B is 19% and 20% larger compared with Type A, for the 8- and 12-story systems respectively. As observed for the 4-stories, Type C required significantly larger steel tonnage for the taller building cases. There is an increase of 85% and 96% of the total steel tonnage compared to Type B with $r_0 = 4.0$, for the 8- and 12-story systems, respectively.

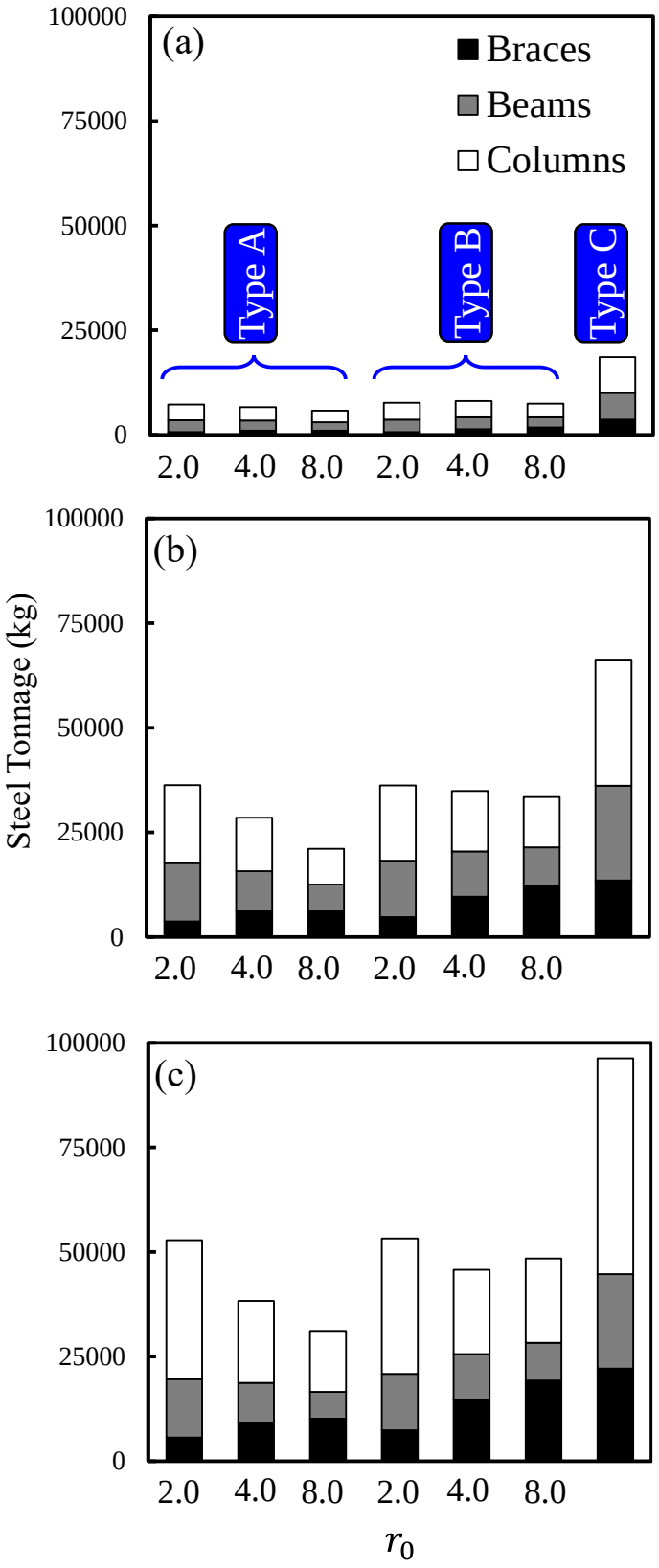

Figure 6.13: Steel Tonnage: (a) 4- Story; (b) 8- Story; and (c) 12- Story.

Table 6.24: Resume of the Steel Tonnage of the braced frame bay [Unit in kg]

Number of Stories	Member	Design approach type A			Design approach type B			Type C
		Model A_r_0=2.0	Model A_r_0=4.0	Model A_r_0=8.0	Model B_r_0=2.0	Model B_r_0=4.0	Model B_r_0=8.0	-
4	Braces	635	1,011	1,016	663	1,341	1,804	3,648
	Beams	2,850	2,417	2,042	3,021	2,895	2,438	6,391
	Columns	3,800	3,223	2,722	4,028	3,860	3,251	8,521
	Total	7,285	6,652	5,780	7,712	8,095	7,493	18,560
8	Braces	3,669	6,099	6,130	4,737	9,611	12,320	13,494
	Beams	13,976	9,590	6,395	13,484	10,827	9,057	22,605
	Columns	18,635	12,787	8,526	17,978	14,436	12,076	30,141
	Total	36,279	28,476	21,051	36,199	34,874	33,452	66,240
12	Braces	5,630	9,093	10,142	7,358	14,723	19,235	22,095
	Beams	13,976	9,590	6,395	13,484	10,827	9,057	22,605
	Columns	33,185	19,595	14,586	32,393	20,178	20,143	51,610
	Total	52,790	38,279	31,123	53,235	45,728	48,435	96,311

7. SEISMIC PERFORMANCE OF LOW– AND MID-RISE CHEVRON-BRACED MRF

7.1 Numerical Model Validation

The numerical analysis results are discussed below. Initially, the behavior of a single brace was modelled. In the sequence, the model of a single-story single bay chevron braced MRF was modelled and described below. The numerical model of the single-story chevron-braced MRF was extended to model the performance of the low- and mid-rise structural systems.

7.1.1 Numerical Modelling of Isolated Braces

The braces were modelled using two force-based beam column elements as shown in Figure 7.1. The brace cross section was discretized into 12 elements in the circumferential direction and 4 elements along the thickness as per Karamanchi et al. [23]. Five Gauss-Lobatto integration points were used. An initial imperfection of 0.1% of the brace length was applied at the center of the brace to account for imperfection and out-of-straightness, as suggested by Uriz et al. [17].

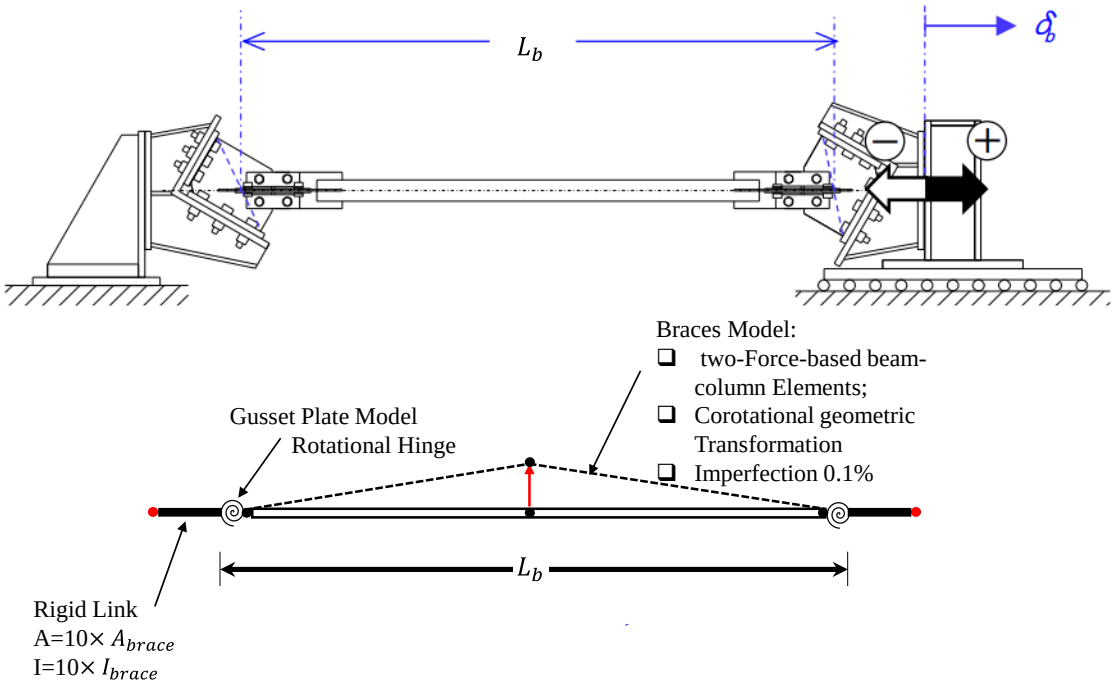

Figure 7.1: *OpenSees* Model for isolated braces including gusset plates.

Each fiber was assigned a uniaxial stress-strain relationship according to the Menegotto-Pinto rule with parameters calibrated based on cyclic-loading material tests by Yamada et al [31]. The OpenSees Menegotto-Pinto (Steel 02) material was used to account for the material response. The monotonic response of the Menegotto-pinto material model is defined by specifying the following parameters: (*i*) its yield stress, F_y; (*ii*) the Young's modulus E; (*iii*) the strain-hardening ratio, *b* and ; (i*v*) and three empirical parameters that controls the transition from the elastic to the plastic branch, R_0, ${}_cR_1$ and ${}_cR_2$. An additional four parameters are required to account for cyclic hardening of the steel material, a1, a2, a3, a4 (Filippou et al.[37]). The Steel 02 material parameters provided by Karamanchi and Lignos [23] for tubular braces listed in Table 7.1 were used. Figure 7.2 shows a comparison between the material models in terms of stress versus strain relationship for an SS400 steel tested by Yamada et al. [31].

The performance of fourteen round HSS brace specimens selected partially from experiments on isolated brace tests by Seki et al. [16], and from a database of brace tests by Zang et al. [38] of experiments on isolated braces [38]–[43], summarized in Table 7.2, with varying boundary conditions, slenderness ratio, and width-to-thickness ratio, were simulated using the model depicted in Figure 7.1 or a variation of that for the braces with fixed bracing connection. The brace slenderness and width-to-thickness ratio ranged between 19 to 107, and 11.8 to 40, respectively. The braces employed both rigid

Table 7.1: Steel 02 Material Model Parameters

Menegotto Pinto Material Model (Karamanchi et al. **[23]**)	HSS Braces
b	0.001
R0	22
CR1	0.925
cR2	0.25
a1	0
a2	1
a3	0.02
a4	2

and flexible bracing connections. The loading protocols used in the numerical analysis of the braces matched the experimental loading protocol.

The comparison between the simulated and experimental response of the isolated braces is shown in Figure 7.3. The accuracy of the numerical two-dimensional OpenSees models varied

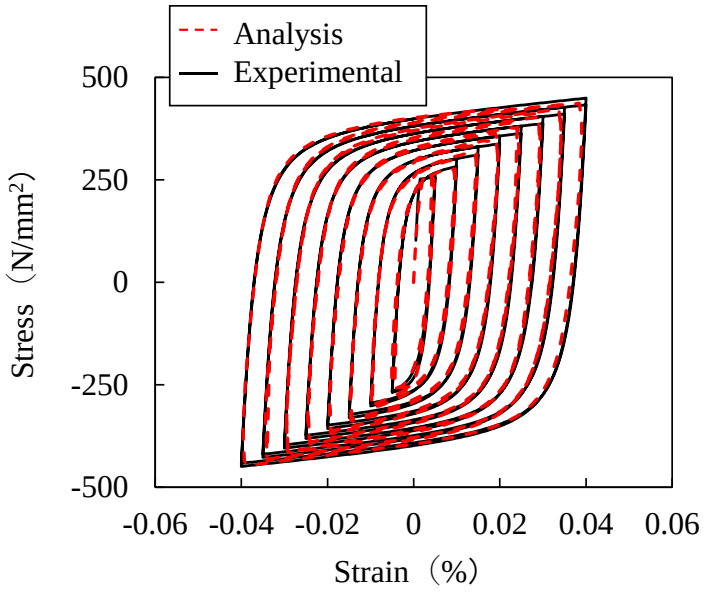

Figure 7.2: Stress Strain Relationship for SN 400 Steel tested by Yamada et al. [31]

depending on the brace bracing connections (boundary conditions), slenderness ratio (l/r) and diameter-to-thickness ratio (D/t). The two-dimensional OpenSees model accurately captured the hysteretic response of the isolated braces, from buckling, yielding and degradation of the compressive strength, for braces with intermediate to large slenderness ratios, but tended to have poor match for braces with small slenderness ratio, particularly, the compressive response in which the two-dimensional OpenSees

Table 7.2: Isolated brace models properties

Model	Source	L (mm)	D (mm)	t (mm)	D/t	k	*kl/r*
M**1**	Seki et. al. [16]	2410	76.3	4.2	18.2	1	107.5
M**2**	Seki et. al. [16]	2410	76.3	4.2	18.2	0.5	107.5
M**3**	Seki et. al. [16]	2180	76.3	4.2	18.2	1.0	107.5
M**4**	Raheem et. al. [44]	1166	139.8	3.6	38.8	0.5	23.0
M**5**	Raheem et. al. [44]	1166	139.8	4.5	31.1	0.5	25.0
M**6**	Raheem et. al. [44]	964	139.8	3.6	38.8	1.0	19.0
M**7**	Brace database [38]	1622	89.1	4.2	21.2	1.0	50.0
M**8**	Brace database [38]	1784	100.8	2.1	48	0.5	25.6
M**9**	Brace database [38]	1930	139.8	3.5	39.9	1	40.0
M**10**	Brace database [38]	520	76.2	3.22	23.7	1	20.0
M**11**	Brace database [38]	1198	60.6	2.32	26.1	0.5	29.0
M**12**	Brace database [38]	1950	165.2	6.72	24.6	1	34.8
M**13**	Brace database [38]	1040	76.2	3.22	23.7	1	40.3
M14	Brace database [38]	2190	101.6	8.6	11.8	0.7	46.4

model was significantly stronger than the tests.

This was expected because, the fiber-based beam-column element, employed in OpenSees, cannot capture the effects of local buckling. Therefore, it is expected that the numerical model would be less effective for stocky braces. Experiments conducted and reported by Raheem et al. [44], showed that the performance of stocky braces is controlled by local buckling of the braces instead of global buckling as is normally the case for intermediate to large slenderness braces. In fact, prior to the occurrence of local buckling, the compressive resistance of the braces resembled the tensile response. Degradation of the brace compressive strength occurs only after the occurrence of local buckling, which were observed to occur after the 2% elongation of the braces.

Model 1 [λ=107.5; D/t=18.2]

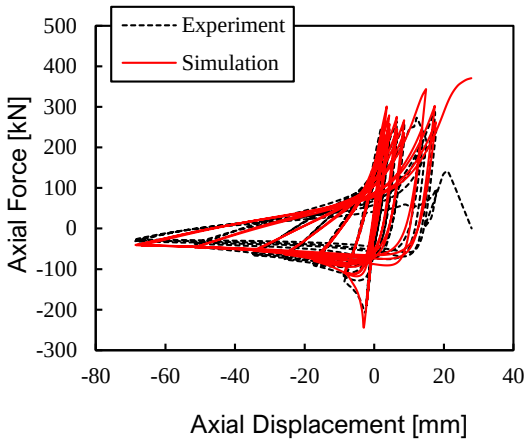

Model 2 [λ=107.5; D/t=18.2]

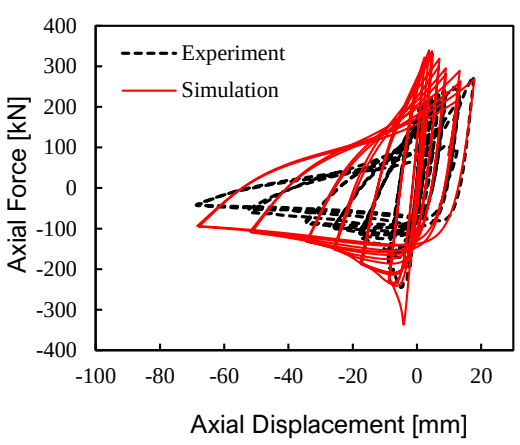

Model 4 [λ=23; D/t=38.8]

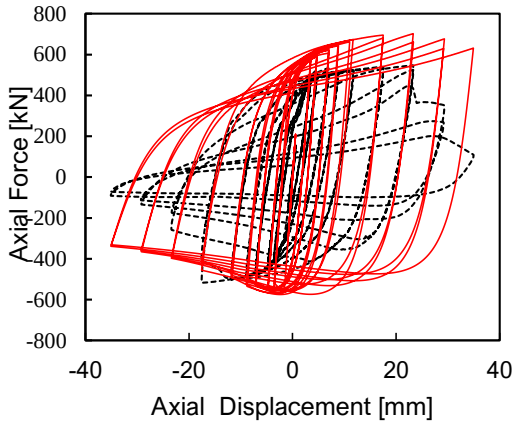

Model 5 [λ=25; D/t=31.1]

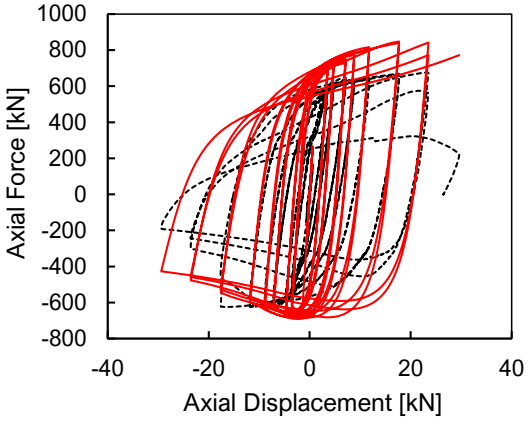

Model 6 [λ=19; D/t=38.8]

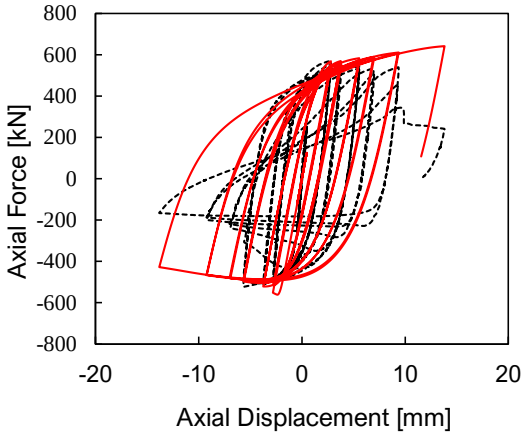

Model 7 [λ= 50; D/t=21.2]

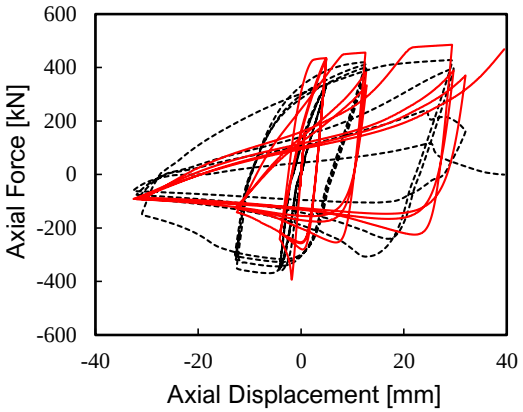

Model 8 [λ=25.6; D/t=48]

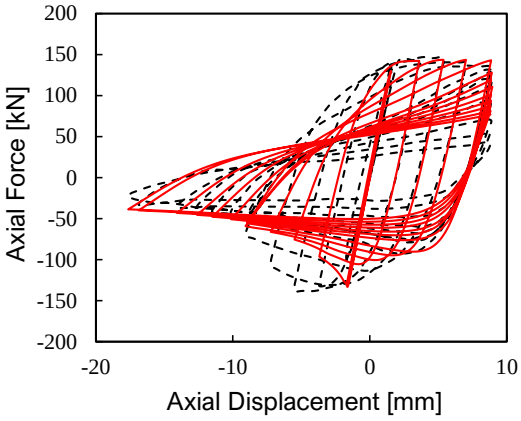

Model 9 [λ=40; D/t=39.9]

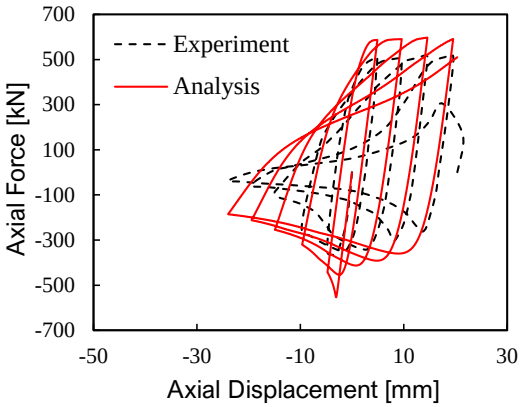

Model 11 [λ=29; D/t=36.1]

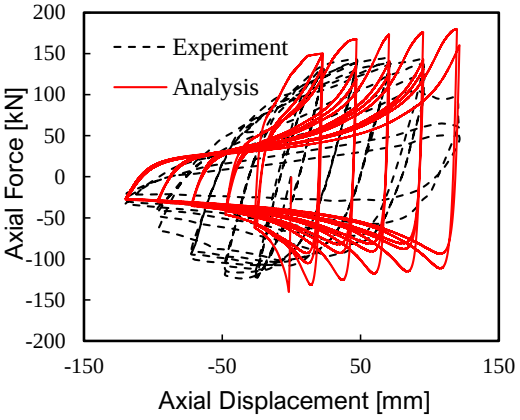

Model 12 [λ=34.8; D/t=24.6]

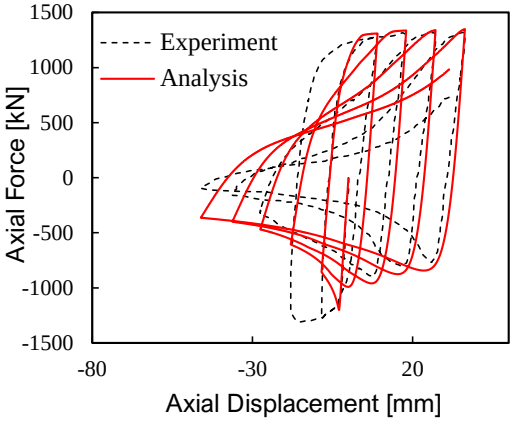

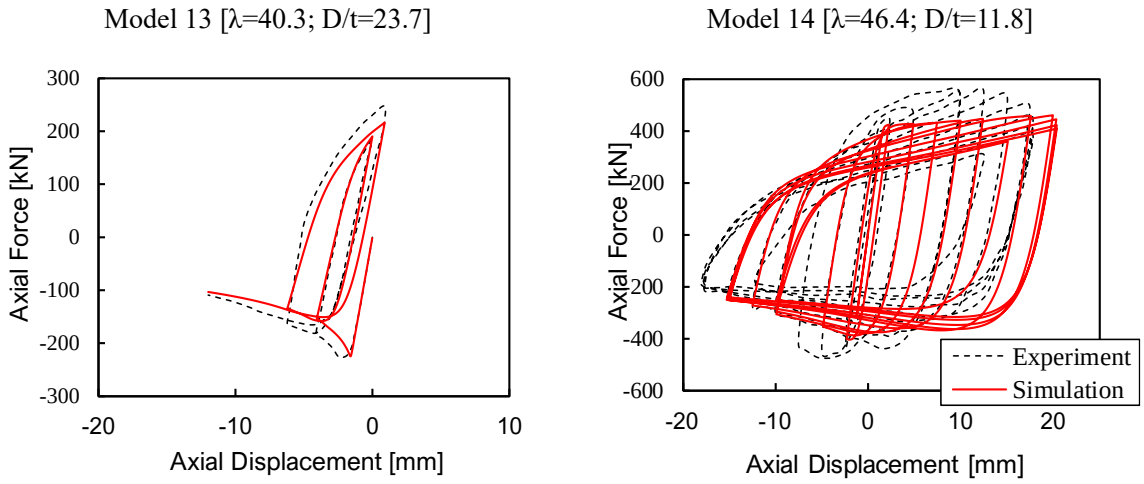

Figure 7.3: Hysteretic Response of the braces: Simulation versus Experimental Response;

As observed for braces 5 and 6, there was a very small reduction in the compressive strength of the braces compared to the experimental response. It is believed that the accuracy of the numerical simulation can be improved if local buckling and fracture of the braces is incorporated in the simulation.

7.1.2 Modelling of Single-Story Single-Bay Chevron Braced MRF

The performance of three single-story single-bay chevron-braced MRFs tested by Seki et al [16] which corresponds to the specimens 1, 2, and 3 was simulated in OpenSees. The model is shown in Figure *7.4*. The cyclic-1 loading protocol introduced in chapter 3 was applied at the top of the north column in displacement control.

Force-based beam-column elements were adopted for all the columns, beams, and braces. The beams were modelled with a single element with five integration points arranged according to the Gauss-Lobatto quadrature rule. Each flange or web element was divided into eight fibers, four in the width direction and two in the thickness direction. The columns were discretized into 4 elements. Corotational transformation was used in the beams and braces whereas, P-delta transformation were used for the columns.

Figure 7.6 shows the numerical model of the bracing connections for the three specimens. In model 1 and 2, the rigid bracing connection was modelled by force-beam column elements. In model 3, the gusset plates was modelled using the procedure described in Hsiao et al. [19]. Hsiao et al. [19] derived a procedure to simulate the performance of gusset plates. The method accounts for the nonlinear out-of-plane rotational response of the gusset plate connections. The bracing connection was model using a rotational spring at the end of the brace connected to a rigid links (Figure 7.5).

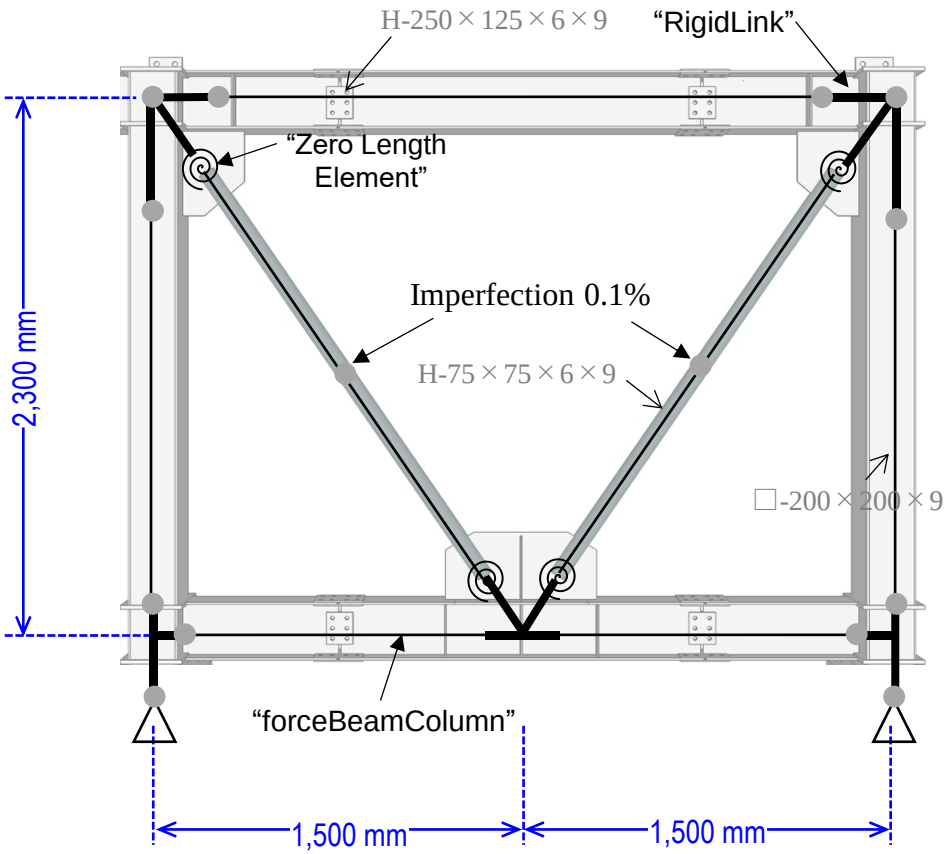

Figure 7.4:Numerical Modelling of the single-story single bay chevron braced MRF

Zero-length nonlinear rotational spring element using steel02 material model was used. Hsiao et al [19] provided a good estimate for the nonlinear rotational stiffness of the gusset plate, shown in eq (7.1) and (7.2).

$$K_{cal}^{Rot} = \frac{E}{L_{ave}}\left(\frac{W_w t^3}{12}\right) \tag{7.1}$$

The yield moment of the gusset plate was computed using the following equation:

$$M_y = \left(\frac{W_w t^2}{6}\right) F_{y,gusset} \tag{7.2}$$

The chevron and corner gusset plate K_{cal}^{Rot} and M_y are listed in Table 7.3 and Table 7.4.

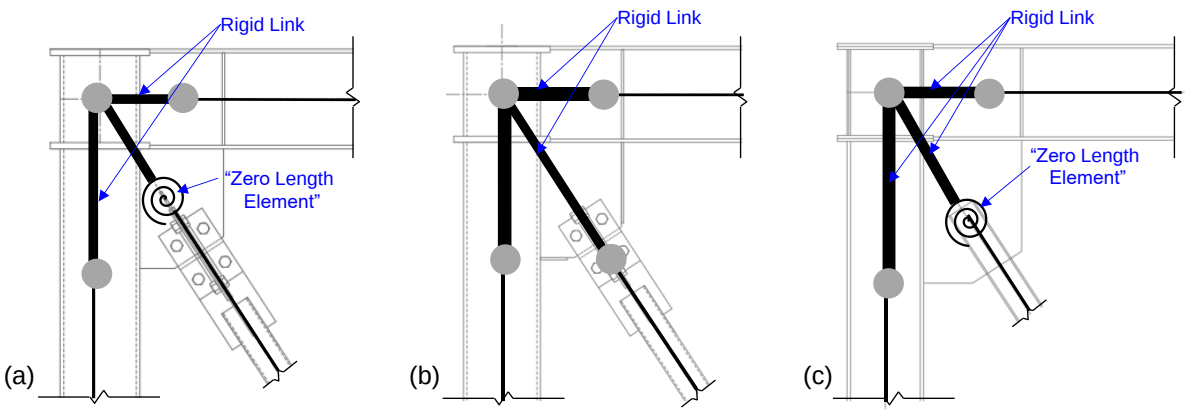

Figure 7.6: Modelling of Bracing Connection: (a) Specimen 1 (b) Specimen 2, and (c) Specimen 3.

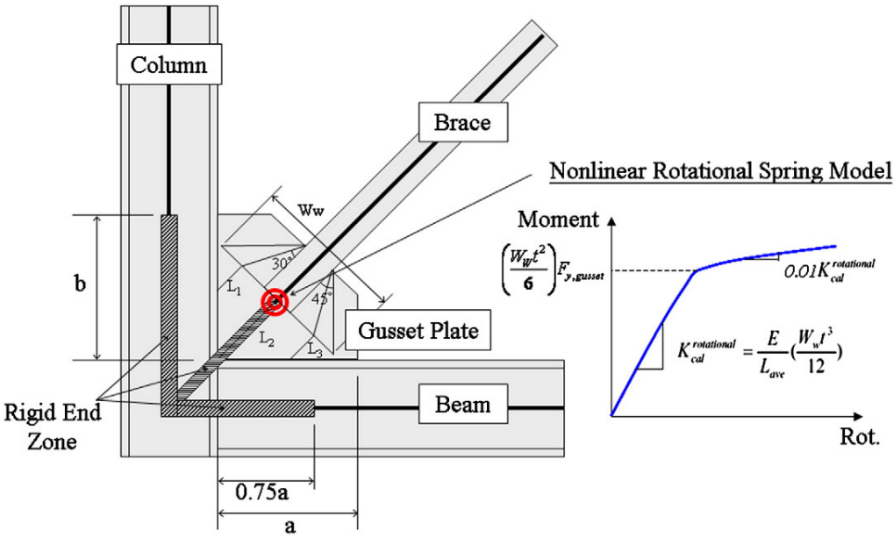

Figure 7.5: Connection Models approach proposed by Hsiao et al. [19].

Table 7.3: Zero length Elements modelling for corner Gusset Plates

	Corner GP						
	L_1	L_2	L_3	L_{avg}	W_W	K_{rot}	M [Nmm]
Specimen 1	59	95	0	51	251	18,042,662	617,460
Specimen 2	59	95	0	51	251	18,042,662	617,460
Specimen 3	119	179	0	99	255	9,468,838	504,900

Table 7.4: Zero Length Elements for Chevron Gusset Plates

	Chevron GP						
	L_1	L_2	L_3	L_{avg}	W_W	K_{rot}	M [Nmm]
Specimen 1	0	62	41	34.33	228	24,504,466	560,880
Specimen 3	0	62	41	34.33	228	24,504,466	560,880
Specimen 3	45.83	127.8	54	75.88	313	15,221,676	619,740

The hysteretic response of OpenSees 2D numerical modeling scheme was validated against the experimental and detailed finite-element method analysis of a single story-single bay chevron braced MRF. Figure 7.7 plots the correlation between the hysteretic response of the braced frames. As observed in the figures, the OpenSees numerical models was able to fairly accurately simulate the performance the single-story single bay chevron-braced MRFs.

7.1.3 Low Cycle Fatigue

A study to include the effects of low cycle fatigue of the braces on the numerical model of the single brace and the isolated chevron-braced MRF was conducted.

The methodology developed by Uriz and Mahin [17] was employed to account for fracture of the braces. In OpenSees this basically means to define the fatigue material wrapper in the material model assigned to the braces. The procedure has been used by many researchers to simulate the fracture of braces [17] [23], and others. The fracture model uses the Coffin-Mason relationship shown in the equation 5.3.

$$\varepsilon_i = \varepsilon_0 (N_f)^m \tag{7.3}$$

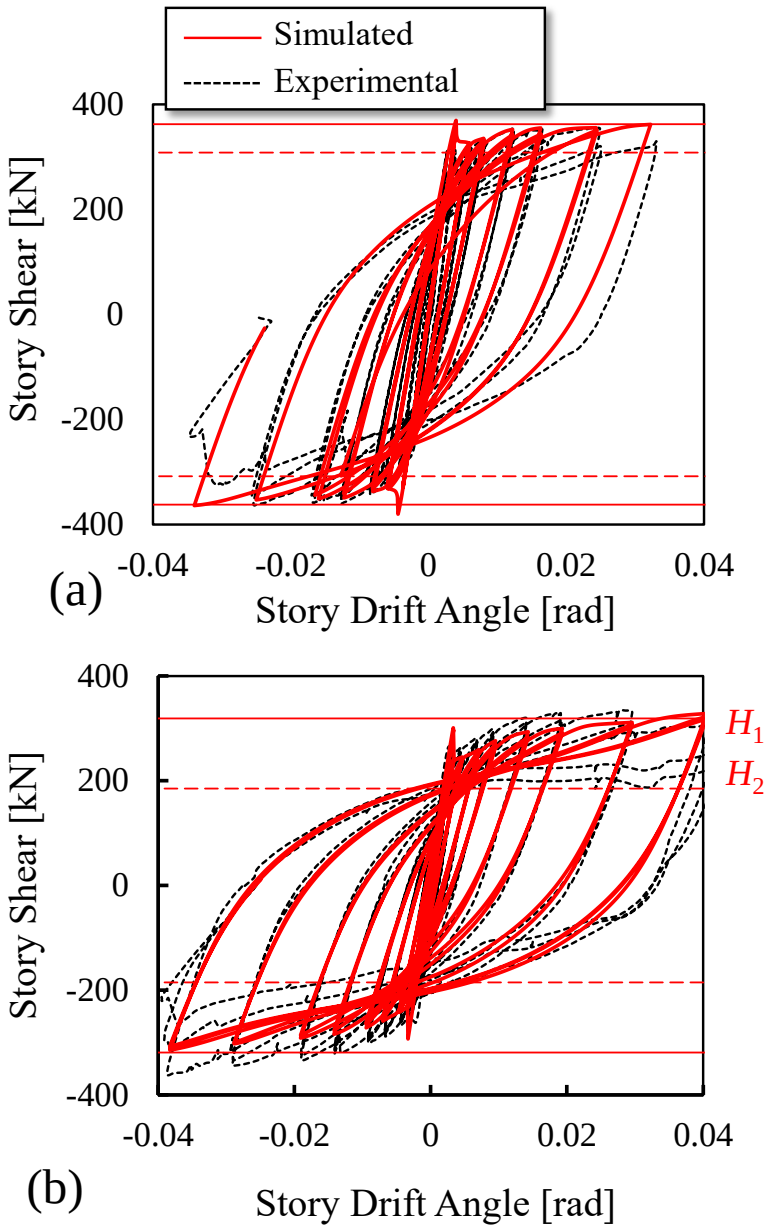

Figure 7.7: Comparison between Numerical and experimental response by Seki et al. [16]: (a) Specimen 1, and (b) Specimen 3.

In the above equation, N_f is the number of cycles to failure, and ε_i is the strain amplitude at each cycle. The two input parameters required by the fracture material defined in OpenSees are: ε_0 which is a material parameter that indicated the strain amplitude that will lead to fracture of the material, and m describes the sensitivity of the log to the total strain amplitude. Karamanchi and Lignos[23] conducted a study in a larger brace database, and developed empirical formulations to compute the ε_0 parameter for the three most commonly used brace shapes. For round-HSS braces, which are used in this study, the ε_0 may be computed as:

$$\varepsilon_0 = 0.748 \cdot \left(\frac{KL}{r}\right)^{-0.399} \cdot \left(\frac{D}{t}\right)^{-0.628} \cdot \left(\frac{E}{F_y}\right)^{0.201} \quad (7.4)$$

where, $\frac{KL}{r}$ is the brace slenderness ratio, $\frac{D}{t}$ is the diameter-to-thickness ratio of the brace, E is the young's modulus and F_y is the brace material yielding strength. The authors provided a constant value for $m = -0.3$. Karamanchi and Lignos[23] proposed two different discretization schemes, depending on the type of element used. The authors suggested the brace to be divided into two force-based beam column elements or eight displacement-base beam column elements. The equation 5.4 is applicable only for $29 \leq KL/r \leq 128$, $12.75 \leq D/t \leq 39.91$, and $326 \leq Fy \leq 521\, M_{pa}$. To account for damage, the Minner's rule is used. Damage is estimated as the ratio of the number of cycles at that amplitude (n_i) over the number of constant amplitude cycles at that amplitude, N_{fi}, necessary to cause fracture. The damage index (*DI*) varying between 0 (no damage) and 1.0 (at failure), is the controlling parameter and is computed as follows:

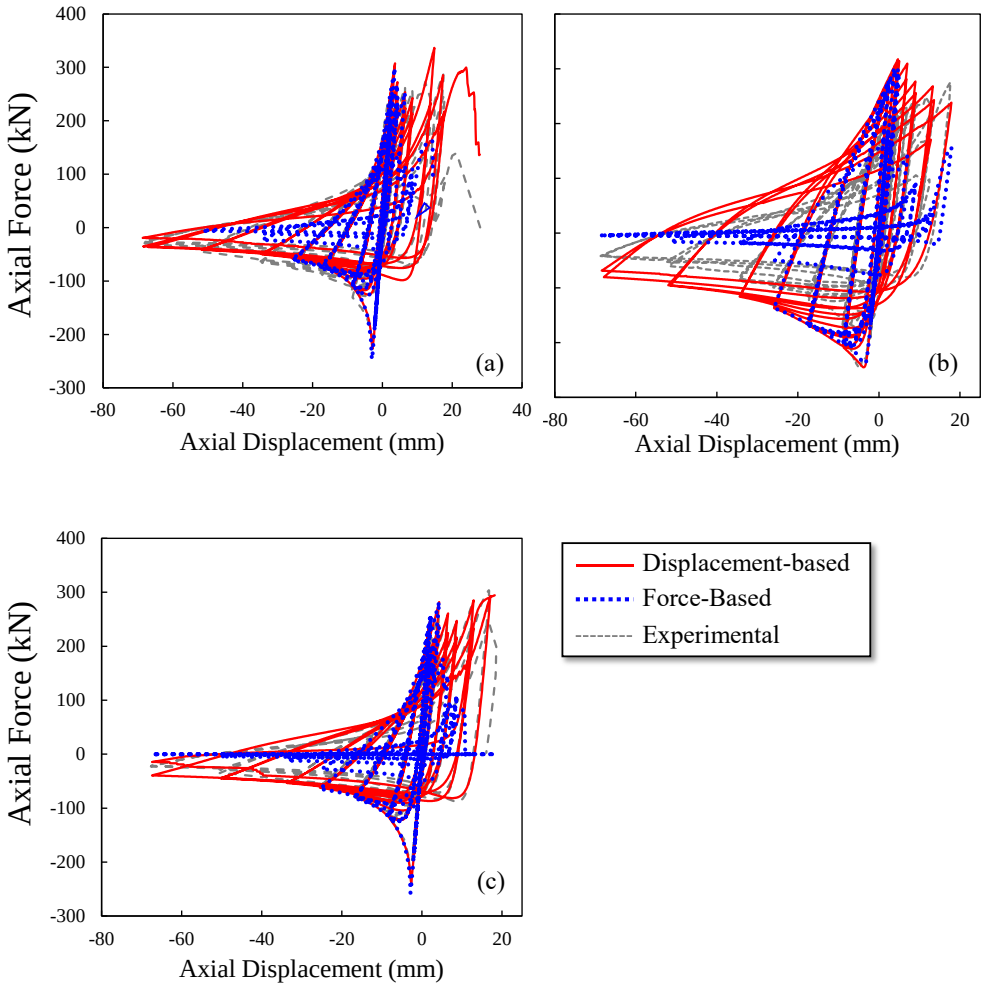

Figure 7.8: Brace Response including fracture due to Low-cycle fatigue: (a) Specimen 1; (b) Specimen 2, and (c) Specimen 3;

$$DI = \sum \frac{n_i}{N_f} \tag{7.5}$$

If, at any fiber, DI exceeds unity, the stiffness and strength of that particular fiber is set to zero.

Fracture of the braces was incorporated in the model of the isolated braces and the single-story single-bay chevron-braced MRFs. To study the accuracy of the proposed equations, both formulation and discretization proposed by the authors was used as shown in Figure 7.8 and Figure 7.9. For the isolated braces cases, the combination of ε_0 and m using force-based Beam-Column elements led to early fracture of the braces. The force-based beam Column Element led to early fracture of the braces, with the braces losing its complete strength early in the loading process, in both the isolated braces simulation case and the CBF. For the CBF simulation, early removal of the brace means that

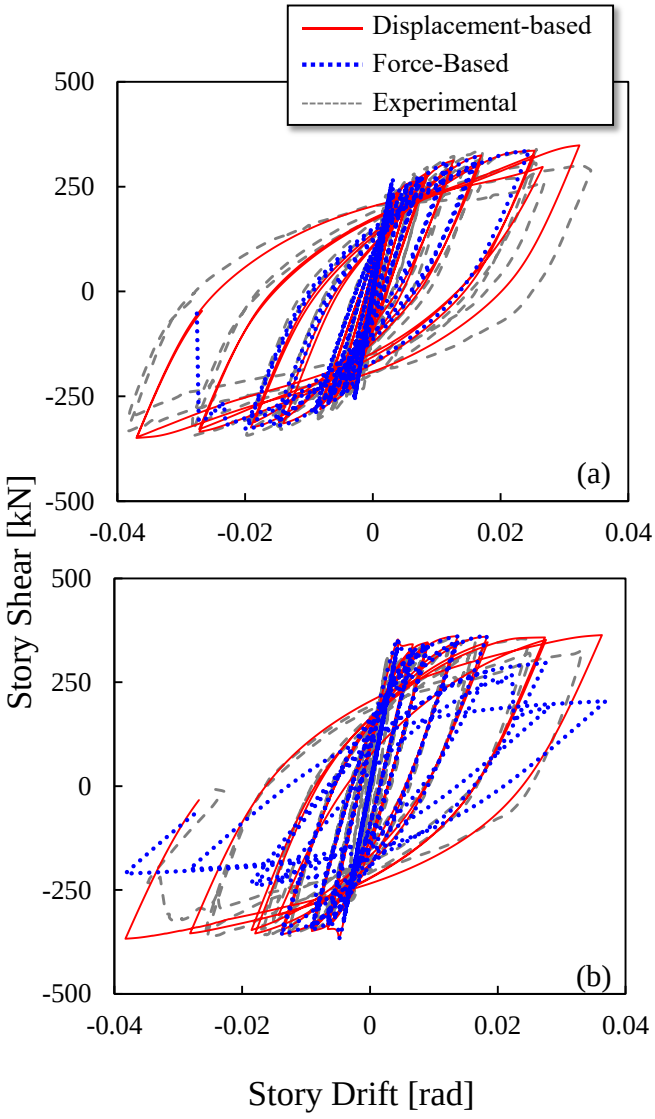

Figure 7.9: Hysteretic response of chevron-braced MRFs including fracture due to Low-cycle fatigue: (a) Specimen 1; (b) Specimen 2;

only the MRF resisted lateral load, and hence the large reduction of the lateral resistance. On the other hand, displacement-based Beam-Column Elements closely matched the experimental response of the braces and the CBFs.

7.1.4 Dynamic Response of a Single-Story Single-bay chevron-braced MRF

A single-story single bay chevron-braced frame was tested at the large-scale table test E-defense in Japan. The test is reported in Okazaki et al. [45]. The CBF specimen (Figure 7.10), represents 70% scale of a typical building, with a span of 4.15 m and height of 2.25 m.

The numerical model is shown in Figure 7.12. The modelling of braces, beams and columns were similar to the numerical built in Figure 7.4.

As in the experimental test, during nonlinear time-history analysis, the frame was subjected seven scaled versions of the Takatori EW ground motion: 10, 12, 14, 28, 28, 42, and finally 70% motion (Figure 7.11). The constant average acceleration scheme with time increments 0.004s was used for integration over time. Rayleigh damping with a critical damping ratio 0.02 was assigned to the first mode. A Seismic mass of 64 tons was applied at the top of the columns. The computed period of the braced frame was 0.21s, matched the experimental period.

The dynamic response of the frame is shown in Figure 7.13. The OpenSees model accurately captured the response of the braced frame model. The numerical model was used to validate the procedure to apply damping to the model and the stiffness of the rigid link. The stiffness of the rigid portion was varied from the same stiffness as the connecting members: (ii) 10 times larger, (i) 100 times larger, and (iii) 1000 times larger.

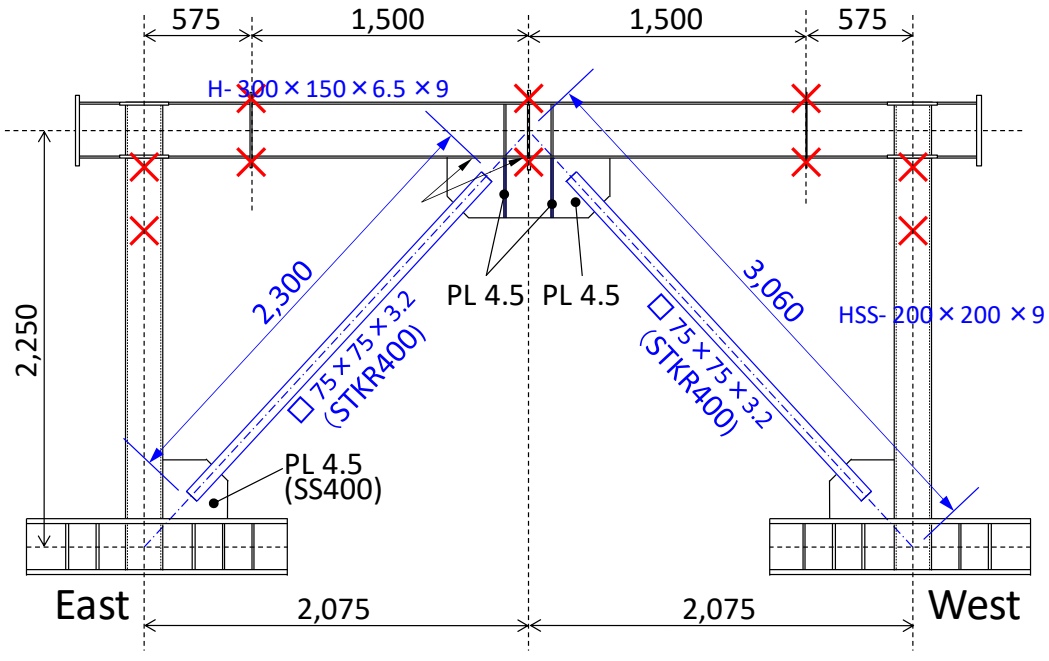

Figure 7.10: Test Specimen and Out-of-plane bracing (Source: Okazaki et al. [45]).

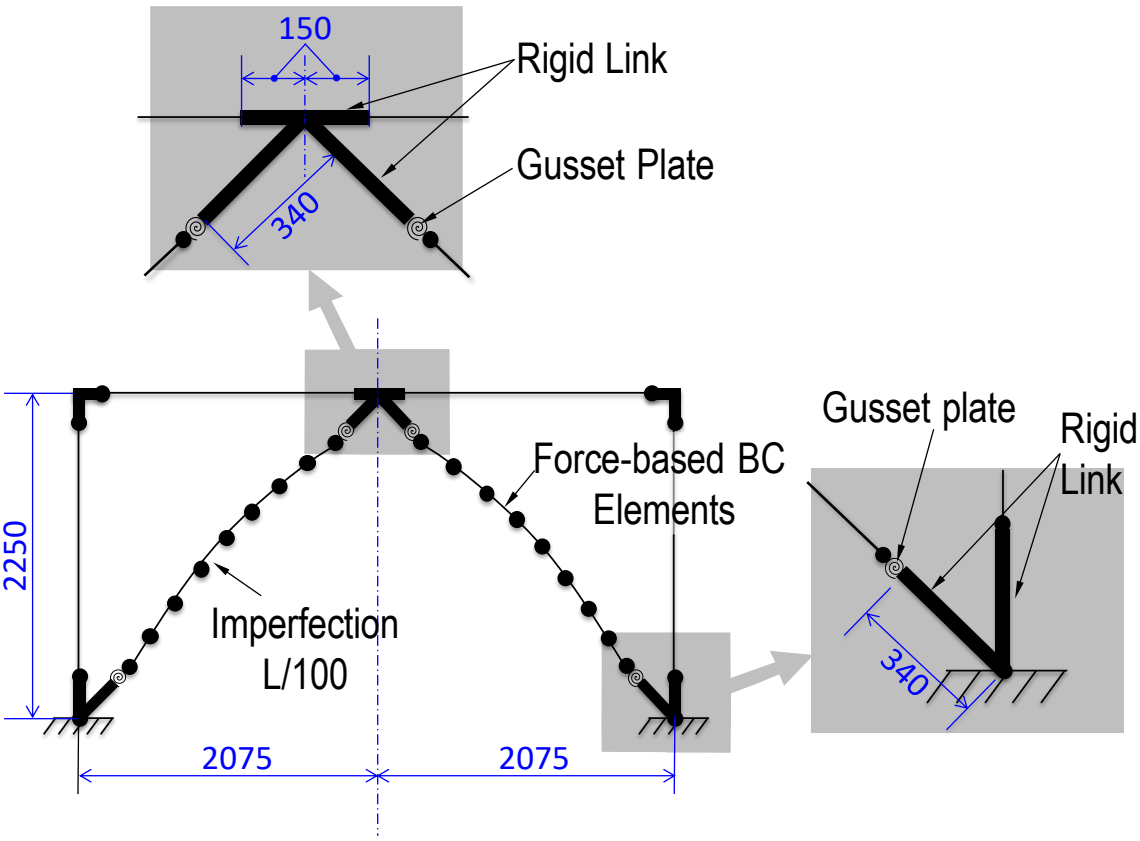

Figure 7.12: OpenSees Numerical Model.

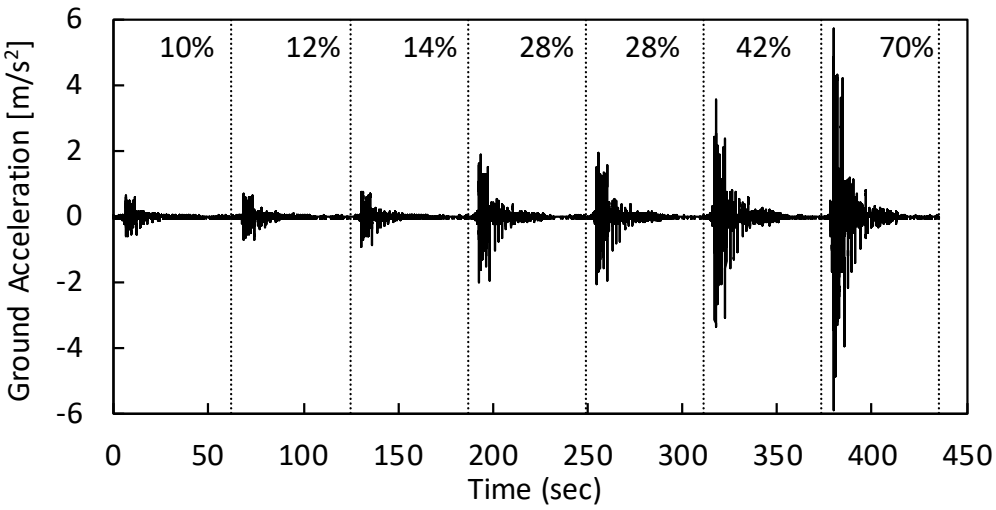

Figure 7.11: JR Takatori EW Acceleration History.

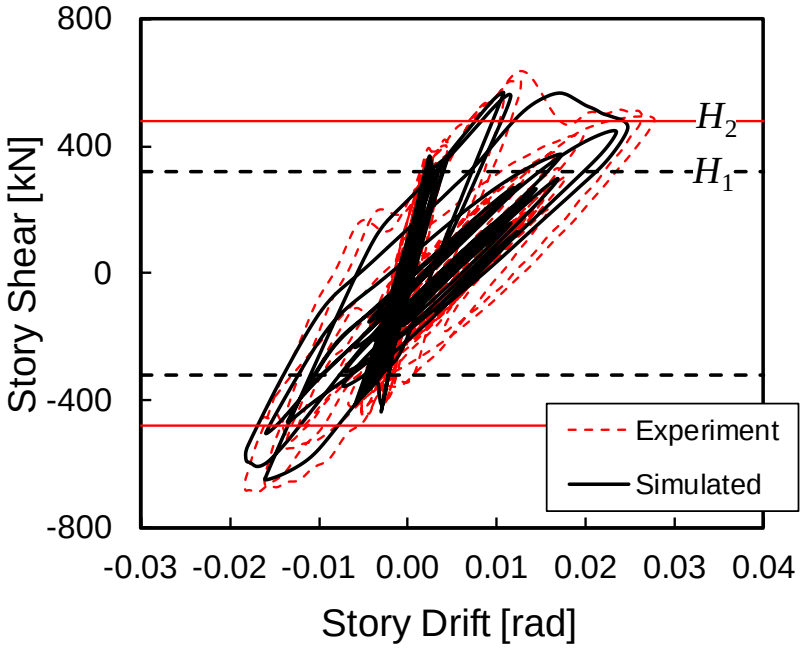

Figure 7.13: Comparison between the numerical simulation and experimental response.

The numerical simulation better match the experimental response for the case with the rigid link stiffness set equal to the area of the connecting members. As observed in the Figure 7.14, increasing the stiffness of the rigid portions led to an increase in the lateral stiffness of the structure, and hence smaller lateral deformation.

A study on the procedure to input damping was conducted by applying the damping to: (*i*) all the elements, (*ii*) excluding the rigid links, and (*iii*) only to the beams and columns. As observed in Figure 7.15, the case where damping was applied only to the beams, braces and columns led to similar response as to the case where damping was applied to all the elements. Between all the cases, the analysis where damping was applied to only the beams and the columns led to flexible structures. The braced frame is subjected to larger story drift response, but the increase in story drift is small.

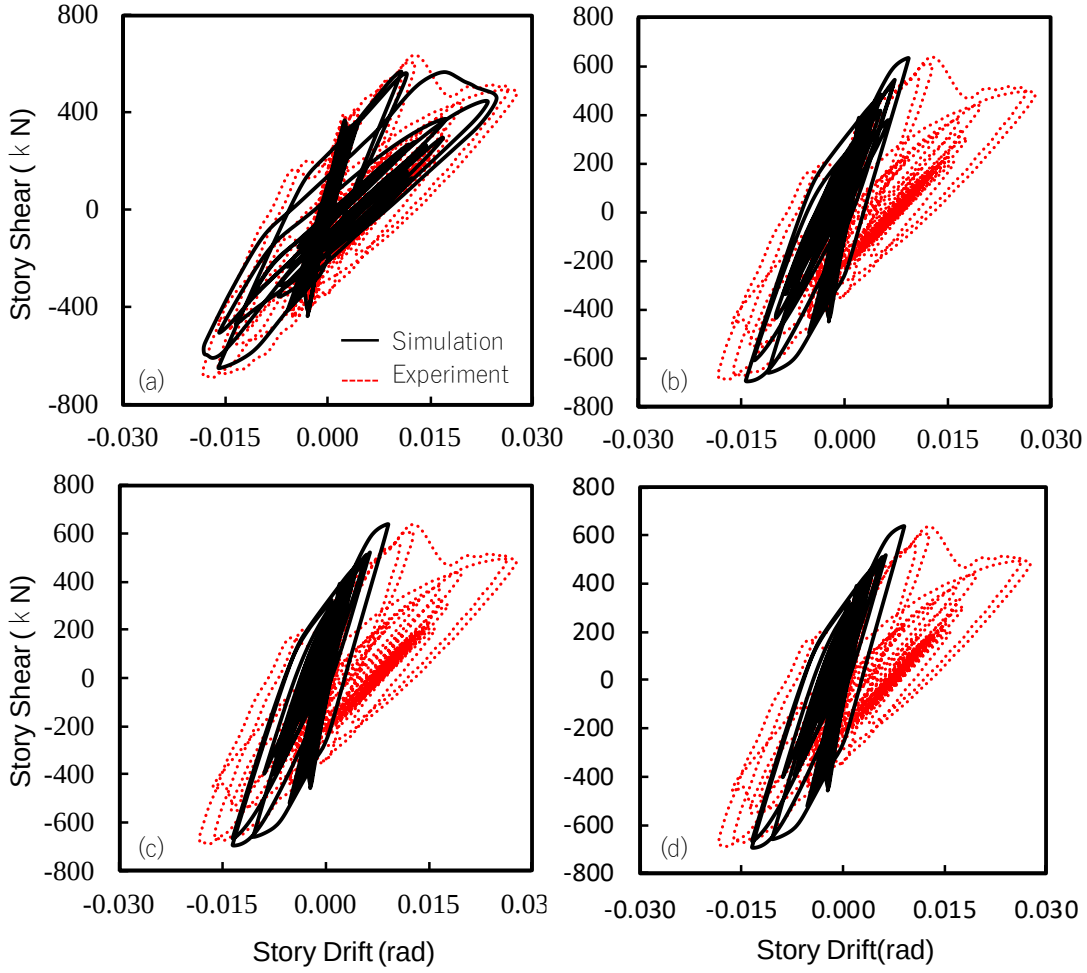

Figure 7.14: Effect of Rigid Link stiffness on the Hysteretic Response : (a) Rigid Link stiffness, EA=1, (b) Rigid Link stiffness, EA=10; (c) Rigid Link stiffness, EA=100; and (c) Rigid Link stiffness, EA=1000.

7.2 Numerical analysis of the Low- and Mid-rise Structures

The OpenSees numerical model developed for the single-story single bay chevron-braced MRF was extended to study the performance of the low- and mid-rise structural systems. The numerical model of the 4-story systems representative of the cases designed according to the Japanese provisions is illustrated in Figure 7.16 and Figure 7.17. The elements type and discretization throughout the length and across the members cross-section was similar as discussed for the single-story single-bay Chevron-braced MRF model, with exception of column modelling. Here, recognizing that the columns will be subjected to high level of axial force demands, and to capture the P-Delta effects, the columns were discretized into four displacement-based beam-column elements. The cross-section discretization remained unchanged. Columns at the base of the frames were considered fixed for the simulation of the structural systems designed with design Type A and B, and pinned for structures designed according to

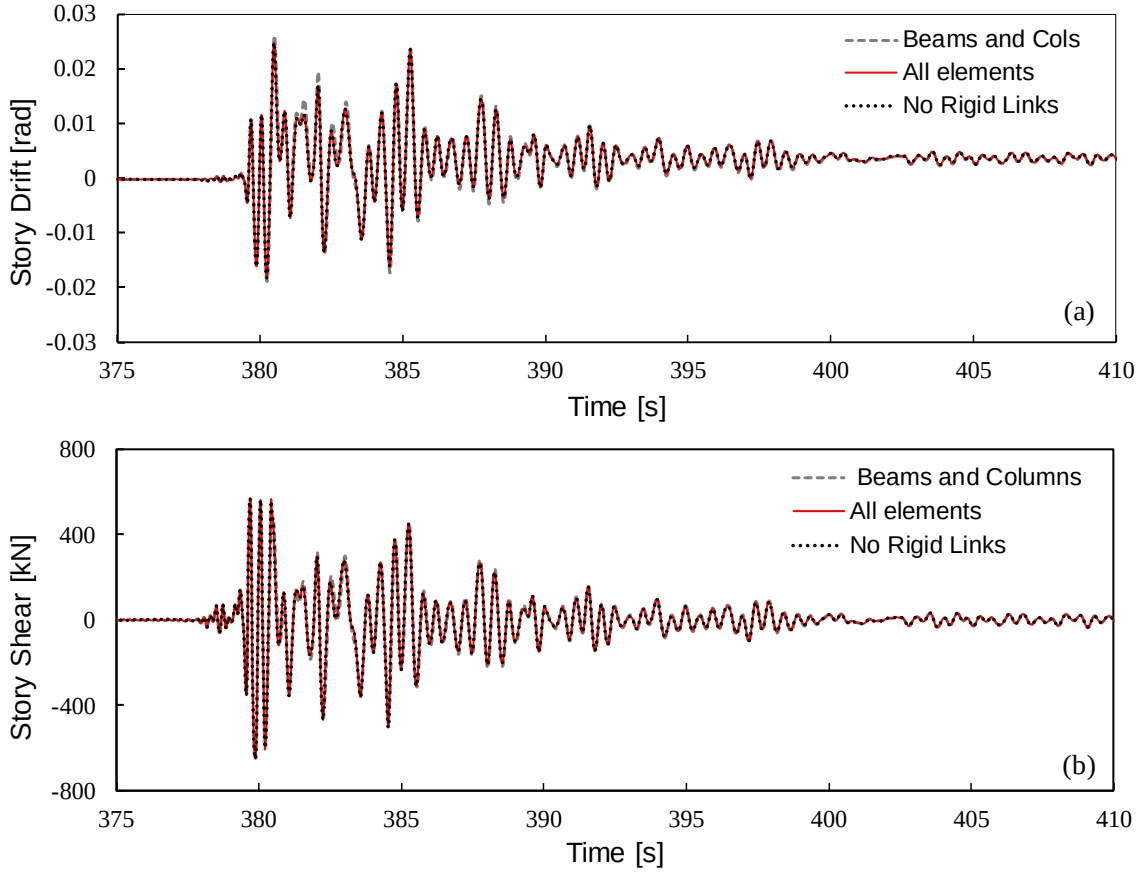

Figure 7.15: Time-history response: (a) Story drift, and (b) Story Shear.

Type C.

Floor diaphragms were modelled with an elastic truss element, with a cross-sectional area equal to the area of the beam. The panel zones were not explicitly modelled. Instead, rigid link elements were used to model the panel zone. Elastic beam column elements were used to model the rigid links. The area and the moment of inertia of the elastic beam column element were defined as 10 times larger than the connecting elements (beams, columns, and braces). A study was conducted to investigate the required element stiffness such that it would have a small effect on the response of the structures. This is reported in section 7.3.

The gusset plates were not explicitly designed. The gusset plate size was extrapolated from the dimensions of the gussets of the single-story braced frame adopted in the experimental program. The dimension of the braced bent is 6×4, which is 2, and 1.74 times larger in the width and height directions respectively, compared to the braced frame tested. Therefore, the width and height of the gusset plates used in the single-story single bay were multiplied by 2 and 1.74, respectively.

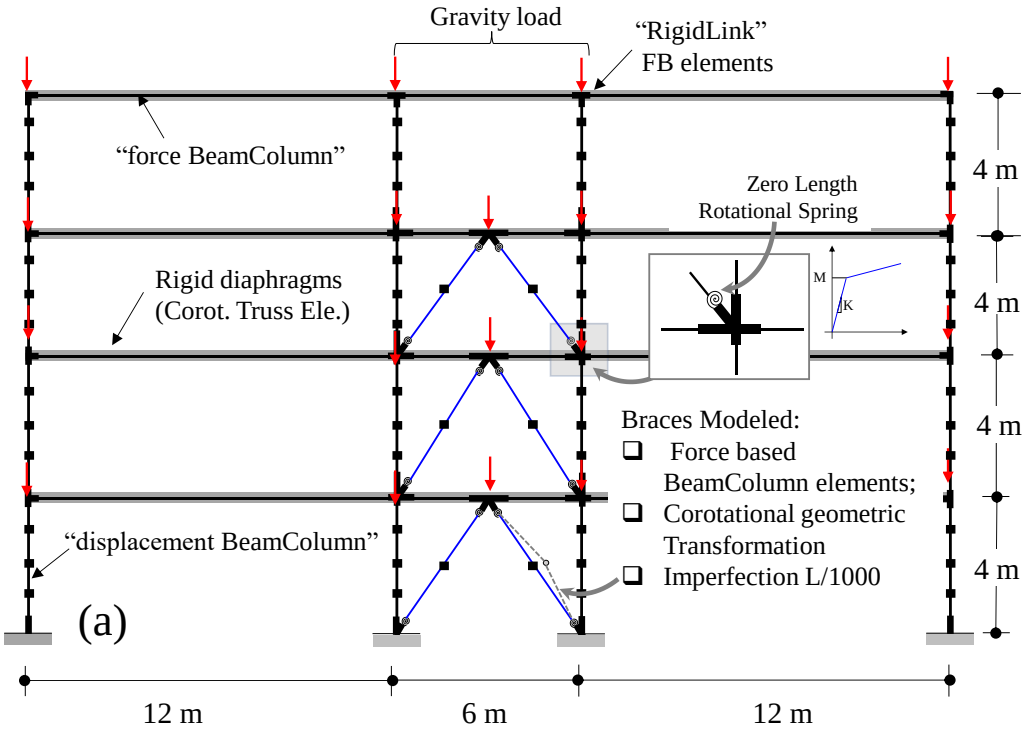

Figure 7.16: Numerical Model Type A and B

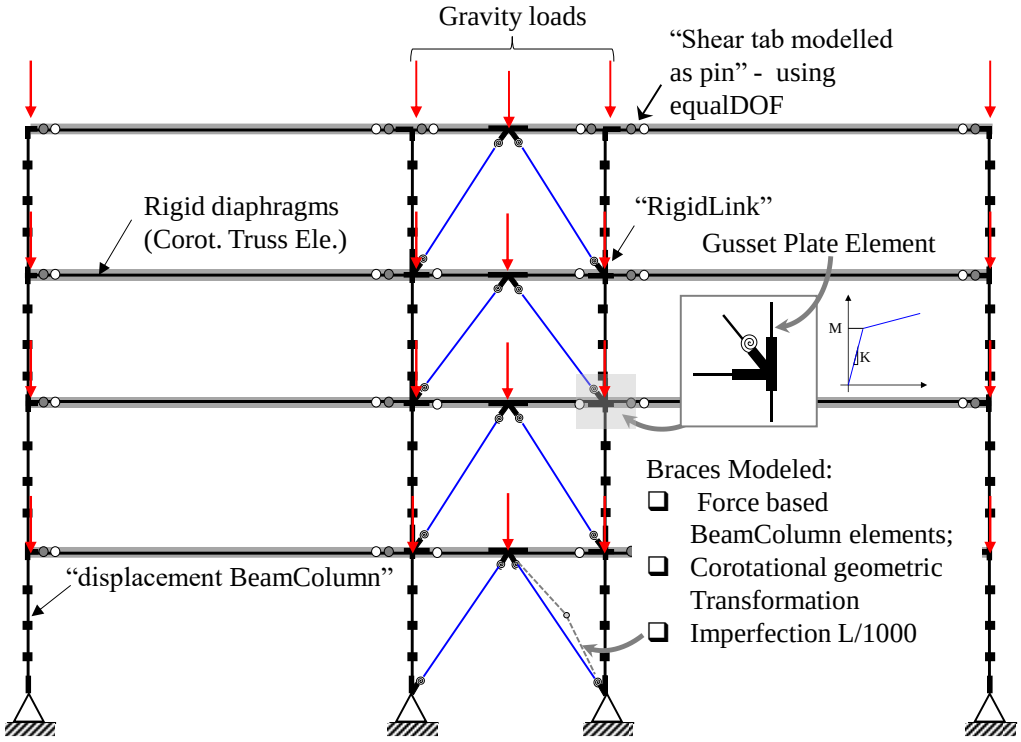

Figure 7.17: Numerical Model Type C

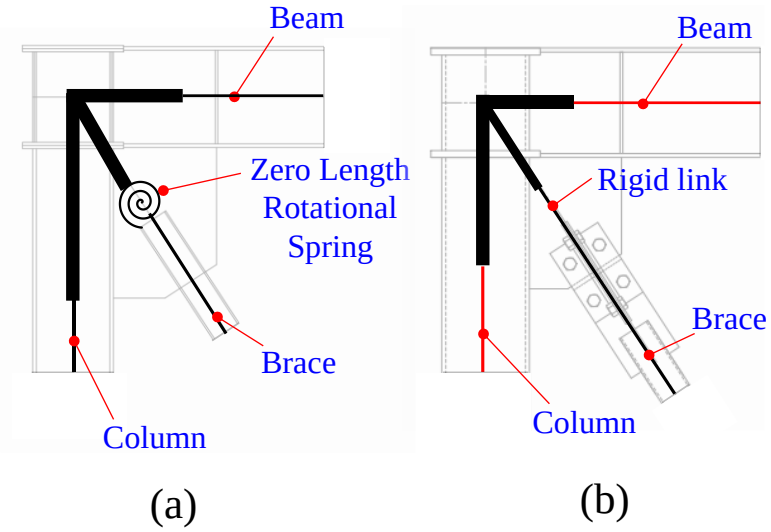

Figure 7.18: Modelling scheme of the bracing connections: a) Flexible Connection; b) Rigid connection;

7.3 Ground Motions Selection and Scaling

A total of 28 pairs of ground motions obtained from the near field ground motion set provided in the FEMA P695 [46] guidelines were used for the time history analysis of the braced frame models.

The ground motions were scaled to match the Japanese level-2 and level-3 target spectrum. According to ASCE 7-16, the two orthogonal components of the ground motions should be used in the time history analysis of the structures. The ground motions were amplitude scaled to matched to the target spectrum between the period range $0.2T_1$ and 2 T_1, where T_1 is the fundamental period of the building.

Table 7.5: Model Fundamental Period

	T_1 (0.03 H)	0.2 T_1	2 T_1
4-Story	0.48	0.1	0.96
8-Story	0.96	0.2	1.92
12-Story	1.44	0.3	2.88

The periods bounds are listed in table 5.7. Scaling of the ground motions was conducted using the PEER Ground motion database (web application)[47]. The geometric mean of the ground motion suite was computed. The mean square error of the ground motion suite average and the target spectra

was used to scale the ground motion records.

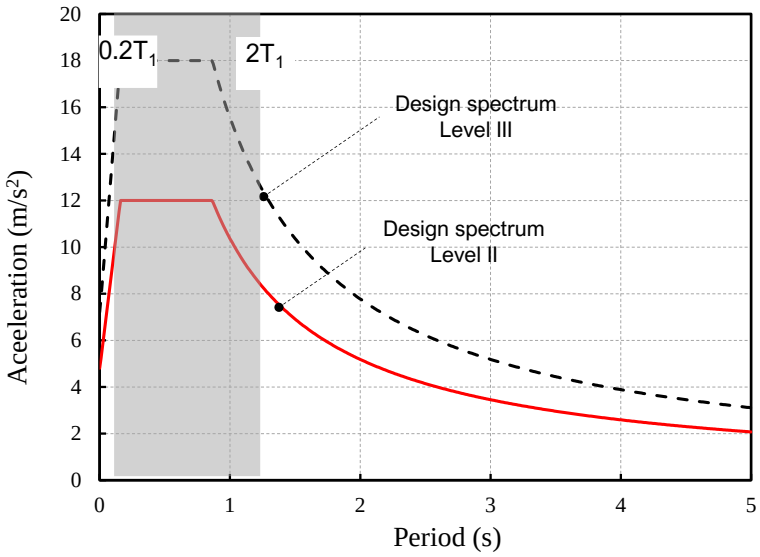

Figure 7.19: Target Spectra: Level-2 and Level-3

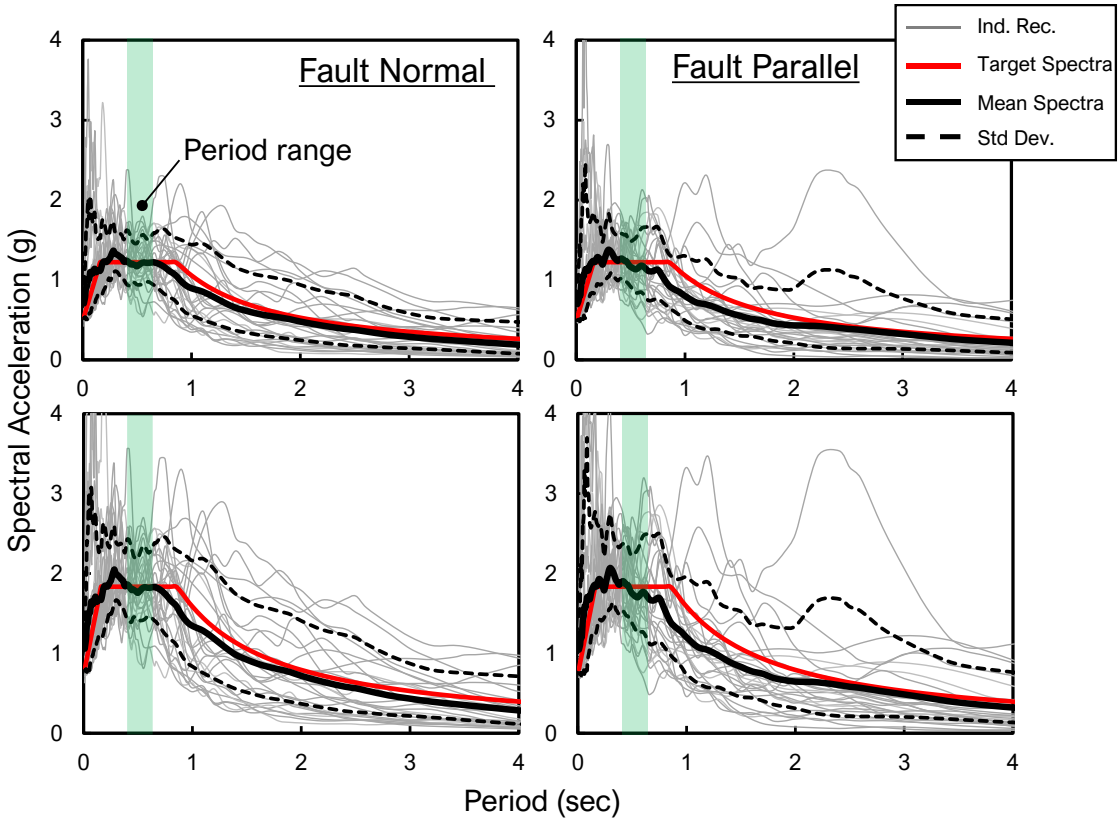

Figure 7.20:Acceleration response spectra for the 4-story systems: a) Level-2; b) Level-3.

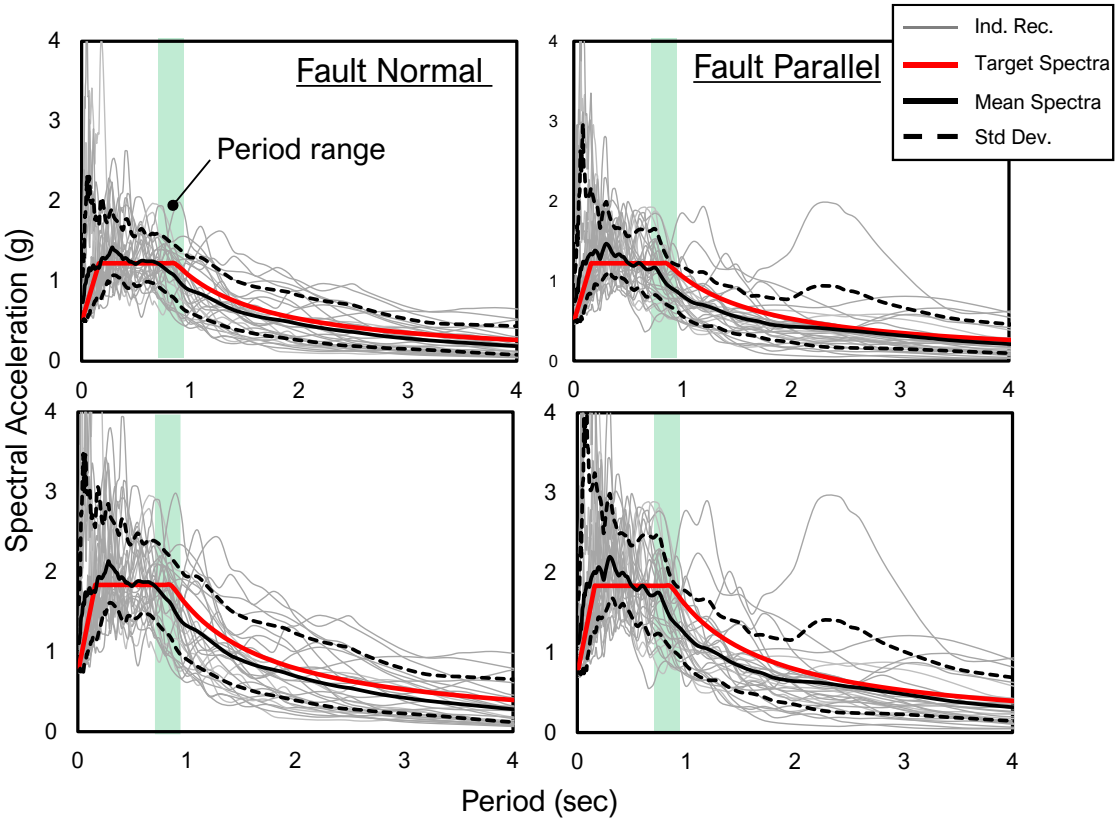

Figure 7.21: Acceleration response spectra for the 8-story systems: a) Level-2; b) Level-3.

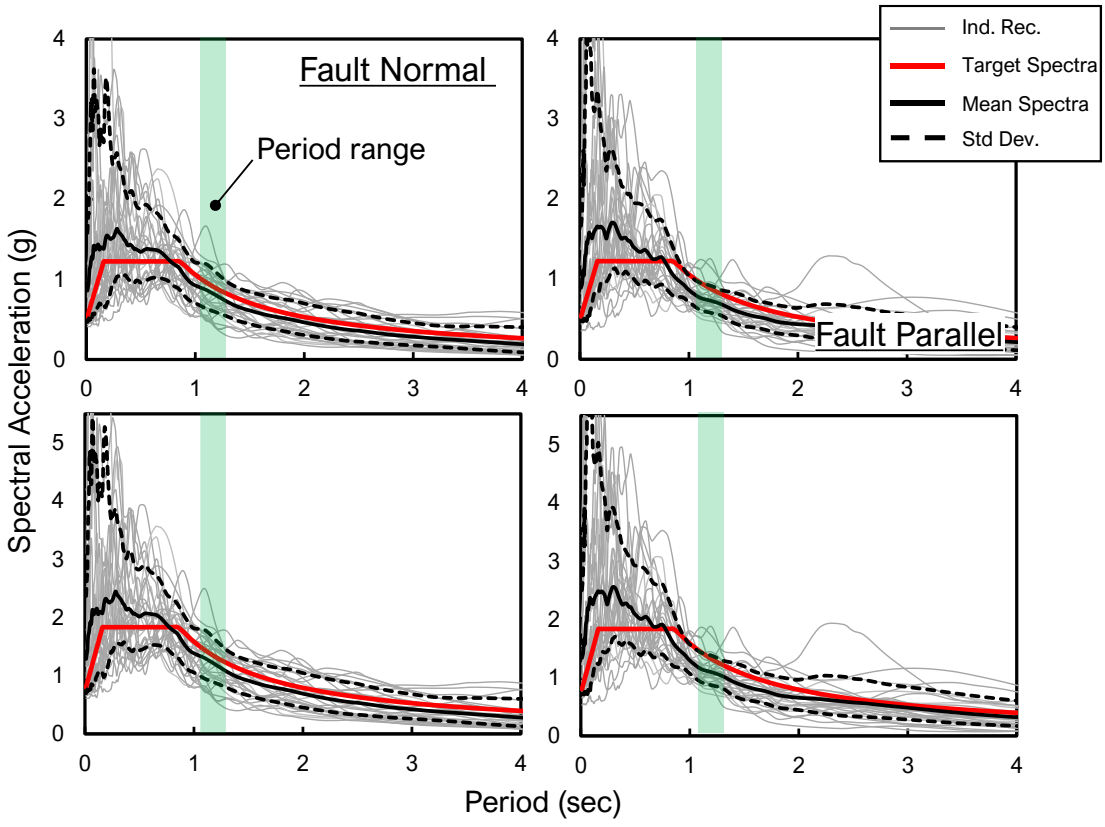

Figure 7.22: Acceleration response spectra for the 12-story systems: a) Level-2; b) Level3.

The fundamental vibration period of the braced frames models are listed in Table 7.6 to Table 7.8.

Table 7.6: 4-Story Model Period

Model	Flexible Connection		Rigid Connection	
	T1 (s)	T2 (s)	T1 (s)	T2 (s)
4A_2.0	0.673	0.264	0.671	0.264
4A_4.0	0.61	0.253	0.60	0.25
4A_8.0	0.625	0.257	0.622	0.256
4B_2.0	0.659	0.26	0.657	0.260
4B_4.0	0.561	0.236	0.559	0.235
4B_8.0	0.534	0.232	0.531	0.231
4C	0.418	0.158	0.417	0.157

Table 7.7: 8-Story Model Period

Model	Flexible Connection		Rigid Connection	
	T1 (s)	T2 (s)	T1 (s)	T2 (s)
8A_2.0	0.90	0.30	0.90	0.30
8A_4.0	0.86	0.29	0.86	0.29
8A_8.0	0.92	0.31	0.92	0.31
8B_2.0	0.88	0.29	0.88	0.29
8B_4.0	0.80	0.26	0.80	0.256
8B_8.0	0.78	0.25	0.78	0.25
8C	0.865	0.267	0.864	0.265

Table 7.8: 12-Story Model Period

Model	Flexible Connection		Rigid Connection	
	T1 (s)	T2 (s)	T1 (s)	T2 (s)
12A_2.0	1.29	0.40	1.29	0.40
12A_4.0	1.25	0.38	1.26	0.38
12A_8.0	1.27	0.40	1.266	0.39
12B_2.0	1.28	0.40	1.28	0.388
12B_4.0	1.22	0.35	1.22	0.348
12B_8.0	1.19	0.33	1.19	0.33
12C	1.17	0.34	1.17	0.335

Table 7.9: Ground motion list and scaling factor

ID	RSN	Earthquake			Recording Station	Fault	PGA	PGV	Scaling Factor					
		M_w	Year	Name		Type	(g)	(cm/s)	4-story		8-story		12-story	
Pulse Record SubSet									FN	FP	FN	FP	FN	FP
1	181	6.5	1979	Imperial Valey -06	El Centro Array#06	Strike-slip	0.44	111.9	1.66	1.60	1.58	1.45	1.46	1.35
2	182	6.5	1979	Imperial Valey -06	El Centro Array#07	Strike-slip	0.46	108.9	2.11	1.39	1.75	1.17	1.65	1.04
3	292	6.9	1980	Irpinia, Italy-01	Sturno	Normal	0.31	45.5	2.10	1.62	1.95	1.69	1.90	1.67
4	723	6.5	1987	Superstition Hills-02	Parachute Test Site	Strike-slip	0.42	106.8	1.40	1.68	1.01	1.47	0.86	1.46
5	802	6.9	1989	Loma Prieta	Saratoga -Aloha	Strike-slip	0.38	55.6	1.62	1.92	1.63	2.11	1.63	2.15
6	821	6.7	1992	Erzican, Turkey	Erzincan	Strike-slip	0.49	95.5	1.63	1.21	1.21	1.16	1.06	1.18
7	828	7	1992	Cape Medocino	Petrolia	Thrust	0.63	82.1	1.18	0.97	1.31	0.94	1.37	0.86
8	879	7.3	1992	Landers	Lucerne	Strike-slip	0.79	140.3	1.29	1.57	1.37	2.23	1.42	2.55
9	1063	6.7	1994	Northridge-01	Rinaldi Receiving Sta	Thrust	0.87	167.3	0.68	0.96	0.57	0.92	0.56	0.90
10	1086	6.7	1994	Northridge-02	Sylmar-Olive View	Thrust	0.73	122.8	1.14	0.70	1.07	0.63	0.98	0.61
11	1165	7.5	1999	Kocaeli, Turkey	Izmit	Strike-slip	0.22	29.8	3.21	2.42	2.79	2.40	2.95	2.56
12	1503	7.6	1999	Chi-Chi, Taiwan	TCU065	Thrust	0.82	127.7	1.21	1.25	1.02	1.01	0.94	0.90
13	1529	7.6	1999	Chi-Chi, Taiwan	TCU102	Thrust	0.29	106.6	2.56	3.81	1.74	2.51	1.39	1.87
14	1605	7.1	1999	Duzcze, Turkey	Dusce	Strike-slip	0.52	79.3	1.27	1.19	1.19	1.01	1.17	0.99

ID	RSN	M_w	Earthquake Year	Earthquake Name	Recording Station	Fault Type	PGA (g)	PGV (cm/s)	Scaling Factor 4-story		Scaling Factor 8-story		Scaling Factor 12-story	
No Pulse Record SubSet									FN	FP	FN	FP	FN	FP
15	126	6.8	1976	Gazli, USSR	Karakyr	Thrust	0.71	71.2	1.00	1.01	1.04	1.17	1.11	1.18
16	160	6.5	1979	Imperial Valey -06	Bonds Corner	Strike-slip	0.76	44.3	0.96	0.68	1.14	0.88	1.18	1.05
17	165	6.5	1979	Imperial Valey -06	Chihuahua	Strike-slip	0.28	30.5	2.18	2.21	2.16	2.09	2.39	2.06
18	495	6.8	1985	Nahanni, Canada	Site 1	Thrust	1.18	43.9	1.02	0.96	1.55	1.39	1.95	1.63
19	496	6.8	1985	Nahanni, Canada	Site 2	Thrust	0.45	34.7	2.54	2.33	2.85	2.53	3.19	2.55
20	741	6.9	1989	Loma Prieta	Bran	Strike-slip	0.64	55.9	0.91	0.95	1.01	1.29	1.10	1.62
21	753	6.9	1989	Loma Prieta	Corralitos	Strike-slip	0.51	45.5	0.96	1.21	1.07	1.27	1.24	1.41
22	825	7	1992	Cape Medocino	Cape Medocino	Thrust	1.43	119.5	0.59	1.29	0.76	1.71	0.93	1.84
23	1004	6.7	1994	Northidge-01	LA - Sepilveda VA	Thrust	0.73	70.1	0.85	0.65	0.84	0.80	0.89	0.90
24	1048	6.4	1994	Northidge-01	Northridge-Saticoy	Thrust	0.42	53.2	1.53	1.01	1.55	0.93	1.63	0.88
25	1176	7.5	1999	Kocaeli, Turkey	Yamarica	Strike-slip	0.31	73	2.17	2.22	1.84	1.76	1.70	1.65
26	1504	7.6	1999	Chi-Chi, Taiwan	TCU067	Thrust	0.56	91.8	1.42	1.48	1.13	1.20	1.02	1.15
27	1517	7.6	1999	Chi-Chi, Taiwan	TCU084	Thrust	1.16	115.1	0.63	1.27	0.48	1.20	0.44	1.21
28	2114	7.9	2002	Denali, Alaska	TAPS Pum Sta.#10	Strike-slip	0.33	126.4	1.81	2.70	1.29	2.03	1.08	1.69

7.4 Damping

The OpenSees software has available various damping models. However, for the analysis conducted, damping was accounted for using the Rayleigh damping. The target damping ratio, ζ was set to 0.02 for the first and the second mode. When using Rayleigh damping, OpenSees allows the user to use either the initial or the committed stiffness when computing the damping ratio coefficients, however, for this work, the damping matrix was computed based on the initial stiffness matrix as follows:

$$C = a_0 M + a_1 K \tag{7.6}$$

The damping coefficients a_0 and a_1 are computed from Eigenvalue analysis. Because the damping is computed using the initial stiffness, a_0 and a_1 are computed in the start of the analysis and are not updated during the analysis. The target damping ζ_n is therefore computed using the following equation:

$$\zeta_n = \frac{a_0}{2\omega_n} + \frac{a_1 \omega_n}{2} \tag{7.7}$$

An additional option would be to use the committed stiffness to compute the damping however this approach significantly impacts the computational time as the damping matrix would have to use the tangent stiffness.

There is a drawback however to using the initial stiffness. As pointed out by many researchers [48]–[50], Rayleigh damping tends to generate large spurious damping forces which would significantly impact the response of the braced frames. The spurious damping forces can be originated when the rigid links stiffness is very high, compared to the joint framing members.

To define the appropriate stiffness of the rigid links, a parametric study was conducted by varying the stiffness of the rigid link portions of the beams, braces, and columns. The properties of the

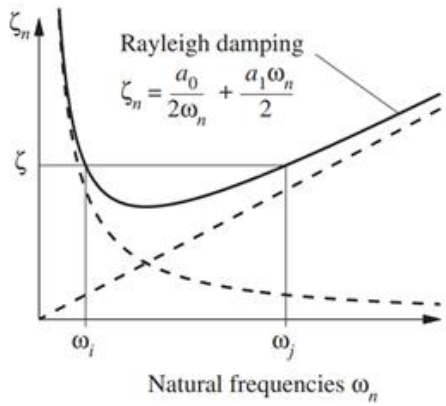

Figure 7.23: Rayleigh Proportional Damping curve.

rigid links were varied from: 1, 10, 100, and 1000 times the moment of inertia and the cross-sectional area of the connecting elements (beams, columns, and braces). A time-history analysis was performed for the 4-, 8- and 12-story systems using the Chi-Chi Taiwan ground motion scaled to the Japanese Level II design spectrum. The analysis was conducted only for the Model designed with Type A with $r_0 = 2.0$. Figure 7.24 plots the story drift response history for Model A with $r_0 = 2.0$. As observed by Charney and Chopra et al, in the elastic range the response is identical for all the cases. However, in the inelastic range, stiffer rigid links led to stronger braced frames systems and hence were subjected to smaller story drift demands. Chopra and McKenna [50] and Charney [48] stated that the larger story shear is due to unbalance moments that originates at the joints. The value of 10 times the cross-section properties was used.

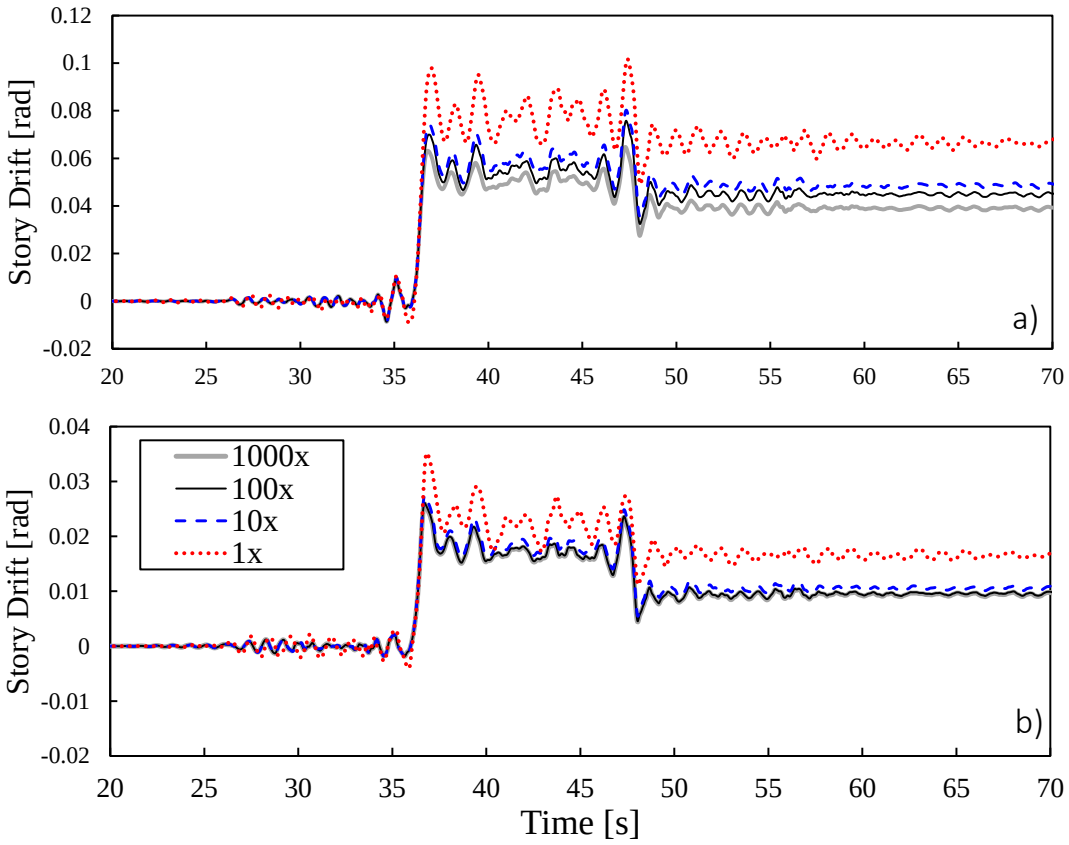

Figure 7.24: Effect of Rigid link stiffness on the story drift history of the 1st story: (a) 4- story systems, and (b) 8-story system.

7.5 Limitations of the Numerical OpenSees Model

Although the numerical model was built to faithfully reproduce the behavior of steel chevron braced MRFs, there are some limitations to the developed numerical model. Some of the main limitations are:

1. local buckling of the braces was not explicitly modelled since fiber-based elements are not able to capture local buckling; The fiber-base beam column element assumes in their formulation that plain section remains plain during deformation and therefore cannot capture the effect of local buckling. Therefore, as observed fort the simulations of the isolated braces for the cases where local buckling controls the inelastic response of the braces, i.e., for braces with small slenderness ratio, the braces will in general develop larger compressive strength than observed from the experimental studies.
2. low-cycle fatigue of the braces and beams-to-column connections were not modelled.
3. strength degradation characteristic of square HSS columns [51], [52] were not modelled, since fiber-based beam column elements were used to model the columns;
4. the bracing connections were assumed to be adequately detailed.

7.6 Nonlinear Pushover Analysis

Pushover analysis of the braced frame models was conducted to study the performance of the braced frame systems in order to draw conclusions on the performance of the systems and the response of the members. During nonlinear pushover analysis, the models were loaded laterally up to a target roof drift of 0.04-rad, with a distribution according to the A_i rule of the Japanese Building Standard.

7.6.1 4-Story Systems

7.6.1.1 Overall Response

Figure 7.25 to Figure 7.30 plots the story shear versus story drift response of the braced frame models during nonlinear pushover analysis employing bracing connection Type I. The reference lines indicate the design base shear, Q_{un}, and lateral strength at plastic mechanism, Q_p.

The story drift was distributed rather uniformly in the 4-story systems for all the cases, except type C, using both bracing connection type I and II. For Type C, the deformation tended to concentrate at the first story. The peak story drift tended to concentrate at the second story. This is justified because the first story was designed with significant overstrength compared to the remaining floors.

Table 7.10 lists the maximum normalized story shear, Q_{max} divided by Q_{un}, Q_{max}/Q_{un}. As observed Q_{max}/Q_{un} ranged from 1.24 to 1.6 for the 4-story systems employing bracing connection type I. When employing bracing connection type II, the braced frame models developed larger lateral strength than the flexible bracing connection detail. The ratio of the lateral strength ranged from 1.35 to 1.69 for the 4-story systems.

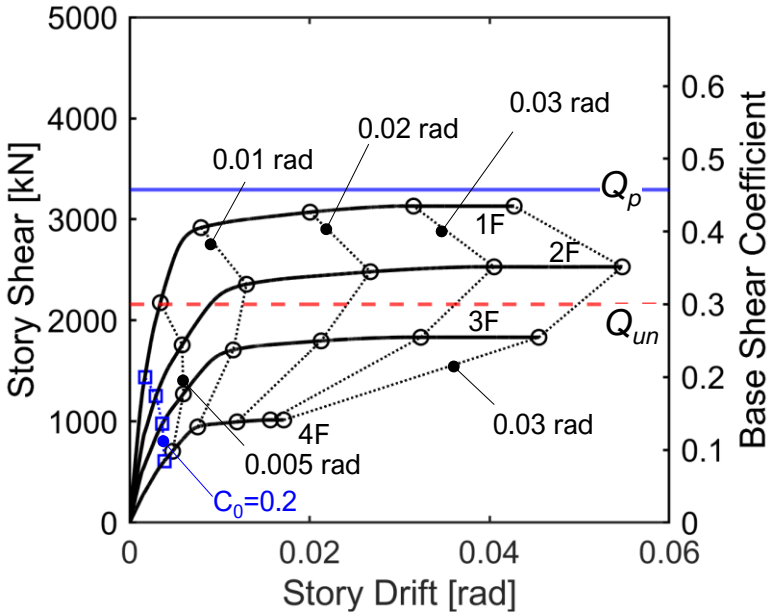

Figure 7.25: Pushover Response of braced frame model designed with Type A with r_0=2.0, employing the flexible bracing connection.

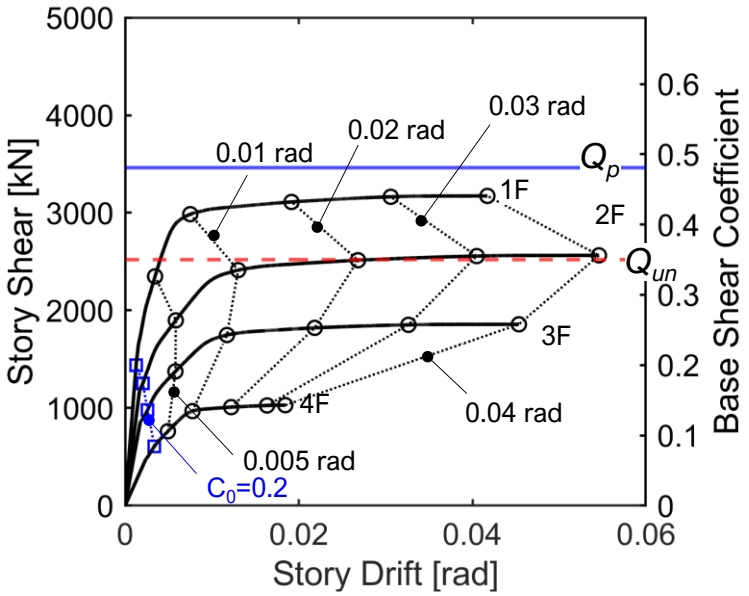

Figure 7.13: Pushover Response of braced frame model designed using with Type A with r_0=4.0, employing the flexible bracing connection.

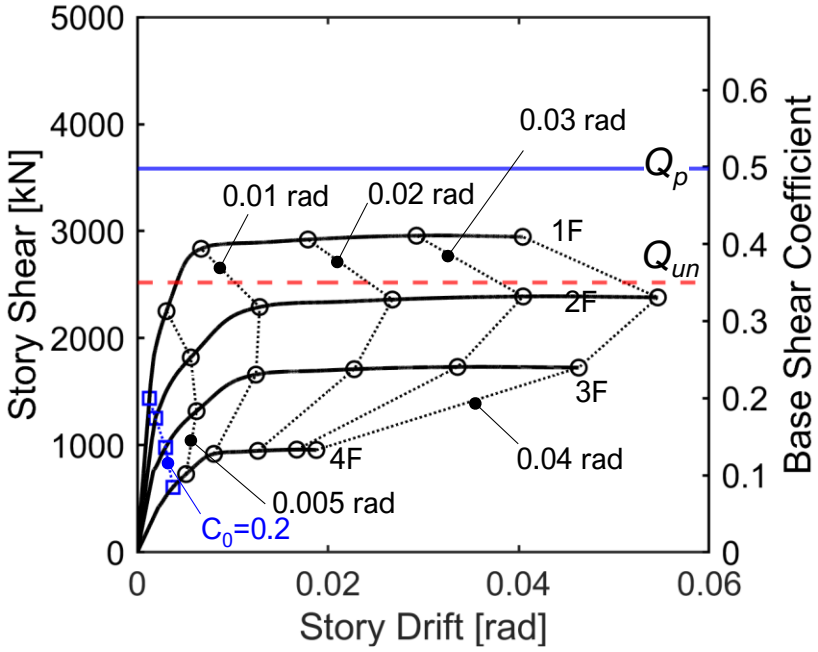

Figure 7.26: Pushover Response of braced frame model designed using design approach Type A with r_0=8.0, employing the flexible bracing connection.

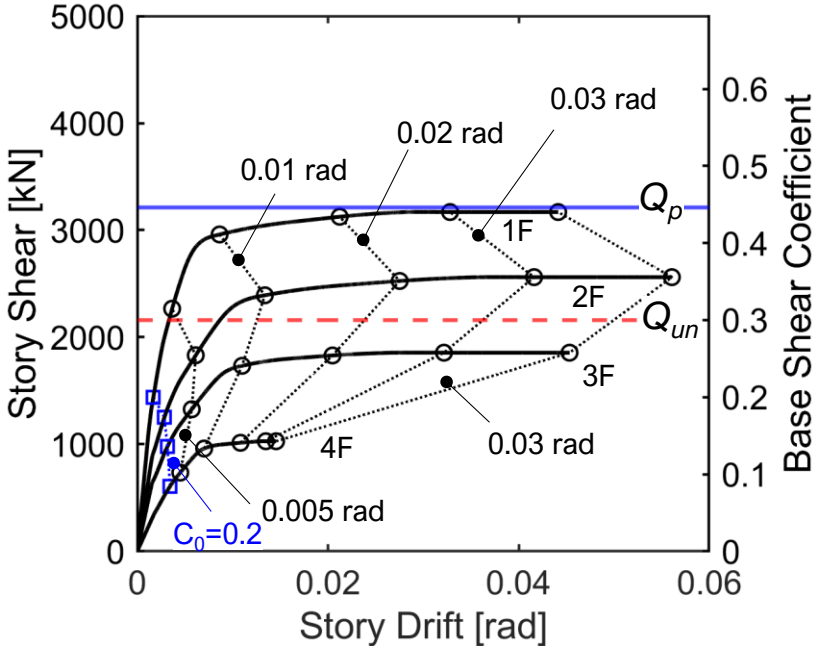

Figure 7.27: Pushover Response of braced frame model designed with Type B with r_0=2.0, employing the flexible bracing connection.

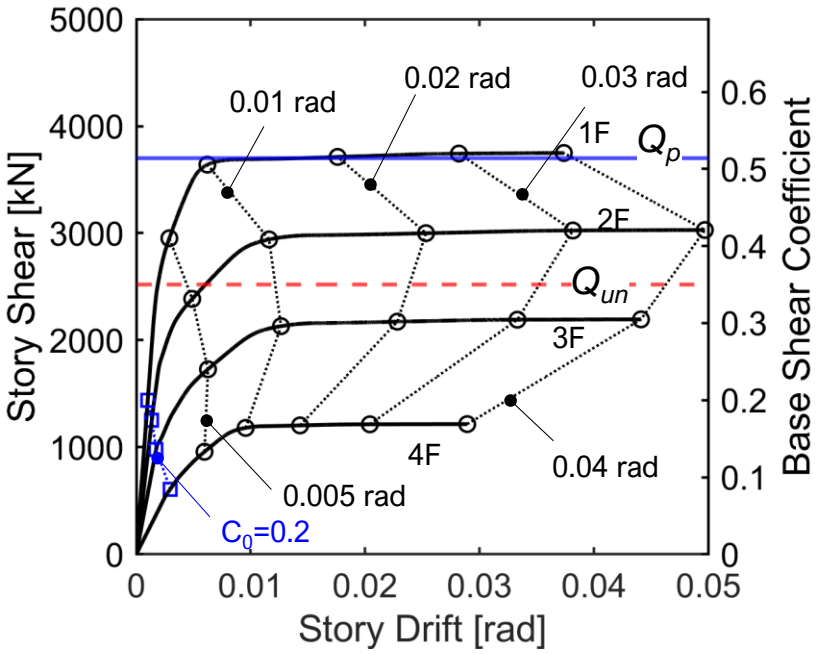

Figure 7.28: Pushover Response of braced frame model designed with Type B with r_0=4.0, employing the flexible bracing connection.

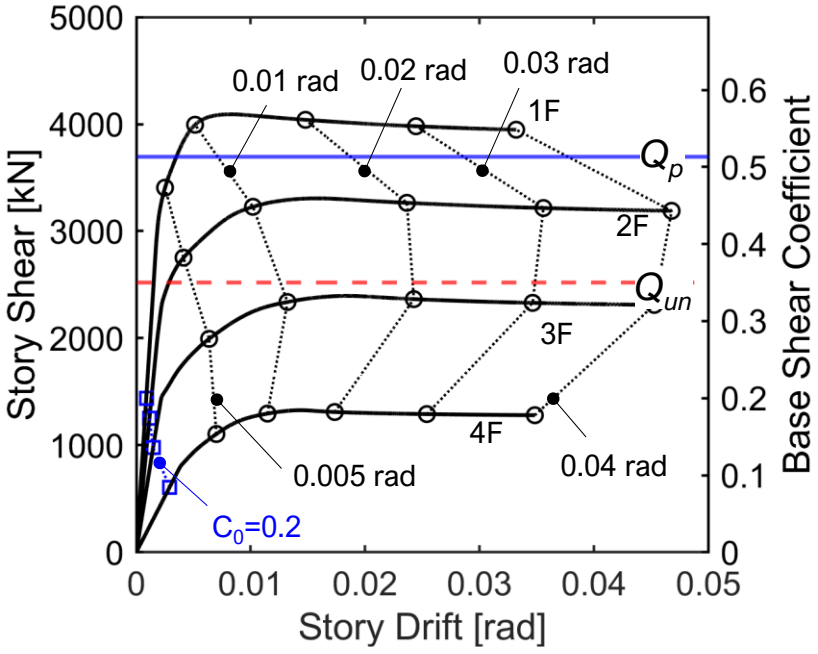

Figure 7.29: Pushover Response of braced frame model designed with Type B with r_0=8.0, employing the flexible bracing connection.

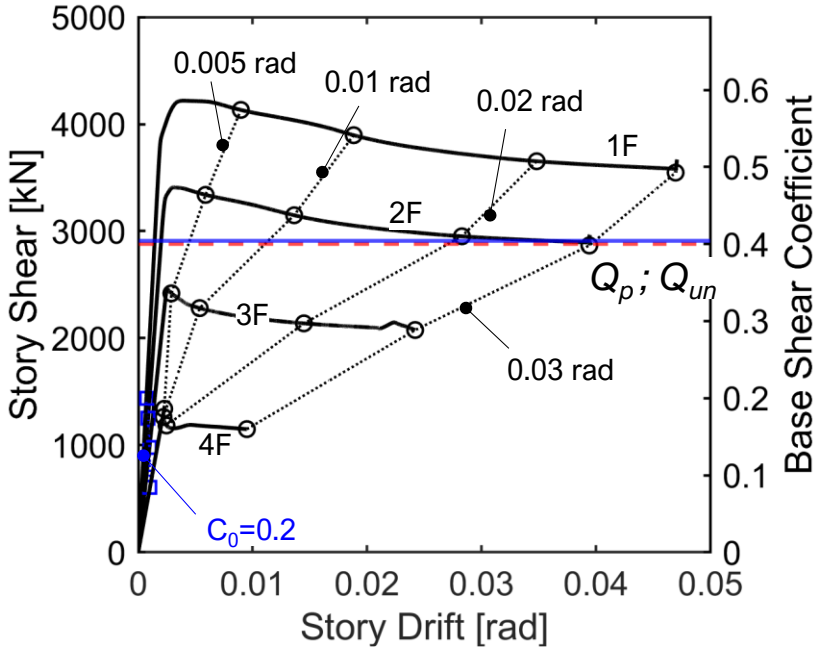

Figure 7.30: Pushover Response of the CBF model designed with Type C, employing the flexible bracing connection.

As observed from the design stage, the pushover analysis produced similar results between Type A and B for r_0= 2.0, however Type B developed 16% and 25% greater strength than Type A for r_0 = 4.0 and 8.0, respectively. The large discrepancy in the lateral resistance between Type A and B can be attributed to the fact that the MRF was designed without taking into consideration the force unbalance developed on the beam. The maximum ratio Q_{max}/Q_{un} ranged from 0.22 to 0.54, in the models designed with Type A with r_0 = 2.0 and Type B with r_0 = 8.0, respectively.

The braced frame models designed with Type A did not develop their predicted plastic strength, Q_p. For Type A with $r_0 = 2.0$, 4.0 and 8.0, the resistance of the frame at 0.02 roof drift was roughly $0.95Q_p$, $0.92Q_p$, $0.83Q_p$, respectively when employing the flexible bracing connection. When the

Table 7.10: Pushover Analysis response:4-story CBF employing the flexible bracing connection

Design	r_0	L/r	Q_{max}	Q_{max}/Q_{un}	$Q_b/Q_{0.02\ rad}$	Mechanism
Type A	2.0	88-104	3298	1.53	0.22	SB
	4.0	88-89	3466	1.60	0.31	WB
	8.0	67-76	3120	1.24	0.38	WB
Type B	2.0	105-146	3381	1.57	0.23	SB
	4.0	68-89	4025	1.86	0.37	WB
	8.0	54-68	3888	1.54	0.54	WB
Type C	-	36-67	4135	1.44	1.0	SB

Notes: WB – Weak-beam mechanism; SB – Strong-Beam mechanism

CM – Combined Mechanism

rigid bracing connection detail was employed, the resistance of the frame at 0.02 roof drift was roughly $1.04Q_p$, $1.06Q_p$, $0.96Q_p$, for $r_0 = 2.0$, 4.0 and 8.0 respectively.

Type B with $r_0 = 4.0$ and 8.0 and Type C develop larger lateral resistance at 0.02 roof drift than the predicted plastic strength. For Type B with $r_0 = 8.0$ and Type C, the resistance of the frame was roughly $1.11Q_p$, and $1.26Q_p$, respectively when employing the flexible bracing connection, and $1.28Q_p$, and $1.57Q_p$, respectively when employing the rigid bracing connection.

Figure 7.31 shows the change of proportion of the lateral strength carried by the braces, Q_b/Q with the loading protocol. As shown in the figure, Q_b/Q is large prior to buckling of the braces and decreases with the increase of the story drift. After 0.01-rad the ratio Q_b/Q stabilizes and remains nearly constant. Table 7.10 lists the Q_b/Q at target story drift ratio. At 0.04-rad drift, the braces were resisting only 15% of the story shear.

7.6.1.2 Brace Response

The response of the braces is shown in Figure 7.32 through Figure 7.38. The figure shows that, during monotonic pushover for the braced frames Models designed using design approach Type A and B with r_0=2.0, and Type C, the braces yielded in tension at all the floor levels. For r_0= 4.0 and 8.0, unlike what expected, the braces yielded at the floor levels but the braces developed limited elongation in tension. The compressive strength of the braces decreased to smaller than the $0.3 \times N_{cr}$.

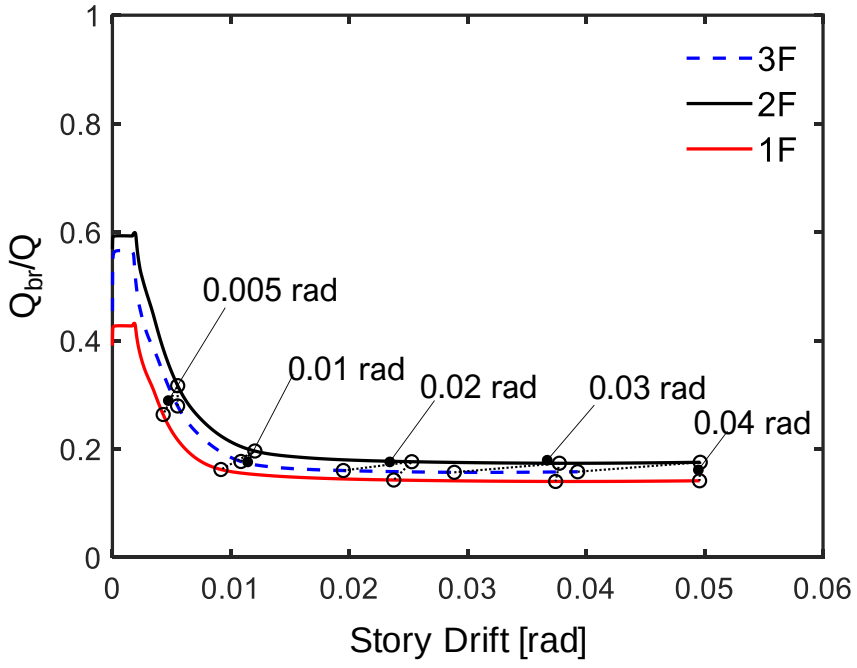

Figure 7.31: Change in Q_{br}/Q throughout the loading history for Type A with r_0=2.0, employing the flexible bracing connection.

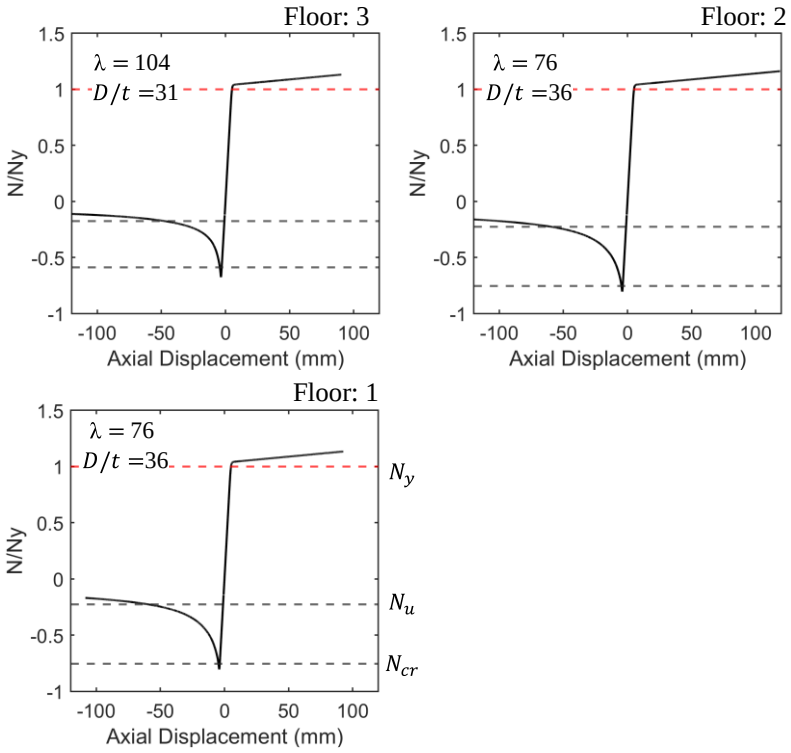

Figure 7.32: Hysteretic response of the braces of Model A with r_0=2.0

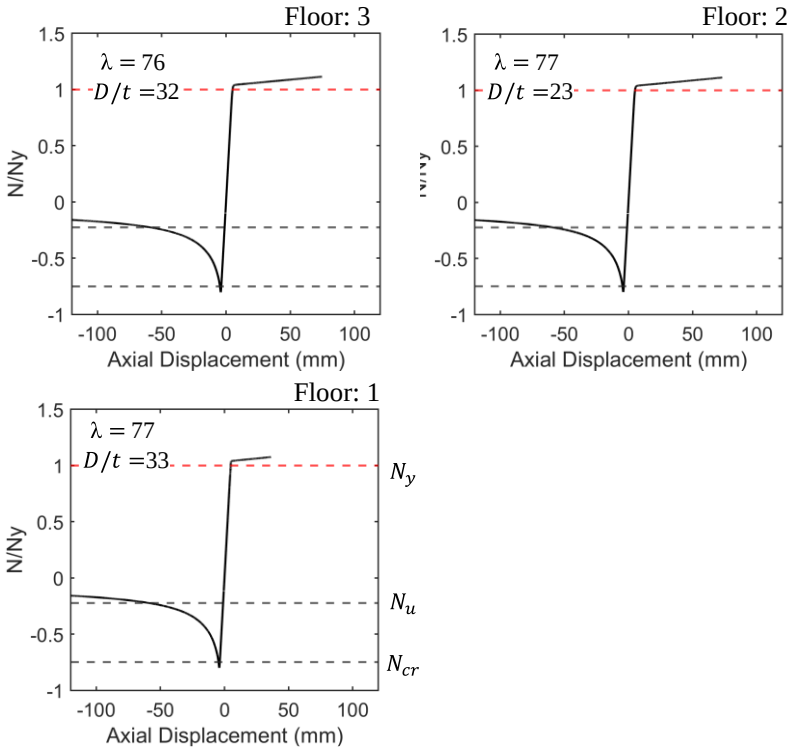

Figure 7.33: Hysteretic response of the braces of Model A with r_0=4.0

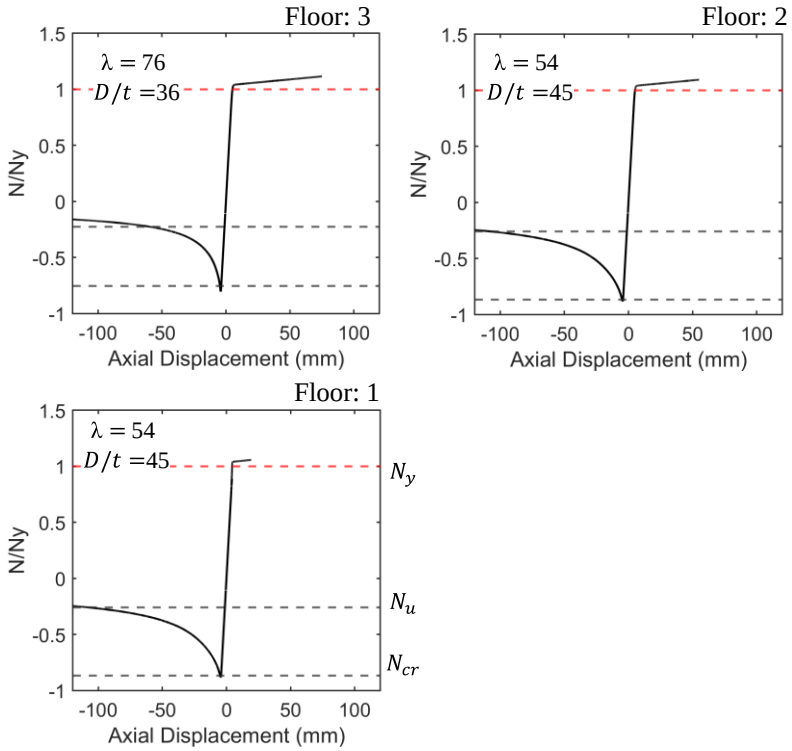

Figure 7.34: Hysteretic response of the braces of Model A with r_0=8.0

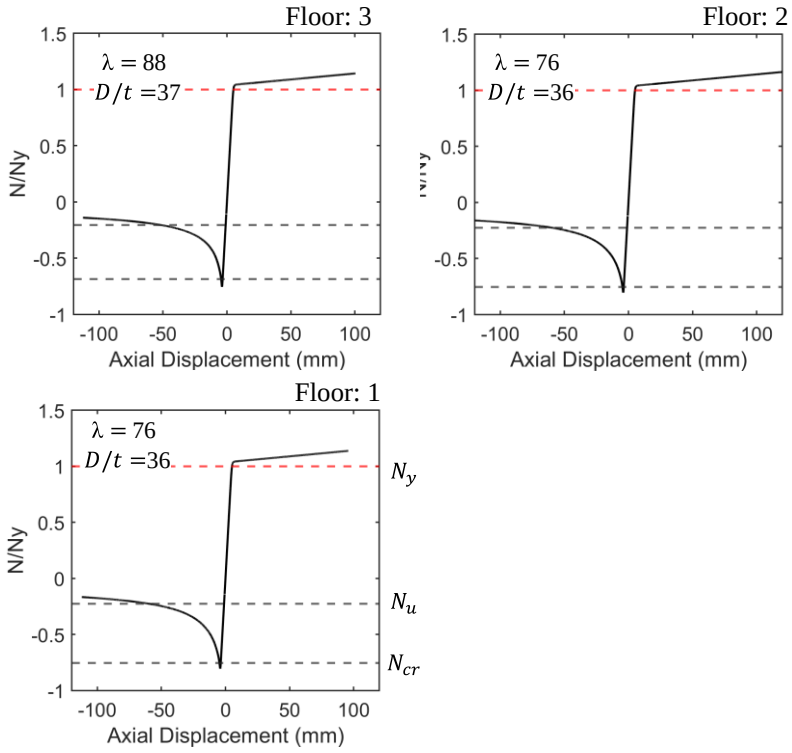

Figure 7.35: Hysteretic response of the braces of Model B with r_0=2.0

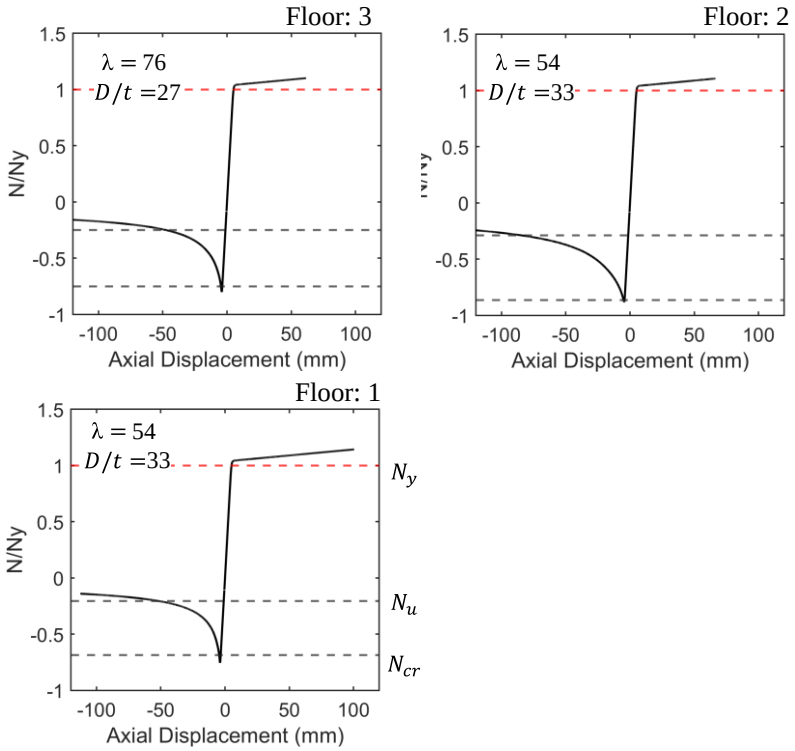

Figure 7.36: Hysteretic response of the braces of Model B with r_0=4.0

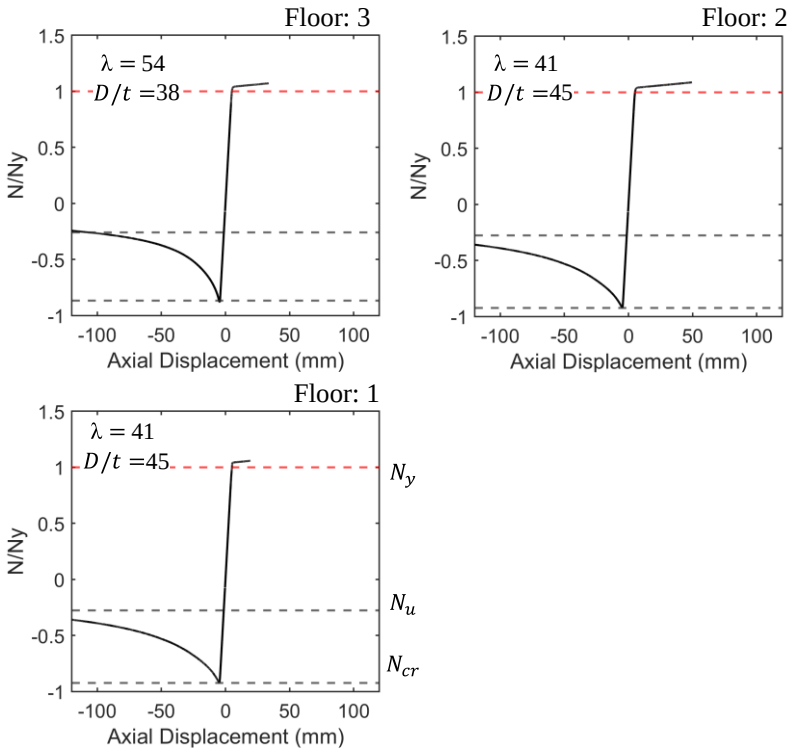

Figure 7.37: Hysteretic response of the braces of Model B with r_0=8.0

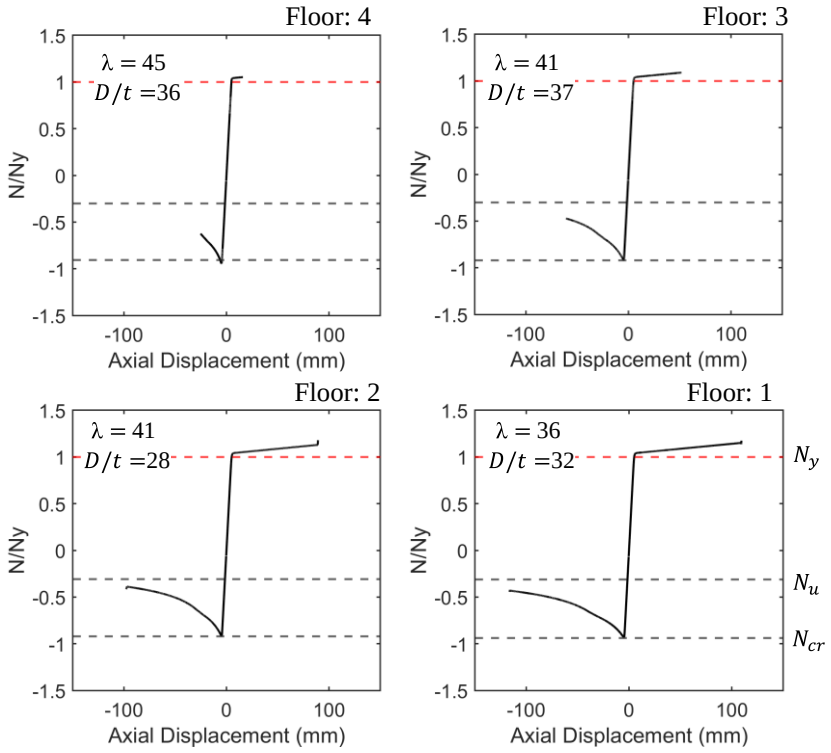

Figure 7.38: Hysteretic response of the braces of Model C

7.6.1.3 Collapse mechanism of the 4-Story chevron-braced frames

The collapse mechanism of the braced frames are depicted in Figure 7.39 through Figure 7.43. As observed in the figures, for the braced frames design approach Type A and B, with $r_0 = 2.0$, inelasticity was concentrated on the end of the beams and braces. Yielding at the center of the beam intersected by the braces at the 3rd floor level was occurred for Type A with $r_0 = 2.0$, by the end of 0.04 rad roof drift. For $r_0 = 8.0$, yielding of the beams intersected by the braces at the ends of the rigid portions occurres for both Type A and B. For Type C, the beams remained elastic as intended from design. Figure 7.44 plots the response at the mid-span of the beam intersected by braces, by plotting the peak bending moment developed nomalized by the beam plastic moment capacity. For design approach Type A, with exception of the case with $r_0 = 2.0$, the beam yielded at all the story levels. For $r_0 = 8.0$, the maximum moment grew to $1.48M_p$at the 3rd floor.

Interestingly, for design approach Type B, the maximum moment developed at the beams were identical to design approach Type A.

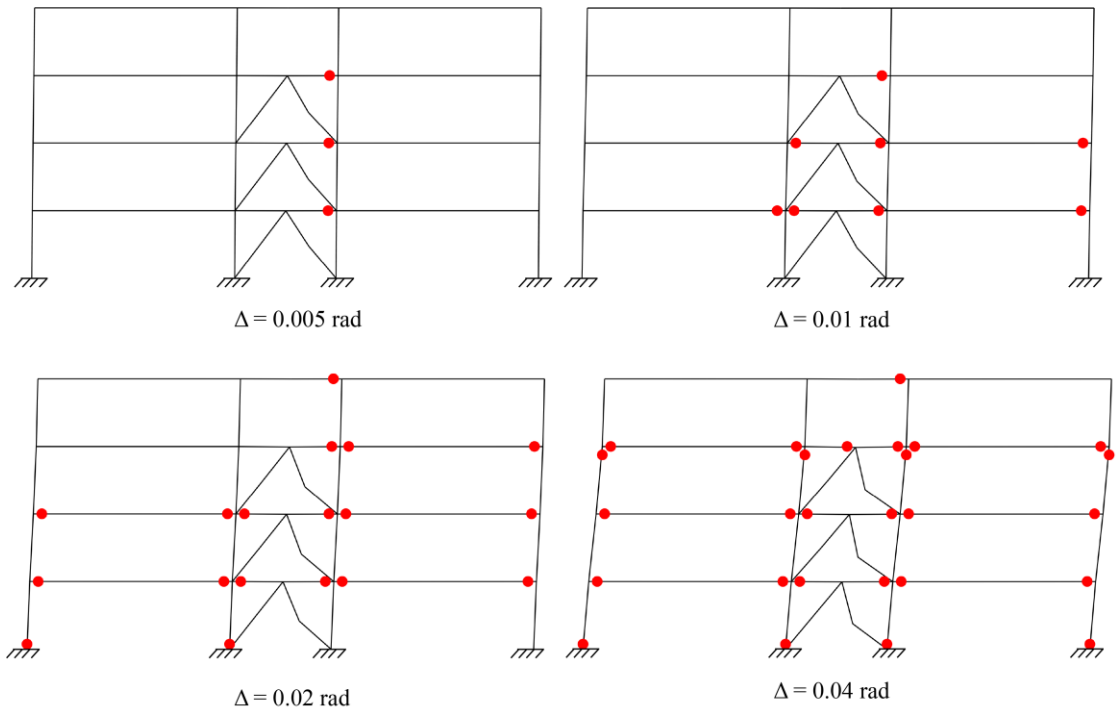

Figure 7.39: Collapse mechanism of the braced frame model designed with Type A with r_0=2.0, employing the flexible bracing connection.

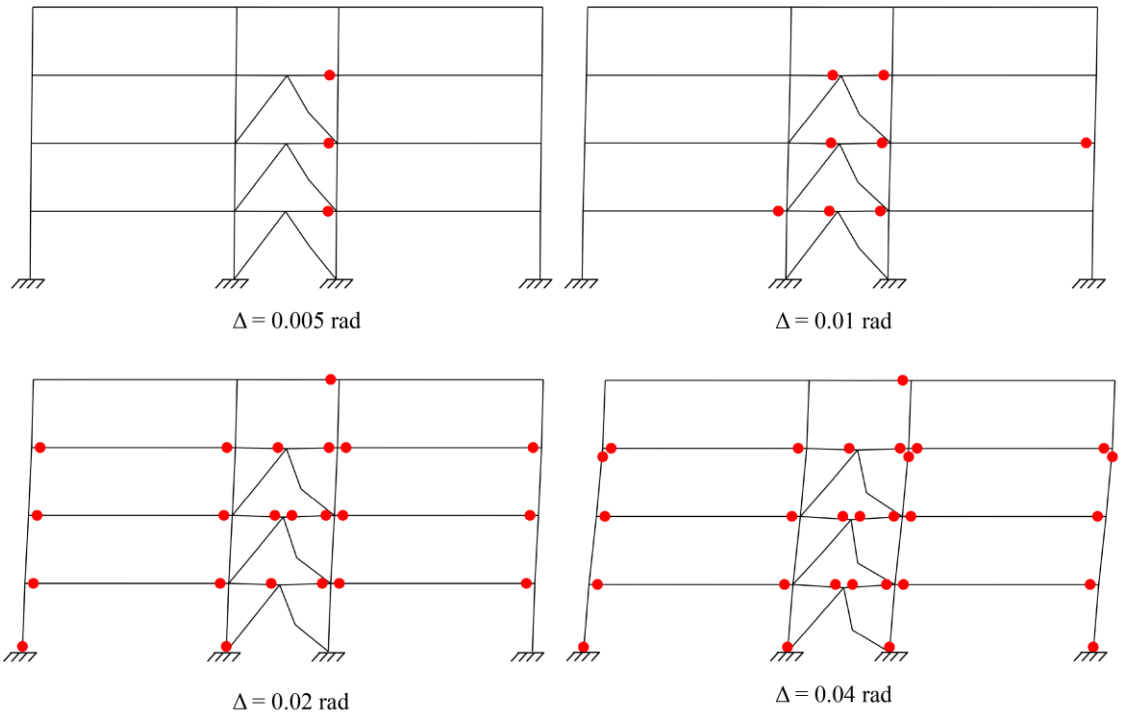

Figure 7.40: Collapse mechanism of the braced frame model designed with Type A with r_0=8.0, employing the flexible bracing connection.

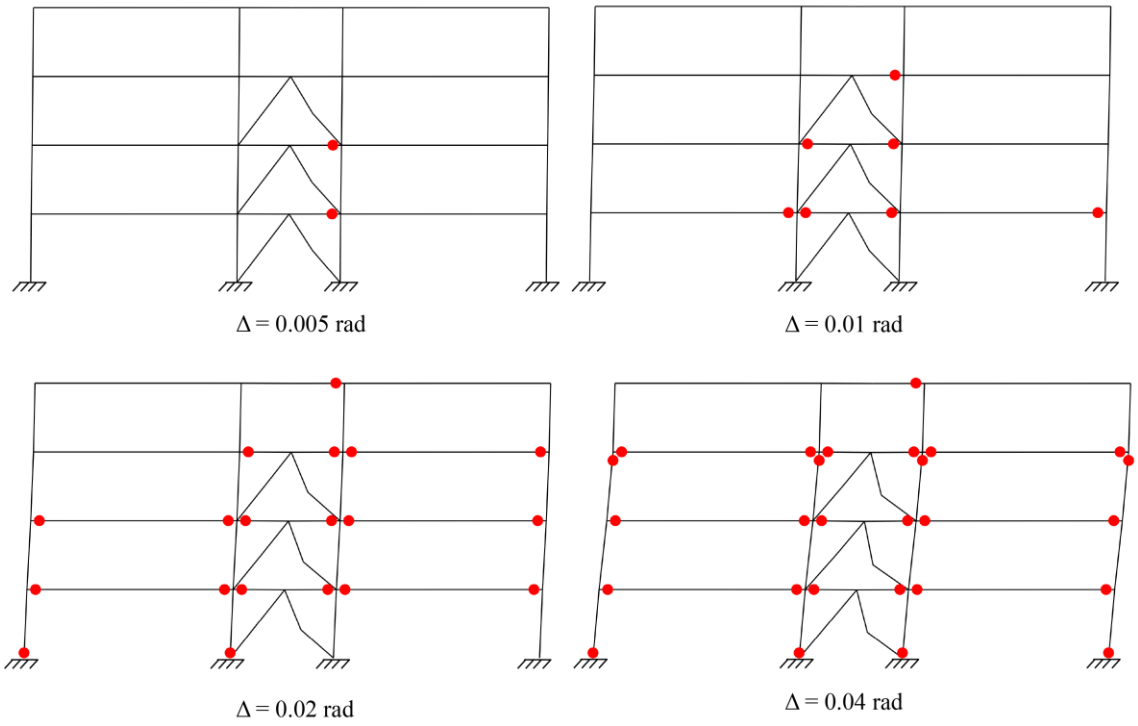

Figure 7.41: Collapse mechanism of the braced frame model designed with Type B with r_0=2.0, employing the flexible bracing connection.

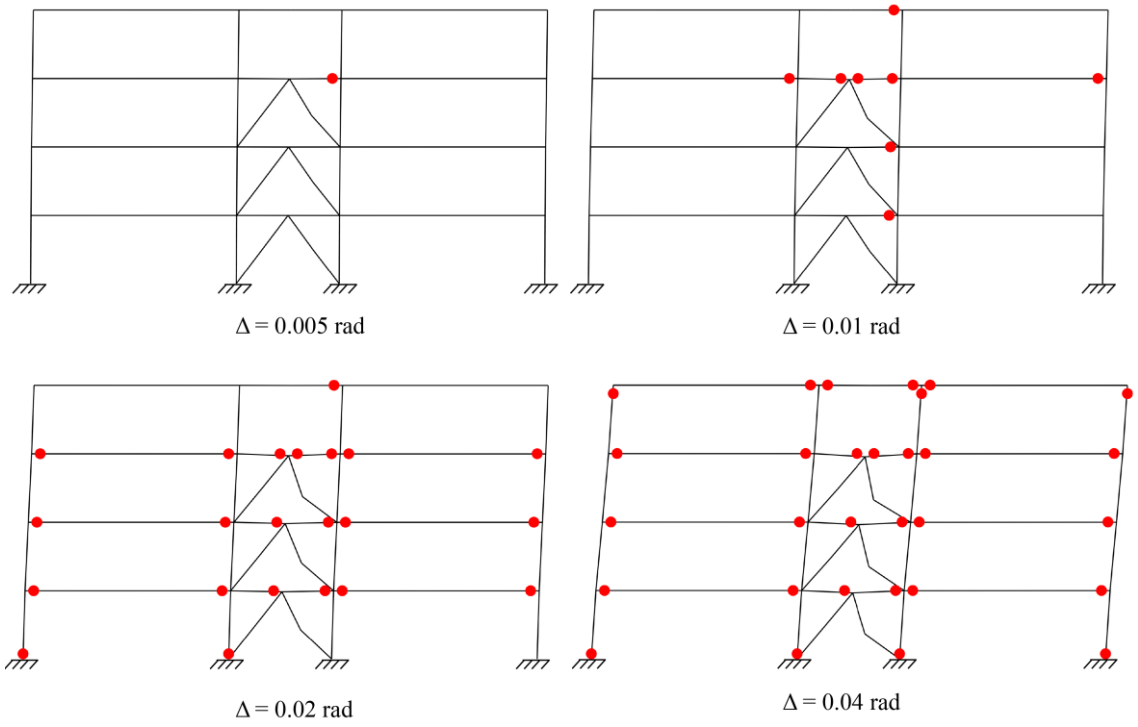

Figure 7.42: Collapse mechanism of the braced frame model designed with Type A with r_0=8.0, employing the flexible bracing connection.

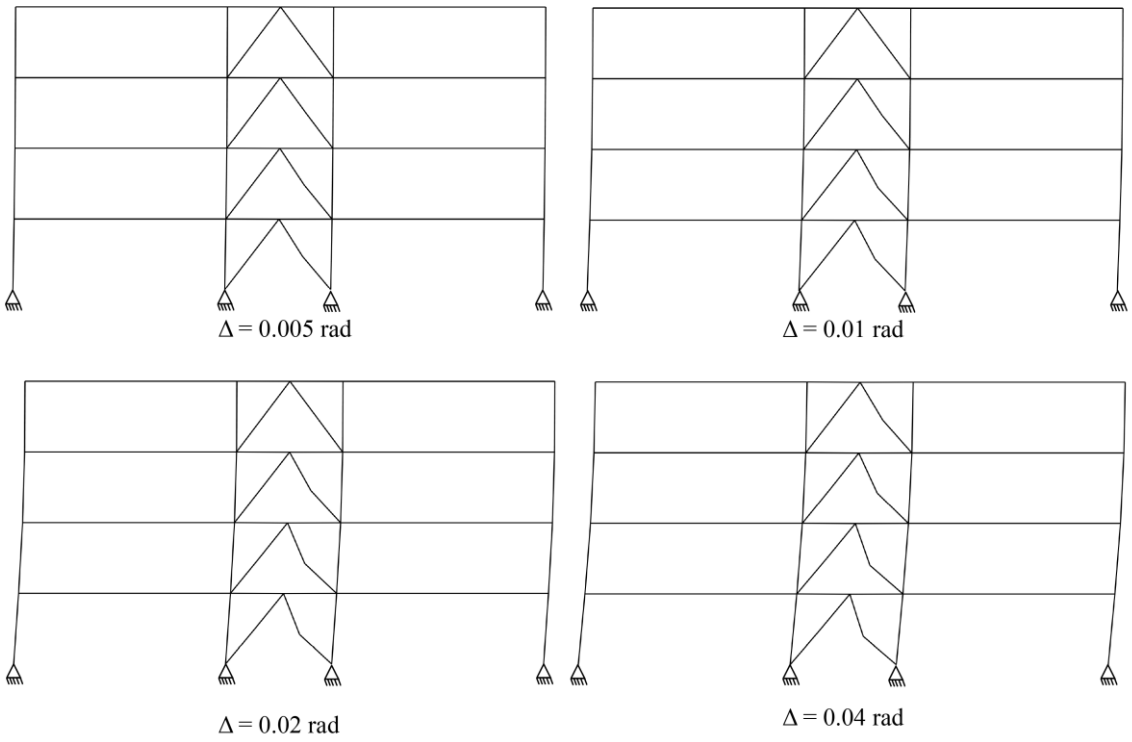

Figure 7.43: Collapse mechanism of the braced frame model designed with Type C, employing the flexible bracing connection.

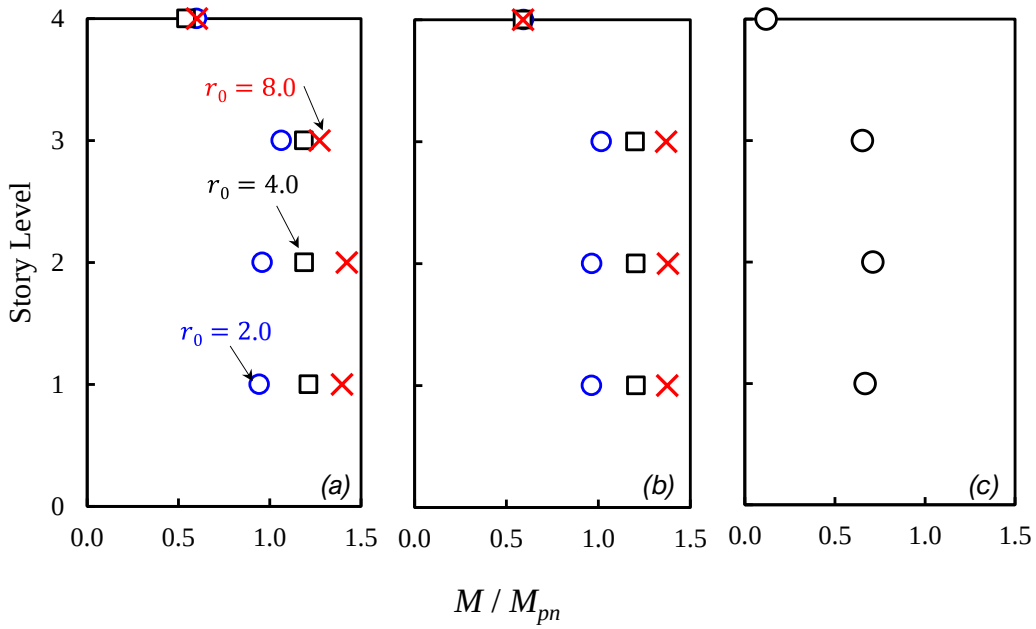

Figure 7.44: Response of the Beam intersected by braces: a) Type A; b) Type B; and c) Type C, all employing the flexible bracing connection.

7.6.2 8-Story Systems

7.6.2.1 Overall Response

Figure 7.45 through Figure 7.51 plots the story shear versus story drift response for all the 8-story chevron-braced frame systems.

For all the braced frame models designed with Type A and B, the story drift concentrated primarily in the bottom 4 stories of the chevron-braced frames, but for Type C, the story drift concentrated in the bottom 3 stories, with the upper stories remaining essentially elastic.

Between Type A and B, Type B led to stronger systems. The maximum normalized story shear Q_{max} over by Q_{un} ranged from 1.26 to 1.74 for the 8-story systems employing the flexible bracing connection. When employing the rigid bracing connection, the braced frame models developed larger lateral strength, with the ratio of the story strength over the design story shear ranging from 1.38 to 1.93.

The braced frame models designed using Type B with r_0 = 8.0 and C developed larger lateral resistance than the predicted plastic capacity. As will be discussed later, the braces developed larger compressive strength than assumed in design.

Similar to the 4-story systems, the braced frame models designed with Type A did not develop their predicted plastic strength, Q_p. For Type A with $r_0 = 2.0$, 4.0 and 8.0, the resistance of the frame at 0.02 roof drift was roughly $0.80Q_p$, $0.82Q_p$, $0.87Q_p$, respectively when employing the flexible bracing connection. When the rigid bracing connection detail was employed, the resistance of the frame at 0.02 roof drift was roughly $0.87Q_p$, $0.93Q_p$, Q_p, for $r_0 = 2.0$, 4.0 and 8.0 respectively.

On the other hand, Type B with $r_0 = 4.0$ and 8.0 and Type C develop larger lateral resistance than the predicted plastic strength. For Type B with $r_0 = 8.0$ and Type C, the resistance of the frame was roughly $1.31Q_p$, and $1.20Q_p$, respectively when employing the flexible bracing connection, and $1.46Q_p$, and $1.67Q_p$, respectively when employing the rigid bracing connection.

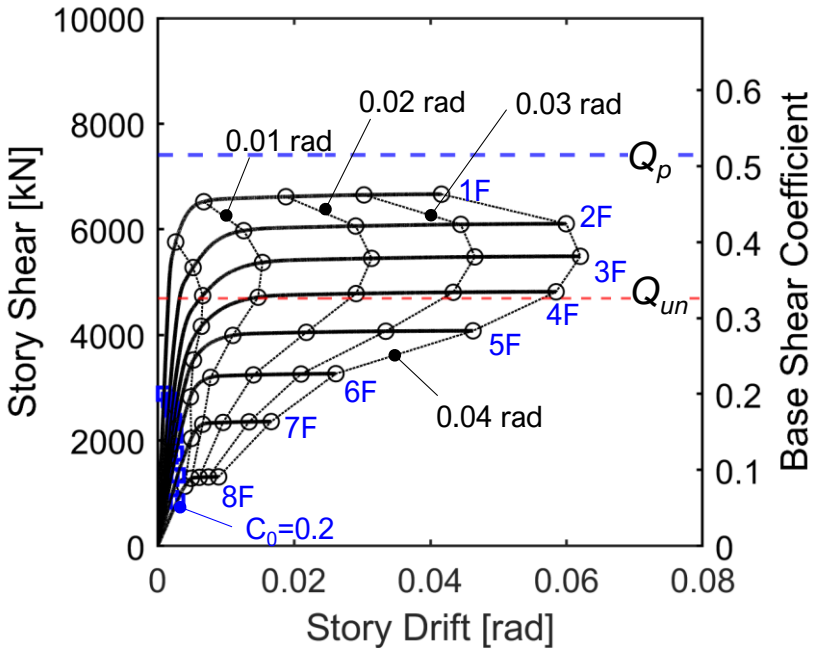

Figure 7.45: Pushover Response of braced frame model designed using with Type A with r_0=2.0, employing the flexible connection.

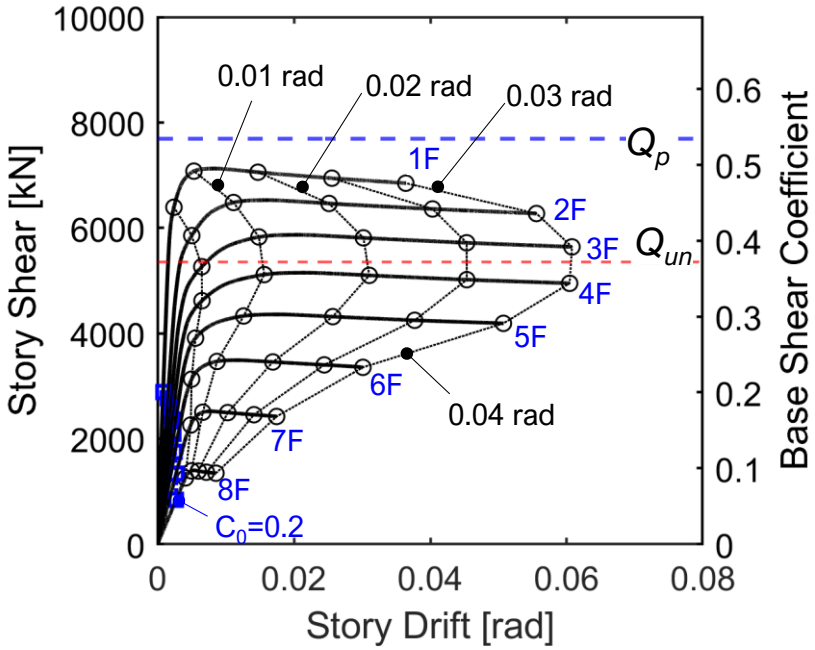

Figure 7.46: Pushover Response of braced frame model designed using with Type A with r_0=4.0, employing the flexible connection.

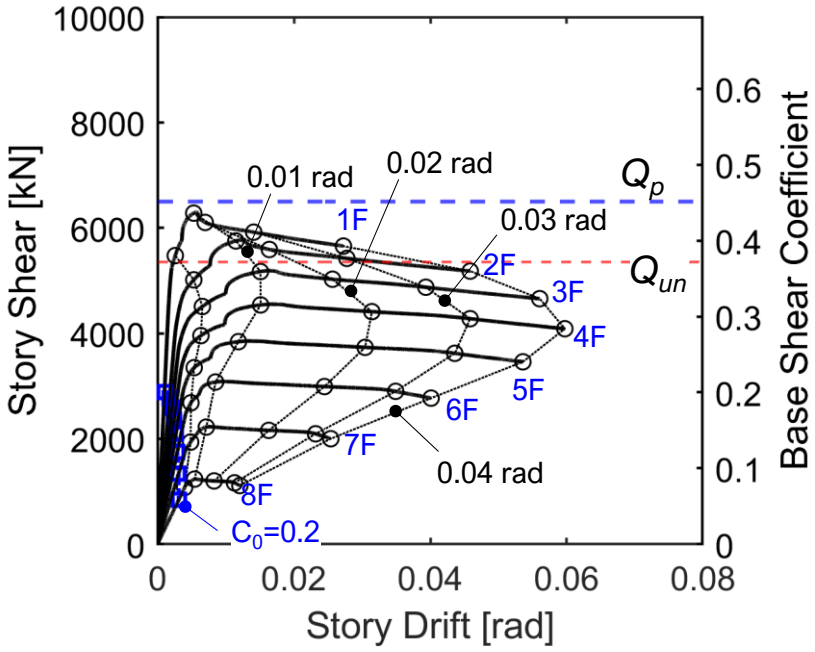

Figure 7.47: Pushover Response of braced frame model designed using with Type A with r_0=8.0, employing the flexible connection.

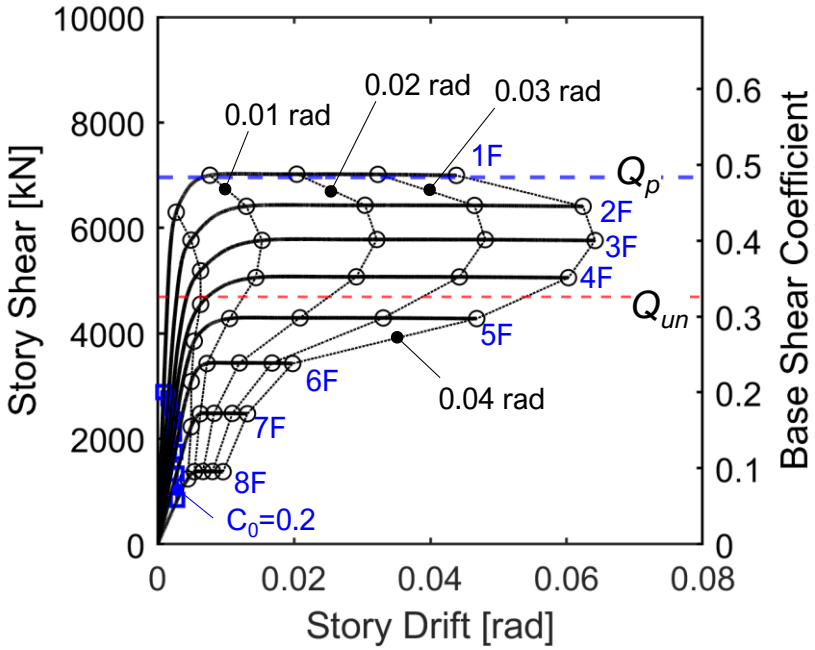

Figure 7.48: Pushover Response of braced frame model designed using with Type B with r_0=2.0, employing the flexible connection.

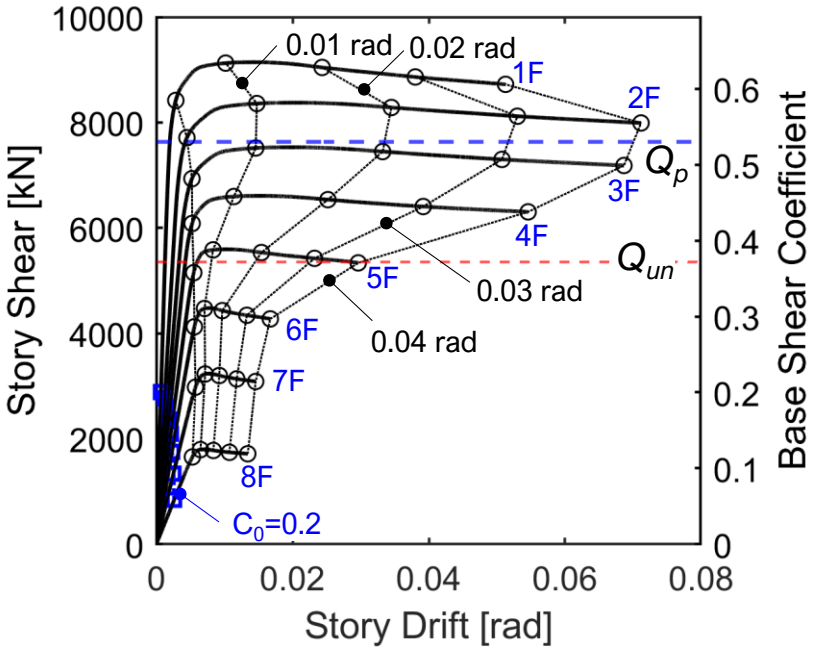

Figure 7.49: Pushover Response of braced frame model designed using with Type B with r_0=4.0, employing the flexible connection.

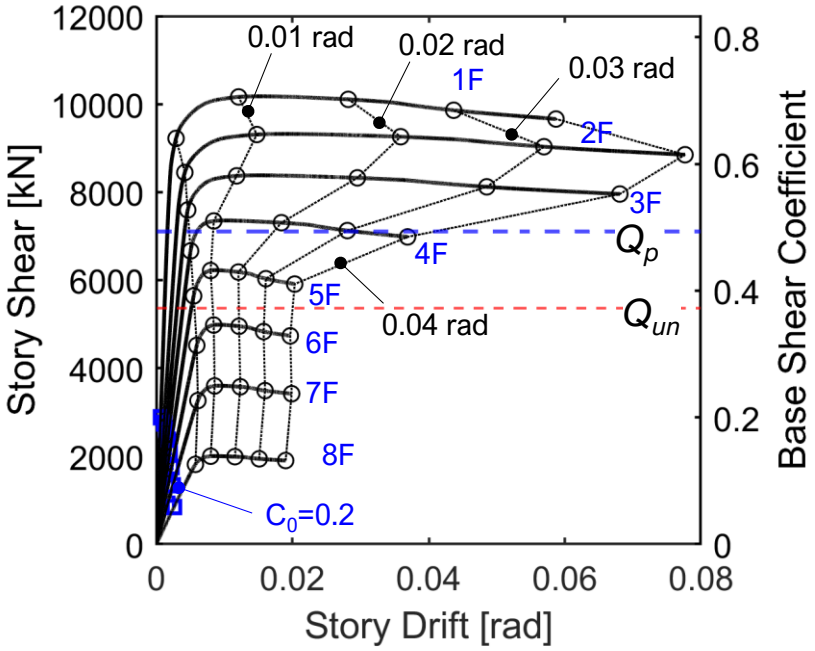

Figure 7.50: Pushover Response of braced frame model designed using with Type B with r_0= 8.0, employing the flexible connection.

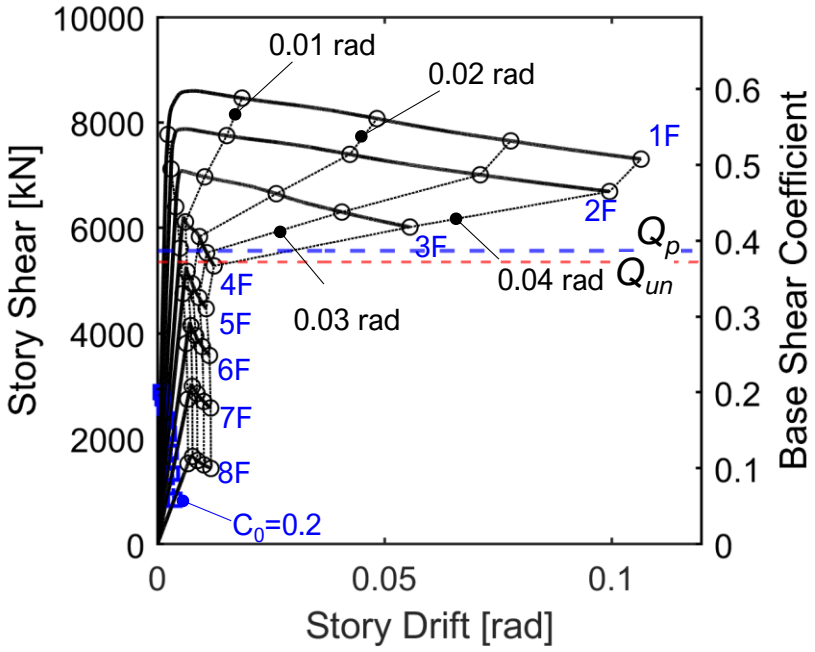

Figure 7.51: Pushover Response of braced frame model designed using with Type Cs, employing the flexible connection.

Table 7.11: Pushover Analysis response: 8-story chevron-braced MRF employing the flexible connection.

Design	r_0	L/r	Q_{max}	Q_{max}/Q_{un}	Q_b/Q, 0.02 rad	Mechanism
Type A	2.0	45-88	5926	1.27	0.42	SB
	4.0	41-88	6278	1.17	0.52	SB
	8.0	46-75	5655	1.06	0.66	WB
Type B	2.0	46-104	6489	1.39	0.41	SB
	4.0	29-89	8472	1.59	0.62	WB
	8.0	32-77	9316	1.74	0.87	WB
Type C	-	21-41	8542	1.60	1.0	SB

Notes: WB – Weak-beam mechanism; SB – Strong-Beam mechanism
CM – Combined Mechanism

7.6.2.2 Brace Response

A sample of the brace response shown in Figure 7.52. As observed in the 4-story systems, the response of the braces is highly affected by the design approach and the relative strength of the beam with respect to the braces, r_0. During monotonic pushover, the braces on the chevron-braced MRFs designed using design approach Type A and B with r_0=2.0, and Type C, yielded in tension at nealy all

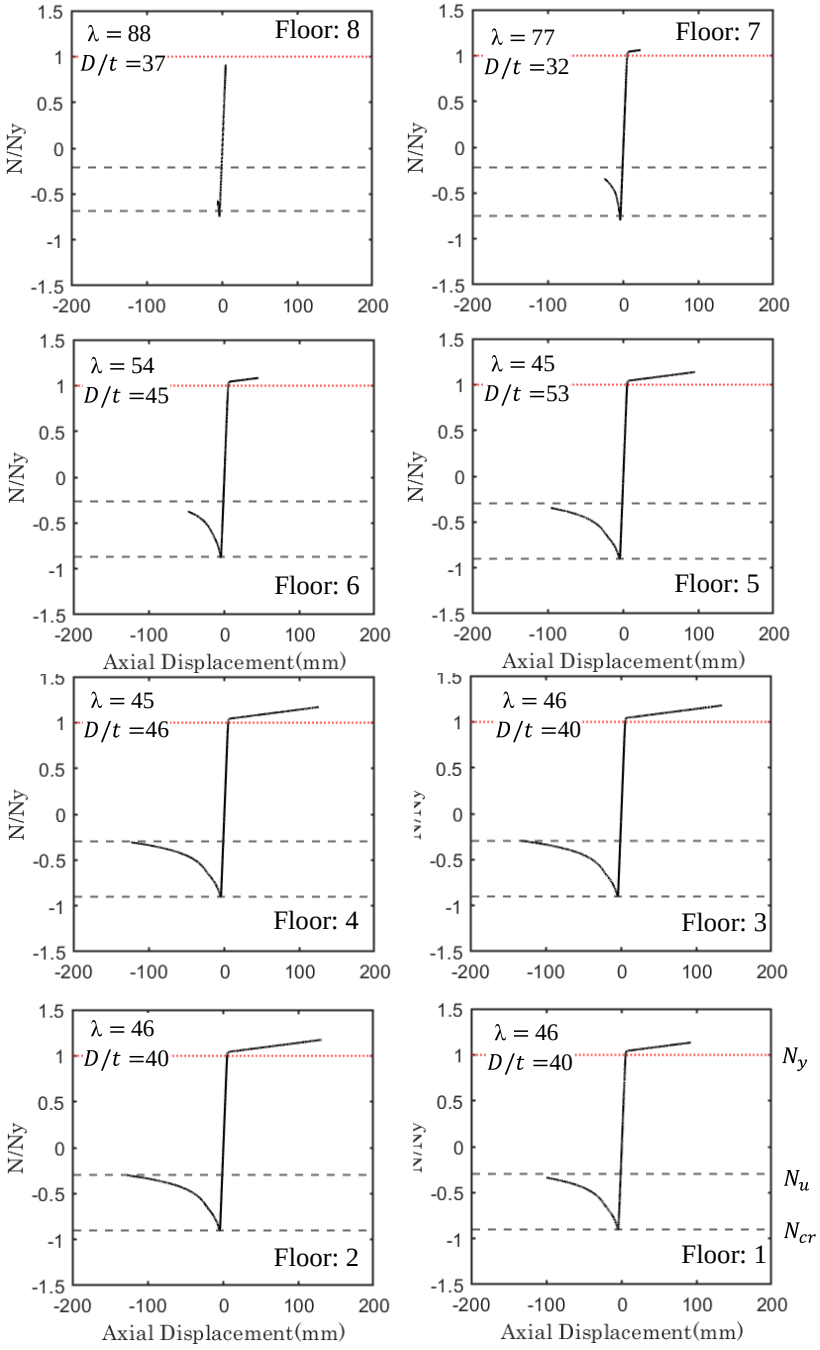

Figure 7.52: Hysteretic response of the braces of Model A with r_0=2.0.

the floor levels and developed large elongation in tension and shortening in compression. For r_0= 4.0 and 8.0, unlike what expected, the braces yielded at the floor levels but the braces developed limited elongation in tension. The compressive strength of the braces decreased to smaller than the $0.3 \times N_{cr}$.

7.6.2.3 Collapse mechanism of the 8-Story chevron-braced frames

The collapse mechanism of the 8-story braced frames systems are depicted in Figure 7.53 through Figure 7.55. The brace response was omited. In the figure, the collapse mechanism of braced frames systems designed using design approach Type B, with $r_0 = 2.0$, was not depicted. As observed in the figure, the inelasticity was concentrated on the bottom six stories, with the two upper stores remaining elastic. Inelastic deamands concentrated at the locations expected from design. For $r_0 = 8.0$, yielding of the beams intersected by the braces occurred for both Type A and B. For Type C, the beams remained elastic as intended from design.

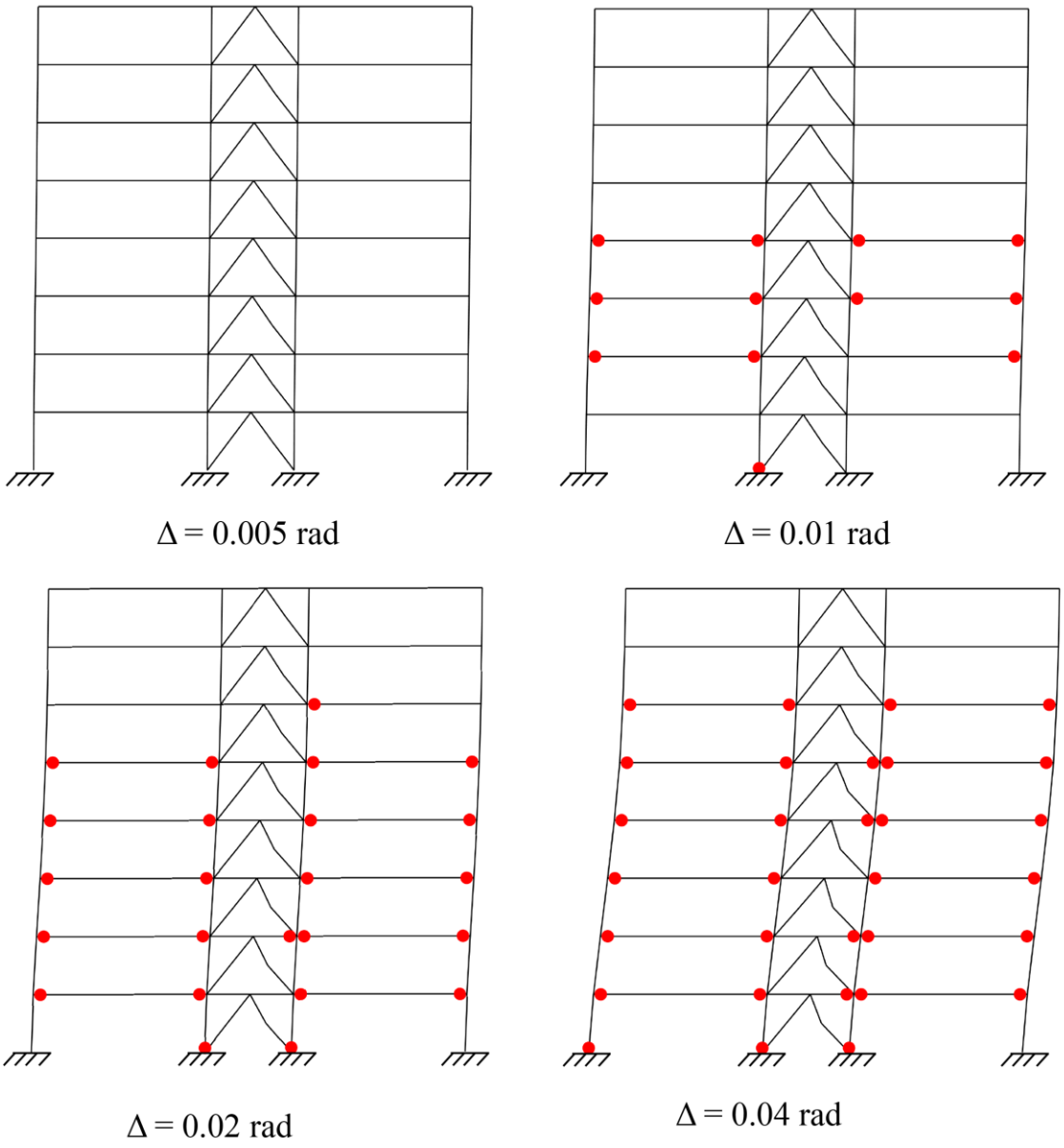

Figure 7.53: Collapse mechanism of the 8-story braced-frame model designed using design approach Type A with r_0=2.0, employing the flexible bracing connection.

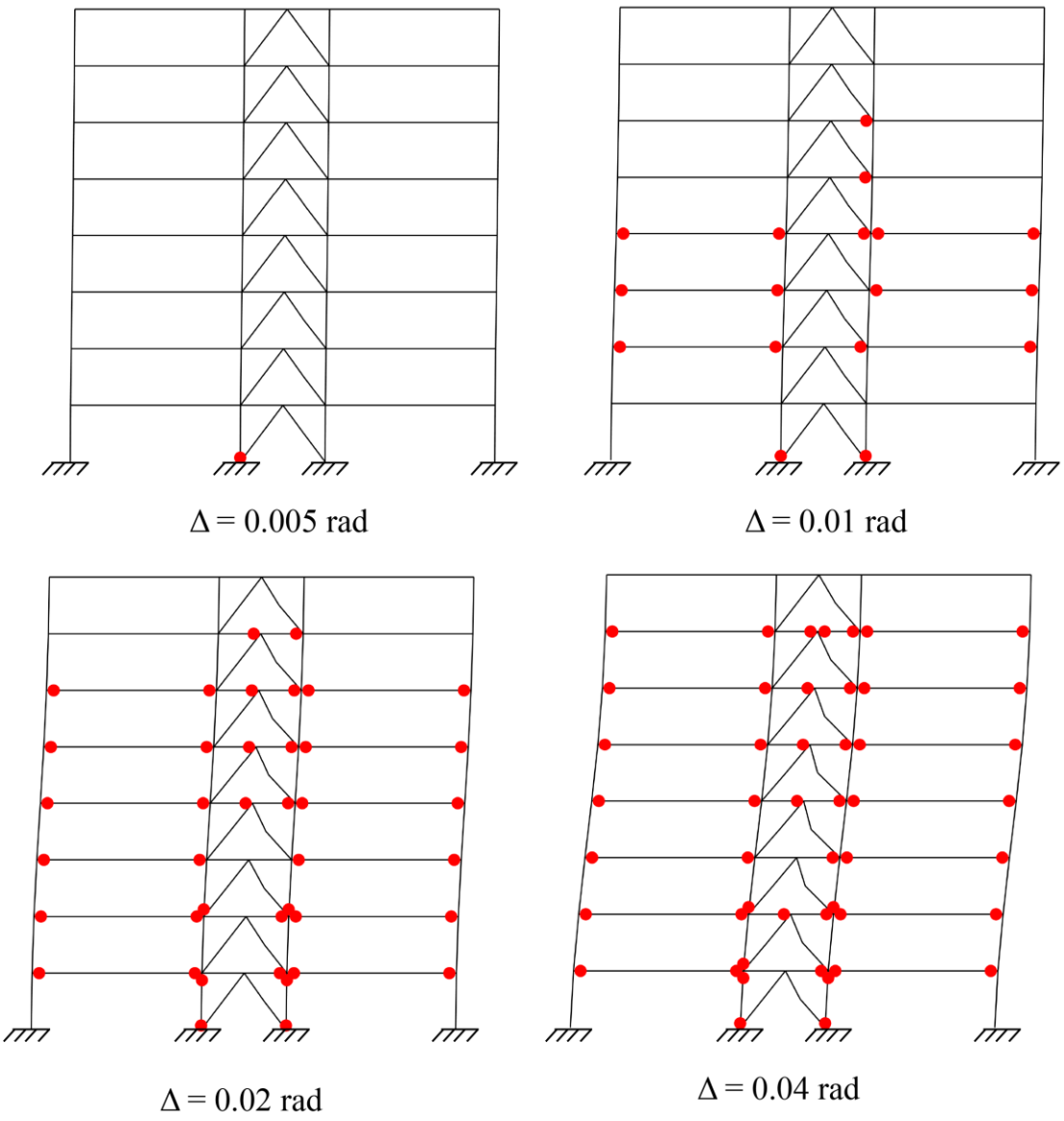

Figure 7.54: Collapse mechanism of the 8-story chevron-braced MRF designed using design approach Type A with r_0=8.0, employing the flexible bracing connection.

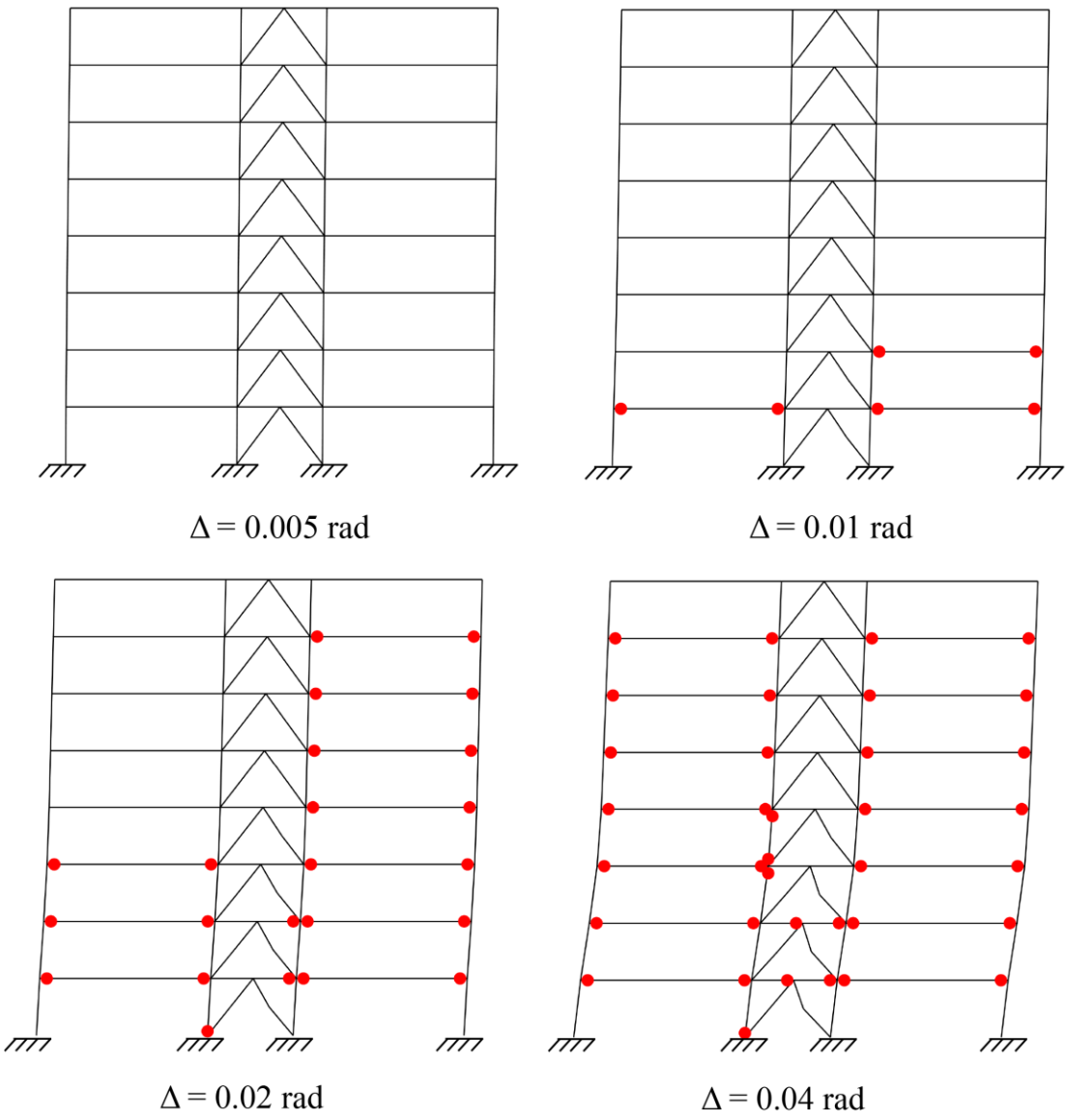

Figure 7.55: Collapse mechanism of the 8-story braced-frame model designed using design approach Type B with r_0=8.0, employing the flexible bracing connection.

7.6.3 12-Story Systems

7.6.3.1 Overall Response

The pushover response of the 12-story braced frames is shown in Figure 7.56 through Figure 7.62. The story drift tended to concentrate at the bottom stories for all the braced frames designed employing either the flexible or rigid connection detail. For the braced frames in Type B with r_0 larger than 4.0 and C, the deformation tended to concentrate at the bottom two or three stories.

The figure shows that all the braced frame models developed large base shear coefficient. The largest base shear coefficient developed for Type C (C_0 = 0.43) followed by Type B r_0 = 8.0 and lastly Type A r_0 = 2.0. For the same r_0, Type B led to stronger base shear coefficient than Type A;

Table 7.12 lists the maximum normalized story shear, Q_{max} over the design story shear Q_{un}, Q_{max}/Q_{un}. As observed Q_{max}/Q_{un} ranged from 1.33 to 1.62 for the braced frame systems employing the flexible connection detail. When employing the rigid bracing connection, the braced frame models developed larger lateral resistance. When employing the rigid bracing connection detail, the overstrength Q_{max}/Q_{un} ranged from 1.44 to 1.68.

Again, the pushover analysis produced similar response between Type A and B for r_0= 2.0 when employing either the flexible or the rigid bracing connection. For r_0 = 4.0 and 8.0, Type B developed 31% and 45% greater lateral resistance than Type A, respectively. The maximum proportion of the lateral strength carried by the braces, Q_b/Q ranged from 0.38 to 0.84, in the braced frame models designed with Type A with r_0 = 2.0 and Type B with r_0 = 8.0, respectively. When employing the rigid bracing connection detail, the ratio Q_b/Q ranged from 0.43 to 0.83, in the Type A with r_0 = 2.0 and Type B with r_0 = 8.0, respectively.

The observation that the braced frame models designed with Type A did not develop their predicted plastic strength, Q_p is consistent for the 12-story systems. For Type A with $r_0 = 2.0$, 4.0 and 8.0, the resistance of the frame at 0.02 roof drift was roughly $0.90Q_p$, $0.87Q_p$, $0.93Q_p$, respectively when employing the flexible bracing connection, but $0.96Q_p$, $0.92Q_p$, $0.92Q_p$ when employing the rigid bracing connection detail.

Type B with $r_0 = 4.0$ and 8.0 and Type C develop larger lateral resistance at 0.02 roof drift than the predicted plastic strength. For Type B with $r_0 = 8.0$ and Type C, the resistance of the frame was close to $1.11Q_p$, and $1.18Q_p$, respectively when employing the flexible bracing connection, and $1.17Q_p$, and $1.54Q_p$, respectively when employing the rigid bracing connection.

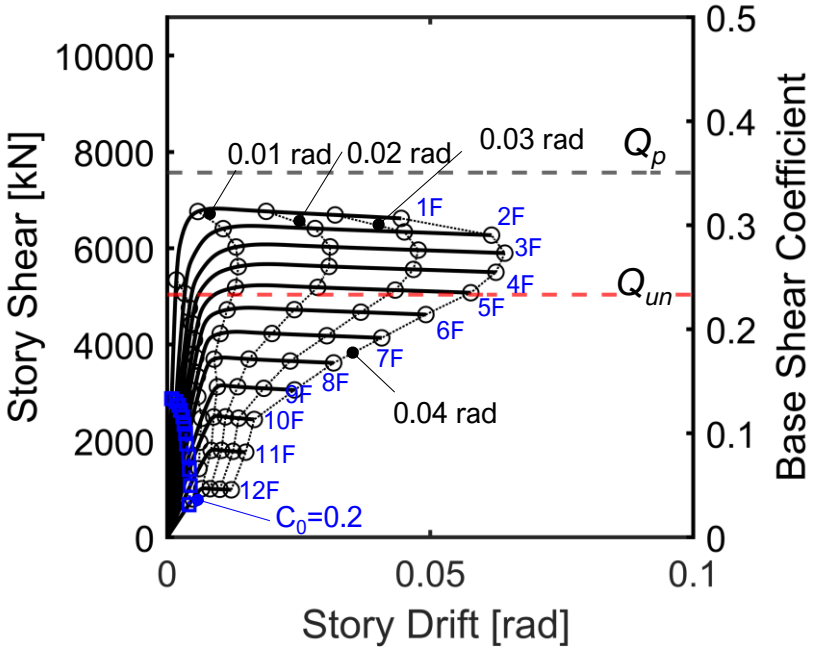

Figure 7.56: Pushover Response of the 12-story braced frame model designed using with Type A with r_0=2.0, employing the flexible connection.

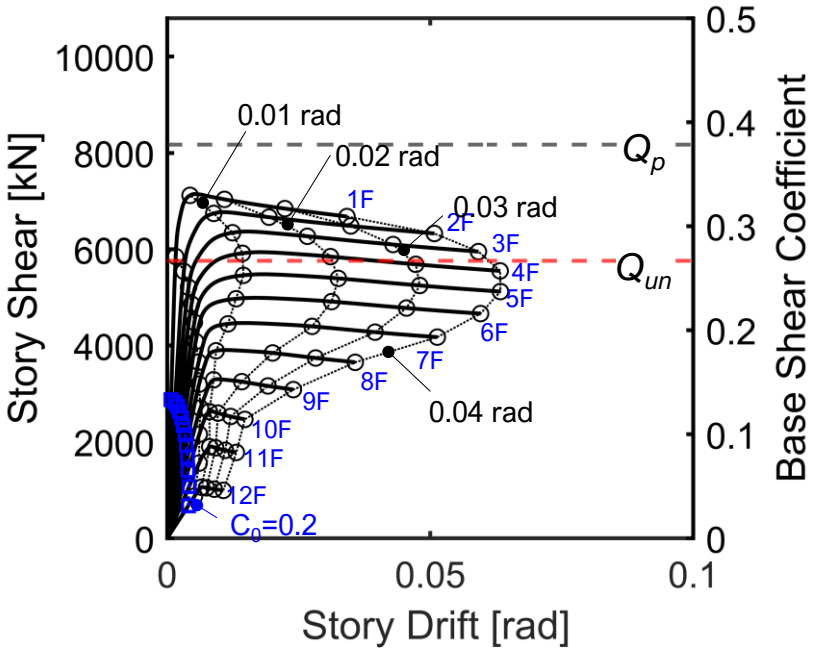

Figure 7.57: Pushover Response of the 12-story braced frame model designed using with Type A with r_0=4.0, employing the flexible connection.

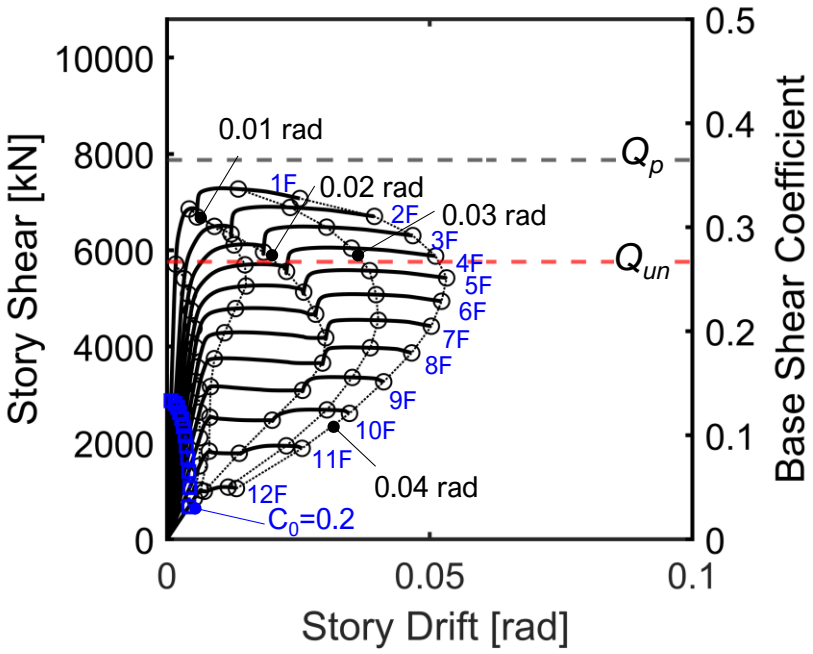

Figure 7.58: Pushover Response of the 12-story braced frame model designed using with Type A with r_0=8.0, employing the flexible connection.

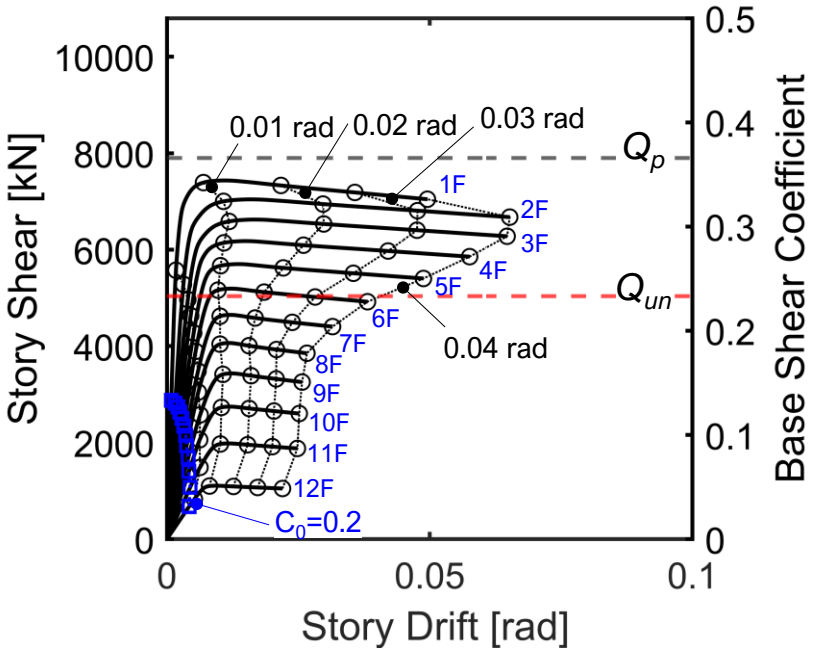

Figure 7.59: Pushover Response of the 12-story braced frame model designed using with Type B with r_0=2.0, employing the flexible connection.

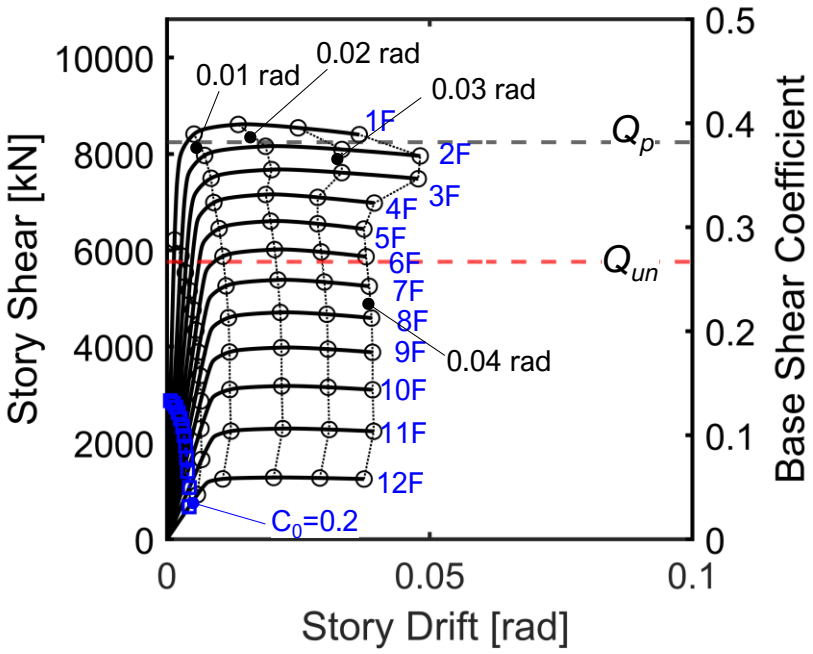

Figure 7.60: Pushover Response of the 12-story braced frame model designed using with Type A with r_0=4.0, employing the flexible connection.

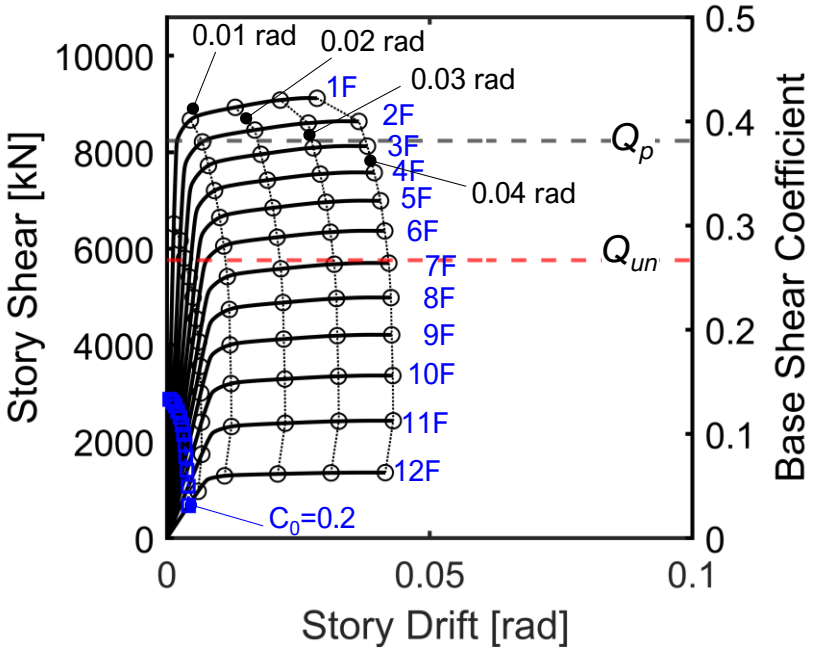

Figure 7.61: Pushover Response of the 12-story braced frame model designed using with Type A with r_0=8.0, employing the flexible connection.

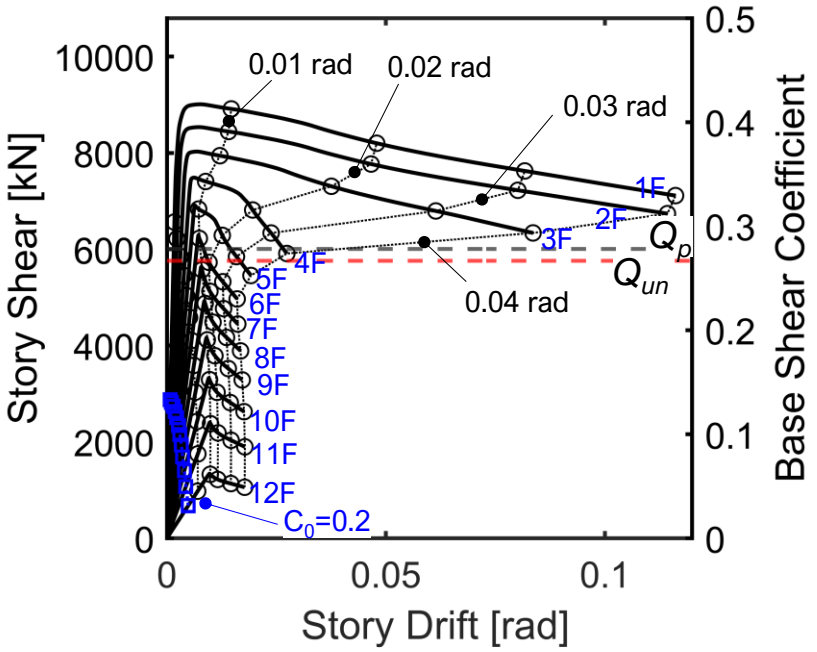

Figure 7.62: Pushover Response of the 12-story braced frame model designed using with Type C, employing the flexible connection.

Table 7.12 lists the computed Q_b/Q sampled at 0.02-rad roof drift for the 12- story systems and the collapse mechanism, strong-beam (SB), weak-beam (WB), or combined mechanism formed at that drift. The Q_b/Q at 0.02 rad was 0.75 for Type A with r_0=8.0, 0.84 for Type B with r_0=8.0.

Table 7.12: Pushover Analysis response: 12-story CBF employing the flexible bracing connection.

Design	r_0	L/r	Q_{max}	Q_{max}/Q_{un}	Q_b/Q 0.02 rad	Mechanism
Type A	2.0	45-129	6703	1.33	0.38	SB
	4.0	41-104	6821	1.18	0.59	SB
	8.0	35-88	6434	1.12	0.75	WB
Type B	2.0	41-127	7316	1.45	0.50	SB
	4.0	26-76	8953	1.55	0.78	WB
	8.0	29-77	9352	1.62	0.84	WB
Type C	-	24-54	8673	1.51	1.0	SB

Notes: WB – Weak-beam mechanism; SB – Strong-Beam mechanism
CM – Combined Mechanism

7.6.3.2 Collapse mechanism of the 12-Story chevron-braced frames

Figure 7.63 to Figure 7.65 shows the collapse mechanism of the braced frames at different target roof drift levels for Model A with r_0=2.0, A with r_0=8.0, and B with r_0=8.0. Here, for the sake of simplicity the collapse mechansim of Model B with r_0=2.0 and 4.0 are omitted. For Model A with r_0=2.0 inelasticity was concentrated at the ends of the beams and in the braces through yielding and buckling (not depicted in the figures). Plastic hinge at the inner columns occurred by Δ = 0.01rad at the bottom of the frame and spread throughout the height with increasing roof drift.

For Model A with r_0=8.0, inelasticity occurred at both the braces, beams, and columns. Yielding at the center of the beam intersecting braces occurred by the end of Δ = 0.02 rad drift, at the intermediate stories, which were submitted to the largest drift demands. By the end of the simulation, signifficant yielding occurred at the columns. The braced frame in Model B with $r_0 = 8.0$ showed improved performance compared to Type A with r_0=2.0. Here, the beams in the chevron-braced beam remained elastic, with the bending moment at the mid-span of the beam intersecting the braces growing up to 0.95M_p. For Type C, the beams remained elastic as intended from design.

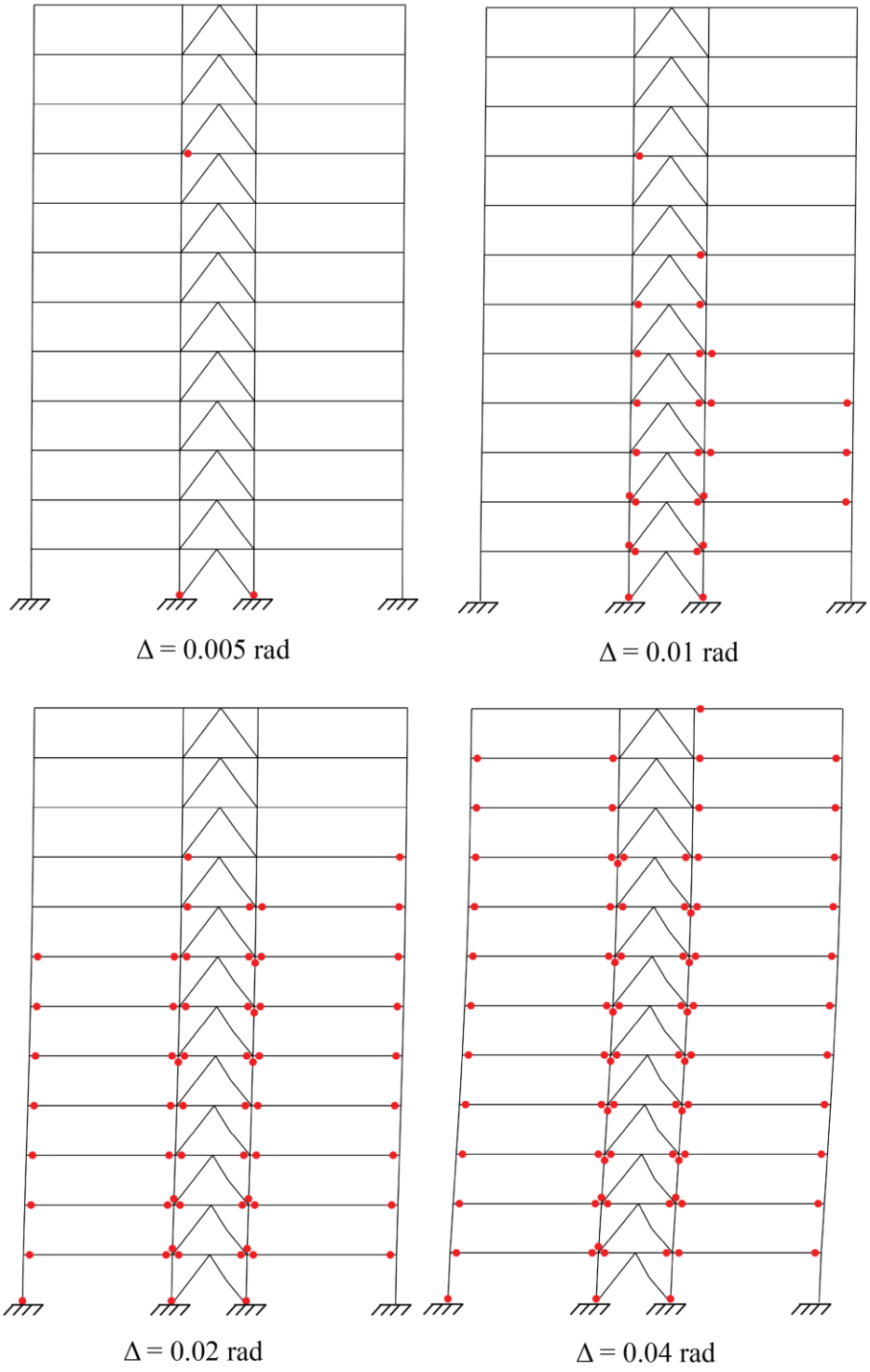

Figure 7.63: Collapse mechanism of the 12-story CBF model designed using design approach Type A with r_0=2.0, employing the flexible bracing connection.

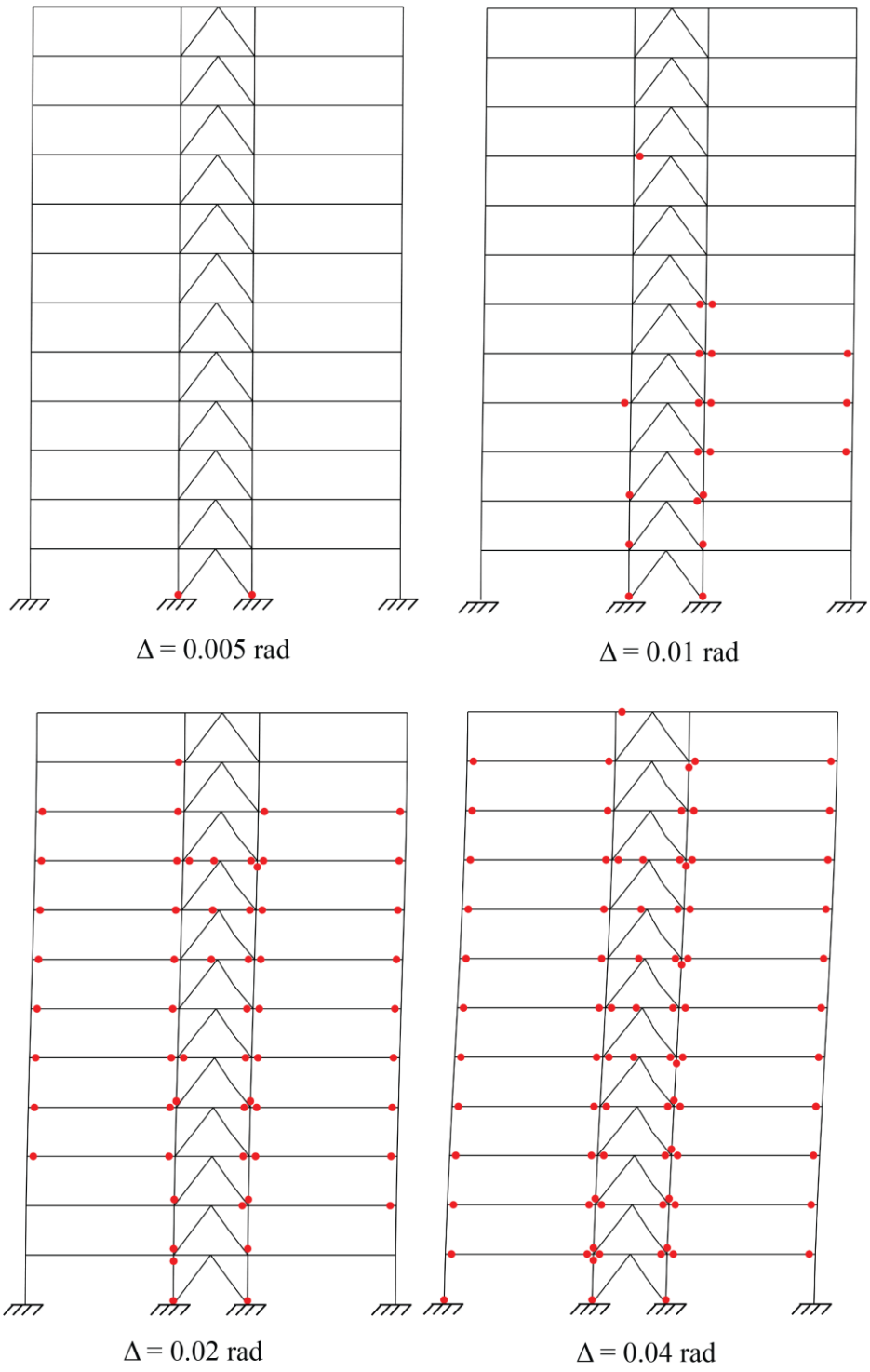

Figure 7.64: Collapse mechanism of the 12-story CBF model designed using design approach Type A with r_0=8.0, employing the flexible bracing connection.

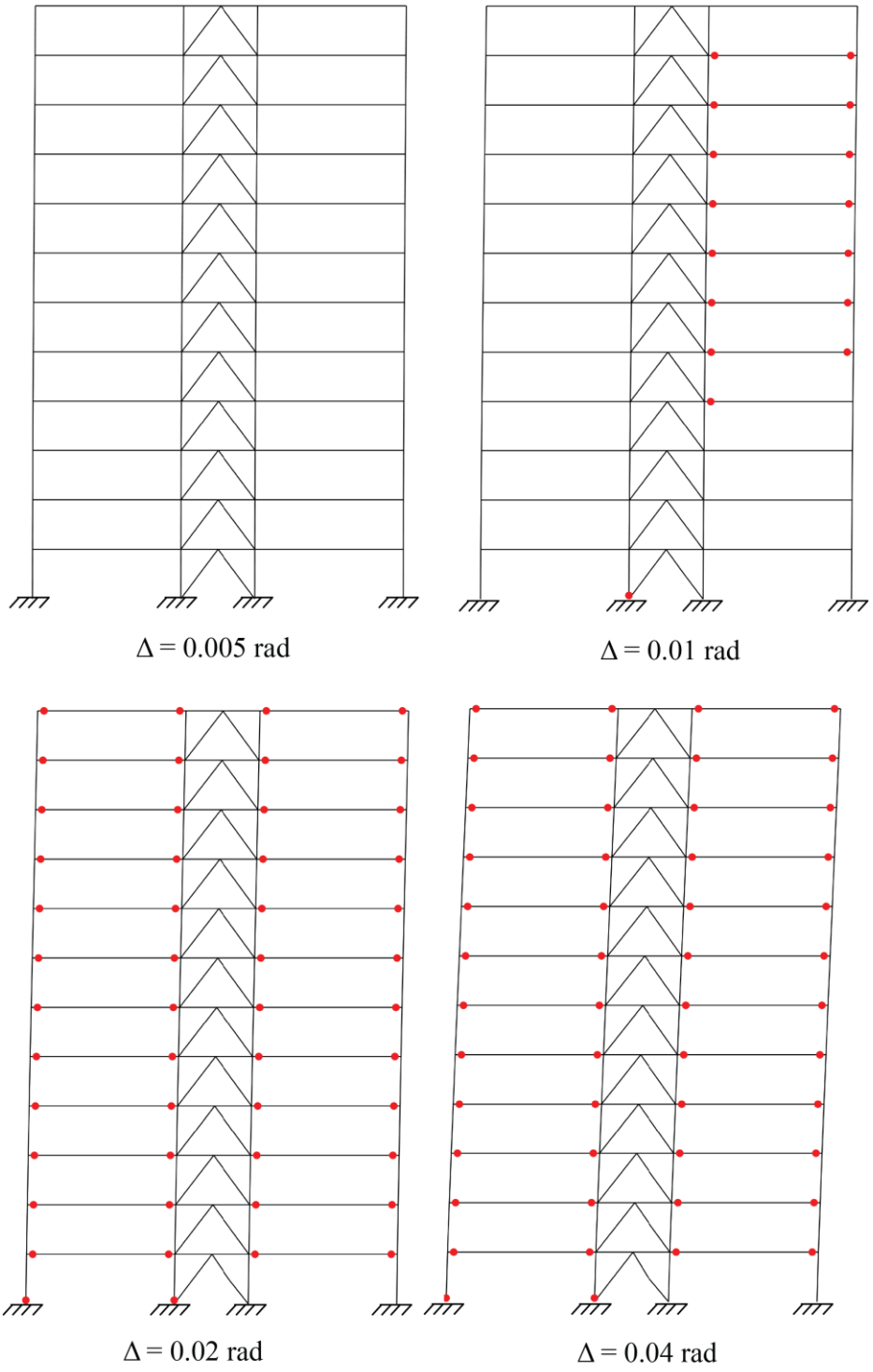

Figure 7.65: Collapse mechanism of the 12-story CBF model designed using design approach Type B with r_0=8.0, employing the flexible bracing connection.

7.7 Nonlinear Time History Analysis

This section discusses the time-history analysis response of the braced frame systems when subjected to the ground motion suit scaled for both Level-2 and Level-3. The responses of interest are the peak story drift and story shear response for all combinations of r_0 and design approach, either A, B, or C, and for the two bracing connections considered.

7.7.1 4-Story Systems

Figure 7.66 and Figure 7.67 shows the story-shear distribution over the height of the 4-story systems. The design base shear and the plastic strength are superimposed. As observed in the figures, all the braced frame models developed larger story shear than the design base shear. When employing the flexible bracing connection, except at the first story, the median story shear exceeded the plastic strength of the braced frame at all the stories. Table 7.13 summarizes the peak story shear and the normalized median peak story shear for all the structural systems under Level-2 demands, employing the flexible and rigid bracing connection, respectively.

All the braced frame systems developed large normalized median peak base shear, with the normalized median peak base shear ranging from 1.39 to 1.80 for the flexible bracing connection and 1.56 to 1.89, for the rigid bracing connection. From all the braced frame specimens, the braced frame designed using design approach A with r_0 = 8.0 developed the smallest lateral resistance, and story shear coefficient than all the other braced frame systems. In contrast, the CBF system designed according to the US specification developed the largest lateral resistance.

For both bracing connection details, the normalized median peak story shear was identical between design approach A and B, with r_0 = 2.0, but for r_0 = 4.0 and 8.0, design approach B led to stronger braced frame systems. The normalized median peak story shear of the braced frames designed with design approach B was roughly 15% and 33% stronger than Type A for r_0 = 4.0 and 8.0, respectively.

The braced frame designed with larger r_0 values were stronger than their counterparts. For design approach B, r_0 = 8.0 over r_0 = 2.0, was 18% larger when employing the flexible bracing connection detail, but the braces frames designed with smaller r_0 values developed larger normalized median base shear. This can be justified because for the braced frames with large r_0 values, beam yielding was permitted, and the braces deformed primarily in compression.

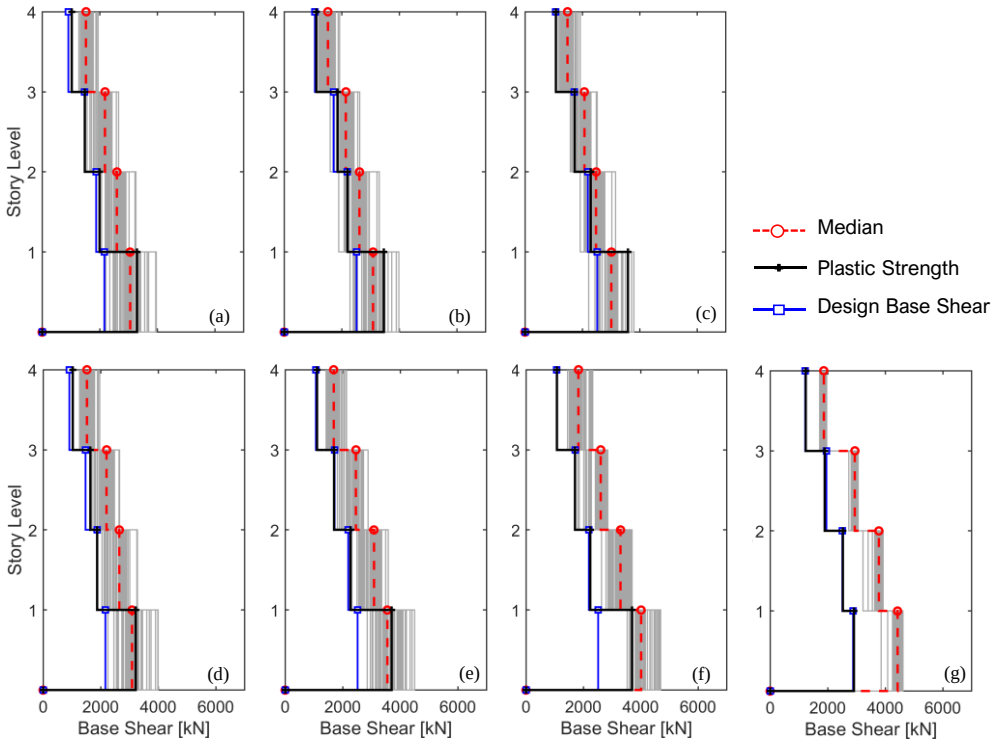

Figure 7.66: Distribution of the peak story shear for the 4-story Models: (a) A with $r_0 = 2.0$, (b) A with $r_0 = 4.0$, (c) A with $r_0 = 8.0$, (d) B with $r_0 = 2.0$, B with $r_0 = 4.0$, (f) B with $r_0 = 8.0$, and (g) C, under level-2 employing the flexible bracing connection.

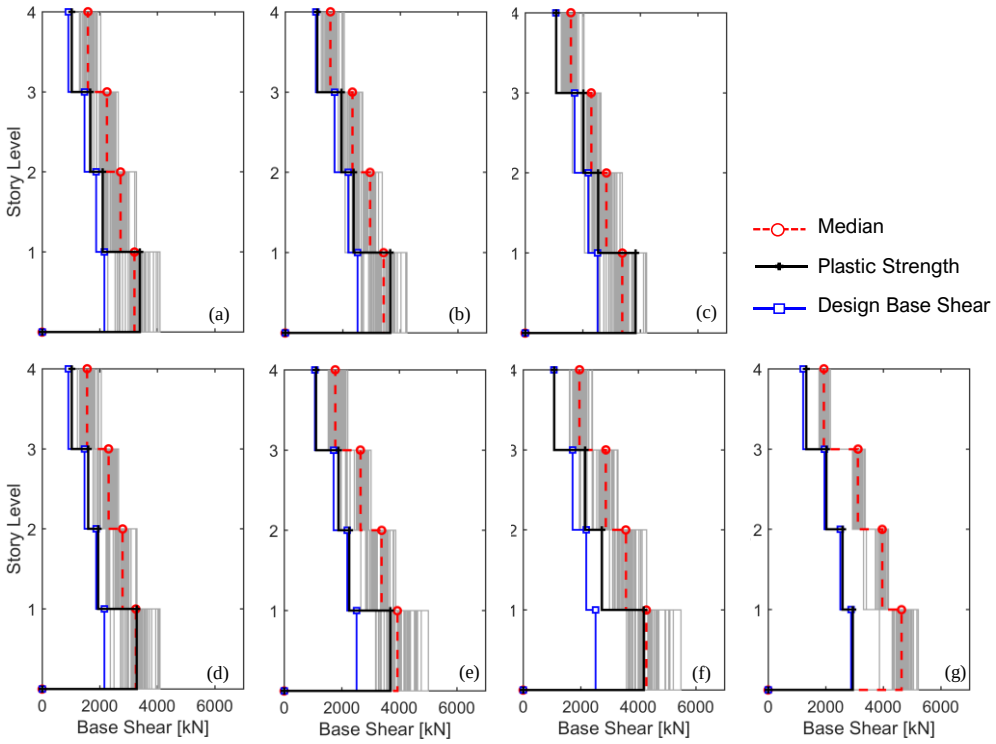

Figure 7.67: Distribution of the peak Story shear for the 4-story Models: (a) A with $r_0 = 2.0$, (b) A with $r_0 = 4.0$, (c) A with $r_0 = 8.0$, (d) B with $r_0 = 2.0$, B with $r_0 = 4.0$, (f) B with $r_0 = 8.0$, and (g) C, under level-2 employing the flexible bracing connection.

Table 7.13: Median base shear demands under Level II ground motions.

Design Approach	r_0	β_0	Flexible Connection		Rigid Connection	
			Q_{max} [kN]	Q_{max}/Q_{un}	Q_{max} [kN]	Q_{max}/Q_{un}
Type A	2.0	0.55	3052	1.67	3205	1.74
	4.0	0.73	3087	1.43	3419	1.48
	8.0	0.85	3011	1.39	3374	1.49
Type B	2.0	0.55	3085	1.67	3254	1.72
	4.0	0.83	3546	1.58	3931	1.67
	8.0	0.87	4012	1.72	4277	1.84
Type C	-	1.0	4424	1.54	4631	1.61

The rigid bracing connection led to stronger braced frame systems. This is more evident for the braced frame systems employing large r_0 values, because these braced frames used braces with smaller slenderness ratio and thus the effect of bracing connection becomes more significant. The largest increase in story shear, up to 12%, occurred on the braced frame model designed using Type A with r_0 = 8.0.

Figure 7.68 to Figure 7.71 shows the distribution of the peak story drift over the height of the building for all the braced frame employing the flexible and the rigid bracing connection detail. The median and 84th percentile values are highlighted in the figures. The story drift tended to concentrate at the second story for all the braced frames designed using design approach A and B, for both bracing connections. Such response was expected because the design procedure explicitly proportioned the first story with greater surplus strength compared to the second story. In contrast for the CBF designed using design approach C, the story drift was largest at the first story.

Under Level-2 ground motions, except for a few ground motions, the peak story drift was within the 5% rad for all the braced frame systems. Notably, the systems designed with design approach C were subjected to relatively smaller drift demands, within 4% rad.

Although the distribution of the story drift is similar for design approach A for all the r_0 values, the median and 84th percentile of the peak story drift shows that the braced frame designed using large r_0 values had a more uniform distribution of the story drift demands. Similar observation was observed for design approach type B, where, as observed in the figure, there was a uniform distribution of the drift over the height of the frame. Between all the systems, Type C showed a more uniform distribution of story drift demand over the height of the building, which is more evident by examining the 84th percentile.

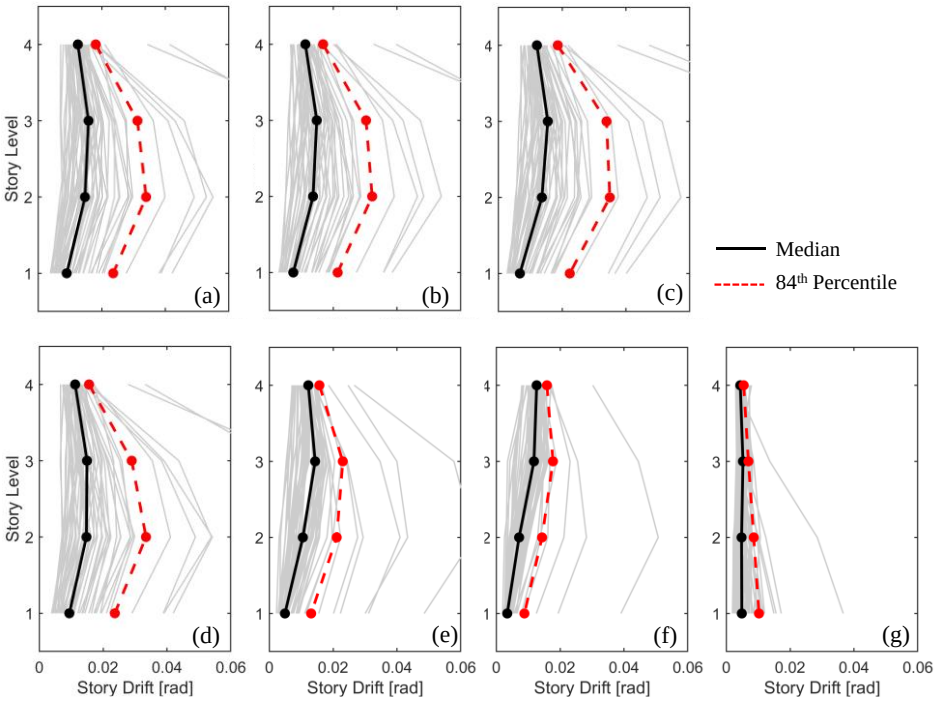

Figure 7.68: Distribution of the peak Story drift for systems: (a) A with $r_0 = 2.0$, (b) A with $r_0 = 4.0$, (c) A with $r_0 = 8.0$, (d) B with $r_0 = 2.0$, B with $r_0 = 4.0$, (f) B with $r_0 = 8.0$, and (g) C, under level-2 ground motions, employing the flexible bracing connection.

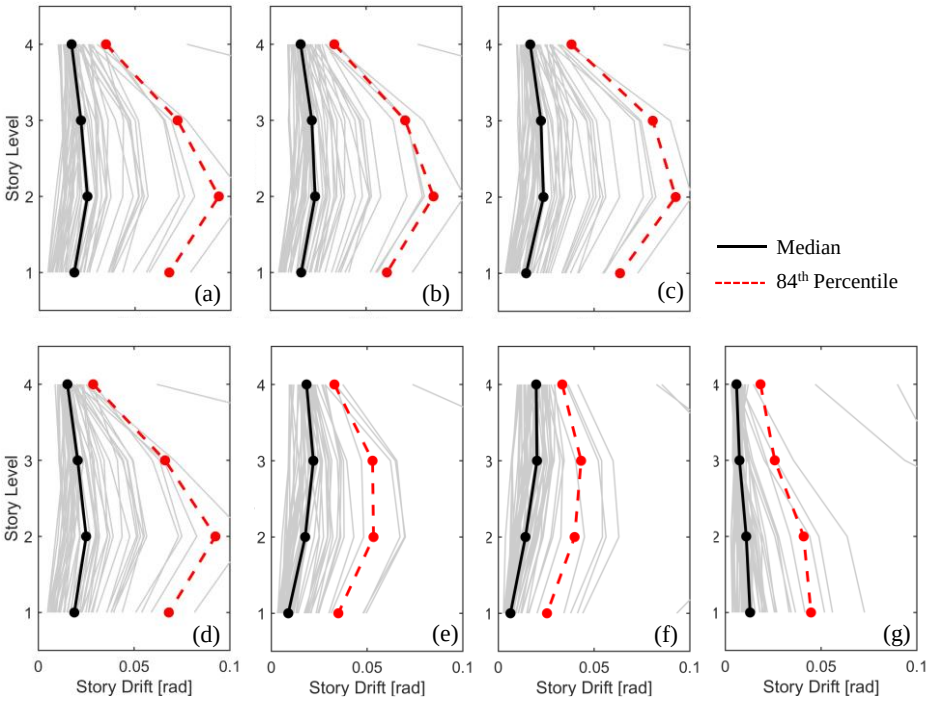

Figure 7.69: Distribution of the peak Story drift for the 4-story braced-frame systems: (a) A with $r_0 = 2.0$, (b) A with $r_0 = 4.0$, (c) A with $r_0 = 8.0$, (d) B with $r_0 = 2.0$, B with $r_0 = 4.0$, (f) B with $r_0 = 8.0$, and (g) C, under level-3 ground motions, employing the flexible bracing connection.

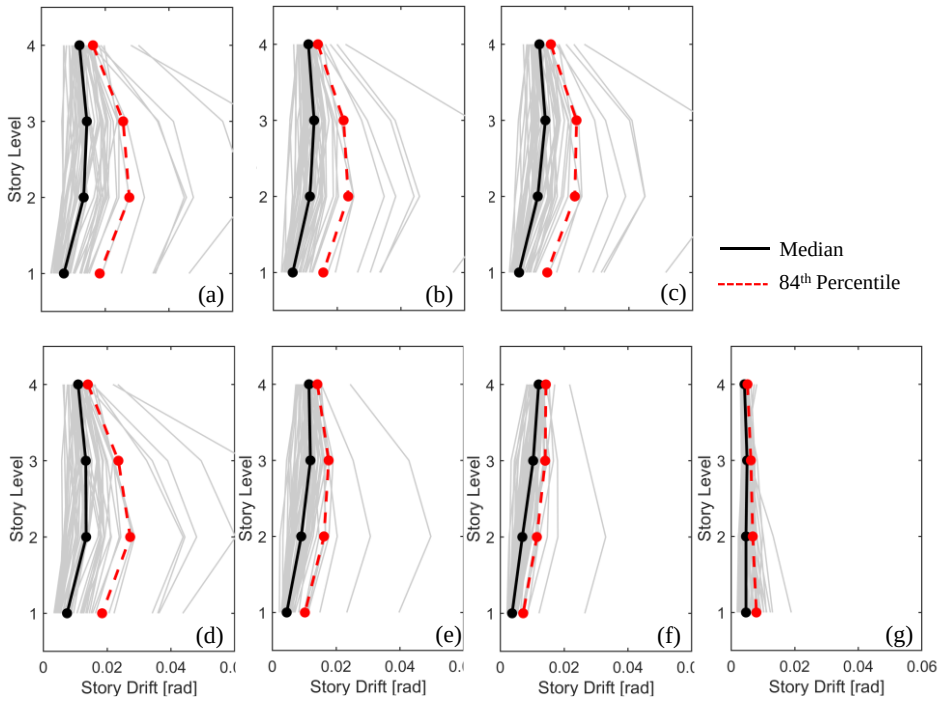

Figure 7.70: Distribution of the peak story drift for Model: (a) A with $r_0 = 2.0$, (b) A with $r_0 = 4.0$, (c) A with $r_0 = 8.0$, (d) B with $r_0 = 2.0$, B with $r_0 = 4.0$, (f) B with $r_0 = 8.0$, and (g) C, under level-2 ground motions, employing the rigid bracing connection;

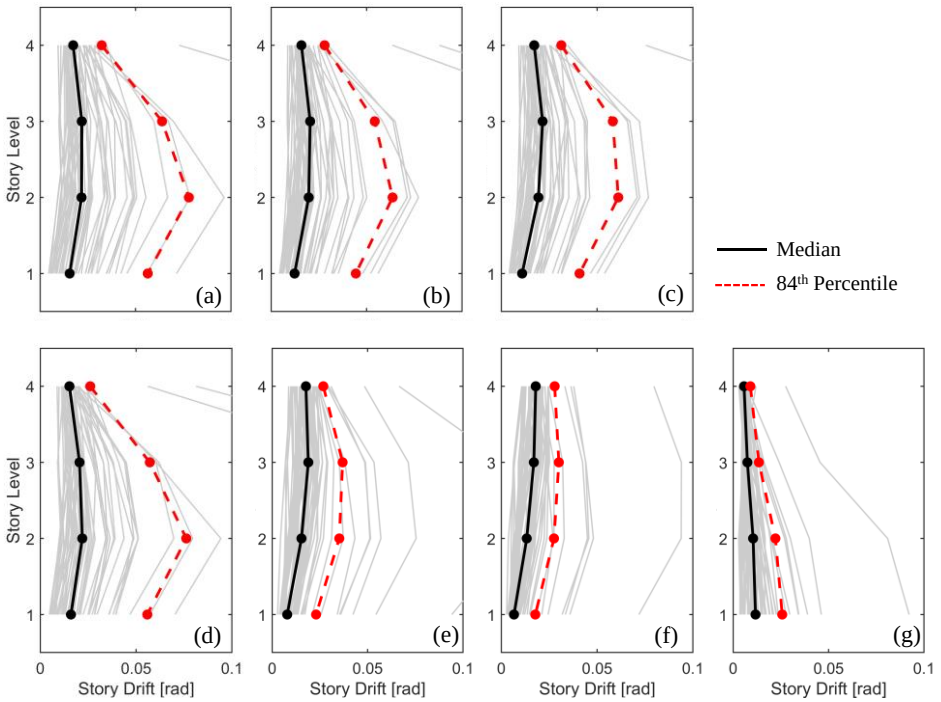

Figure 7.71: Distribution of the peak Story drift for the 4-story braced-frame systems: (a) A with $r_0 = 2.0$, (b) A with $r_0 = 4.0$, (c) A with $r_0 = 8.0$, (d) B with $r_0 = 2.0$, B with $r_0 = 4.0$, (f) B with $r_0 = 8.0$, and (g) C, under level-3 ground motions, employing the rigid bracing connection;

Under Level-3 ground motions, the braced frames were subjected to significantly larger drift demands. Again, for the braced frames designed using design approach A and B, the peak story drift concentrated at the second story, whereas for Type C the story drift concentrated at the bottom story. The structures designed with design approach Type C were subjected to relatively smaller drift demands.

The braced frame systems using rigid bracing connection were subjected to smaller μ- story-drift demands compared to the flexible bracing connection: 15%, 14%, and 3% for the structural systems designed according to design approach A and B with r_0=4.0, and Type C, respectively, under Level-2 ground motions and 11%, 13%, and 10% for Level-3 ground motions, for design approach A and B with r_0=4.0, and Type C, respectively.

Figure 7.72 plots the response of the braces for ground motion that led to the largest story-drift demands, Chi-Chi Taiwan (GM#26). The figure plots the response of the north and south braces. As observed in the figure, the response of the north brace was accurately modelled, but the south braces developed larger compressive strength than predicted. This because the frame was subjected to large unidirectional stroke, forcing buckling of the north brace and yielding of the south brace. Because the south brace is stretched in tension, the initial out-of-straightness of the brace is removed. Upon load reversal, due to the absence of imperfection, the brace develops larger buckling strength than the opposing brace and the prediction.

For both design approach A and B with r_0 =2.0, the braces deformed in both tension and compression. As expected, the braces yielded in tension and their ultimate compressive strength decrease after buckling. For $r_0 = 4.0$ and 8.0, the braces deformed primarily in compression, developing limited elongation in tension regardless of the design approach. Unlike what expected from design, the braces yielded in tension due to the large unidirectional stroke, characteristic of near-field ground motions.

Under the Chi-Chi Taiwan ground motions, the compressive strength of the braces reduced to smaller than the $0.3 \times N_{cr}$ assumed in design for all the chevron-braced frame models, except for Model B with $r_0 = 4.0$ and 8.0 and Model C.

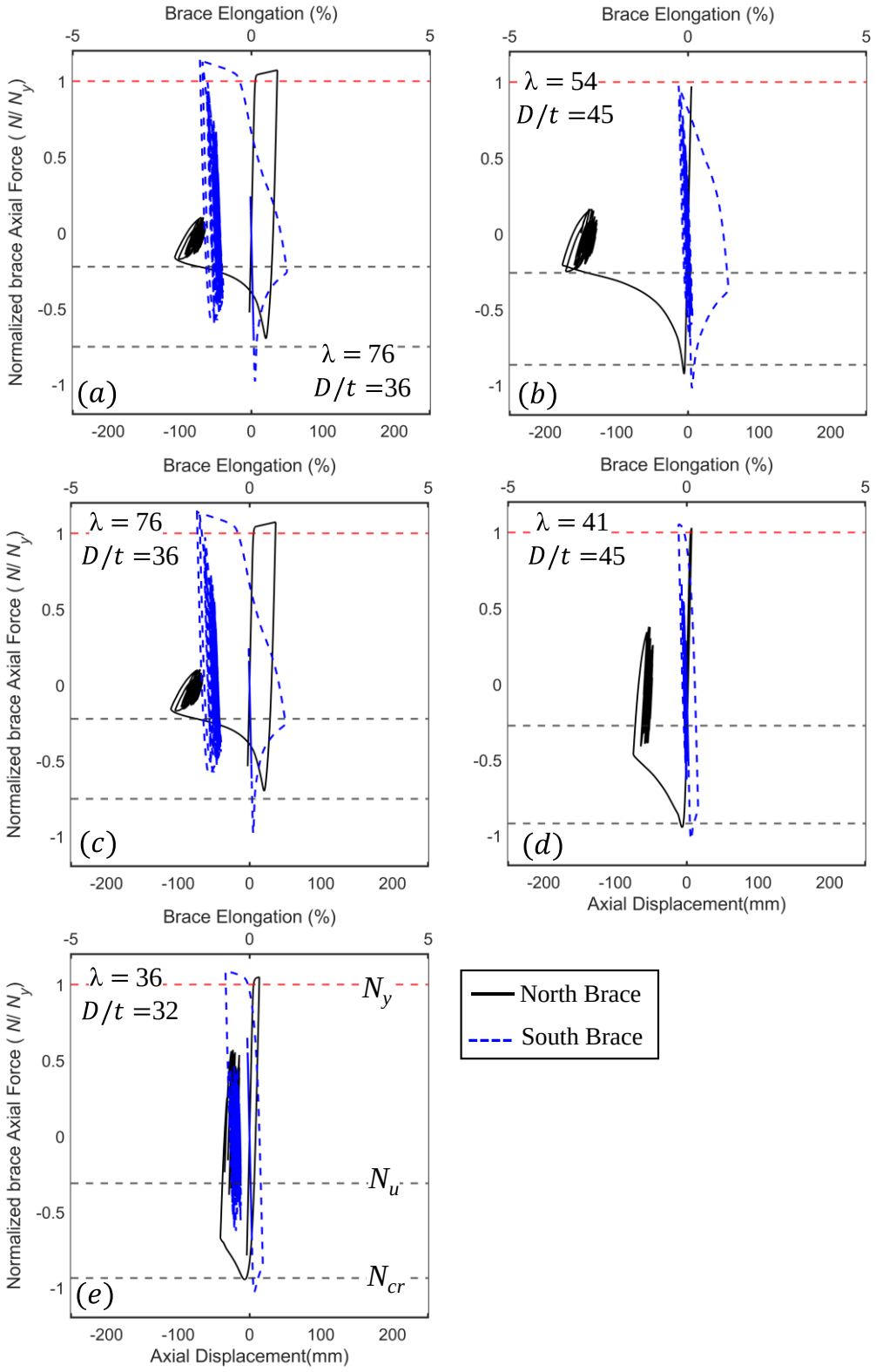

Figure 7.72: First Story brace response: (a) Type A with r_0= 2.0; (b) Type A with r_0= 8.0; (c) Type B with r_0= 2.0; (d) Type B with r_0= 8.0; and (e) Type C, all under Level-2 demands, employing bracing connection I.

7.7.1.1 Decomposed response

The lateral strength of the braced frame at each story level was decomposed into the contribution of the pair of braces and the MRFs (interior and exterior MRF). Figure 7.73 plots the decomposition of the lateral resistance for the first story. The reference lines indicate the predicted resistance of the braces (introduced in chapter 3), H_{2b} and the lateral resistance of the MRF, H_{2f}. The figure shows that for the braced frame models designed with design approach Type A and B with r_0 =

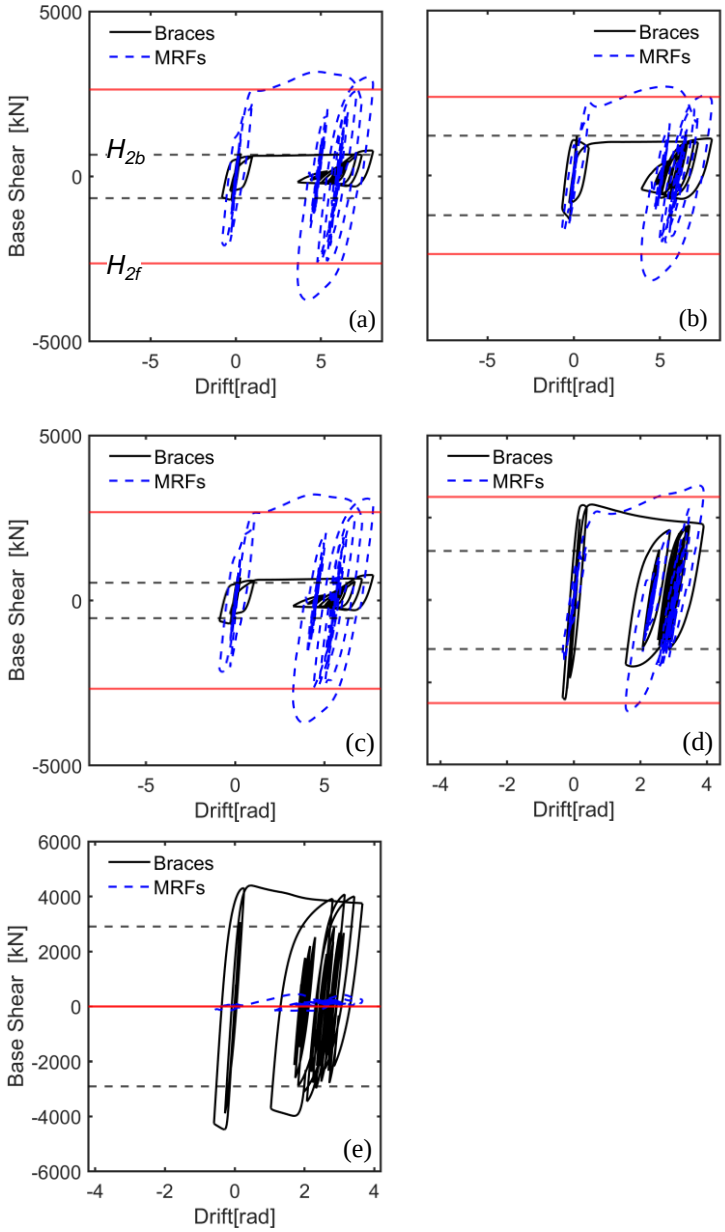

Figure 7.73: Lateral strength decomposition for the first story: (a) Type A with r_0= 2.0; (b) Type A with r_0= 8.0; (c) Type B with r_0= 2.0; (d) Type B with r_0= 8.0; and (e) Type C, all under level-2 ground motions, employing bracing connection I.

2.0, the resistance of the pair of braces matched the predicted strength derived from the pair of braces, but the lateral resistance of the MRF was slightly larger.

For design approach B with r_0 = 4.0, and 8.0, and Type C, (models employing large braces), the lateral resistance derived from the pair of braces exceeded the predicted strength of the braces, because as observed in Figure 7.72, the compressive strength of the braces did not reduce to the $0.3 \times N_{cr}$ assumed in design, after buckling of the braces.

7.7.2 8-Story Systems

Figure 7.74 to Figure 7.75 plots the story shear distribution over the height of the braced frames. The design base shear and the plastic strength are superimposed on the figures. As observed in the figures, all the braced frame models developed larger strength than the design bases shear, for bracing connections. When employing the flexible bracing connection, except at the first story, the median story shear exceeded the plastic strength of the braced frame for all the stories.

Table 7.14 lists the peak base shear and the normalized median peak base shear for all the structural systems under ground motion Level II for both bracing connection details. The braced frames models developed large normalized median peak base shear ranging from 1.09 to 1.72 and 1.25 to 1.87 for the flexible bracing connection, and the rigid bracing connection detail, respectively.

As observed for the 4-story systems, from all the braced frame specimens, the braced frame designed using design approach type A with r_0 = 8.0 developed the smaller lateral strength and base shear coefficient.

For the 8-story, for both bracing connections, the normalized median peak base shear was identical between design approach Type A and B, with r_0 = 2.0. For r_0 = 4.0 and 8.0, design approach Type B led to larger normalized median peak base shear: 13% and 32 for r_0 = 4.0 and 8.0, respectively.

The structural systems designed with larger r_0 values were stronger than their counterparts. For design approach Type A and B, r_0 = 8.0 over r_0 = 2.0, was 2% and 44% for the braced frame systems employing the flexible bracing connection detail and 3% and 38 % for the braced frame systems employing the rigid bracing connection. For design approach A, the braces frames with smaller r_0 values developed larger normalized median base shear, however for design approach B, the braces frames with larger r_0 values developed larger normalized median base shear, for both bracing connections.

As observed in the table, the rigid bracing connection detail led to stronger braced frame systems than the flexible bracing connection, and hence the models developed larger normalized base

shear.

The distribution of the peak story drift response for the 8-story systems is shown in Figure 7.74 to Figure 7.79, for all combinations of design approach and r_0 values, when employing both bracing connections subjected to level-2 and level-3 ground motions.

As observed in the plots, for all the cases designed using design approach Type A, the story drift tended to concentrate at the bottom stories. Similarly, for design approach type B, the story drift tended to concentrate at the bottom stories for $r_0 = 2.0$ but for the chevron-braced frame models designed with large r_0 values, there was a uniform distribution of the story drift over the height of the building. For Type C, the story drift distribution of the tended to concentrate at the top of the building.

When subjected to level-3 ground motions, the braced frames were subjected to larger story drift demands, but the distribution over the height was similar as to the level-2 ground motions.

The rigid bracing connection led to stronger braced frame systems, and hence the braced frames systems were subjected to smaller story drift demands.

The 8-story braced frames are subjected to considerably smaller story drift demands than the 4-story systems.

Table 7.14: Median base shear demands for the 8-story systems under Level II ground motions.

Design Approach	r_0	β_0	**Flexible Bracing Connection**		**Rigid bracing Connection**	
			Q_{max} [kN]	Q_{max}/Q_{un}	Q_{max} [kN]	Q_{max}/Q_{un}
Type A	2.0	0.55	6493	1.43	6737	1.49
	4.0	0.73	6861	1.28	7107	1.34
	8.0	0.85	6123	1.14	6303	1.18
Type B	2.0	0.55	6850	1.52	7186	1.62
	4.0	0.83	8827	1.66	9035	1.74
	8.0	0.87	9837	1.85	10038	1.93
Type C	-	1.0	8732	1.63	8847	1.67

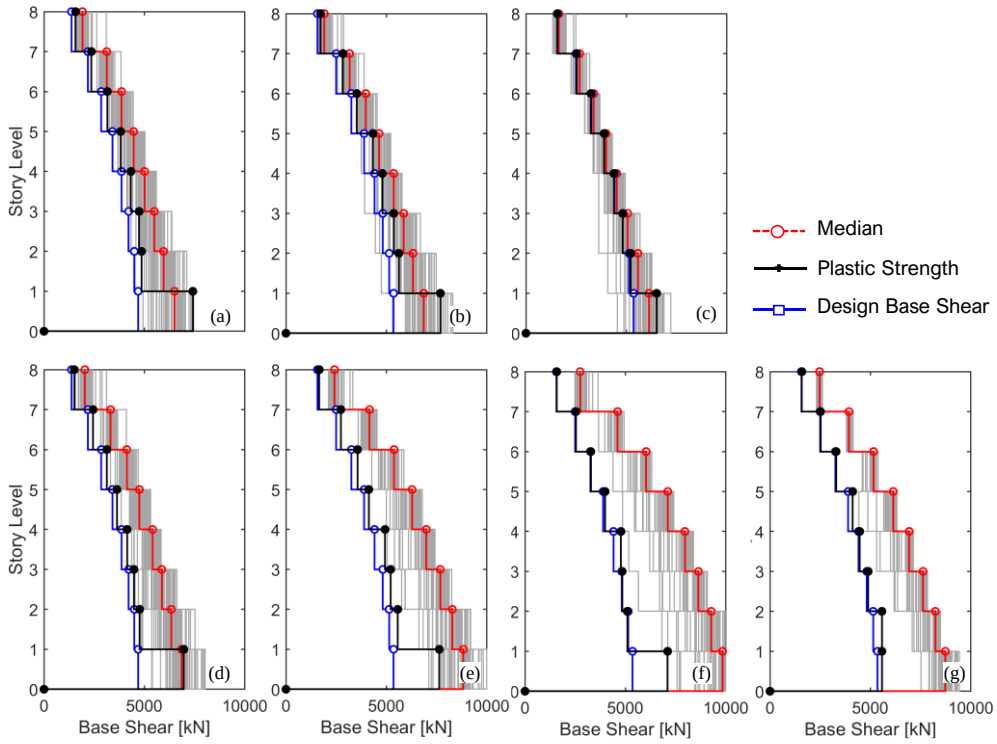

Figure 7.74: Distribution of the Peak Story shear for the 8-story systems under level II ground motions employing bracing connection I: (a) A with $r_0 = 2.0$, (b) A with $r_0 = 4.0$, (c) A with $r_0 = 8.0$, (d) B with $r_0 = 2.0$, B with $r_0 = 4.0$, (f) B with $r_0 = 8.0$, and (g) C, under level III employing the flexible bracing connection.

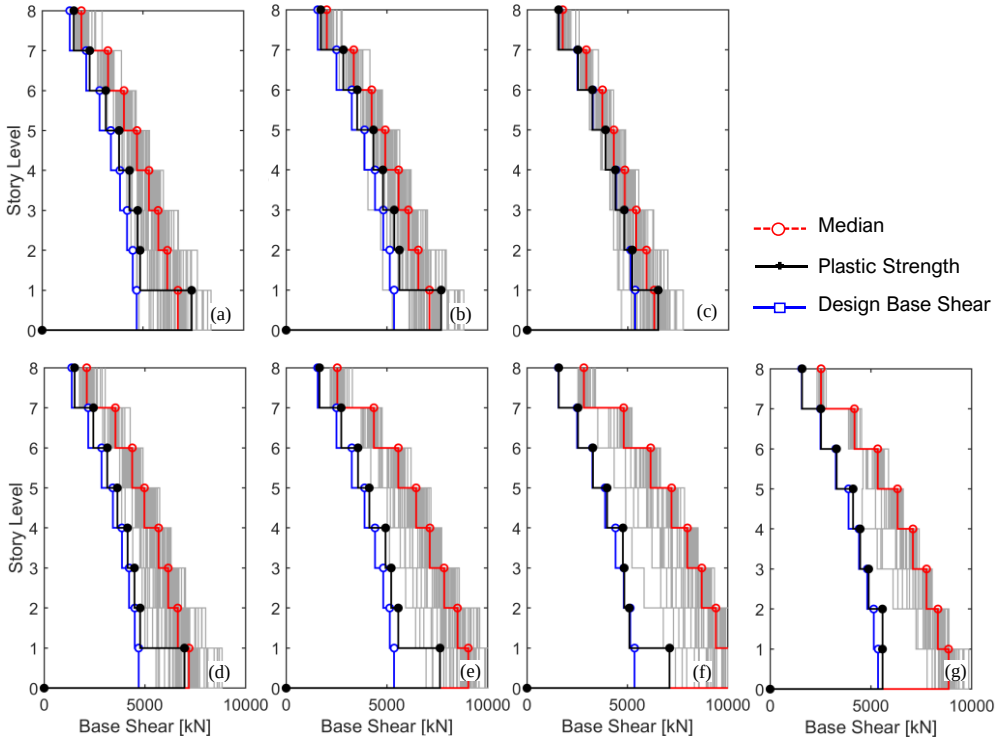

Figure 7.75: Distribution of the Peak Story shear for the 8-story systems under level II ground motions employing bracing connection II: (a) A with $r_0 = 2.0$, (b) A with $r_0 = 4.0$, (c) A with $r_0 = 8.0$, (d) B with $r_0 = 2.0$, B with $r_0 = 4.0$, (f) B with $r_0 = 8.0$, and (g) C, under level III employing the flexible bracing connection.

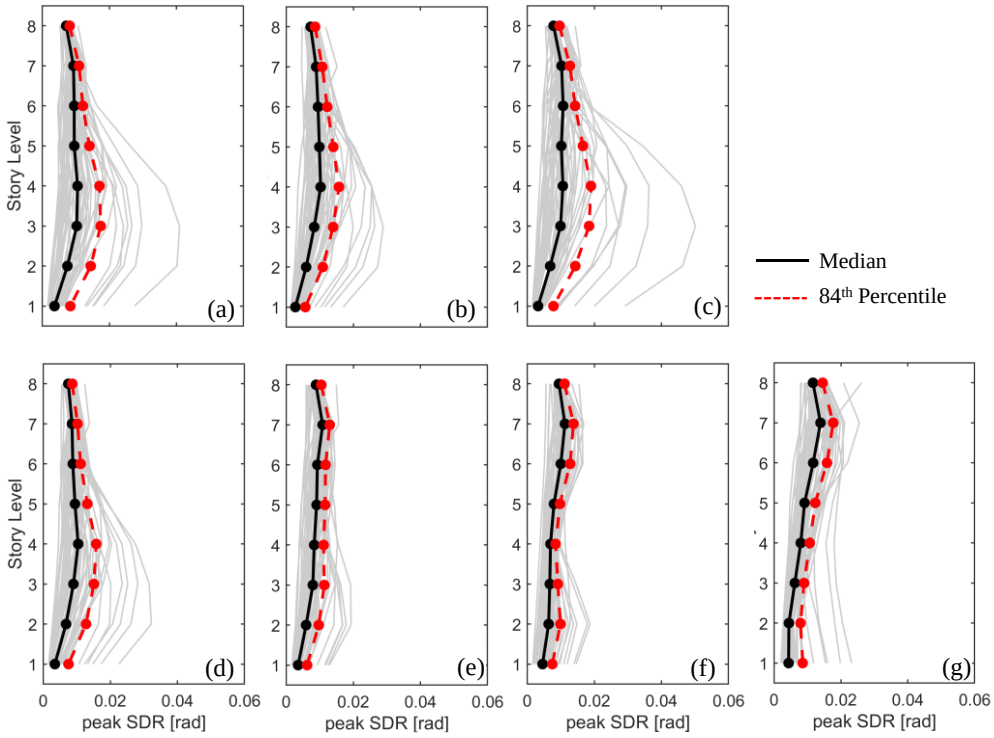

Figure 7.76: Distribution of the peak Story drift for the 8-story braced-frame Model: (a) A with $r_0 = 2.0$, (b) A with $r_0 = 4.0$, (c) A with $r_0 = 8.0$, (d) B with $r_0 = 2.0$, B with $r_0 = 4.0$, (f) B with $r_0 = 8.0$, and (g) C, under level-2 employing the flexible bracing connection.

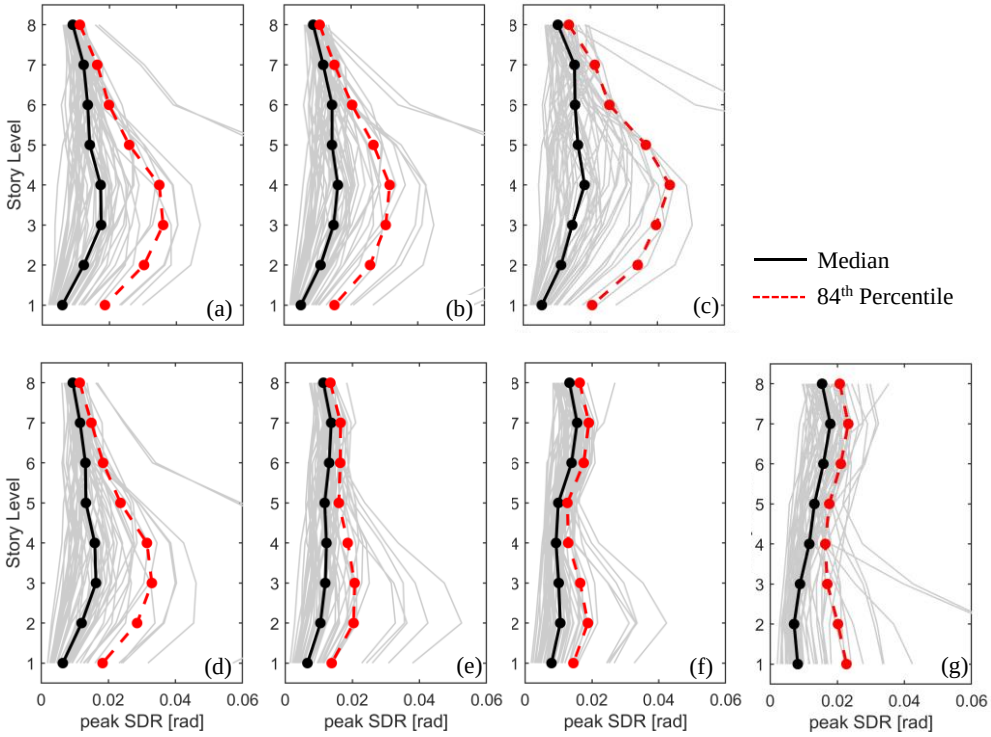

Figure 7.77: Distribution of the peak Story drift for the 8-story braced-frame Model: (a) A with $r_0 = 2.0$, (b) A with $r_0 = 4.0$, (c) A with $r_0 = 8.0$, (d) B with $r_0 = 2.0$, B with $r_0 = 4.0$, (f) B with $r_0 = 8.0$, and (g) C, under level-3 employing the flexible bracing connection.

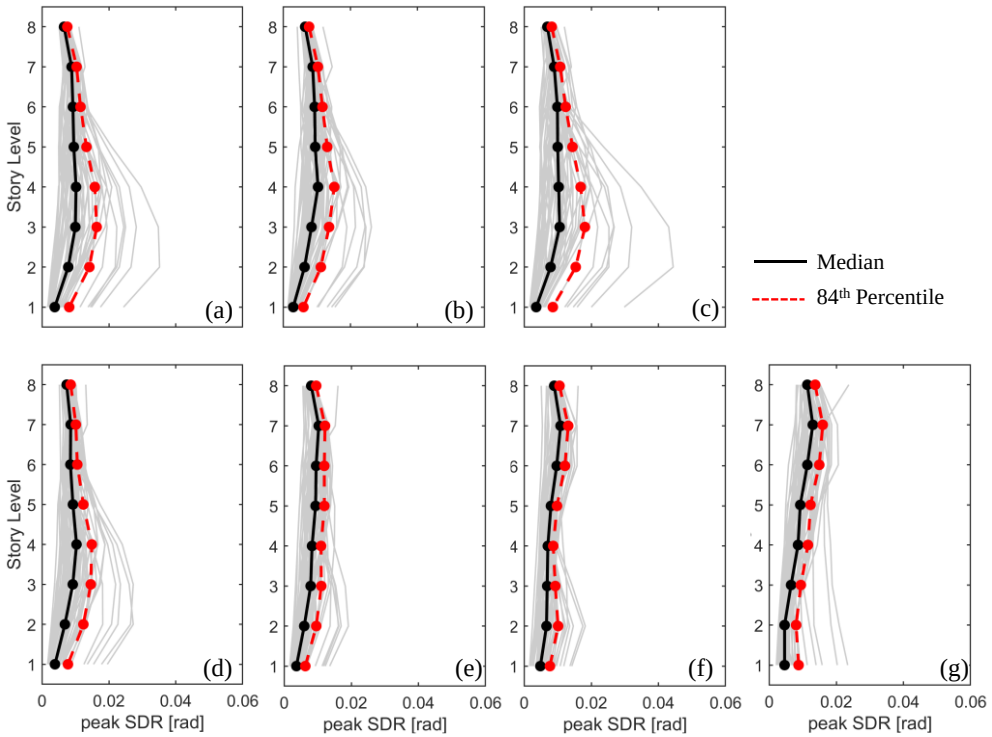

Figure 7.78: Distribution of the peak Story drift for the 8-story braced-frame Model: (a) A with $r_0 = 2.0$, (b) A with $r_0 = 4.0$, (c) A with $r_0 = 8.0$, (d) B with $r_0 = 2.0$, B with $r_0 = 4.0$, (f) B with $r_0 = 8.0$, and (g) C, under level II employing the rigid bracing connection.

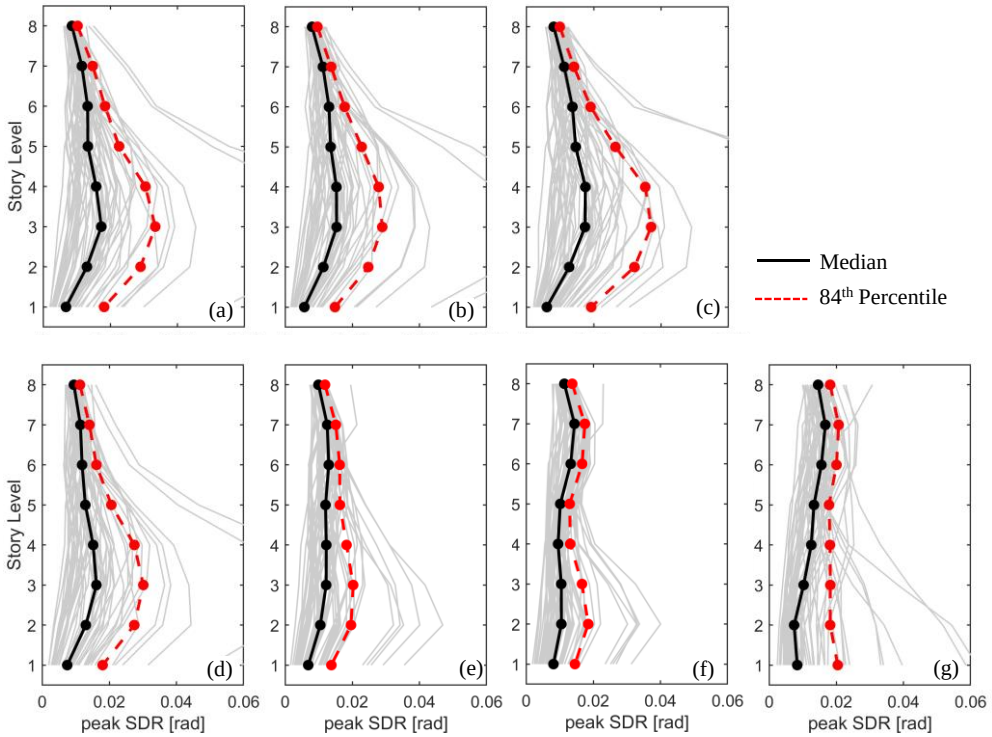

Figure 7.79: Distribution of the peak Story drift for the 8-story braced-frame Model: (a) A with $r_0 = 2.0$, (b) A with $r_0 = 4.0$, (c) A with $r_0 = 8.0$, (d) B with $r_0 = 2.0$, B with $r_0 = 4.0$, (f) B with $r_0 = 8.0$, and (g) C, under level III employing the rigid bracing connection.

Figure 7.80 plots the response of the first story braces for the Chi-Chi Taiwan ground motion (GM#26) scaled for level-2 demands. As observed in the 4-story systems, the chevron braces developed primarily in contraction and developed their tensile yielding strength in tension. For the braced frames designed using design approach A and B with $r_0 = 2.0$ in the post buckling range, the compressive

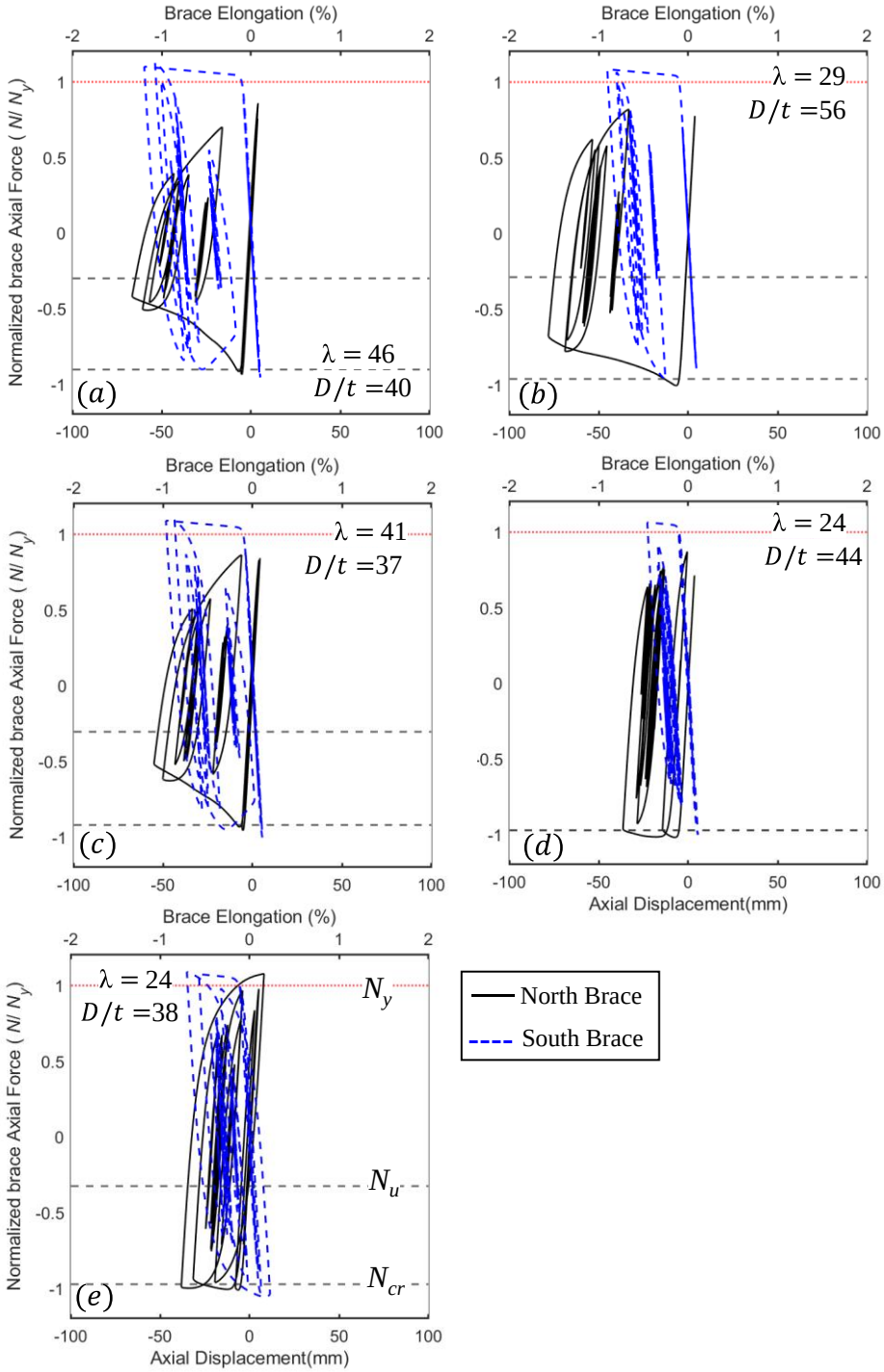

Figure 7.80: Brace hysteretic response for the 8-story braced frames systems: (a) Type A with r_0= 2.0; (b) Type A with r_0= 8.0; (c) Type B with r_0= 2.0; (d) Type B with r_0= 8.0; and (e) Type C, under ground motion level-2 employing the flexible bracing connection.

strength of the braces decreased but at the ultimate state developed slight larger buckling strength than the expected. For the braced frames designed using design approach A and B with $r_0 = 8.0$, and Type C, there was limited reduction of the brace compressive strength, much smaller than strength assumed in design. This agrees with the monotonic pushover analysis where the reduced buckling strength of the brace was as close to $0.7\times N_{cr}$;

As observed, for all the chevron-braced frame models, the soft-story mechanism formed for a couple of ground motions but in general had a uniform deformation of the story drift over the height of the building.

7.7.2.1 Decomposed response

To further understand the response of the 8-story systems, a study in the lateral strength of the chevron-braced frames is warranted to understand the reason for such response. The lateral strength of the braced frame at each story level was decomposed into the contribution of the pair of braces and the MRFs (interior and exterior MRF), as shown in Figure 7.81. The figure plots the decomposed response of the first story frame by plotting the shear carried by the braces and the MRF against the story-drift angle. The predicted strength of the braces at the two key instants as defined in Seki et al. [16], H_{1b}, H_{2b}, and H_{2f}, are superimposed. The figure shows that for the braced frames designed with large r_0 values (Figure 7.81(b), (d) and (e)), the simulated resistance of the braces was larger than the strength predicted form plastic mechanism analysis. In fact, the strength of the braces was close to the contribution of the braces at the onset of braced buckling, H_{1b}, instead of the reduced strength, H_{2b}.

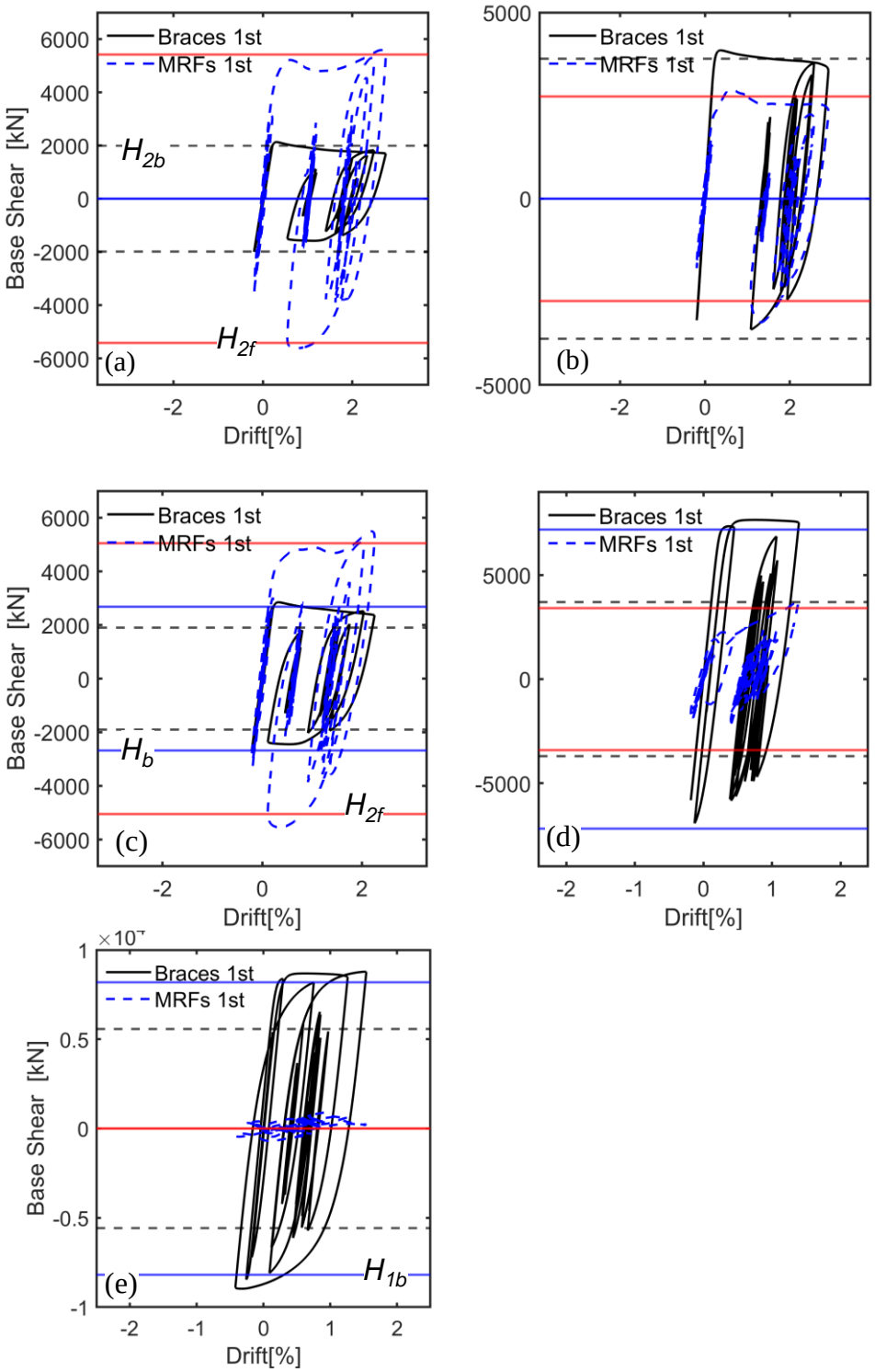

Figure 7.81: Lateral strength decomposition for the first story: (a) Type A with r_0= 2.0; (b) Type A with r_0= 8.0; (c) Type B with r_0= 2.0; (d) Type B with r_0= 8.0; and (e) Type C, all under ground motion level-2 employing the flexible bracing connection.

7.7.3 12-Story Systems

Figure 7.82 and Figure 7.83 plots the distribution of the story shear over the height of the 12 story braced frames systems for all the design cases and combinations. The design base shear and the predicted plastic strength are superimposed in the figures.

All the braced frame systems developed larger strength than the design bases shear. When employing the flexible bracing connection detail, except at the first story, the median story shear exceeded the predicted plastic strength for all the braced frame at all the stories. Table 7.15 summarizes the median base shear demands of the braced frames, and the overstrength values under ground motion Level-2 for both bracing connections. Between design approach Type A and B, the braced frame systems designed with design approach Type B were significantly stronger than Type A for all r_0 values. Under level-2 ground motions, the braced frames models developed normalized median peak base shear ranging from 1.11 to 1.63 for the flexible bracing connection and 1.22 to 1.72, for the rigid bracing connection.

For design approach Type B, the structural systems designed with larger r_0 values were stronger than their counterparts, but for Type A, the ratio of the lateral strength of the braced frame designed with r_0 = 8.0 over r_0 = 2.0, was negligible. For Type B the strength of braced frame designed with r_0 = 8.0 over r_0 = 2.0 was 31% larger for the braced frame systems employing the flexible bracing connection detail, and 29 % for the braced frame systems employing the rigid bracing connection. For Type A, the braces frames designed with smaller r_0 values developed larger

Table 7.15: Median base shear demands for the 12-story systems under Level II ground motions.

Design Approach	r_0	β_0	Flexible Bracing Connection		Rigid bracing Connection	
			Q_{median} [kN]	Q_{max}/Q_{un}	Q_{median} [kN]	Q_{max}/Q_{un}
Type A	2.0	0.55	6362	1.29	6584	1.35
	4.0	0.73	6687	1.16	6887	1.21
	8.0	0.85	6422	1.11	6655	1.16
Type B	2.0	0.55	6870	1.38	7119	1.44
	4.0	0.83	8411	1.49	8537	1.56
	8.0	0.87	9026	1.70	9178	1.74
Type C	-	1.0	9079	1.59	9258	1.65

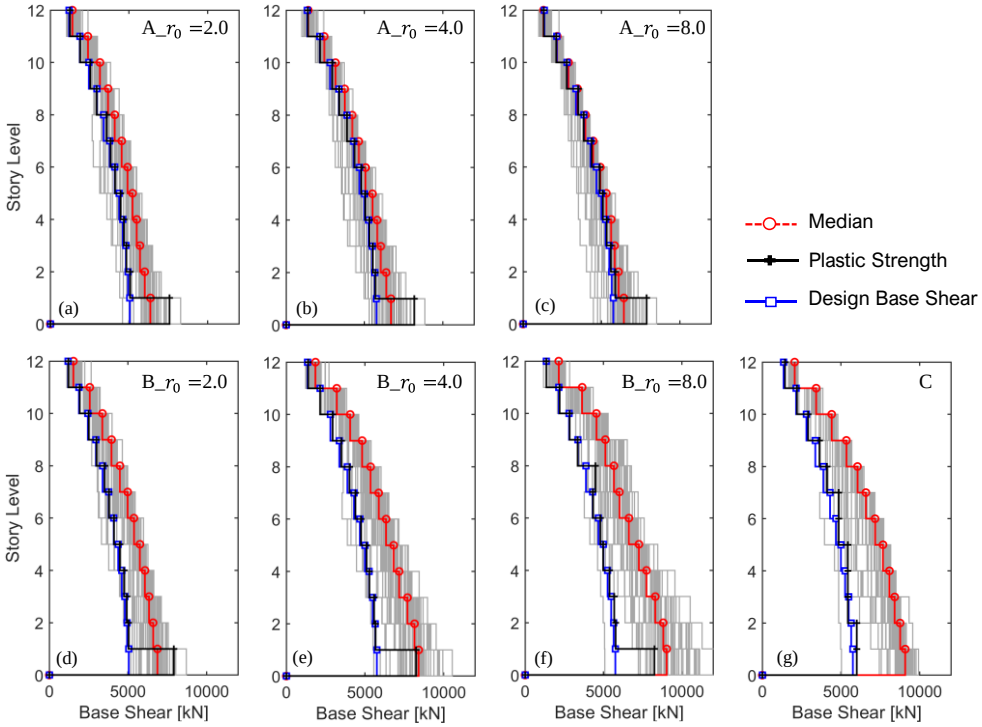

Figure 7.82: Distribution of the Peak Story shear for the 12-story systems under level-2 ground motions employing the flexible bracing connection.

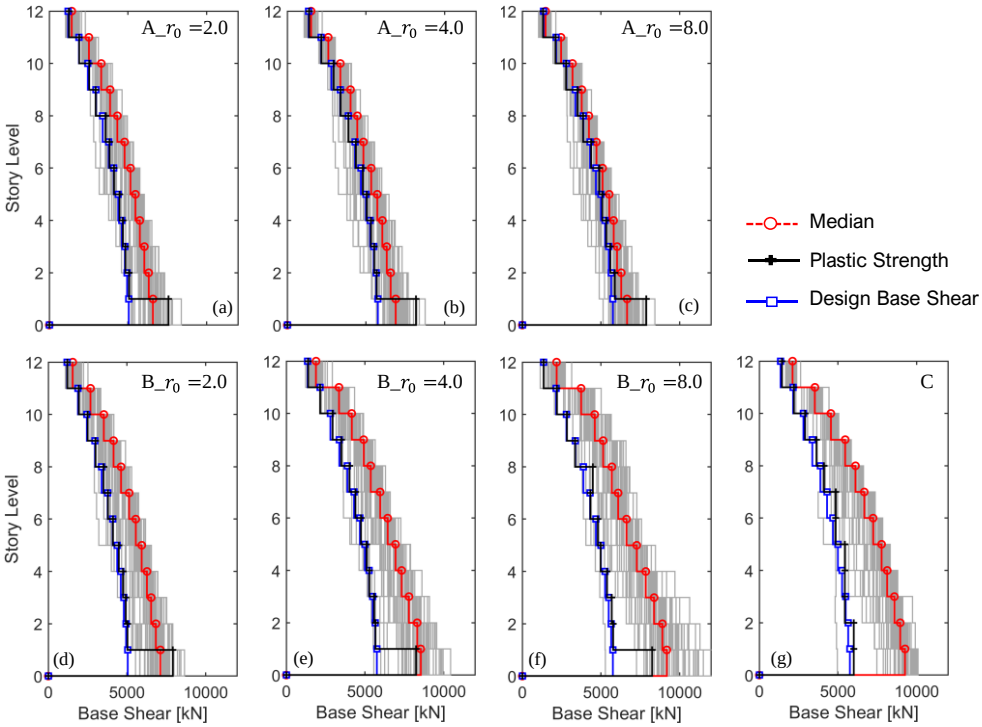

Figure 7.83: Distribution of the Peak Story shear for the 12-story systems under level-2 ground motions employing the rigid bracing connection.

normalized median base shear, however for design approach Type B, the braces frames designed with larger r_0 values developed larger normalized median base shear, for both bracing connection detail. Between all the braced frame models, Type B with $r_0 = 8.0$ and Type C led to stronger structural systems.

As observed in the table, the rigid bracing connection led to stronger braced frame systems than its counterpart, and hence the models developed larger normalized base shear.

The distribution of the peak story drift response for the 12-story systems is shown in Figure 7.84 to Figure 7.87, for all design cases and bracing connections.

For all the cases designed with Type A and B, there was a uniform distribution of the story drift over the height of the building under level-2 ground motions. The peak story drift was within 0.02 rad drift.

Under level-3 demands, there was not a major change in the response of the braced frames. The distribution remained linear, except for Type C, where the drift response tended to be larger at the top of the braced frame systems. This behavior can be assigned to higher modes effects.

The rigid bracing connection led to stronger braced frame systems, and hence the braced frames systems were subjected to smaller story drift demands, and similar to the 8- story systems, the 12-story systems were subjected to considerably smaller story drift demands than the 4-story systems.

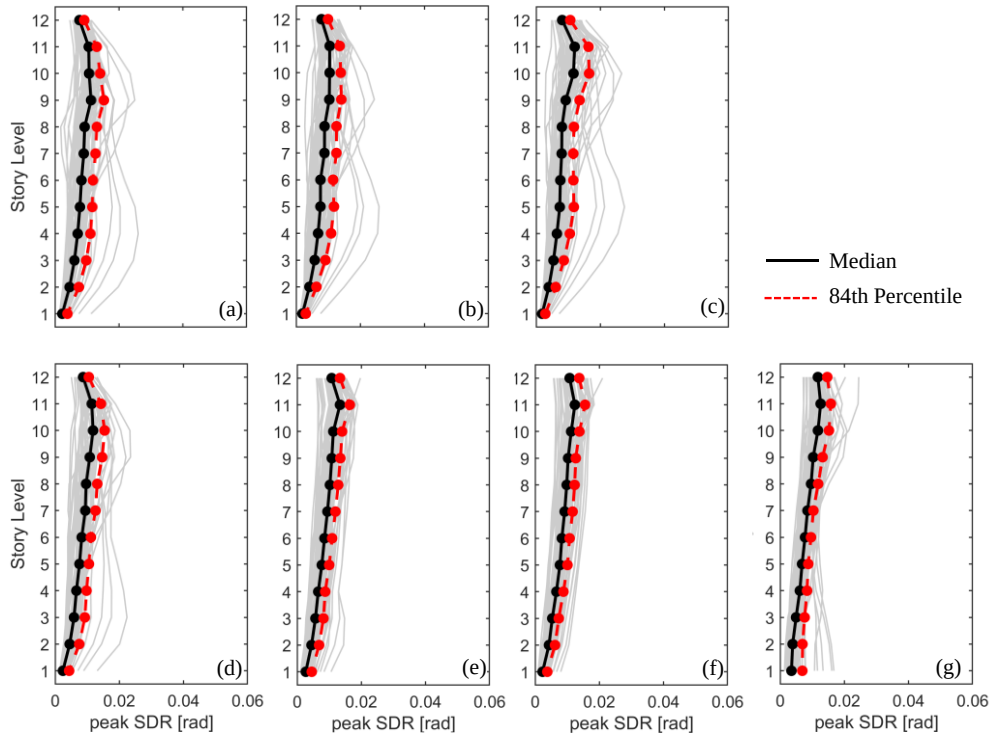

Figure 7.84: Distribution of the peak Story drift for the 12-story braced-frame Model: (a) A with $r_0 = 2.0$, (b) A with $r_0 = 4.0$, (c) A with $r_0 = 8.0$, (d) B with $r_0 = 2.0$, B with $r_0 = 4.0$, (f) B with $r_0 = 8.0$, and (g) C, under level 2 employing the flexible bracing connection .

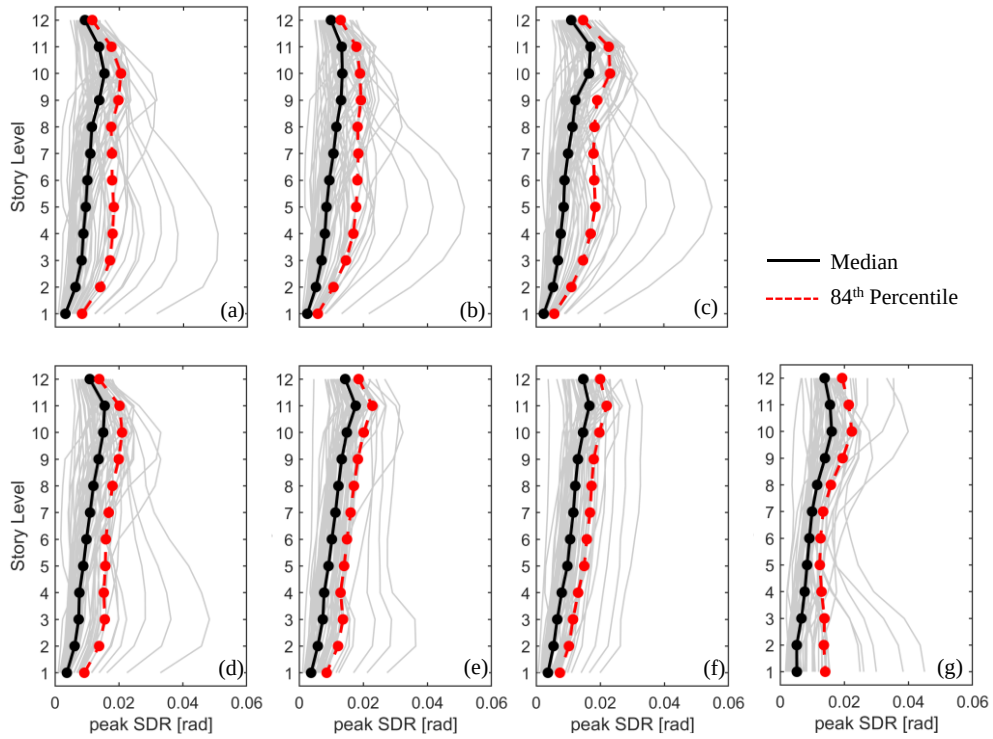

Figure 7.85: Distribution of the peak Story drift for the 12-story braced-frame Model: (a) A with $r_0 = 2.0$, (b) A with $r_0 = 4.0$, (c) A with $r_0 = 8.0$, (d) B with $r_0 = 2.0$, B with $r_0 = 4.0$, (f) B with $r_0 = 8.0$, and (g) C, under level 3 employing the flexible bracing connection.

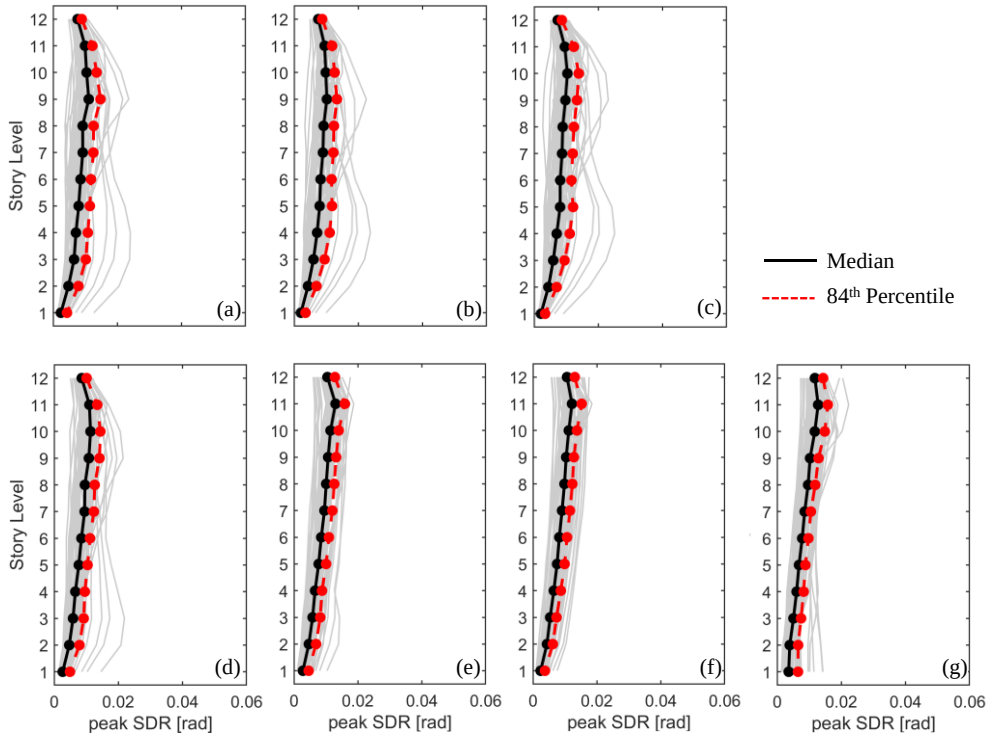

Figure 7.86: Distribution of the peak Story drift for the 12-story braced-frame Model: (a) A with $r_0 = 2.0$, (b) A with $r_0 = 4.0$, (c) A with $r_0 = 8.0$, (d) B with $r_0 = 2.0$, B with $r_0 = 4.0$, (f) B with $r_0 = 8.0$, and (g) C, under level 2 employing the flexible bracing connection.

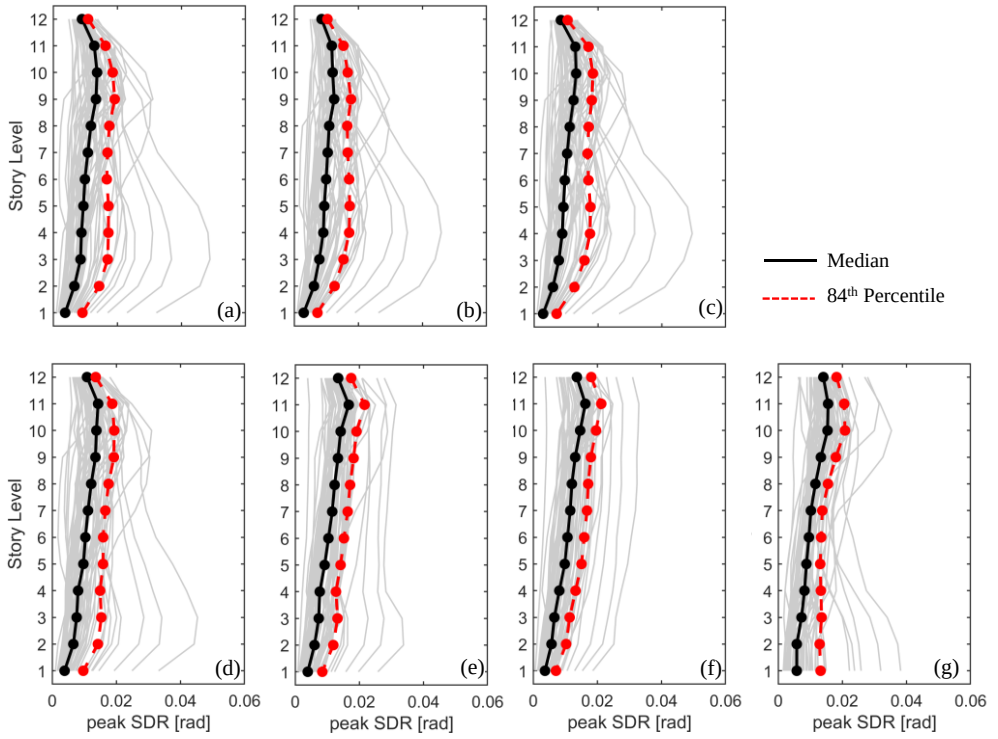

Figure 7.87: Distribution of the peak Story drift for the 12-story braced-frame Model: (a) A with $r_0 = 2.0$, (b) A with $r_0 = 4.0$, (c) A with $r_0 = 8.0$, (d) B with $r_0 = 2.0$, B with $r_0 = 4.0$, (f) B with $r_0 = 8.0$, and (g) C, under level 3 employing rigid bracing connection.

Figure 7.88 plots the response of the north brace of the first story, for the ground motion that caused the largest first-story drift.

As observed in the 4- and 8-story systems, the braces developed primarily in contraction.

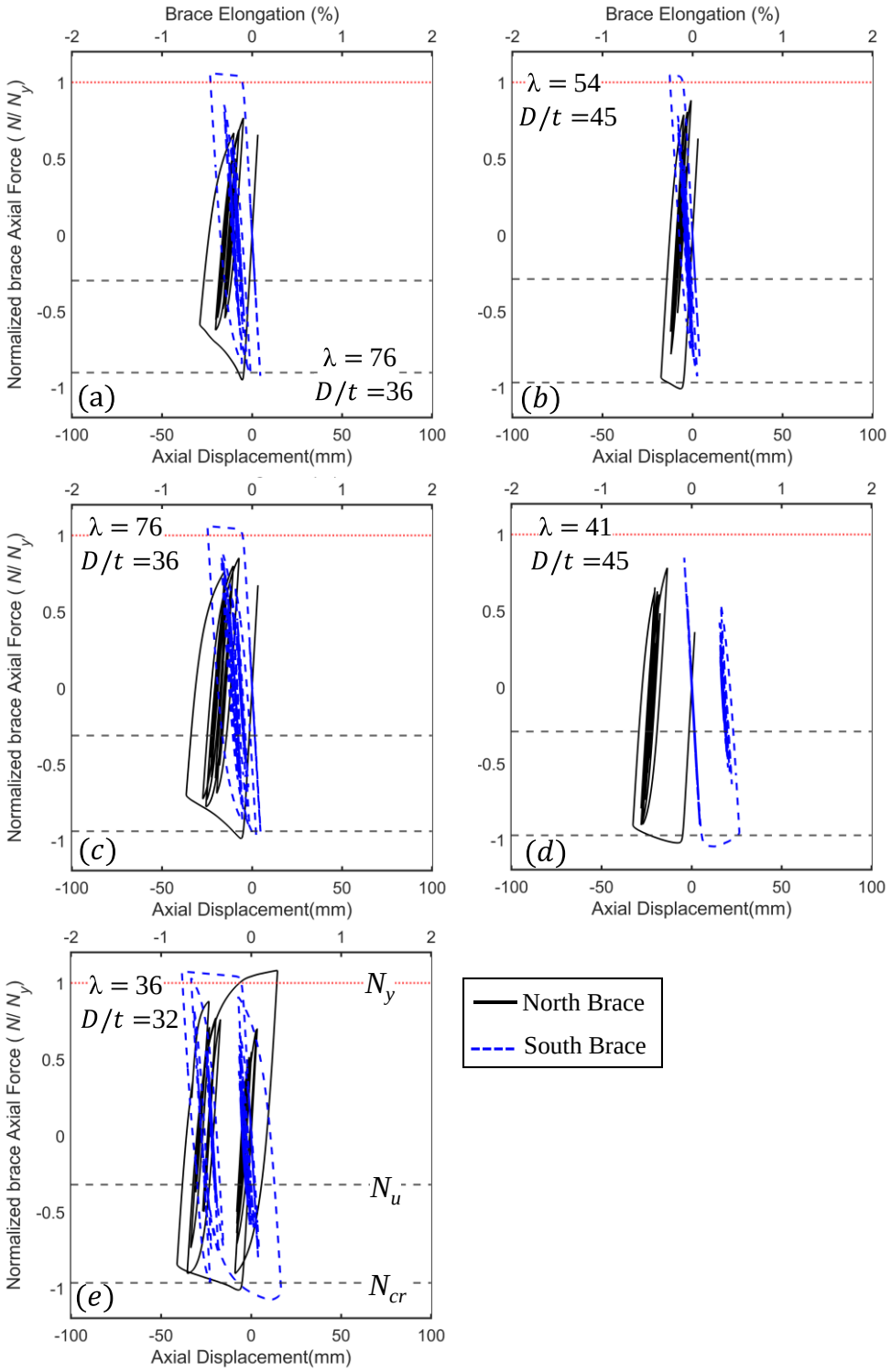

Figure 7.88: Brace hysteretic response for the 12-story braced frames systems: (a) Type A with r_0= 2.0; (b) Type A with r_0= 8.0; (c) Type B with r_0= 2.0; (d) Type B with r_0= 8.0; and Type C.

However, unlike what observed for the low-rise braced frame systems, for the braced frames designed with small r_0 values, the reduction of the brace compressive strength was significantly smaller than the $0.3 \times N_{cr}$ assumed in design. For the braced frame systems designed with large r_0 values and Type C, there was limited degradation of the brace compressive strength.

The formation of the soft-story mechanism, which is characteristic of chevron-braced MRF was not observed for the 8- and 12- systems, particular for the braced frame designed using design approach C. It should be noted that for chevron-braced frames, the soft-story mechanism is induced by the degradation of the brace compressive strength and subsequent yielding of the beams. In these simulations, because of the limited reduction of the brace compressive strength, the formation of the week-beam mechanism did not occur. In essence, the braces behave similar as buckling restraining braces (BRB), in which buckling of the braces is avoided and then the soft story mechanism does not form.

7.7.3.1 Decomposition of the Lateral strength

To further understand the response of the 12-story braced frame systems, a study in the lateral strength of the chevron-braced frames is warranted to understand the reason for such response. The lateral strength of the braced frame at each story level was decomposed into the contribution of the pair of braces and the MRFs (interior and exterior MRF). Figure 7.89 depicts the decomposition of the lateral strength for the 1st story for all the cases considered. The predicted strength of the braces at the two key instants as defined in Seki et al. [16], H_{1b}, H_{2b}, and H_{2f}, are superimposed.

As observed for the 8-story systems, for models with r_0 = 4.0, 8.0, and Type C, the simulated strength derived from the braces developed is significantly larger than the strength predicted from plastic mechanism analysis.

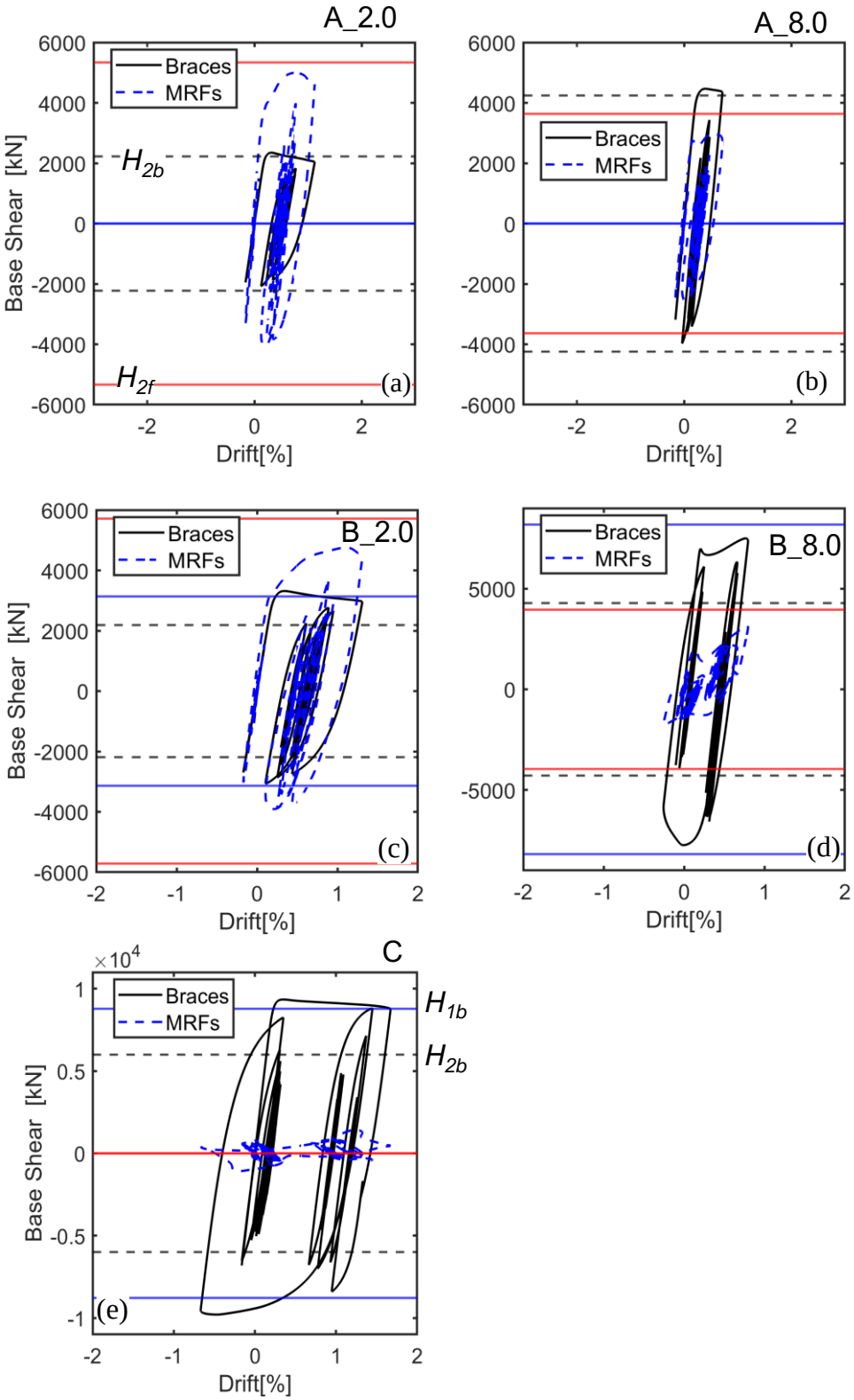

Figure 7.89: Lateral strength decomposition for the first story: (a) Type A with r_0= 2.0; (b) Type A with r_0= 8.0; (c) Type B with r_0= 2.0; (d) Type B with r_0= 8.0; and Type C, all under ground motion II employing the flexible bracing connection.

7.8 Summary

This section studied the performance of the members of the chevron-braced MRFs. The effect of r_0 value depends on the design approach. While for design approach Type B increasing the r_0 value is effective in reducing the story drift demands for the 4-story systems, for Type A increasing the r_0 value is not effective in reducing the story drift demands because for this case the beam yields and the braced frames are subjected to larger deformation demands. Type C which requires larger braces, beams and columns were effective in reducing the story drift demands, with the braced frames being subjected to smaller deformation demands.

For the 4-story systems, Type A caused no adverse design result for all the design cases. Although yielding of the beam occurred for r_0 = 4.0 and 8.0, the distribution of the story drift over the height of the braced frame was nearly uniform for all the cases. For Type B, the cases where yielding of the beams was permited had better performance than the cases where beam yielded was precluded. Between all the cases, the braced frame models designed with Type C experienced smaller story drift demands than any of the subcases of Type A and B. There was a uniform distribution of the story drift over the height of the braced frame, and the formation of soft story mechanism, characteristic of this type of structures did not occur.

The performance of the braced frames is highly affected by the brace slenderness ratio. The OpenSees model is not suitable to simulate the performance of braced frames with small slenderness ratio.

8. DISCUSSION

8.1 Story Shear Response

Figure 8.1 to Figure 8.2 plots the median of the peak story shear demands for the 4-, 8-, and 12-story systems. For the 4-, 8- and 12-story systems, Type B led to stronger brace frame than Type A for both the flexible and rigid bracing connection.

For the 4-story systems, Type B with r_0= 8.0 developed larger median normalized story shear Q_{max}/Q_{un} than any of the other subcases. Under level-2 ground motions the median Q_{max}/Q_{un} equaled 1.72 and 1.84 for the flexible and rigid bracing connection, respectively.

For the 8-story systems, Type B with r_0= 8.0 developed larger median lateral strength and median Q_{max}/Q_{un} than any of the subcases of Type A or Type C. Under level-2 ground motions demands the median Q_{max}/Q_{un} equaled 1.85 and 1.93 for the flexible and rigid bracing connection, respectively. Similarly, for the 12-story systems, Type B with r_0= 8.0 developed larger median Q_{max}/Q_{un} than any of the subcases of Type A or Type C. The ratio Q_{max}/Q_{un} equaled to 1.70 and 1.74, for the flexible and rigid bracing connection, respectively.

The braced frame models designed with Type A did not develop their predicted plastic strength, Q_p. For Type A with $r_0 = 2.0$, 4.0 and 8.0, the median story shear was close to $0.93Q_p$, $0.89Q_p$, $0.84Q_p$, respectively for the 4-story systems, $0.88Q_p$, $0.89Q_p$, $0.94Q_p$, respectively for the 8-story systems, and $0.84Q_p$, $0.82Q_p$, $0.82Q_p$, respectively for the 12-story systems, employing the flexible bracing connection detail. For Type B, the median base shear equaled the predicted plastic strength for $r_0 = 2.0$, but for r_0 = 4.0 and 8.0 and Type C, the median base shear was within $0.96Q_p$, $1.09Q_p$, and $1.52Q_p$, respectively, for the 4-story systems, $1.16Q_p$, $1.39Q_p$, and $1.57Q_p$, respectively, for the 8-story systems and $1.02Q_p$, $1.10Q_p$, and $1.51Q_p$, respectively, for the 12-story systems, employing the flexible bracing connection detail.

Similarly, for the models employing the rigid bracing connection, the frame models using Type A did not develop their predicted plastic strength. Type A with $r_0 = 2.0$, 4.0 and 8.0, the median story shear was close to $0.95Q_p$, $0.95Q_p$, $0.92Q_p$, respectively for the 4-story systems, $0.91Q_p$, $0.92Q_p$, $0.97Q_p$, respectively for the 8-story systems, and $0.87Q_p$, $0.84Q_p$, $0.84Q_p$, respectively for the 12-story systems.

For Type B, the median base shear equaled the predicted plastic strength for $r_0 = 2.0$, but for r_0 = 4.0 and 8.0 and Type C, the median base shear was within $1.06Q_p$, $1.05Q_p$, and $1.62Q_p$, respectively, for the 4-story systems, $1.18Q_p$, $1.41Q_p$, and $1.59Q_p$, respectively, for the 8-story systems and 1.04 Q_p,

1.11Q_p, and 1.54 Q_p, respectively, for the 12-story systems, employing the flexible bracing connection detail.

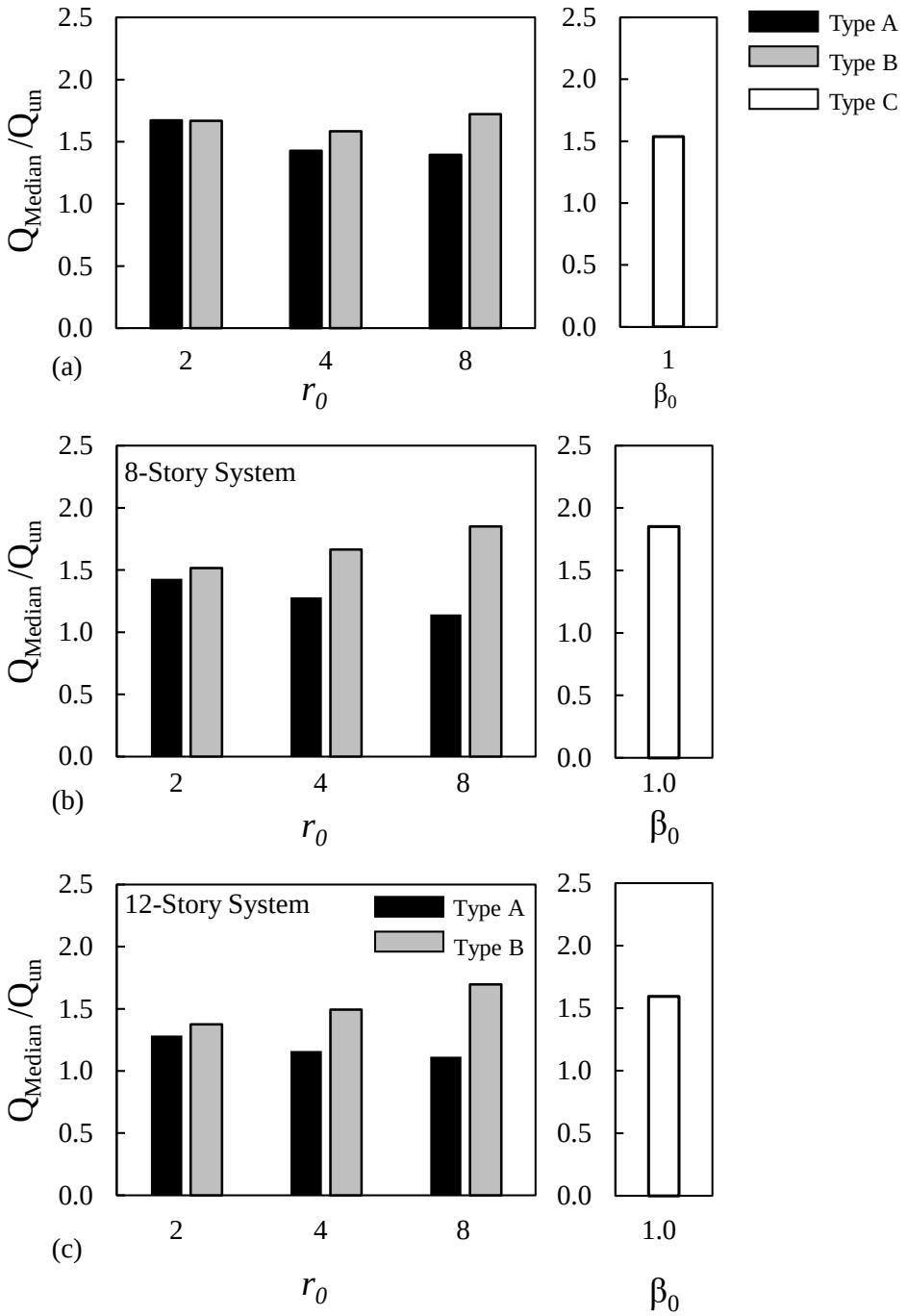

Figure 8.1: Median peak story shear: (a) 4-story systems; (b) 8-story systems; (c) 12-story systems employing the flexible bracing connections under level-2 demands.

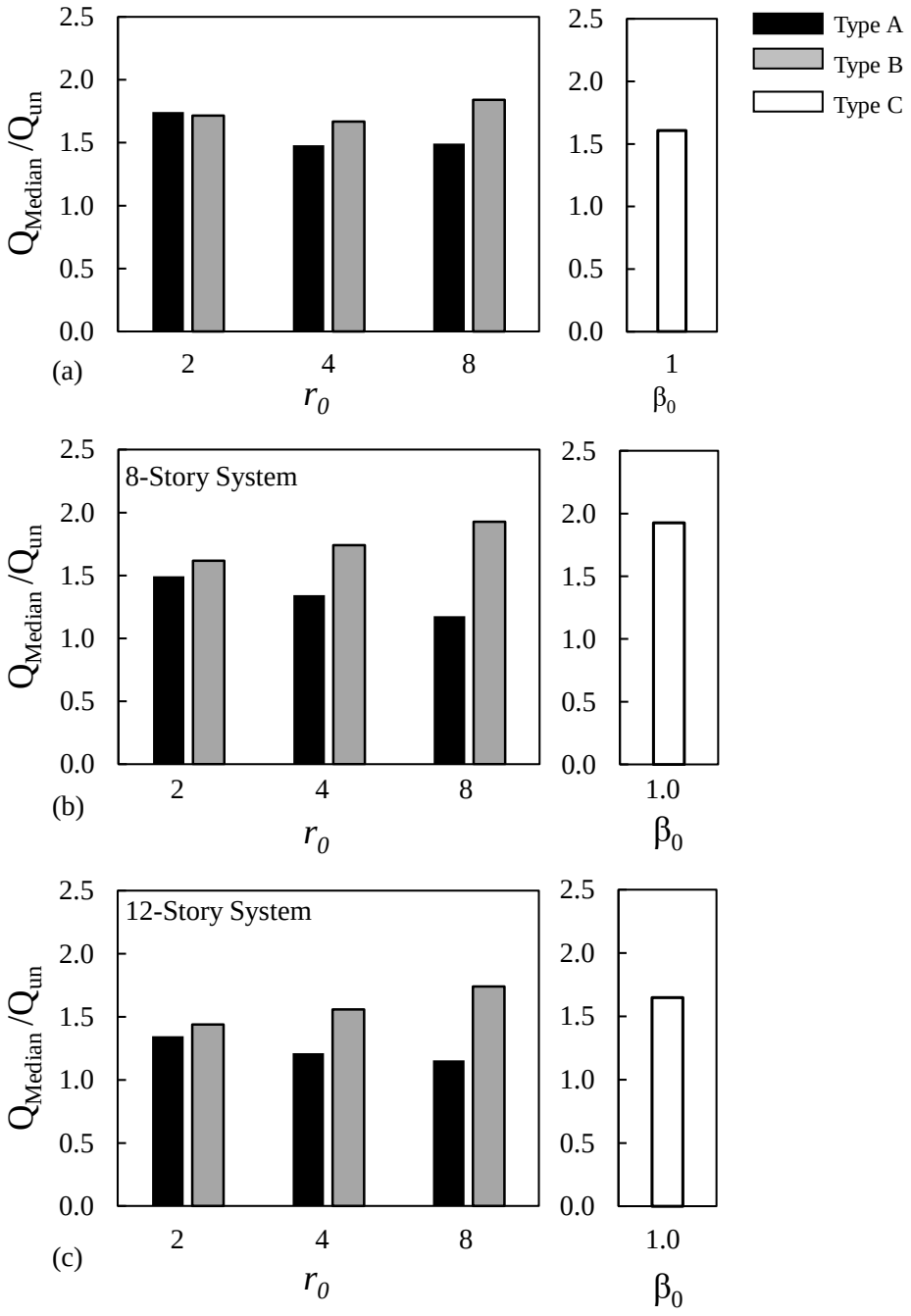

Figure 8.2: Median peak story shear: (a) 4-story systems; (b) 8-story systems; (c) 12-story systems employing the rigid bracing connection under level-2 demands.

8.2 Story Drift Response

Figure 8.3 plots the median (50th percentile) and 84th percentile of the maximum story drift demands for the 4-, 8- and 12-story systems. The figure shows that, the median story drift demand was within the 0.02 rad for all structural systems. This suggests that the braced frame systems met the design requirements stipulated by the Japanese code when subjected to level-2 ground motions.

Between design approach Type A and B, the story-drift demand was similar for the cases

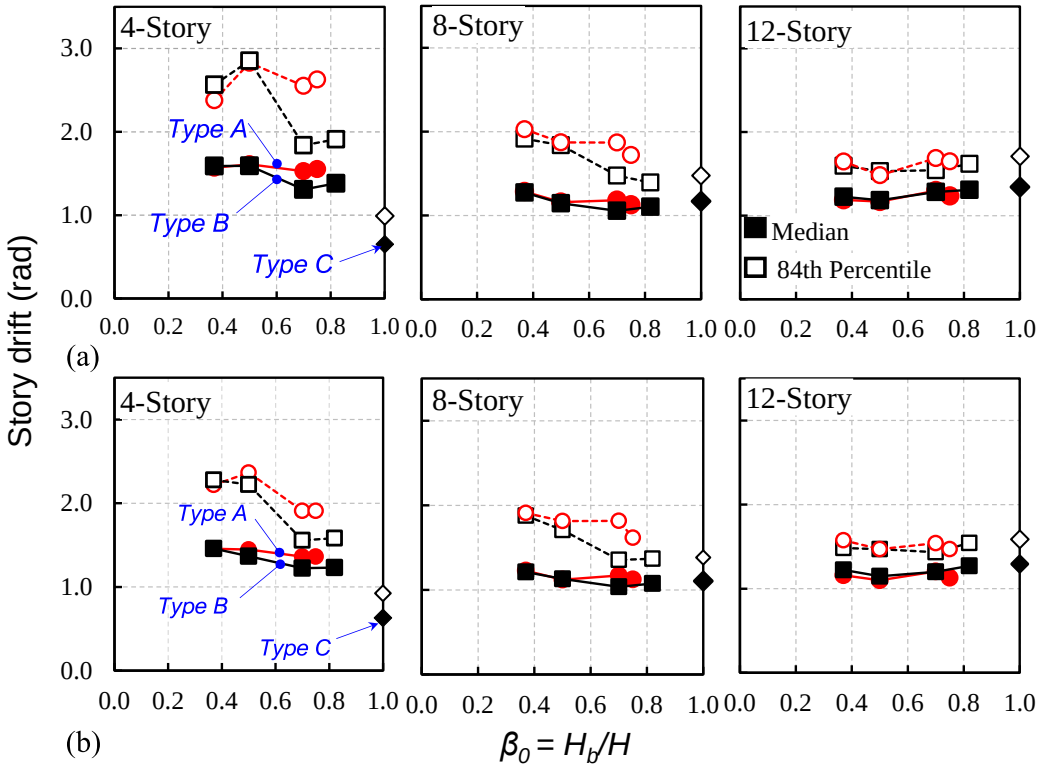

Figure 8.3: 50th and 84th percentile of the peak story drift demands: (a) Flexible bracing, and (b) Rigid bracing Connection.

designed assuming r_0= 2.0, however for r_0= 4.0 and 8.0 the drift demands were notably greater for the braced frame systems designed using Type A. Type C developed smaller drift demands than any of the subcases of the braced frames designed with Type A or B.

For the 4-story systems, the 84th percentile drift demands exceeded 0.02 rad for all the cases under level-2 ground motions, with the exception of Type C. Under level-3 ground motion demands the 84th percentile drift demands exceeded 0.02-rad drift for all the cases. For design approach Type A, the 50th and 84th demand was similar for all the r_0 values, but Type B with r_0= 4.0 or 8.0, which permitted beam yielding, led to lower 84th percentile story drift demands which suggests a more uniform story drift distribution than r_0= 2.0.

Although designed for the same standard base shear coefficient, the 50th and 84th percentile story drift demands were significantly smaller for the 8- and 12- story braced frame systems. This can be attributed to two main reason: (*i*) the suite of ground motions was less severe for the 8- and 12- story systems because, as seen in Figure 7.21 and Figure 7.22 the ground motions were scaled over periods beyond the constant acceleration domain of the design spectra, and *ii*) for all the cases, the 8- and 12-story systems developed larger overstrength factors. This is due to the larger compressive strength of the braces and flexural strength of the columns.

For both the 8- and 12-story systems, the 84th percentile of the story drift demands was smaller than 0.02 rad for all cases under level-2 ground motion demands but exceeded 0.02-rad drift for all the cases under level-3 demands. For the 8- story systems, the effect of the relative horizontal strength of the braced frames with respect to the beams, r_0, and hence the proportion of the lateral strength carried by the braces, β_0 was relatively smaller compared to the 4-story systems.

Similarly, for the 12-story systems, both the relative horizontal strength of the braced frames with respect to the beams, r_0, and the proportion of the lateral strength carried by the braces, β_0 had virtually no effect on the distribution of the median and the 84th percentile story drift demands over the height of the structures, except at the top of the frame.

8.3 Structural Member Seismic Demand and Behavior

The behavior and demands on the main structural members are discussed next. The performance of the braces, beams and columns are of main interest. The engineering demand parameters (EDP) of interest are: (*i*) the brace axial force developed in tension and compression and the ductility demands; (*ii*) the beam bending moment and axial force demands, and the vertical deflection demands at the center of the chevron-braced bay beam; and (*iii*) the bending moment and axial force demands of the columns.

8.3.1 Brace Response: Behavior and Demands

For design of braced frames in Japan, assumptions to the maximum axial force developed on the tension and compression braces are commonly made. The maximum axial force developed in the braces when in tension and compression are discussed. In addition, the ductility demands on the braces are also discussed during this section. The tensile ductility (μ_t) and compressive ductility (μ_c) demands were computed as:

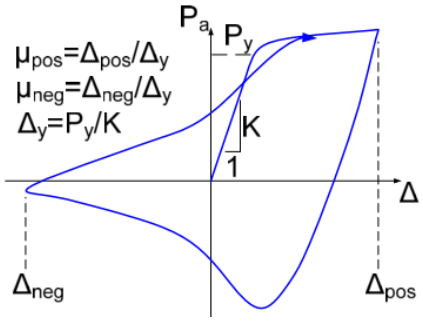

Figure 8.4: Illustration for calculation of the brace ductility demands.

$$\mu_t = \frac{\Delta_t}{\Delta_y} \text{ , and } \mu_c = \frac{\Delta_c}{\Delta_y}$$

The brace tension force is normalized by the brace yielding strength, and the brace compression

strength is normalized by the brace buckling strength.

Figure 8.5 to Figure 8.7 plots the maximum brace tensile force demands developed under all the ground motions for both Level-2 and Level-3 ground motions, normalized by the brace tensile yielding strength, N_y=$A_g \times F_y$, assumed in design.

As shown in the figure, for the 4-story systems, the brace yielded under all the ground motions for the braced frames designed using design approach Type A and B with r_0= 2.0. For r_0= 4.0 and 8.0, although yielding of the braces was not predicted in design, the braces developed their yielding strength for most of the ground motions. Under level-2 ground motion demands, the braces remained elastic in a maximum of the ground motions for r_0= 4.0 and 8.0. For Type C, unlike what was predicted in design, the braces yielded in only 79% of the ground motions. For the 8- and 12-story systems, the effect of the design approach was negligible. As observed in figures the braces yielded for nearly all the ground motions for all the design cases.

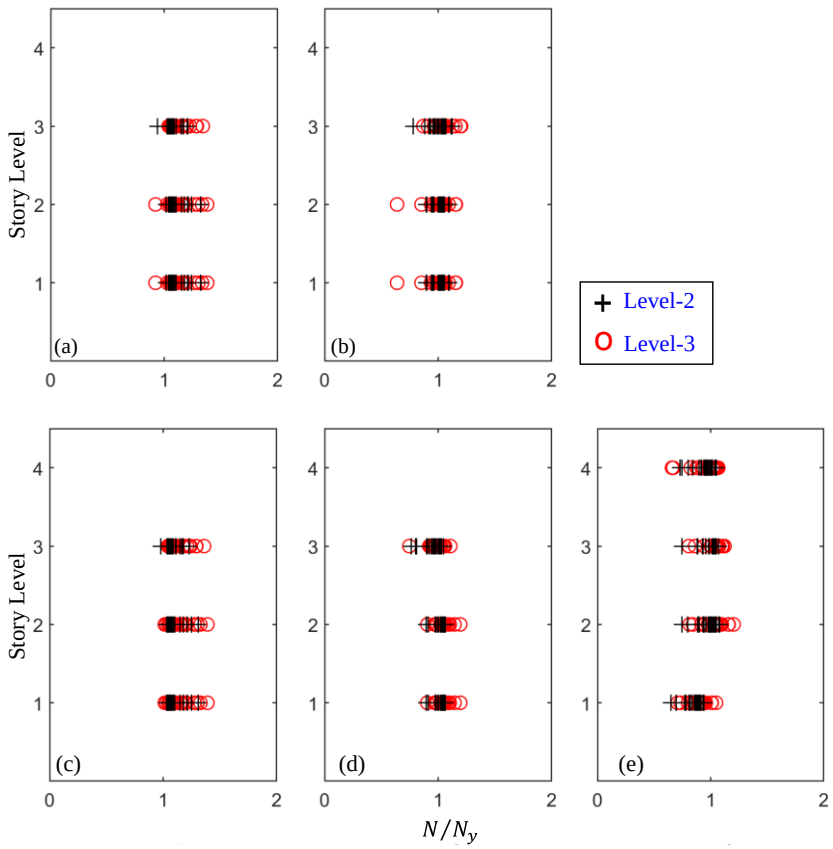

Figure 8.5: Normalized brace axial tensile force for the 4-story systems employing the flexible bracing connection: (a) Type A with r_0= 2.0; (b) Type A with r_0= 8.0; (c) Type B with r_0= 2.0; (d) Type B with r_0= 8.0; and (e) Type C.

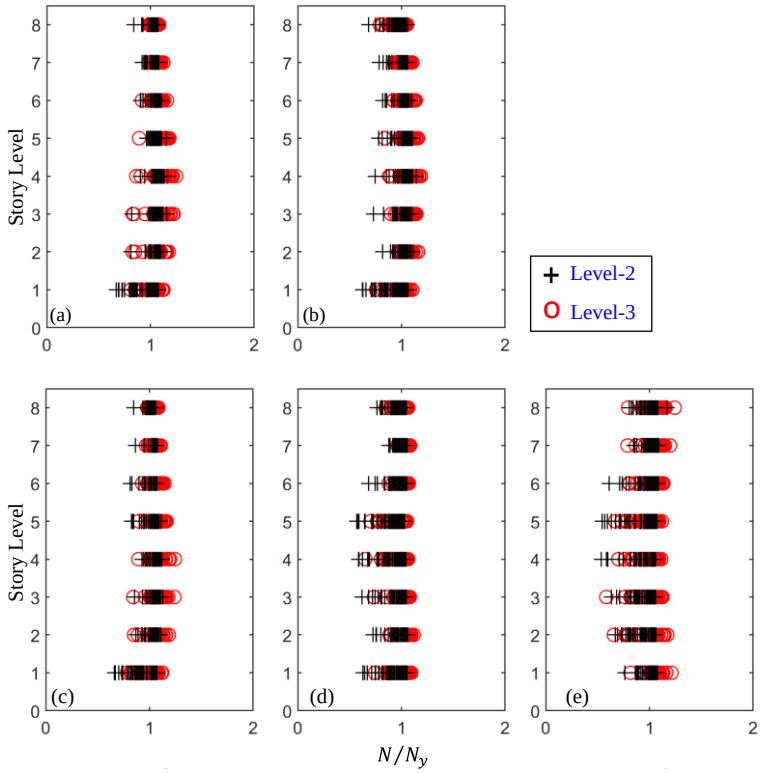

Figure 8.6: Normalized brace tensile force for the 8-story systems employing the flexible bracing connection: (a) Type A with r_0= 2.0; (b) Type A with r_0= 8.0; (c) Type B with r_0= 2.0; (d) Type B with r_0= 8.0; and (e) Type C.

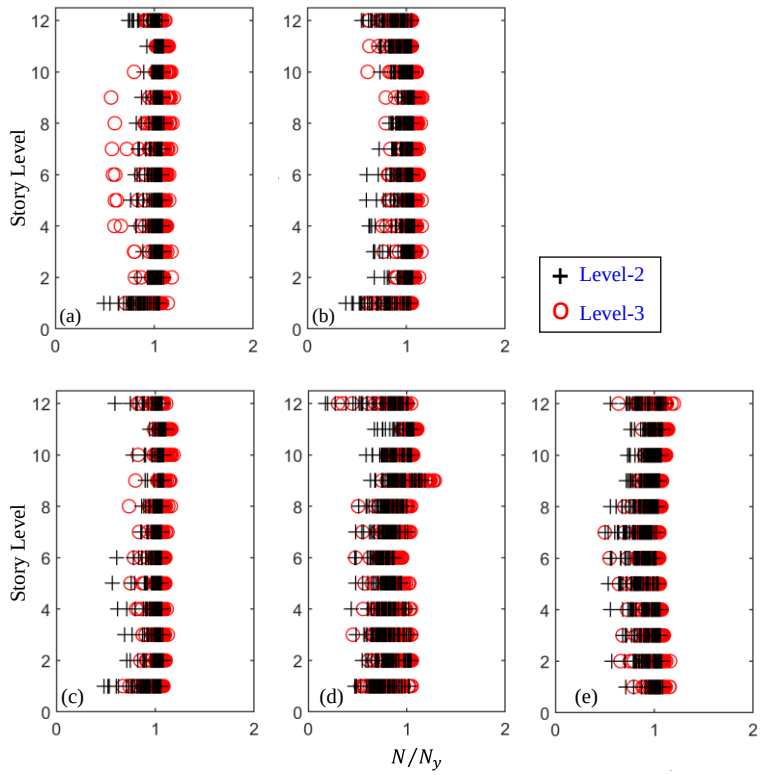

Figure 8.7: Normalized brace tensile force for the 12-story systems employing the flexible bracing connection: (a) Type A with r_0= 2.0; (b) Type A with r_0= 8.0; (c) Type B with r_0= 2.0; (d) Type B with r_0= 8.0; and (e) Type C.

Type A and B with r_0= 2.0 behaved as intended in design, but for r_0= 4.0 and 8.0, the braces yielded, for practically all the ground motions, thus violating the design assumption. This response can be associated with the nature of the near field ground motions which induces a unidirectional pulse thus forcing tensile yielding of the braces. Therefore, the assumption that, if the beam is allowed to yield the tension brace will not yield does not hold true for structures near fault locations.

Figure 8.8 through Figure 8.10 plots the distribution of the ultimate brace compressive force demands developed under all the ground motions employing the flexible bracing connections. The ultimate brace compressive strength demands were normalized by the expected brace compressive strength, N_{cr}, computed taken the effective length factor, k, equal 1.0.

As shown in the figure, the compressive response of the braces is highly affected by the r_0 values. The braced frame systems designed with larger r_0 values (and thus larger β_0 values) required larger braces with slenderness ratio. For the s4-story systems there was a large reduction of the brae compressive strength, especially for design approach Type A and B with r_0 = 2.0. The

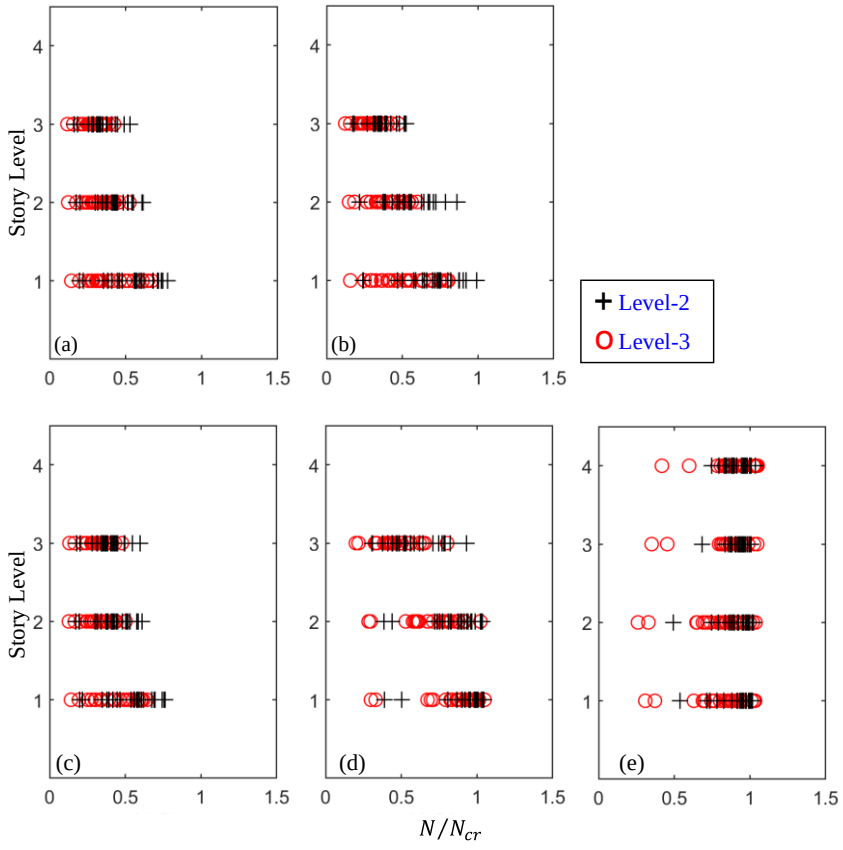

Figure 8.8: Brace Compressive Response for the 4-story systems employing the flexible bracing connection: (a) Type A with r_0= 2.0; (b) Type A with r_0= 8.0; (c) Type B with r_0= 2.0; (d) Type B with r_0= 8.0, and (e) Type C.

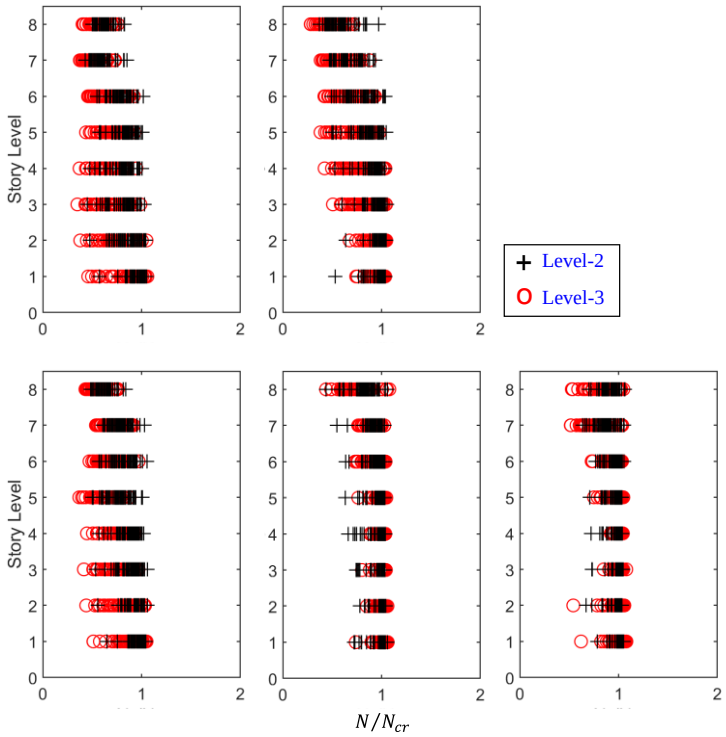

Figure 8.9: Brace Compressive Response for the 8-story systems employing the flexible bracing connection : (a) Type A with r_0= 2.0; (b) Type A with r_0= 8.0; (c) Type B with r_0= 2.0; (d) Type B with r_0= 8.0, and (e) Type C.

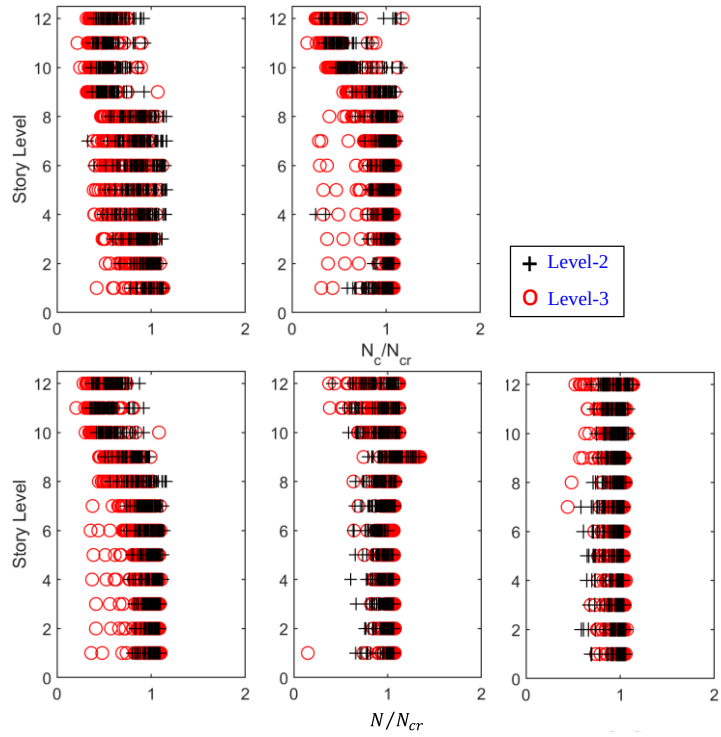

Figure 8.10: Brace Compressive Response for the 12-story systems employing the flexible bracing connection: (a) Type A with r_0= 2.0; (b) Type A with r_0= 8.0; (c) Type B with r_0= 2.0; (d) Type B with r_0= 8.0, and (e) Type C.

median N/N_{cr} within $0.33N_{cr}$ to $0.56N_{cr}$ and $0.36N_{cr}$ to $0.54N_{cr}$ for Type A and B, for level-2 ground motion demands.

For r_0= 4.0 and 8.0, there was a smaller reduction of the brace compressive strength with the median ultimate compressive strength of the braces in the range between $0.35N_{cr}$ to $0.72N_{cr}$ and $0.52N_{cr}$ to N_{cr} for r_0 = 8.0. The braces at the top floor developed larger reduction of the compression strength. Similarly, for Type C, there was limited reduction of the brace compressive strength. Although there were some outliers, the median value was in the range from 0.96 N_{cr} to N_{cr}.

Similarly as for the 4-story systems, the compressive response of the braces on the 8- and 12-story systems, was highly dependent on the $r_0$value. Except for r_0 = 2.0, the reduction of the brace compression strength was relatively small. For both design approach Type A and B with r_0 = 2.0, the median reduction of the brace compressive strength N/N_{cr} was between $0.62N_{cr}$ and N_{cr} for all the stories for Type A, and $0.60N_{cr}$ and N_{cr} for Type B. For r_0 = 4.0 and 8.0, the reduction of the brace compressive strength was smaller than assumed in design, between $0.57N_{cr}$ and N_{cr} for Type A, and $0.85N_{cr}$ and N_{cr} for level-2 ground motions. This is consistent with the pushover analysis results. The same observation is extended to Type C where the reduction of the brace compressive strength was limited. The figure shows that, for the tall frames, the braces at the top of braced frames were subjected to larger inelastic demands, and hence larger reduction of the brace compressive strength.

Figure 8.11 to Figure 8.13 plots the relationship between the brace compressive strength and the brace contraction. As expected, the braces that experienced large contraction had large reduction of its compressive strength. For the 4-story systems the braces in the models designed with Type A and B with r_0 = 2.0 developed large brace contraction, with the maximum normalized brace contraction over brace length exceeding 0.06. The braces in the braced frame models designed with Type B with r_0 = 8.0 and Type C developed small normalized brace contraction, within 0.03 and 0.02, respectively. For the taller braced frames, the brace contraction was small. From all the models, the peak brace contraction occurred in the models designed with design approach Type A.

The compressive response is further discussed in Figure 8.14 to Figure 8.16. The figure shows the relationship between brace contraction and the story drift angle for the 4-, 8-, and 12-story systems, respectively. The figure shows the relationship between brace contraction and the story drift angle all the stories. The figure shows that there is a linear relationship between the contraction of the braces and the story-drift angle.

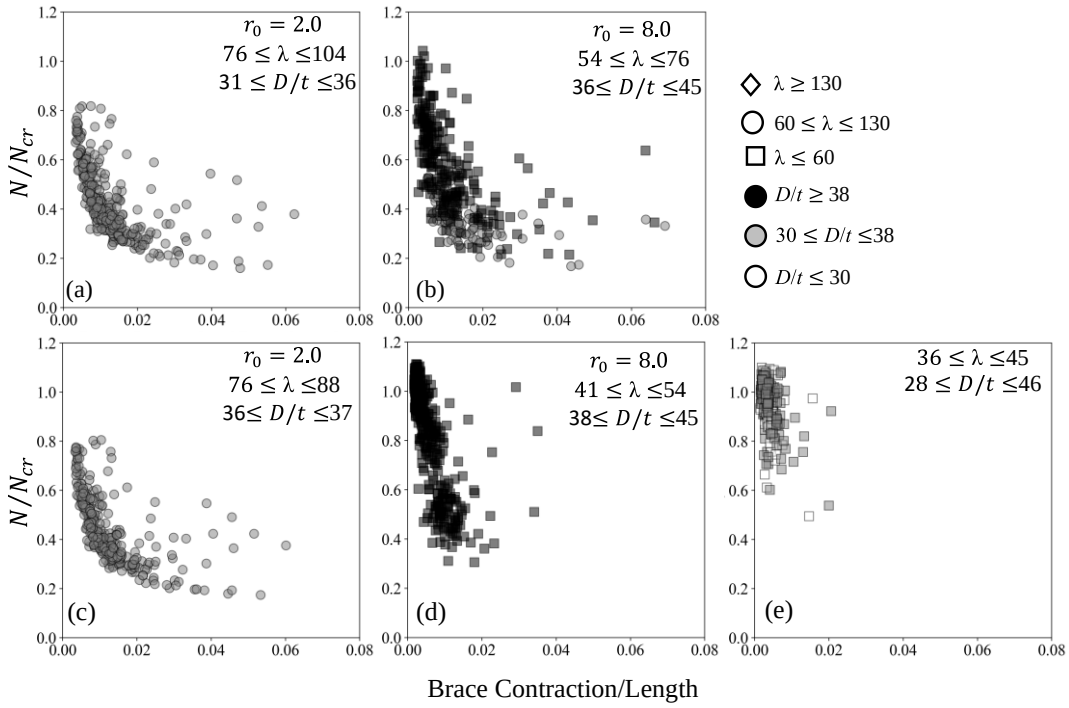

Figure 8.11: Brace Compressive Response for the 4-story systems employing the flexible bracing connection: (a) Type A with r_0= 2.0; (b) Type A with r_0= 8.0; (c) Type B with r_0= 2.0; (d) Type B with r_0= 8.0, and (e) Type C.

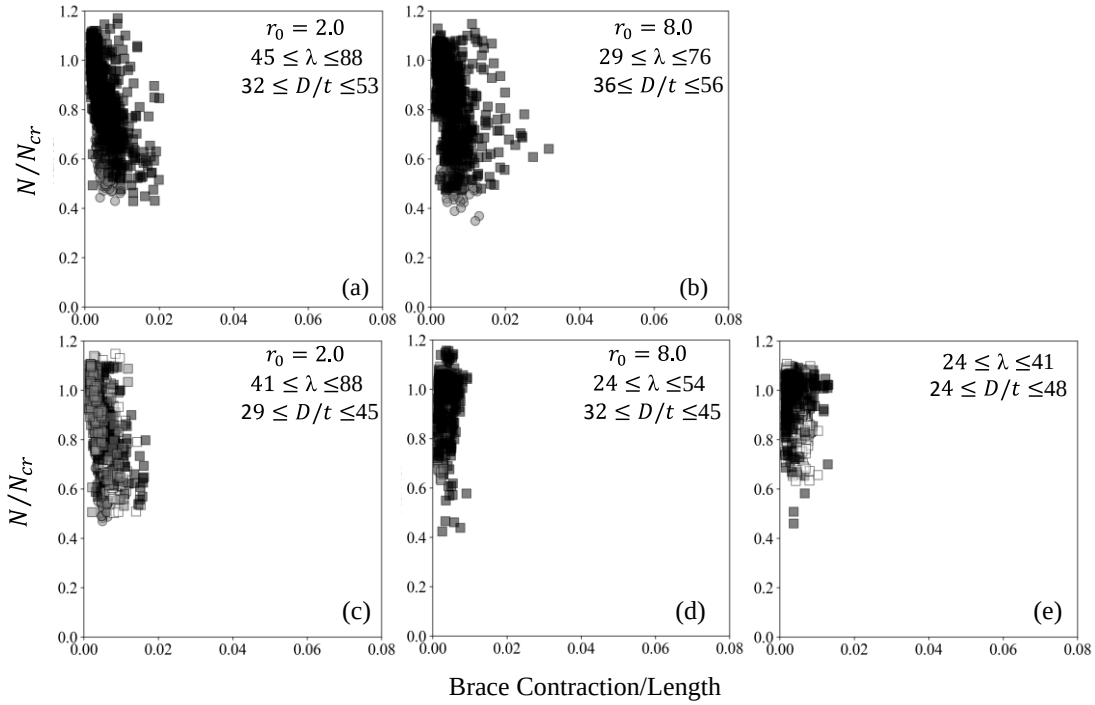

Figure 8.12: Brace Compressive Response for the 8-story systems employing the flexible bracing connection: (a) Type A with r_0= 2.0; (b) Type A with r_0= 8.0; (c) Type B with r_0= 2.0; (d) Type B with r_0= 8.0, and (e) Type C.

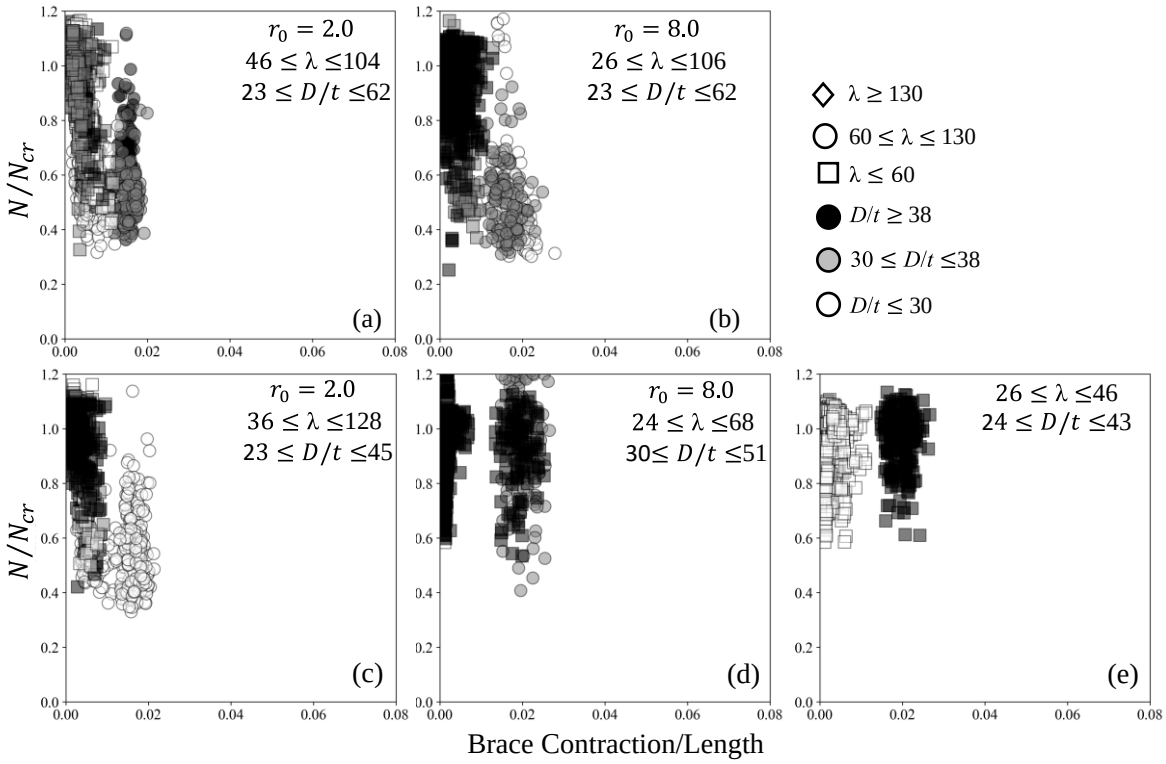

Figure 8.13: Brace Compressive Response for the 12-story systems employing the flexible bracing connection: (a) Type A with r_0= 2.0; (b) Type A with r_0= 8.0; (c) Type B with r_0= 2.0; (d) Type B with r_0= 8.0, and (e) Type C.

Except for the braced frame models with Type A with r_0= 8.0 and C, the contraction of the braces was small compared to the remaining cases.

Figure 8.17 to Figure 8.19 plots the ductility demands for both braces under tension and compression for the 4-, 8-, and 12- story systems employing the flexible bracing connection under level-2 and level-3 ground motion demands. The figure plots the peak ductility demand at any story. The figure shows that, for the chevron-braced MRFs designed design approach Type A and B with r_0 = 2.0, and Type C, the braces exhibit larger ductility demands in both tension and compression. On the other hand, for the 4-story systems the frames designed with r_0 = 4.0 and r_0 = 8.0, the braces deformed primarily in compression, which is typical of chevron braced frames where beam yielding is allowed. Despite yielding of the braces, the tension ductility was significantly small.

For the 8-, and 12- story systems, the braces were subjected to smaller ductility demands in both tension and compression compared to the 4-story systems. Here, because beam yielding did not occur for most of the ground motions, the brace developed larger ductility demands in tension than for the 4-story systems.

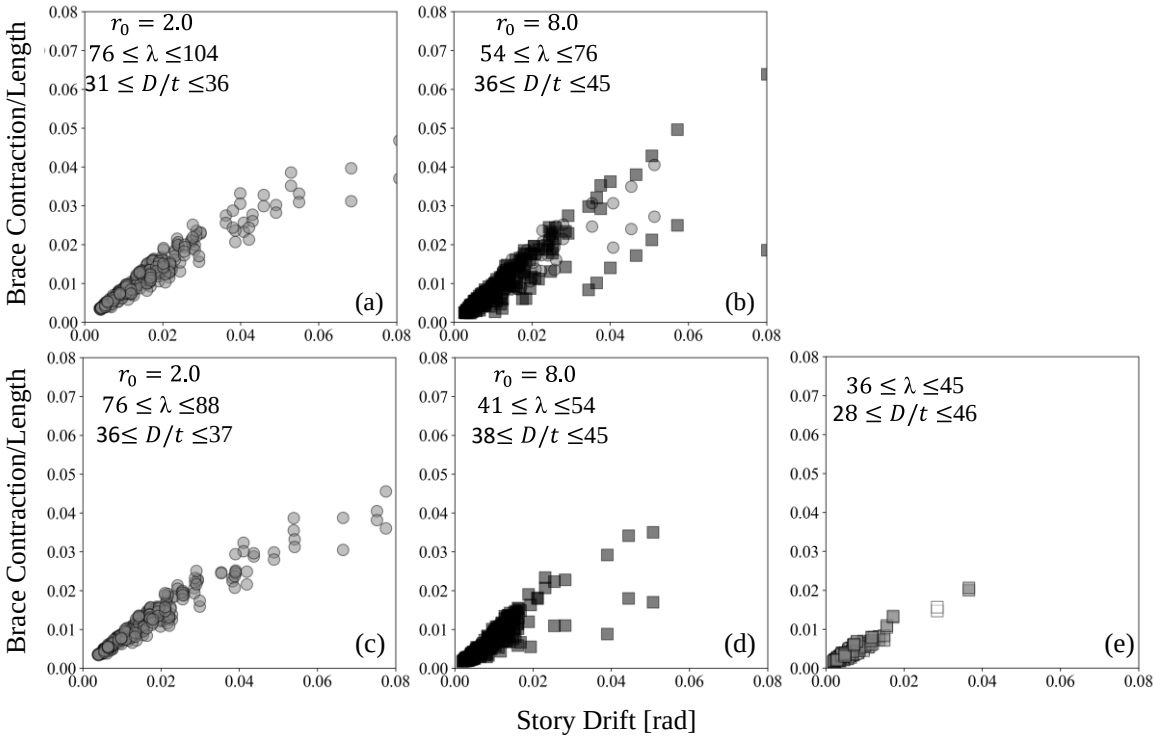

Figure 8.14: Correlation between braces contraction and story drift angle for the 4-story systems employing the flexible bracing connection: (a) Type A with r_0= 2.0; (b) Type A with r_0= 8.0; (c) Type B with r_0= 2.0; (d) Type B with r_0= 8.0, and (e) Type C.

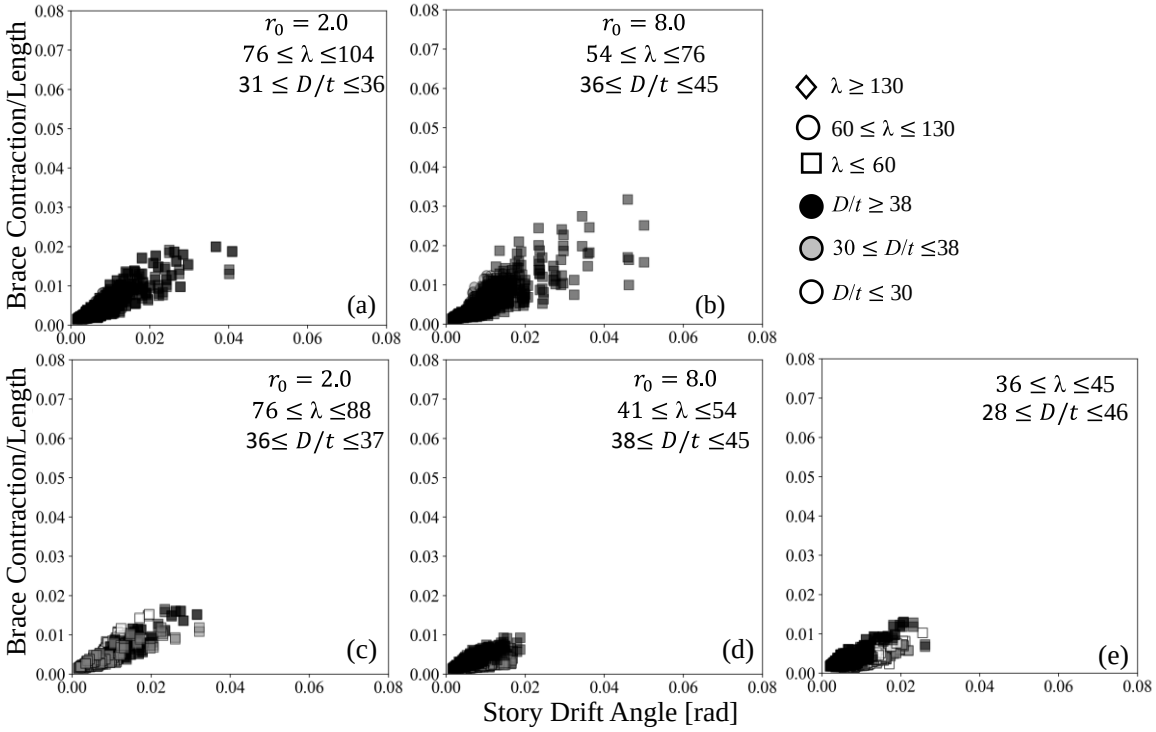

Figure 8.15: Correlation between braces contraction and story drift angle for the 8-story systems employing the flexible bracing connection: (a) Type A with r_0= 2.0; (b) Type A with r_0= 8.0; (c) Type B with r_0= 2.0; (d) Type B with r_0= 8.0, and (e) Type C.

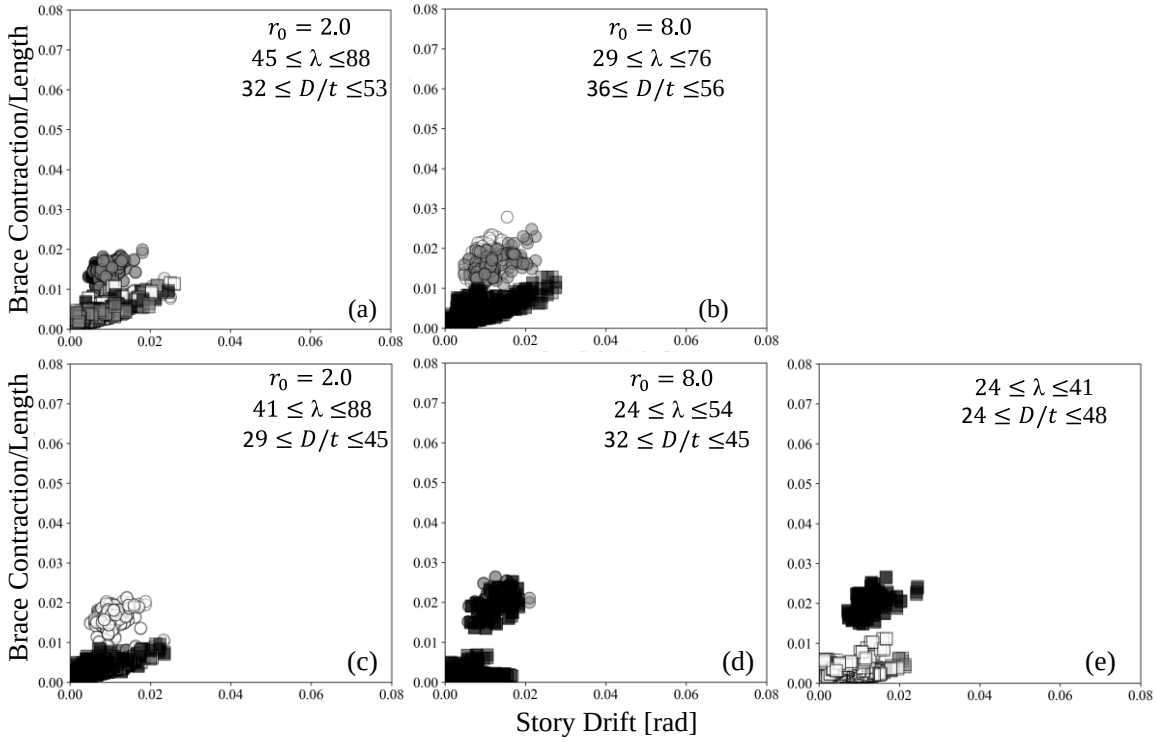

Figure 8.16: Correlation between braces contraction and story drift angle for the 12-story systems employing the flexible bracing connection: (a) Type A with r_0= 2.0; (b) Type A with r_0= 8.0; (c) Type B with r_0= 2.0; (d) Type B with r_0= 8.0, and (e) Type C.

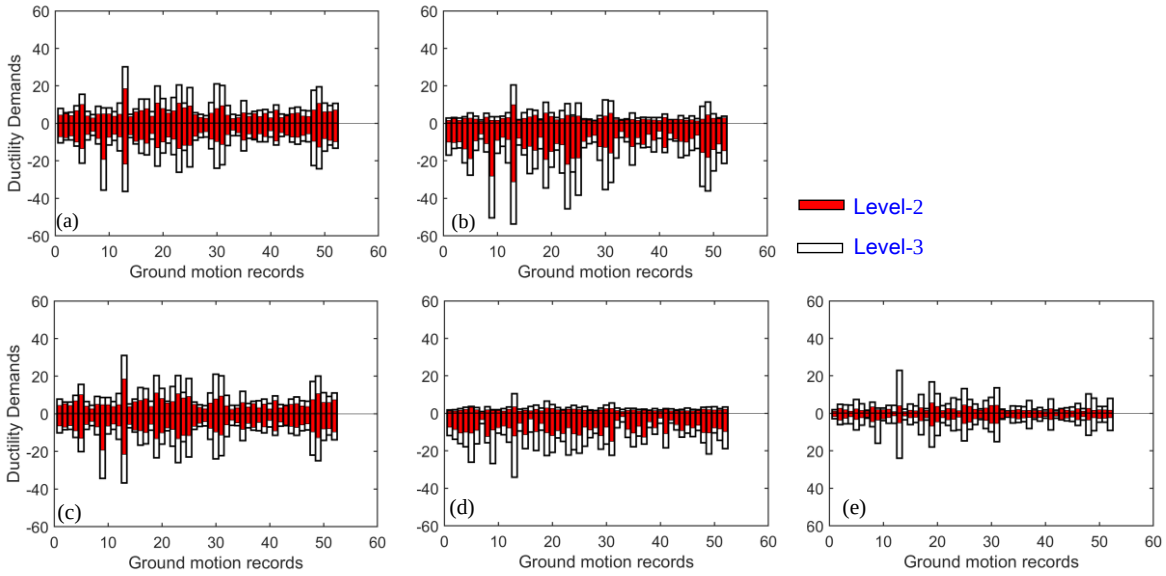

Figure 8.17: Brace ductility response for the 4-story systems employing the flexible bracing connection: (a) Type A with r_0= 2.0; (b) Type A with r_0= 8.0; (c) Type B with r_0= 2.0; (d) Type B with r_0= 8.0; and (e) Type C.

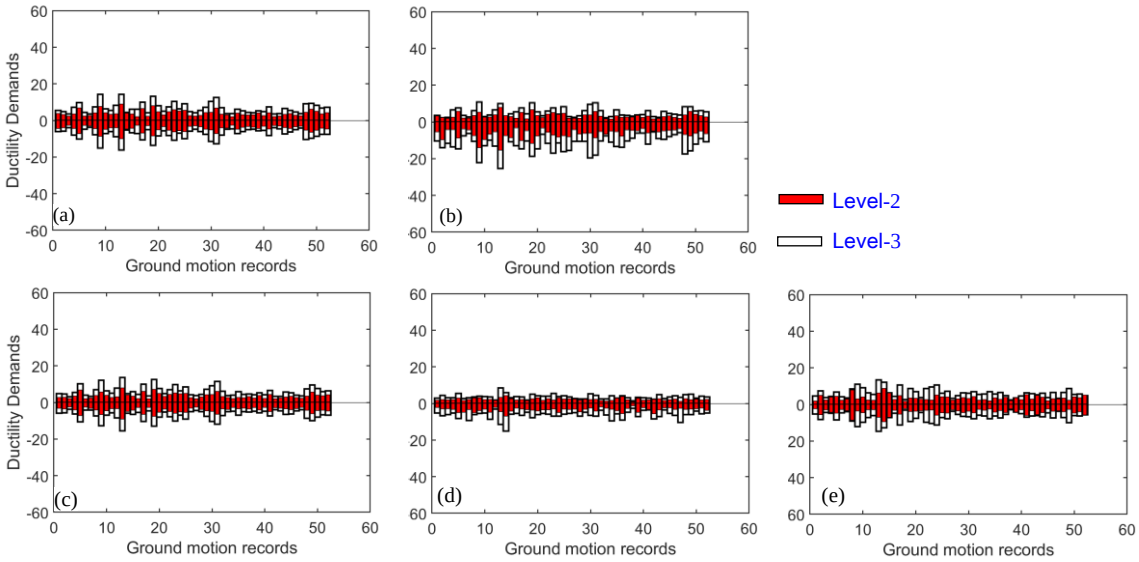

Figure 8.18: Brace ductility response for the 8-story systems employing the flexible bracing connection: (a) Type A with r_0= 2.0; (b) Type A with r_0= 8.0; (c) Type B with r_0= 2.0; (d) Type B with r_0= 8.0; and (e) Type C.

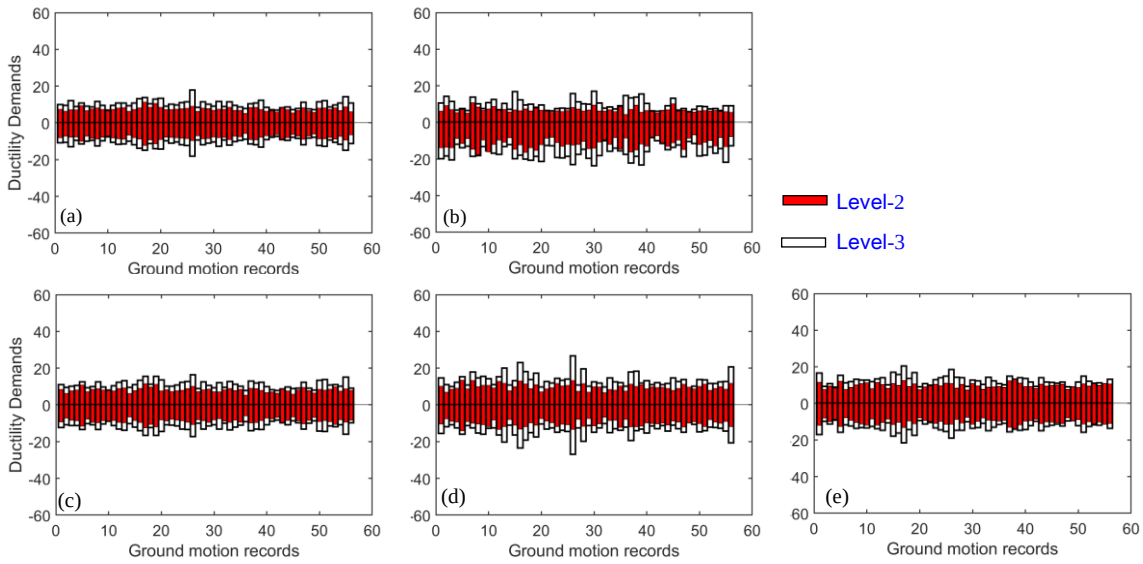

Figure 8.19: Brace ductility response for the 12-story systems employing the flexible bracing connection : (a) Type A with r_0 = 2.0; (b) Type A with r_0 = 8.0; (c) Type B with r_0 = 2.0; (d) Type B with r_0 = 8.0; and (e) Type C.

8.3.2 Beam Response: Behavior and Demands

In chevron-braced MRFs, the performance of the beam is critical. Therefore, the bending moment, the axial force and the deflection demand on the chevron beam are examined.

8.3.2.1 Flexural demands on the beam

The bending moment demands on the chevron-braced beam were sampled to evaluate the performance of the beams. The peak bending moment demands on the beam at the brace to beam intersection were normalized by the beam full plastic capacity, M_p.

Figure 8.20 to Figure 8.22 plots the distribution of the bending moment demands over the height of the structures for the 4-, 8-, and 12- story systems under level-2 and level-3 ground motions. The figures show that, except for a few ground motions, the beams remained elastic under level-2 and level-3 ground motion demands for the braced frames designed using design approach A and B, with r_0=2.0 and Type C.

For design approach A and B, with r_0 = 4.0 and 8.0, there was significant yielding of the beams under level-2 and level-3 ground motions, especially for the 4- story systems. As observed in the distribution of the bending moment demands over the height of the structure for the 8- and 12-story systems shown in Figure 8.21 and Figure 8.22, respectively, yielding of the beams occurred at the upper 4 stories for Type A with r_0 = 8.0 and at the upper 2 stories for Type B with r_0 = 8.0.

There is significant scatter on the response of Type A with r_0 = 8.0. For the 12-story systems, the response was identical to the 8-story systems, with the inelastic demands of the beams concentrating the top 6 stories. The beams remained elastic for the remaining cases

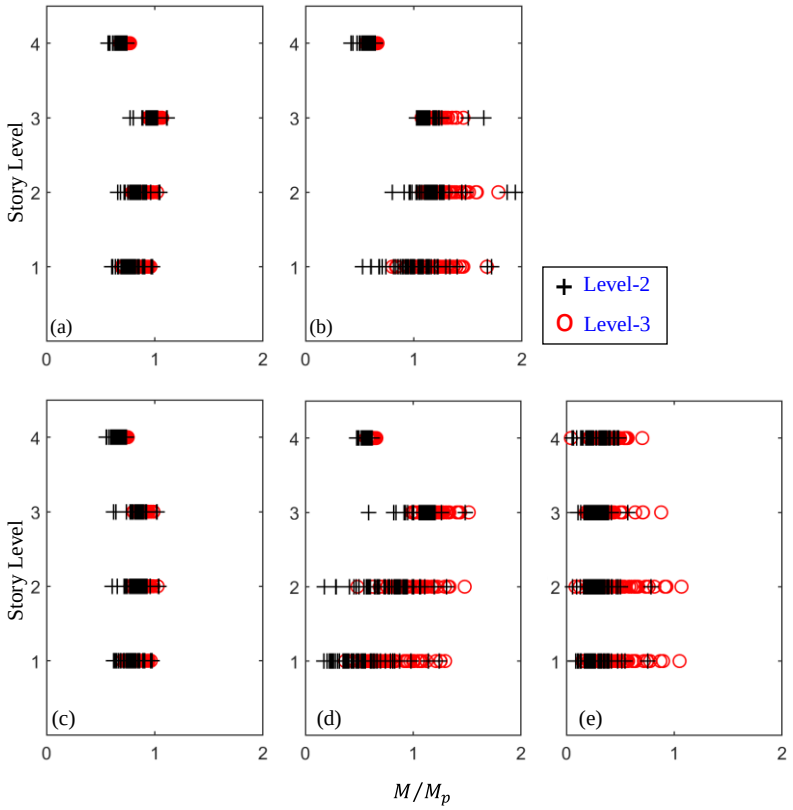

Figure 8.20: Beam flexural response for the 4-story systems employing the flexible bracing connection: (a) Type A with r_0= 2.0; (b) Type A with r_0= 8.0; (c) Type B with r_0= 2.0; (d) Type B with r_0= 8.0; and (e) Type C.

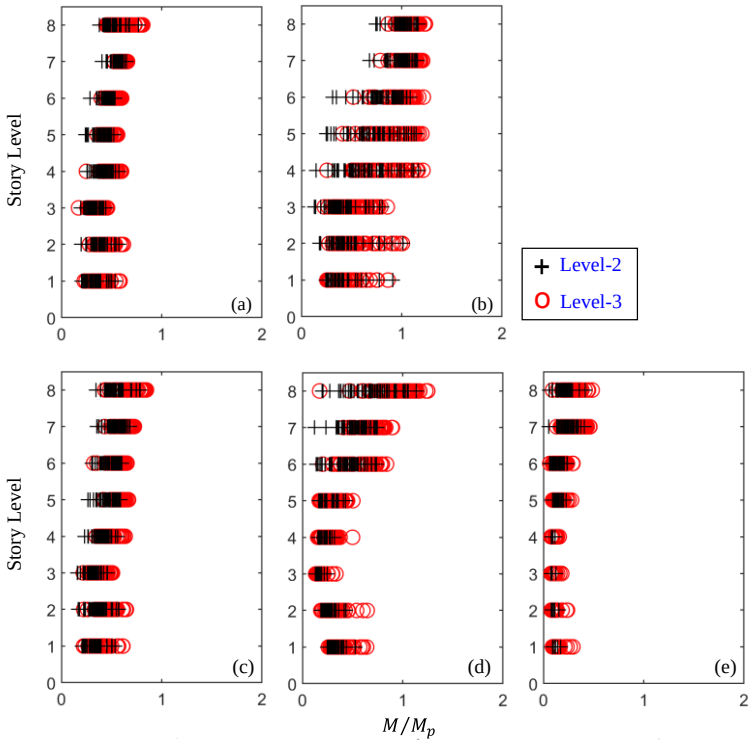

Figure 8.21: Beam flexural response for the 8-story systems employing the flexible bracing connection: (a) Type A with r_0= 2.0; (b) Type A with r_0= 8.0; (c) Type B with r_0= 2.0; (d) Type B with r_0= 8.0; and (e) Type C.

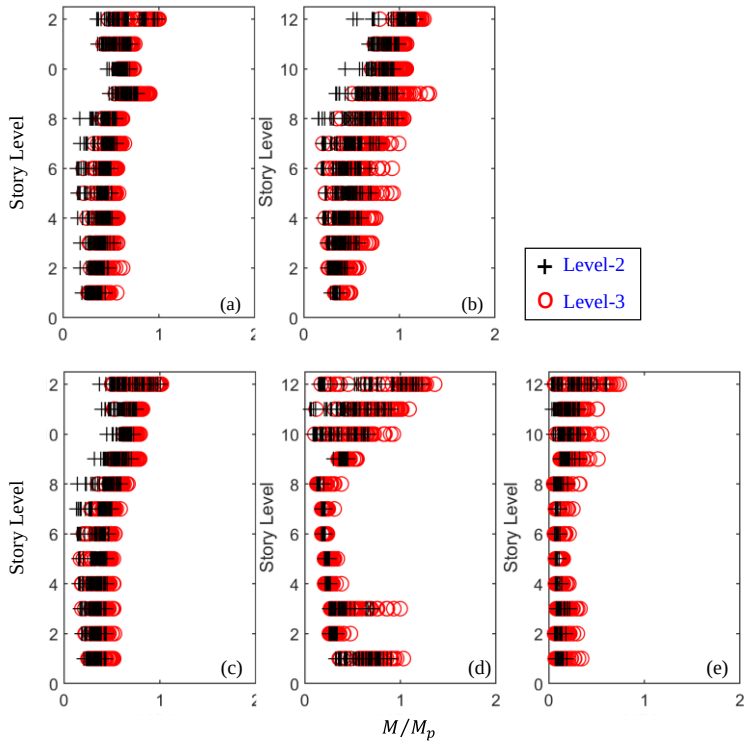

Figure 8.22: Beam flexural response for the 12-story systems employing the flexible bracing connection: (a) Type A with r_0= 2.0; (b) Type A with r_0= 8.0; (c) Type B with r_0= 2.0; (d) Type B with r_0= 8.0; and (e) Type C.

8.3.2.2 Chevron-braced Beam vertical deflection

The vertical deflection at the center of the beam is plotted in Figure 8.23 to Figure 8.25, for the 4-, 8- and 12 story systems. The figure compares the median deflection response of all the braced frame models. As shown in Figure 8.23, for the 4-story systems, the braced frames designed using design approach Type A and B with $r_0 = 2.0$ and Type C were subjected to relatively small beam vertical deflections (within 10 mm). Between design approach A and B, with $r_0 = 2.0$ there is negligible difference on the magnitude of the beam deflection at midspan. But for $r_0 = 4.0$ and $r_0 = 8.0$, the beam intersecting braces were subjected to large median vertical deflection demands due to unbalance force which forces yielding of the beam. For $r_0 = 4.0$ and $r_0 = 8.0$, Type A was subjected to larger median beam deflection demands at the first and second story, compared to Type B. The discrepancy is particularly large for $r_0 = 8.0$. For both $r_0 = 4.0$ and $r_0 = 8.0$, the largest median beam deflection occurred at the 3rd story level, but the largest difference between design approach type A and B was

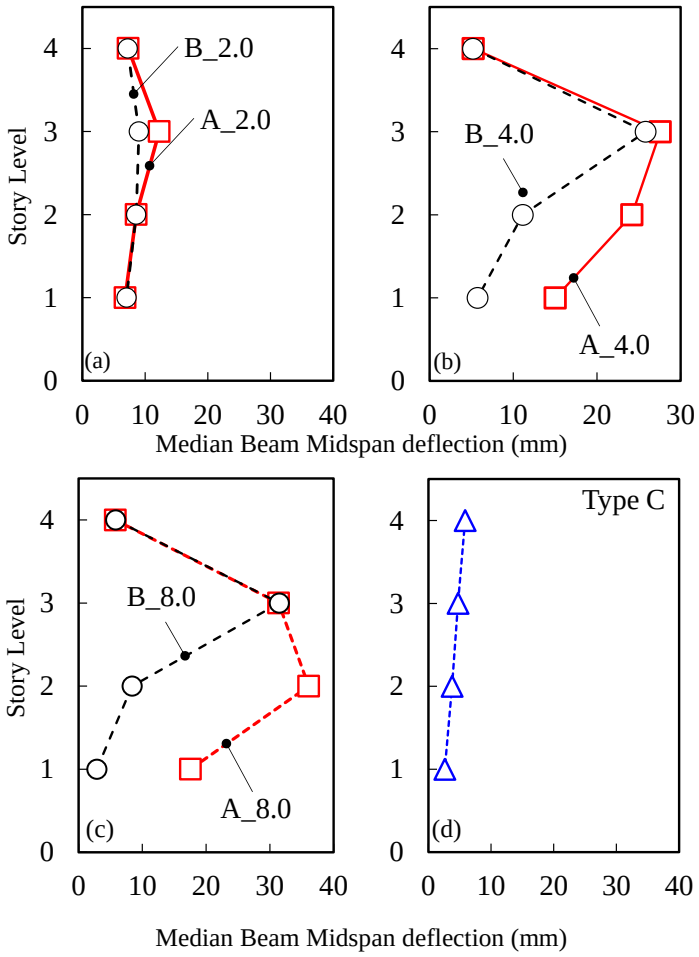

Figure 8.23: Simulated Mean Midspan deflection of chevron beam for the 4-story systems under level 2 ground motions employing the flexible bracing connection: (a) $r_0 = 2.0$, (b) $r_0 = 4.0$, (c) $r_0 = 8.0$ and (d) Type C.

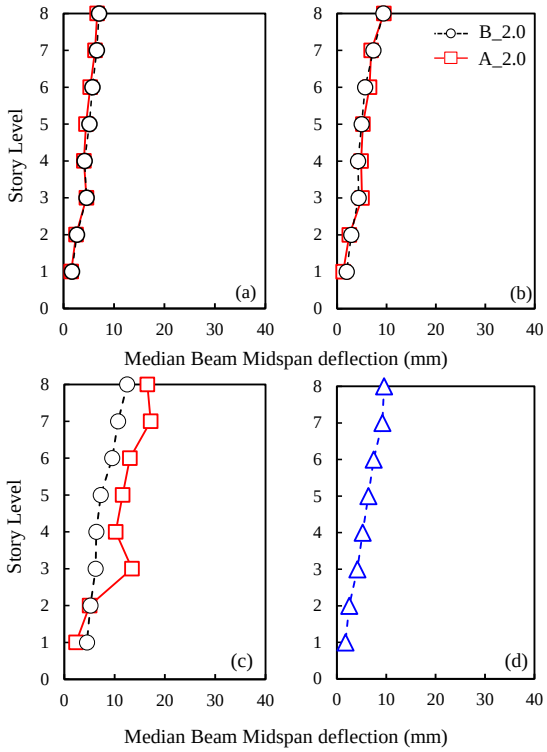

Figure 8.24: Simulated Mean Midspan deflection of chevron beam for the 8-story systems under level 2 ground motions employing the flexible bracing connection: (a) $r_0 = 2.0$, (b) $r_0 = 4.0$, (c) $r_0 = 8.0$ and (d) Type C.

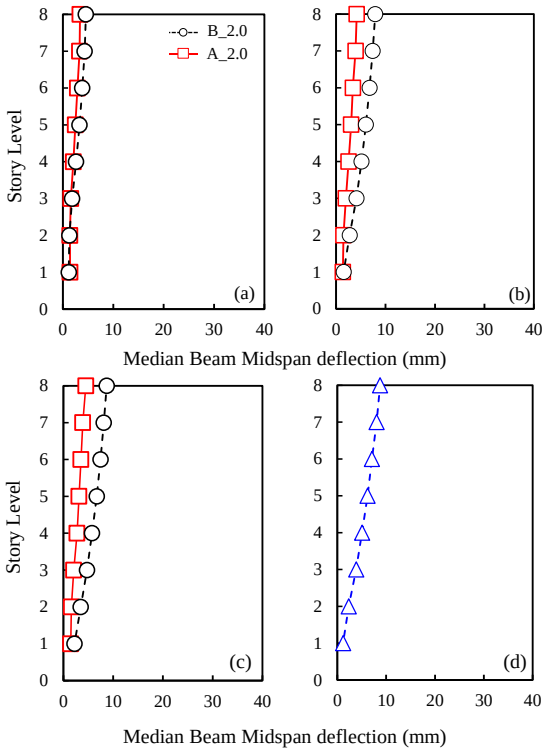

Figure 8.25: Simulated Mean Midspan deflection of chevron beam for the 12-story systems under level 2 ground motions employing the flexible bracing connection: (a) $r_0 = 2.0$, (b) $r_0 = 4.0$, (c) $r_0 = 8.0$ and (d) Type C.

observed at the 2nd story floor level. Type A led to 54% and 77% larger median beam deflection for $r_0 = 4.0$ and $r_0 = 8.0$, respectively.

From all the cases, Type C was subjected to smaller median vertical deflections compared to the remaining braced frame systems. For the 8- and 12-story systems, the beams were subjected to smaller beam deflection demands compared to the 4-story systems, because, as discussed previously, degradation of th brace compressive strength was limited and hence the force unbalance induced on the beam was small.

8.3.3 Column Response: Behavior and Demands

Damage to columns due to buckling or the formation of plastic hinges may be detrimental to the performance of the braced frame systems as it may lead to collapse of the building structures. Thus, the behavior of the structures must be monitored to ensure the columns behaved as intended in design or if undesirable failure modes such as buckling, yielding, and or formation of plastic hinges occurred.

8.3.3.1 Bending Moment demands on the Column

Similarly, as for the beams, the flexural demands of the columns were studied. Figure 8.26 plots the bending moment against story-drift response of the first story columns for the braced frame

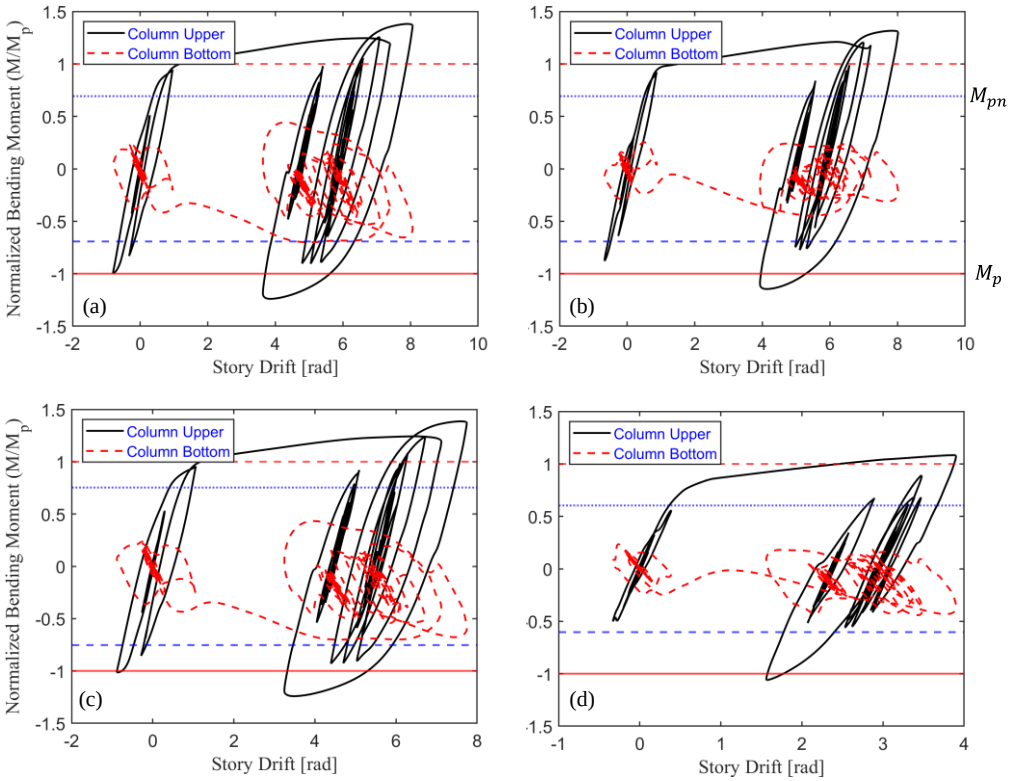

Figure 8.26: Bending moment versus Story drift relationship for the first story column: (a) Case A with r_0= 2.0; (b) Case A with r_0= 8.0; (c) Case B with r_0= 2.0; (d) Case B with r_0= 8.0;

models designed with design approach Type A and B, with $r_0 = 2.0$ and 8.0 for the Chi-Chi Taiwan ground motion. The figure shows that under this ground motion, the columns are subjected to significantly large story drift demands. Experimental observation by Mukaide et al. [53] and subsequent numerical simulation by Suzuki et al. [51], [52] showed that the flexural strength of rectangular-HSS columns tends to deteriorate with cyclic-loading larger than 5% drift.

In the numerical simulations however, because the fiber model cannot capture local buckling of the columns, cyclic-deterioration of the strength of the rectangular-HSS columns did not occur. In fact, the column strength increased due to strain hardening and no degradation occurred despite undergoing close to 10% rad story drift in Model A with r_0= 8.0. This response does not represent the true response and the columns may be having significantly better performance than expected. This highlights one of the limitations of the numerical model used to study the seismic performance of the braced frames.

Figure 8.27 to Figure 8.29 plot the distribution of the bending moment demands at the bottom of the

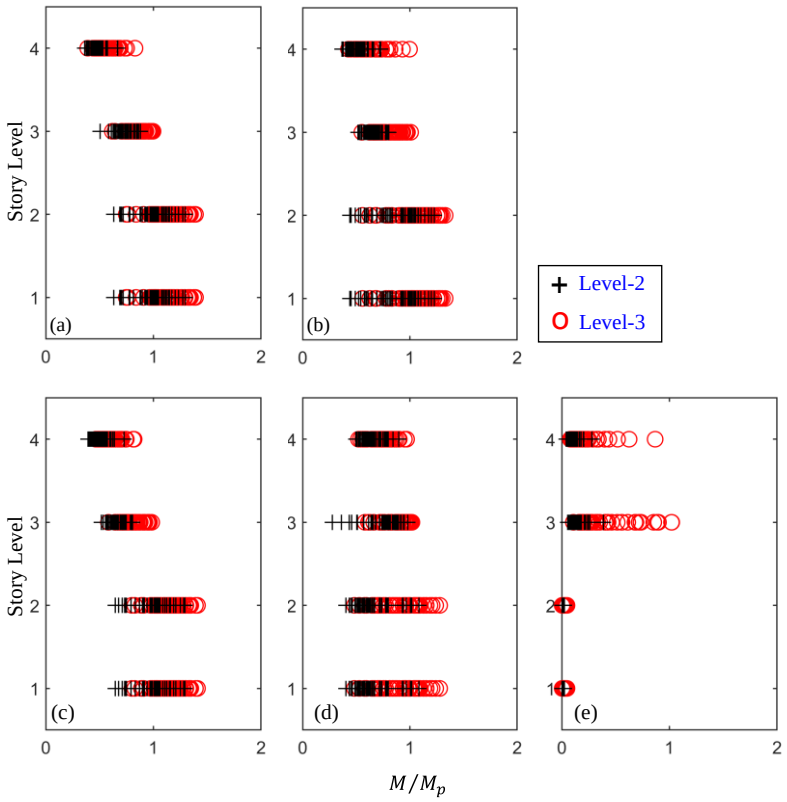

Figure 8.27: Bending moment demands at the bottom of the columns for the 4-story systems employing the flexible bracing connection: (a) Type A with r_0= 2.0; (b) Type A with r_0= 8.0; (c) Type B with r_0= 2.0; (d) Type B with r_0= 8.0; and (e) Type C.

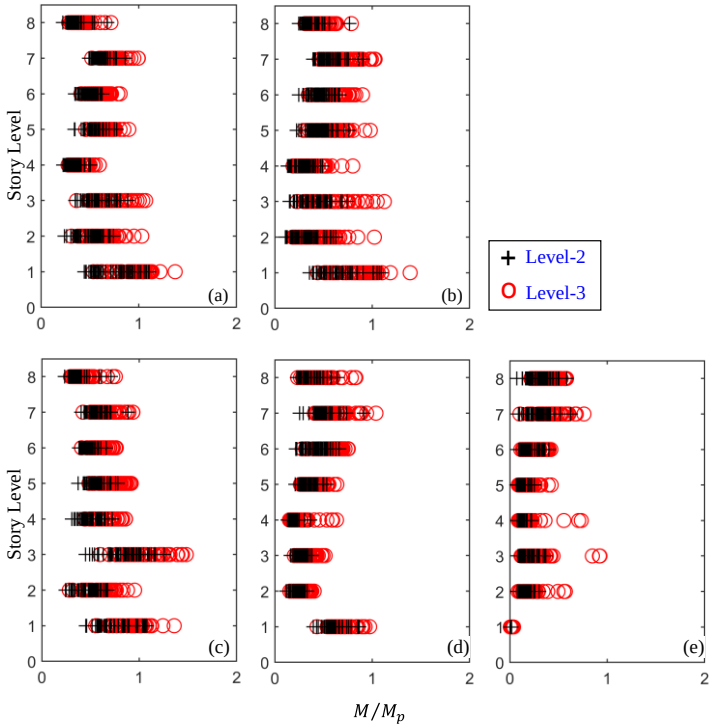

Figure 8.28: Bending moment demands at the bottom of the columns for the 8-story systems employing the flexible bracing connection: (a) Type A with r_0= 2.0; (b) Type A with r_0= 8.0; (c) Type B with r_0= 2.0; (d) Type B with r_0= 8.0; and (e) Type C.

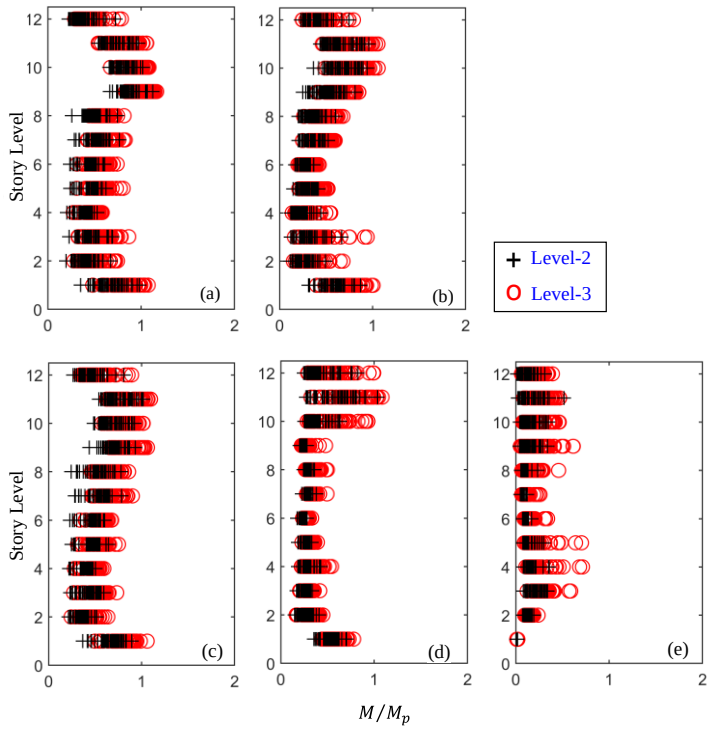

Figure 8.29: Bending- moment demands at the bottom of the columns for the 8-story systems employing the flexible bracing connection I: (a) Type A with r_0= 2.0; (b) Type A with r_0= 8.0; (c) Type B with r_0= 2.0; (d) Type B with r_0= 8.0; and (e) Type C.

column over the height of the building. The bending moment is normalized by the reduced plastic moment of the column. Here, only the maximum normalized bending moment at the top and bottom ends of the columns in the same story are discussed. For the sake of simplicity, only the maximum, mean and mean plus one standard deviation are shown.

8.3.3.2 Axial force demands on the Column

This section discusses the peak axial force demands on the chevron braced frame columns. The peak axial force demands for each column were sampled for all the ground motion records. The column demand includes only the lateral seismic loads. The contribution due to gravity loads were not included.

The peak values were normalized by both the yielding strength of the column and the column design axial force.

The first will help to verify the behavior of the columns whereas, the later will help to judge the demands used in the design stage. The normalized column axial force demands are shown in Figure 8.31 to Figure 8.33 for both level-2 and level-3 ground motions. As observed in the figure, both level-2 and level-3 ground motions led to identical normalized column axial force demands for all the braced frames considered. The figure shows that for design approach type A, the normalized column demands were close to unity which suggests that the assumption that all the braces buckled simultaneously over the height of the column does not lead to over overdesigned columns. For design approach type B with $r_0 = 8.0$ however, the normalized column axial force demands exceeded the axial force used in design, by close to 35% at the first story, but otherwise matched the axial force demands used in the design for the upper stories. Similarly, for type C the normalized axial force demands were smaller than unity throughout the height of the building. This suggest that for the low-rise braced frames, the assumption that the braces buckled simultaneously over the height of the frame will in most cases, not lead to over conservative axial force demands on the columns.

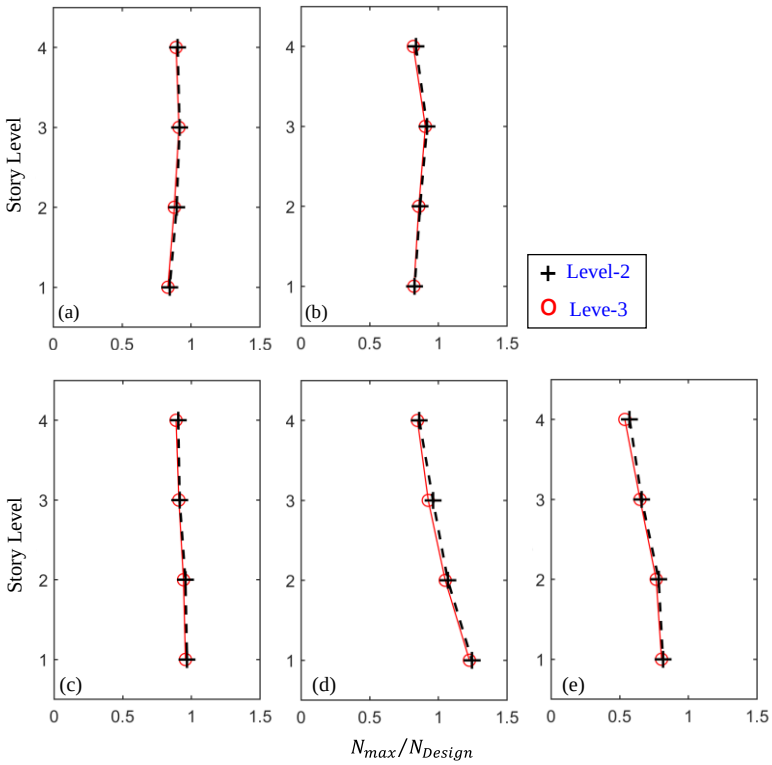

Figure 8.31: Axial force demands on the columns of the 4- story systems: (a) Type A with r_0= 2.0; (b) Type A with r_0= 8.0; (c) Type B with r_0= 2.0; (d) Type B with r_0= 8.0; and (e) Type C.

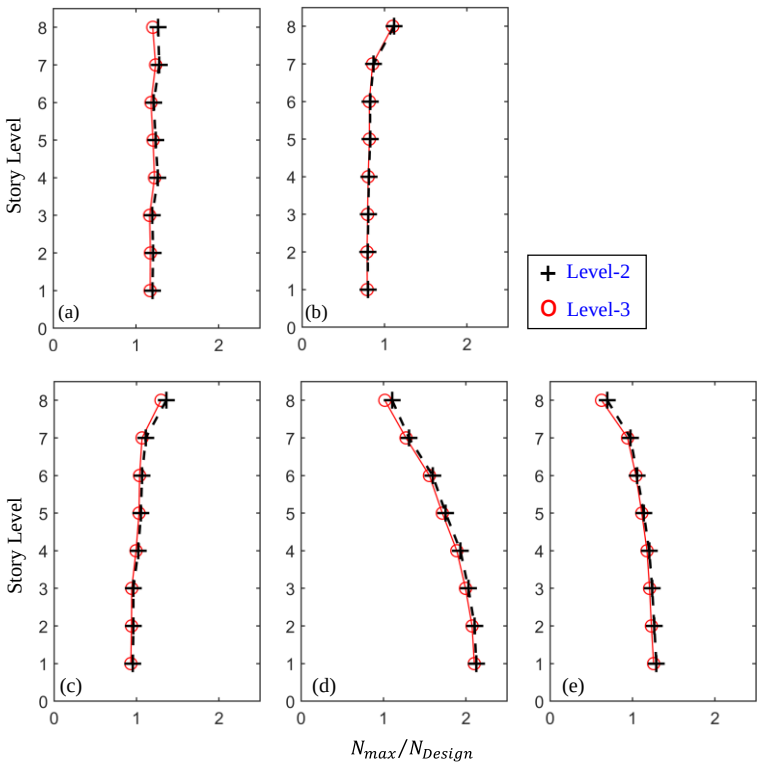

Figure 8.32: Axial force demands on the columns of the 8- story systems: (a) Type A with r_0= 2.0; (b) Type A with r_0= 8.0; (c) Type B with r_0= 2.0; (d) Type B with r_0= 8.0; and (e) Type C.

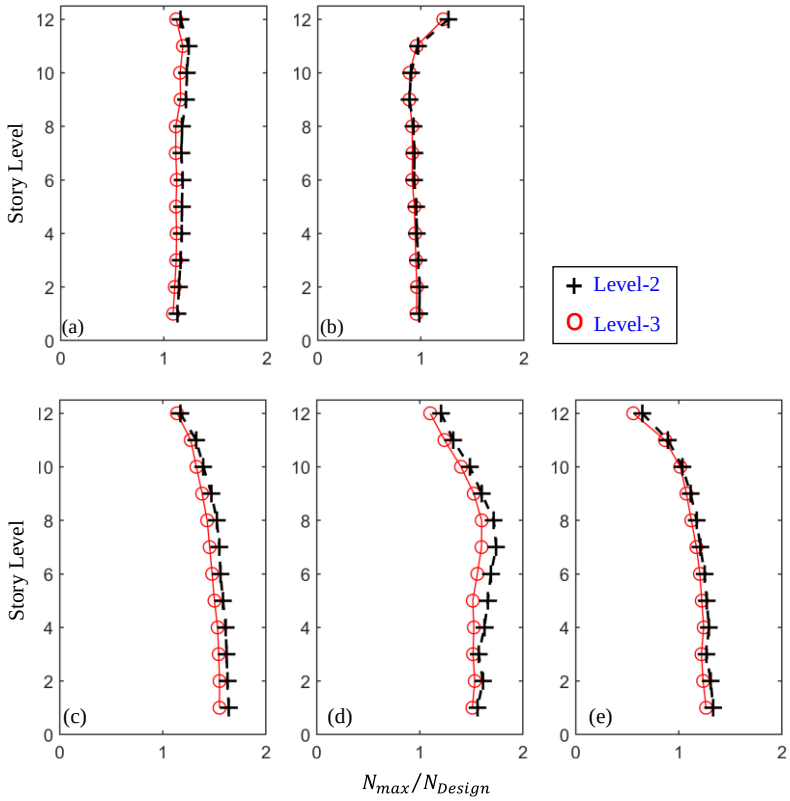

Figure 8.33: Axial force demands on the columns of the 12- story systems: (a) Type A with r_0= 2.0; (b) Type A with r_0= 8.0; (c) Type B with r_0= 2.0; (d) Type B with r_0= 8.0; and (e) Type C.

The axial force versus bending moment interaction plots for the 4-, 8-, and 12-story systems are shown in Figure 8.34 to Figure 8.36, for Chi-Chi Taiwan ground motion. For the 4-story systems, the column axial force grew large growing close to $0.3N_y$ for Type A and B with r_0=2.0 but grow larger for the braces frames with large r_0 value. For the 8- and 12- story braced frame systems, the columns were subjected to small bending moment demands but to large axial force demands. Under the Chi-Chi Taiwan, the columns developed large axial force demands with the braced frame yielding for Type B with r_0=8.0 and Type C.

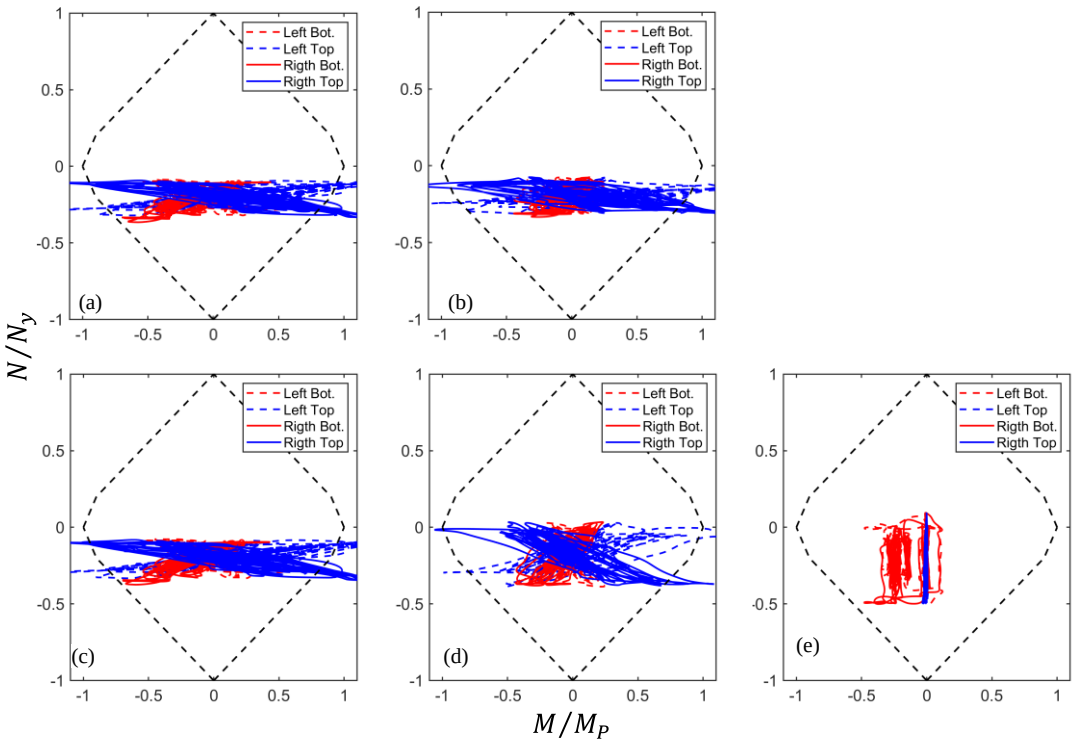

Figure 8.34: Interaction curve for the 4-story structures subjected to the Chi-Chi Taiwan ground motion under level-2 demands: (a) Type A with r_0=2.0, (b) Type A with r_0=8.0, (c) Type B with r_0=2.0, (d) Type B with r_0=8.0, and (a) Type C.

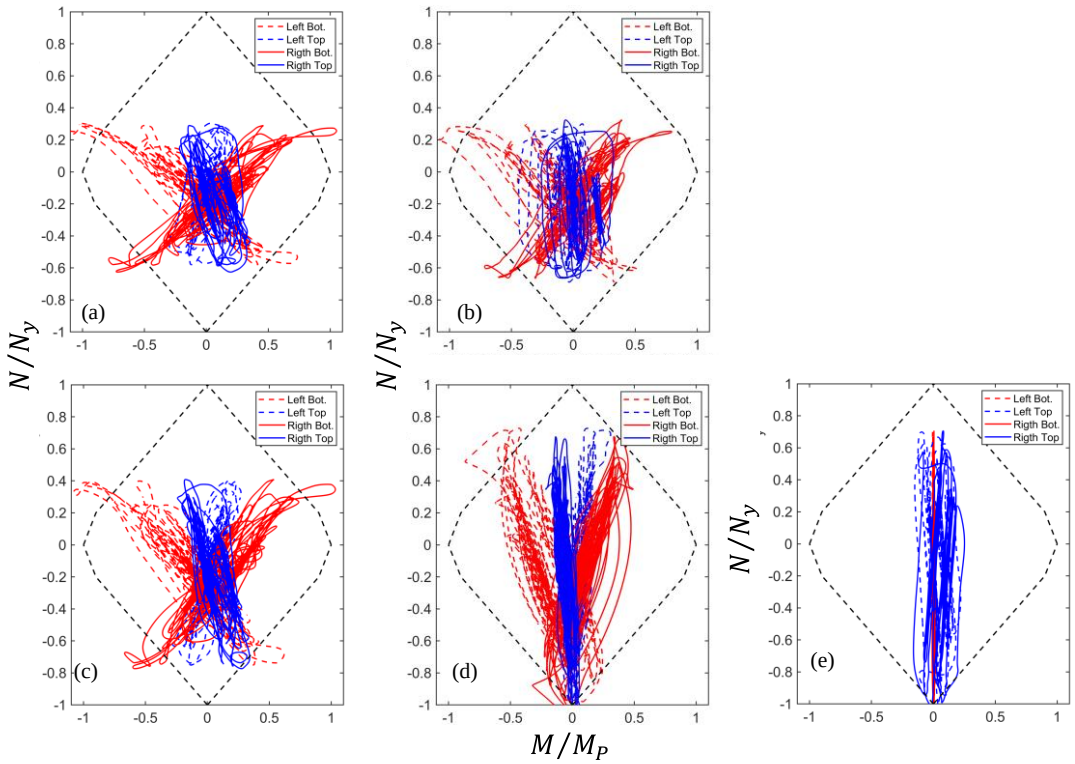

Figure 8.35: Interaction curve for the 8-story structures subjected to the Chi-Chi Taiwan ground motion under level-2 demands: (a) Type A with r_0=2.0, (b) Type A with r_0=8.0, (c) Type B with r_0=2.0, (d) Type B with r_0=8.0, and (a) Type C.

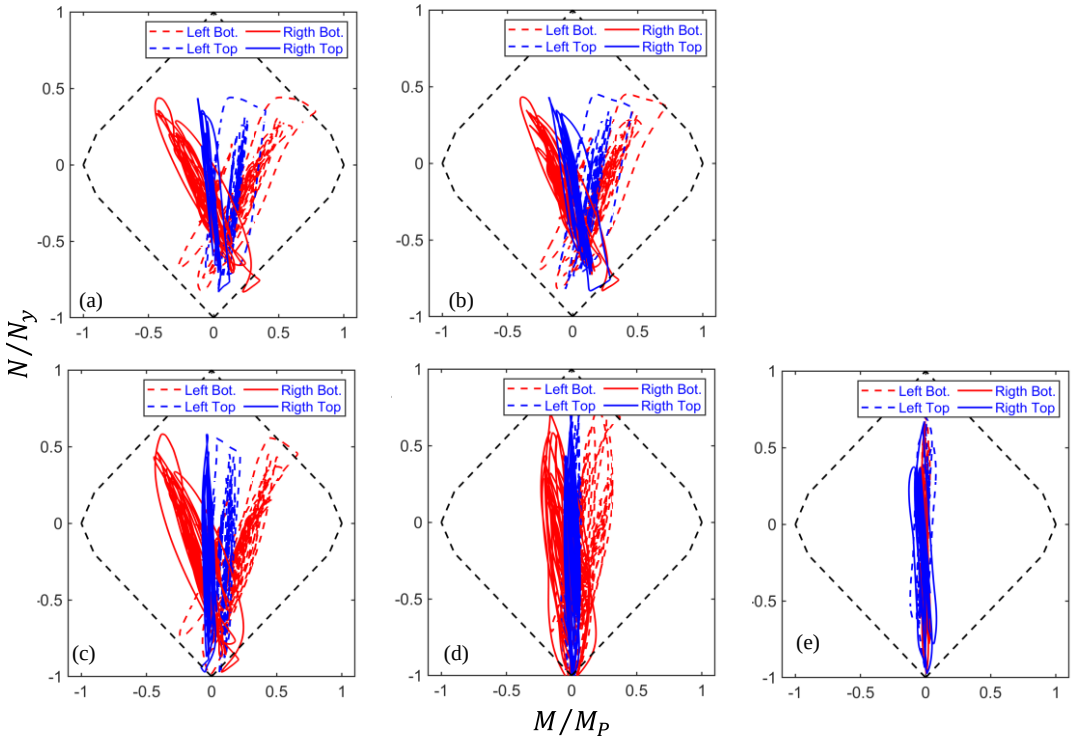

Figure 8.36: Interaction curve for the 8-story structures subjected to the Chi-Chi Taiwan ground motion under level-2 demands: (a) Type A with r_0=2.0, (b) Type A with r_0=8.0, (c) Type B with r_0=2.0, (d) Type B with r_0=8.0, and (a) Type C.

8.3.4 Energy dissipation mechanism

The performance of steel chevron-braced MRF is highly dependent on its energy dissipating mechanism. The probability of formation of the strong-beam (SB), the weak-beam(WB) or the combined mechanism(CM), is discussed next.

Figure 8.37 shows the percentage of ground motions where each of the energy dissipation mechanism controlled the energy dissipation mechanism of the braced frames for the 4-story systems.

For design approach Type A with r_0 = 2.0 the strong-beam mechanism controlled the energy dissipation mechanism of the braced frames for 82 % of the ground motions. For Type B with r_0= 2.0, the frame behaved as intended in design, with the braces yielding for nearly all the ground motions.

For design approach Type A with r_0= 4.0 and 8.0, and Type B with r_0= 4.0, the combined mechanism controlled for most of the ground motions. The combined mechanism also controlled the energy dissipated mechanism for most of the ground motion (61%) for Type B with r_0= 8.0, however, the weak-beam mechanism controlled, for 27% of the ground motions.

For Type C, the braces yielded for all the combinations of bracing connections and earthquake hazard level.

As observed in Figure 8.37(b), regardless of the design approach and the r_0 value, the rigid bracing connection forced yielding of the braces for more cases than the flexible bracing connection, because the braced frames were subjected to smaller deformation demands. Level-3 ground motion demands forced the formation of the combined-mechanism for most cases for both Type A and B with

r_0= 4.0 and 8.0.

Figure 8.38 shows the probability of beam and brace yielding for the 8-story systems. For r_0= 2.0 and 4.0, the effect of the design approach was negligible. The braces yielded for almost all the ground motions. For $r_0 = 8.0$, the combined mechanism controlled the energy-dissipation mechanism for more cases for the braced frame systems designed using Type A than Type B. Similar to the 4-story systems, for Type C the braces yielded for all the ground motions. The rigid bracing connection forced yielding of the braces in all the braced frame systems, regardless of the design philosophy or r_0.

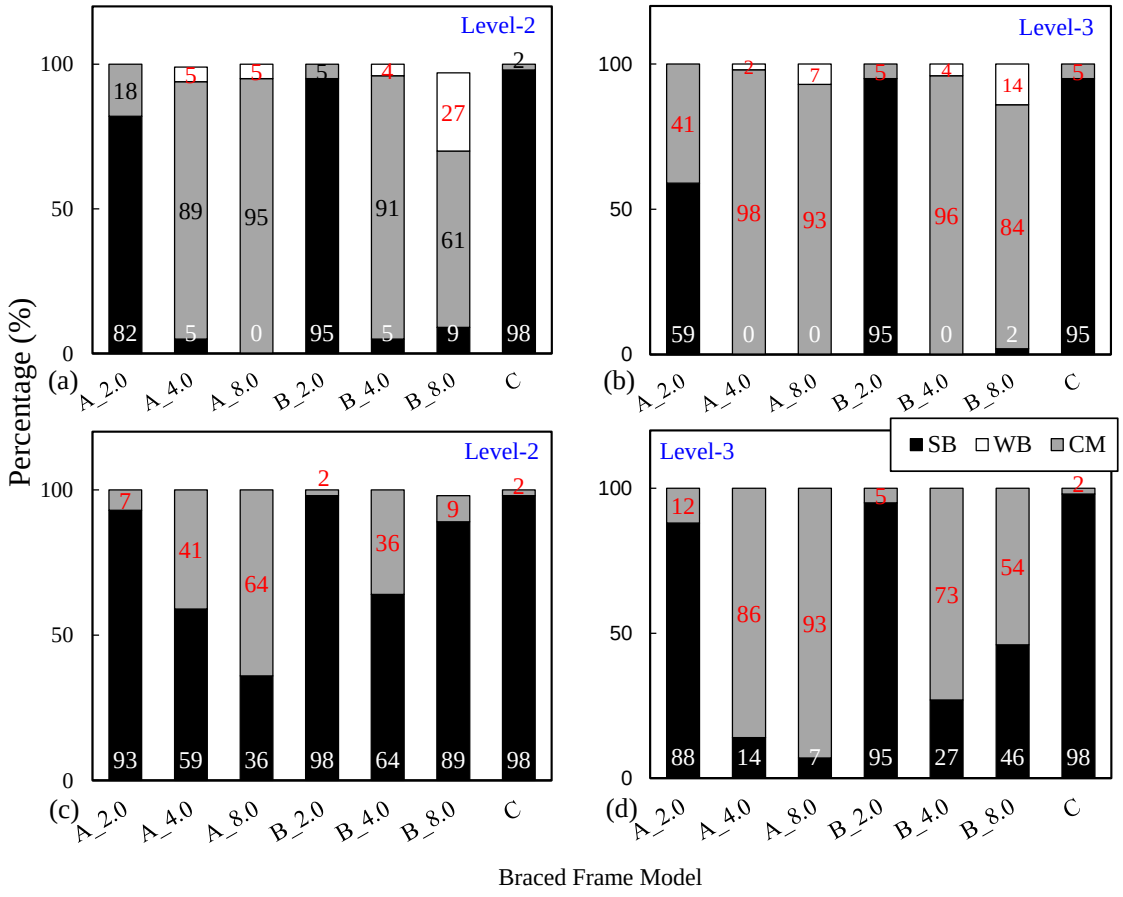

Figure 8.37: Percentage to formation of energy-dissipation mechanism for the 4-story structures under level-2 and level-3: (a) and (b) flexible bracing connection , and (c) and (d) rigid bracing connection.

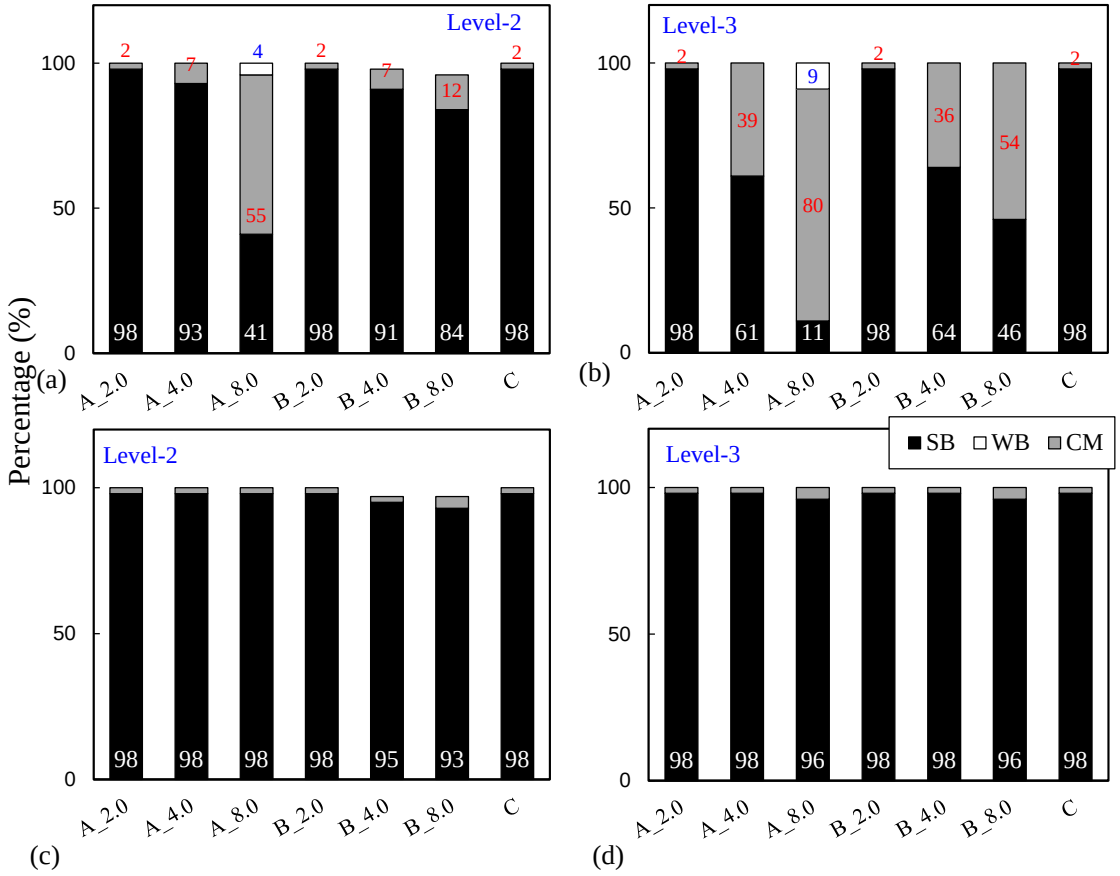

Figure 8.38: Percentage to formation of energy-dissipation mechanism for the 8-story structures under level-2 and level-3: (a) and (b) flexible bracing connection , and (c) and (d) rigid bracing connection.

For the 12-story systems, the braced frames designed with r_0= 2.0 and Type C behaved as intended in design. The beams remained elastic for practically all the ground motions. For r_0=4.0 and 8.0, design approach Type A forced yielding of the beams for more cases than Type B for both Level-2 and Level-3. As observed for the 4- and 8-story systems, the rigid bracing connection forced yielding of the braces for nearly all the ground motions, for all the braced frame systems.

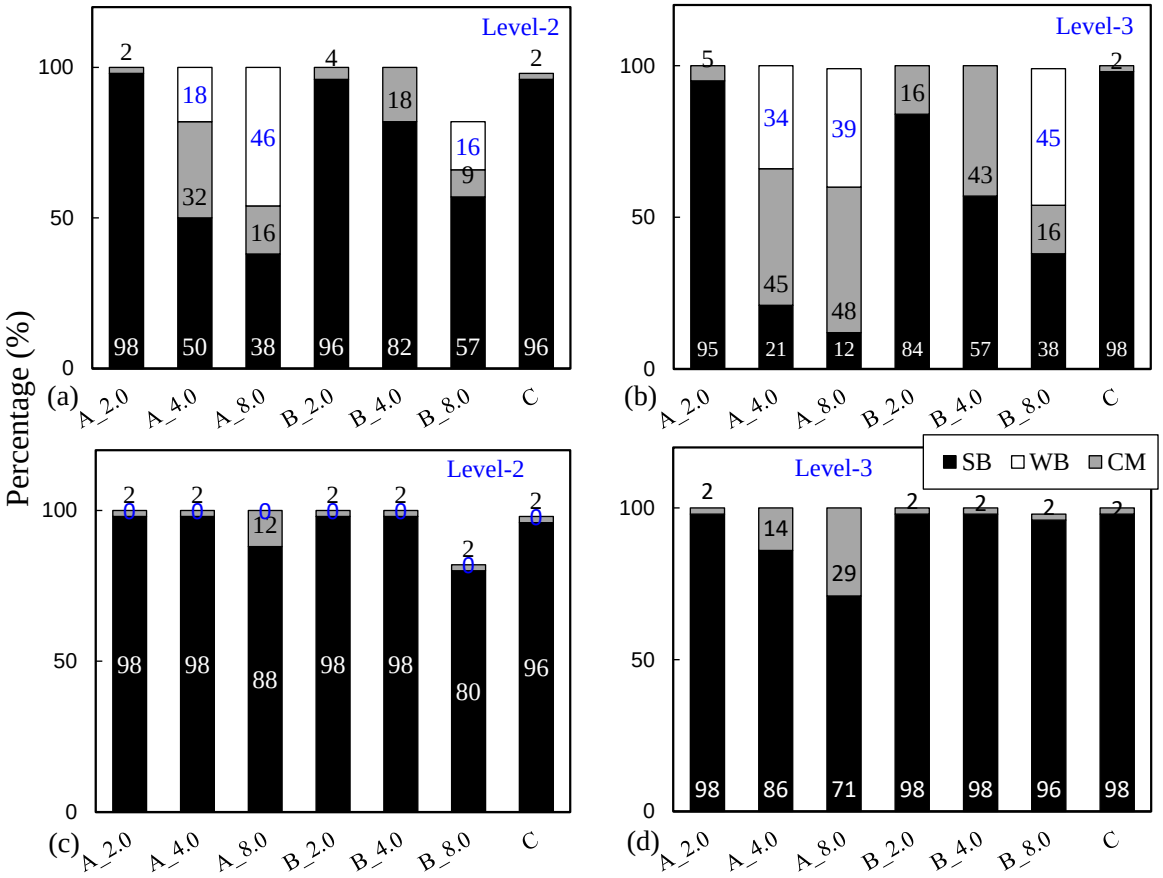

Figure 8.39: Percentage to formation of energy-dissipation mechanism for the 12-story structures under level-2 and level-3: (a) and (b) flexible bracing connection , and (c) and (d) rigid bracing connection.

9. SUMMARY AND CONCLUSIONS

8.1 Summary

This research investigated the seismic performance of Japanese steel chevron-braced MRFs. Design equations able to predict the proportion of the lateral strength carried by the braces and the energy-dissipation mechanism of chevron-braced MRFs were proposed and validated using three-dimensional nonlinear finite element simulations. A parametric study on a single-story single-bay chevron-braced MRF was conducted to understand the lateral bracing requirements for the beam intersecting braces and the relative lateral strength of the beam with respect to the braces the on the performance of this structural system. Subsequently, a streamlined design procedure for chevron-braced MRFs was proposed, and numerical simulations on the seismic performance of low- and mid-rise chevron-braced MRFs was performed.

The main observations and findings of the study are:

8.2 Relative strength of the braces with respect to the beam

A set of design equations were proposed for proportioning chevron-braced MRFs. These equations which were derived from plastic analysis, can accurately predict the energy-dissipation mechanism of chevron-braced MRFs, based on the relative strength of the braces with respect to the beams, and the proportion of the lateral strength carried by the braces, β_0. The accuracy of the design equations were validated for a total of sixteen chevron-braced MRFs .

The seismic performance of sixteen chevron-braced MRFs simulated to study the effect of relative strength of the braces with respect to the beam on the seismic performance of the chevron CBFs showed that:

- The proposed design equations accurately predicted the proportion of the lateral strength carried by the braces, β_0 and the energy-dissipation mechanism of the braced frames.
- A key design parameter to control the energy dissipating mechanism of chevron-braced MRFs is the factor κ to proportion the beam intersected by braces. The factor κ changes over the loading sequence, but generally reaches 1.5 under monotonic loading or large monotonic pulses and develops a smaller value close to unity under gradually increasing cyclic loading. Rather than the value $\kappa = 1.5$ previously used by Seki et al. [16], $\kappa = 1.25$ was more representative over the examined proportions and loading sequences and better matched the test results by Seki et al.[16]. Although κ affects the predicted mechanism, it does not affect the predicted lateral plastic strength of the chevron-braced MRF.

8.3 Lateral bracing requirements for the beam intersecting the braces

A parametric study on the lateral bracing requirements of the beam intersecting the braces was conducted. The parameters included the stiffness of the rotational and translational bracing (modelled using springs), the number of bracing points, and the bracing connection. The main observations are as follows:

- lack of lateral bracing of the beam intersected by the braces can lead to severe twist and out-of-plane deflection of the beam but may not affect the lateral-load resistance of the chevron-braced MRF system. In order to control lateral-torsional deformation of the beam, lateral bracing at the intersection of the braces and the beam should be accompanied by adequate rotational bracing.
- If the bracing connection is rigid and the braces are oriented to buckle out-of-plane, the braces deliver large torsional moment to the beam intersected by braces. In such bracing connections, both braces are forced to buckle in the same orientation, and therefore, the tensile brace counters the torsional moment delivered by the compression brace. An unfavorable condition is realized by large monotonic pulses that allow only one of the chevron braces to buckle, in which case the tension brace remains straight, and thereby produces zero countering moment.

- The torsional moment delivered by the braces may be estimated conservatively as the sum of four components: the moment produced through eccentricity of the action line of the deformed brace and out-of-plane bending moment at the brace ends, each from the compression and tension braces.

8.4 Seismic performance of low and mid-rise chevron-braced MRF

The seismic performance of 4-, 8- and 12-story steel chevron-braced MRFs designed using three different design assumptions, four different r_0 values and two different bracing connection types was investigated. Nonlinear time history analysis suggest that all systems meet the design requirements stipulated by the Japanese code.

- For the 4-story systems, the fictitious mechanism assumed in Type A caused no adverse design result for r_0 smaller than 2.0 but for r_0 larger than 2.0, Type B seems to be more adequate.
- All the systems had good seismic performance with the median SDR within the 2%rad drift specified for buildings in Japan. Between all the design philosophies, the American system in Type C had better performance although it uses considerable larger amount of steel.
- The 4 - story systems developed larger deformation demands than the taller braced frames, thus being susceptible to significantly more damages during earthquakes.
- For the 8- and 12-story systems, there was little difference between the design cases, because

the design requirement inherently provides these systems with greater surplus strength compared to 4-story systems. For the 8- and 12-story systems the deformation tended to concentrate at the top of the building unlike what is expected for chevron-braced MRFs.

- The fixed bracing connection commonly adopted in Japan, leads to stronger braced frames systems than the flexible connection detail commonly adopted in the United States, which is designed to accommodate out-of-plane rotation of the braces, and hence showed better performance.
- The reduced strength of the brace used in the design is not very conservative. The post-buckling strength of the braces, N_u should be evaluated as a function of the slenderness ratio,

8.5 Recommendations and Future Works

The research work discussed in this thesis had some limitations which could not be addressed at the time. Therefore, considerable research is warranted in order to fully understand the performance of the chevron-braced MRFs specially for multi-story structures. Most of the recommendations here are concerned with numerical modelling of chevron-braced MRFs, in order to improve the modelling approach currently available to use.

1. Develop a more realistic procedure to model braces, representative of braces usually adopted in low- and mid-rise chevron-braced frames in Japan. Therefore, a procedure to account for the effects of braces and columns local buckling on the numerical modelling is necessary to accurately simulate the response of the braced frame models.
2. Improve the numerical model so that the effect of brace post-buckling behavior, fracture and beam fracture can be incorporated in the numerical model.
3. Modify the scaling procedure to understand the if the scaling procedure has an effect on the seismic performance of the braced frame structures.

REFERENCES

[1] K. F. Ibrahim, "Seismic Behavior of Concentrically Braced Frame," *Earthq. Eng. Reserach Cent.*, vol. 88/01, 1988.

[2] Architectural Institute of Japan (AIJ), "Recommendation for Limit State Design of Steel Structures," Maruzen, Tokyo, Japan, 2010.

[3] Architectural Institute of Japan (AIJ), "Recommendations for Design of Connections in Steel Structures," Maruzen, Tokyo, Japan, 2021.

[4] Ministry of Land Infrastructure Transport and Tourism (MLIT), *Manual for Structural Regulations for Building Design*. Building Center of Japan, Tokyo, Japan, 2020.

[5] R. Tremblay, Peter Timler, M. Bruneau, and Andre Filliatrault, "Performance of Steel Structures during the 1994 Northridge earthquake," *Can. J. Civ. Eng.*, vol. 22, no. 2, pp. 438–451, 1995, doi: 10.1139/l95-052.

[6] D. J. Kelly, D. R. Bonneville, and S. J. Bartoletti, "1994 NORTHRIDGE EARTHQUAKE : DAMAGE TO A FOUR-STORY STEEL BRACED FRAME BUILDING AND ITS SUBSEQUENT UPGRADE," in *12WCEE 2000*, 2000, pp. 1–7.

[7] F. Naeim, "PERFORMANCE OF 20 EXTENSIVELY-INSTRUMENTED BUILDINGS DURING THE 1994 NORTHRIDGE EARTHQUAKE," *Struct. Des. Tall Build.*, vol. 194, no. December 1997, pp. 179–194, 1998.

[8] Nist, "The January 17, 1995 Hyogoken-Nanbu (Kobe) Earthquake," 1995.

[9] T. Okazaki, D. G. Lignos, M. Midorikawa, J. M. Ricles, and J. Love, "Damage to steel buildings observed after the 2011 Tohoku-oki earthquake," *Earthq. Spectra*, vol. 29, no. SUPPL.1, 2013, doi: 10.1193/1.4000124.

[10] B. Hiroyuki Yamanouchi, M. Midorikawa, A. Member, I. Nishiyama, and M. Watabe, "SEISMIC BEHAVIOR OF FULL-SCALE CONCENTRICALLY BRACED STEEL BUILDING STRUCTURE," 1989. [Online]. Available: http://pubs.asce.org/copyrigh

[11] M. Wakabayashi, M. Shibata, T. Imamura, and T. Nishino, "Experimental study of the hysteretic behavior of K-type braced frame." Bulletin of the Disaster Prevention Research Institute, Kyoto University, pp. 171–183, 1981.

[12] T. Fukuta, I. Nishiyama, and H. Yamanouchi, "ELASTIC AND PLASTIC BEHAVIOR OF STEEL FRAMES WITH ' CONCENTRIC K-BRACES," 1988.

[13] T. Fukuta and H. Yamanouchi, "Ultimate Lateral Shear Capacity of Steel Frames with Inverted V Braces," 1989.

[14] C. W. Roeder *et al.*, "Effect of beam yielding on chevron braced frames," *J. Constr. Steel Res.*, vol. 159, pp. 428–441, Aug. 2019, doi: 10.1016/J.JCSR.2019.04.044.

[15] A. D. Sen *et al.*, "Experimental Investigation of Chevron Concentrically Braced Frames with Yielding Beams," 2016, doi: 10.1061/(ASCE)ST.1943-541X.0001597.

[16] A. Seki, K. Inoue, T. Okazaki, S. Hashioka, and H. Asada, "Seismic performance of steel chevron

braced frames designed according to Japanese practice," *J. Constr. Steel Res.*, vol. 189, p. 107066, 2022, doi: 10.1016/j.jcsr.2021.107066.

[17] P. Uriz and S. a Mahin, "Toward Earthquake-Resistant Design of Concentrically Braced Steel-Frame Structures," *Pacific Earthq. Eng. Res. Cent.*, no. November, pp. 1–401, 2008.

[18] Y. Huang and S. A. Mahin, "Simulating the Inelastic Seismic Behavior of Steel Braced Frames," *Pacific Earthq. Eng. Res.*, no. April, 2010.

[19] P. C. Hsiao, D. E. Lehman, and C. W. Roeder, "Improved analytical model for special concentrically braced frames," *J. Constr. Steel Res.*, 2012, doi: 10.1016/j.jcsr.2012.01.010.

[20] P. C. Hsiao, D. E. Lehman, and C. W. Roeder, "A model to simulate special concentrically braced frames beyond brace fracture," *Earthq. Eng. Struct. Dyn.*, 2013, doi: 10.1002/eqe.2202.

[21] A. D. Sen, C. W. Roeder, D. E. Lehman, and J. W. Berman, "Nonlinear modeling of concentrically braced frames," *J. Constr. Steel Res.*, vol. 157, pp. 103–120, 2019, doi: 10.1016/j.jcsr.2019.02.007.

[22] A. Sen *et al.*, "Numerical and Experimental Assessment of Chevron Braced Frames with Weak Beams," *10th U.S. Natl. Conf. Earthq. Eng.*, 2014, doi: 10.4231/D3862BC3Z.

[23] E. Karamanci and D. G. Lignos, "Computational Approach for Collapse Assessment of Concentrically Braced Frames in Seismic Regions," *J. Struct. Eng.*, 2014, doi: 10.1061/(ASCE)ST.1943-541X.0001011.

[24] H. Asada, A. D. Sen, T. Li, J. W. Berman, D. E. Lehman, and C. W. Roeder, "Seismic performance of chevron-configured special concentrically braced frames with yielding beams," *Earthq. Eng. Struct. Dyn.*, vol. 49, no. 15, pp. 1619–1639, 2020, doi: 10.1002/eqe.3320.

[25] R. Tremblay and N. Robert, "Seismic performance of low- and medium-rise chevron braced steel frames," *Can. J. Civ. Eng.*, vol. 28, no. 4, pp. 699–714, 2001, doi: 10.1139/cjce-28-4-699.

[26] P. W. Richards, "Seismic Column Demands in Ductile Braced Frames," *J. Struct. Eng.*, vol. 135, no. 1, pp. 33–41, 2009, doi: 10.1061/(asce)0733-9445(2009)135:1(33).

[27] H. Kuramoto, "Seismic Design Codes for Buildings in Japan," *J. Disaster Res.*, vol. 1, no. 3, pp. 341–356, 2006, doi: 10.20965/jdr.2006.p0341.

[28] AISC 341-10, *Seismic Provisions for Structural Steel Buildings*. American Institute of Steel Construction, Inc (AISC), 2010.

[29] C. W. Roeder, E. J. Lumpkin, and D. E. Lehman, "A balanced design procedure for special concentrically braced frame connections," *J. Constr. Steel Res.*, vol. 67, no. 11, pp. 1760–1772, 2011, doi: 10.1016/j.jcsr.2011.04.016.

[30] Adina R&D Inc, "Theory and Modeling Guide Volume I : ADINA Solids & Structures Theory and Modeling Guide Volume I : ADINA Solids & Structures," vol. I, no. October, 2021.

[31] Y. Satoshi, I. Tomoko, and K. Okada, "Simple hysteresis model of structural steel considering the Bauschinger effect," *J. Structual Constr. Eng.*, no. No. 559, pp. 225–232, 2002.

[32] R. Tremblay, "Inelastic seismic response of steel bracing members," *J. Constr. Steel Res.*, vol. 58, no. 5–8, pp. 665–701, 2002, doi: 10.1016/S0143-974X(01)00104-3.

[33] M. Wakabayashi, T. Nakamura, and N. Yoshida, “Experimental Studies on the Elastic-Plastic Behavior of Braced Frames under Repeated Horizontal Loading: Part I,” *Bull. Disaster Prev. Res. Inst.*, 1980.

[34] H. Krawinkler, A. Gupta, R. Medina, and N. Luco, “Development of Loading Histories for Testing of Steel Beam-to-Column Assemblies,” *SAC Backgr. Rep.*, vol. SAC/BD-00/, pp. 1–10.

[35] BCJ, “Structural provisions for building structures (1997 Edition). Building Center of Japan,” Tokyo, 1997.

[36] K. Inoue and K. Suita, *Building Steel Structure-Theory and Design*.

[37] F. C. Filippou, E. P. Popov, and V. V. Bertero, “Effects of bond deterioration on hysteretic behavior of reinforced concrete joint (EERC 83-19),” *Earthq. Eng. Res. Center, Univ. California, Berkeley*, no. August, p. 212, 1983.

[38] Y. Zhang, R. Matsui, T. Okazaki, and T. Takeuchi, “Database of steel braces with respect to dimension properties and strutural performance,” in *AIJ Proceedings*, 2020, no., p. 2.

[39] H. Hodzumi, Y. Makino, M. Sakai, and M. Hirano, “Hodzumi-1997-Study of Elasto-plastic Behavior of Steel Member under Cyclic Axial Force and Its Fracture (No. 1),” *J. Struct. Constr. Eng., AIJ*, vol. 491, pp. 111–119, 1997.

[40] B. Kato and H. Akiyama, “Restoring Force Characteristics of Steel Frames Equipped with Diagonal Bracings,” *Arquit. Institue Japan*, vol. 260, pp. 99–107.

[41] Tsuji, “A Study on Elastic-Plastic Deformation and Collapse Properties of Steel Pipes -Part 1”.

[42] Matsumoto, “Experimental Study on the Plastic Deformation Performance of Braces Considering Post-Buckling Behavior - Part 1,” 2016.

[43] G. Black, W. A. B. Wenger, and E. P. Popov, “Inelastic Buckling of Steel Struts Under Cyclic Load Reversals,” no. October, pp. 1–163, 1980.

[44] I. A. . Raheem and R. Matsui, “Cyclic-Loading Performace of Squat Steel Braces,” Hokkaido University, 2022.

[45] T. Okazaki, D. G. Lignos, T. Hikino, and K. Kajiwara, “Dynamic Response of a Chevron Concentrically Braced Frame,” *J. Struct. Eng.*, vol. 139, no. 4, pp. 515–525, 2013, doi: 10.1061/(ASCE)ST.1943-541X.0000679.

[46] FEMA P695, *Quantification of Building Seismic Performance Factors*. 2009.

[47] P. G. motion Database, “https://ngawest2.berkeley.edu/spectras/new?sourceDb_flag=1.”

[48] F. A. Charney, “Unintended consequences of modeling damping in structures: Rayleigh damping,” *17th Anal. Comput. Spec. Conf.*, vol. 2006, no. April, p. 3, 2006, doi: 10.1061/40878(202)12.

[49] J. F. Hall, “Problems encountered from the use (or misuse) of Rayleigh damping,” *Earthq. Eng. Struct. Dyn.*, vol. 35, no. 5, pp. 525–545, 2006, doi: 10.1002/eqe.541.

[50] A. k. Chopra and F. McKenna, “Modeling Viscous Damping in Nonlinear Response history Analysis of Buildings for Earthquake Excitation,” *Earthq. Eng. Struct. Dyn.*, 2016.

[51] Y. Suzuki and D. G. Lignos, “Development of collapse-consistent loading protocols for experimental testing of steel columns,” no. January, pp. 1–18, 2019, doi: 10.1002/eqe.3225.

[52] Y. Suzuki and D. G. Lignos, “Fiber-based hysteretic model for simulating strength and stiffness deterioration of steel hollow structural section columns under cyclic loading,” no. July, pp. 1–19, 2020, doi: 10.1002/eqe.3324.

[53] S. Mukaide, N. Oku, K. Matsuo, and M. Tada, “Loading Test in the Range of Large Deformation for RHS Columns With Different Manufacturing Processes,” *Steel Constr. Eng.*, vol. 23, no. 90, pp. 9051–9064, (in Japanese), 2016.

Appendix A: Computation of Beam Torsional Stiffness

The governing equation for a member subjected to constant torsional Moment, *T* is:

$T=GJø'-EI_w ø'''$

In the above equation,

G= shear constant;

J= St. Venant's Torsional Constant;

I_w- Warping Constant;

Taking $T=T_{con}$=Constant

$EI_w ø'''- GJø' = - T_{con}$

$$ø''' - \frac{GJ}{EI_w} ø' = -\frac{T_{con}}{EI_w}$$

Assume $\frac{GJ}{EI_w} = \lambda^2$: $ø''' - \lambda^2 ø' = -\frac{T_{con}}{EI_w}$

General Solution: $ø = C_1 + C_2 cosh\lambda z + C_3 sinh\lambda z + \frac{T_{con}}{GJ} z$

Considering symmetry: $0 \leq z \leq L/2$ where $T_{con}=T_0/2$

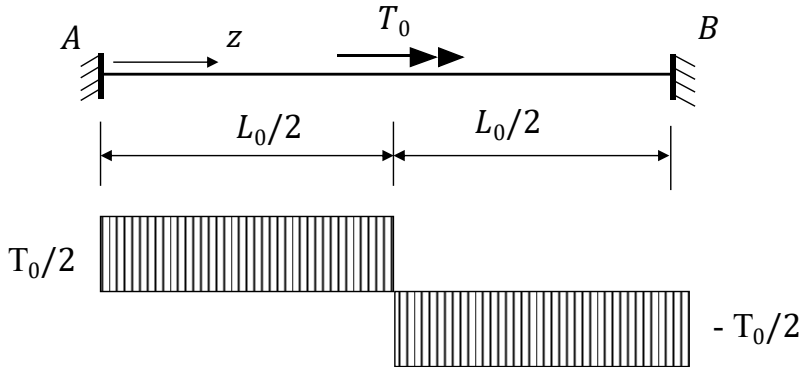

General Solution: $ø = C_1 + C_2 cosh\lambda z + C_3 sinh\lambda z + \frac{\frac{T_0}{2}}{GJ} z$

Boundary Conditions: Three conditions are needed to solve for the three integration constants C_1, C_2 and C_3:

Ø(z=0) = 0 Ø' (z=0) = 0 → no twist, no warping

Ø' (z=L/2) = 0 → no warping (Symmetry)

Cross Section Properties:

Warping Torsional Constant I_w

$$I_w = \frac{(d-t)\text{^}2 \times I_y}{4} = \frac{(250-9)^2 \times 294 \times 10^4}{4}$$

$$I_w = 4.26 \times 10^6 mm^6$$

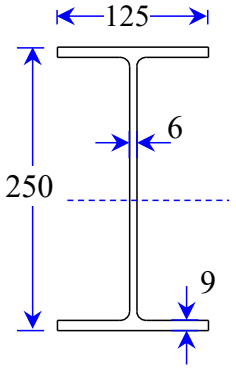

Torsional Constant - J

$$\text{J} = \sum \frac{bt^3}{3} = \frac{1}{3}(2 \times (125 \times 9^3) + (232 \times 6^3))$$

$$\text{J} = 77454\, mm^4$$

E/G=2(1+ν) = 2×(1+0.3)=2.6

$$\lambda = \sqrt{\frac{GJ}{EI_w}} = \sqrt{\frac{77454 \times (10^2 mm)}{2.6 \times 4.26 \times 10^{10}}} = 0.836\, m$$

Computation of the Angle of twist

Ø(z=0) = 0 → $C_1+C_2=0$

Ø' (z=0) = 0 → $C_3 = -\frac{\frac{T_0}{2}}{\lambda GJ}$

Thus the general solution becomes:

$$ø = -C_2 + C_2 \cosh(\lambda z) - \frac{\frac{T_0}{2}}{\lambda GJ} \sinh(\lambda z) + \frac{\frac{T_0}{2}}{\lambda GJ} z$$

Using Symmetry : Ø' (z=L/2) = 0

$$C_2 = \frac{T_0}{2\lambda GJ} \times \frac{\left(1 - \cosh\left(\lambda {}^{L}/_{2}\right)\right)}{\sinh\left(\lambda {}^{L}/_{2}\right)}$$

$$ø = -\left[\frac{T_0}{2\lambda GJ} \times \frac{\left(1-\cosh\left(\lambda {}^{L}/_{2}\right)\right)}{\sinh\left(\lambda {}^{L}/_{2}\right)}\right] + \left[\frac{T_0}{2\lambda GJ} \times \frac{\left(1-\cosh\left(\lambda {}^{L}/_{2}\right)\right)}{\sinh\left(\lambda {}^{L}/_{2}\right)}\right]\cosh(\lambda z) - \frac{\frac{T_0}{2}}{\lambda GJ}\sinh(\lambda z) + \frac{\frac{T_0}{2}}{\lambda GJ} z$$

$$ø = \frac{T_0}{2\lambda GJ} + \left[\frac{\left(1-\cosh\left(\lambda {}^{L}/_{2}\right)\right)}{\sinh\left(\lambda {}^{L}/_{2}\right)} \times (1-\cosh(\lambda z)) - \sinh(\lambda z) + \lambda z\right]$$

Denoting $Ø_m$= Ø (z=L/2)

$$ø_m = \frac{T}{2\lambda GJ} + \left[\frac{\left(1-\cosh\left(\lambda {}^{L}/_{2}\right)\right)}{\sinh\left(\lambda {}^{L}/_{2}\right)} \times (1-\cosh(\lambda L/2)) - \sinh(\lambda L/2) + \lambda\frac{L}{2}\right]$$

$$ø_m = \frac{T}{2\lambda GJ} + \left[\frac{\left(1-\cosh\left(\lambda {}^{L}/_{2}\right)\right)^2}{\sinh\left(\lambda {}^{L}/_{2}\right)} - \sinh(\lambda L/2) + \lambda\frac{L}{2}\right]$$

$$ø_m = \frac{T}{2\lambda GJ} + \left[\frac{\left(1-\cosh\left(\lambda {}^{L}/_{2}\right)\right)^2 - \sinh^2(\lambda L/2)}{\sinh\left(\lambda {}^{L}/_{2}\right)} + \lambda\frac{L}{2}\right]$$

Beam Torsional Stiffness

$$\frac{T}{ø_m} = \frac{2\lambda GJ}{\left[\frac{\left(1-\cosh\left(\lambda {}^{L}/_{2}\right)\right)^2 - \sinh^2(\lambda L/2)}{\sinh\left(\lambda {}^{L}/_{2}\right)} + \lambda\frac{L}{2}\right]}$$

cosh(λL/2)= 1.8933

sinh(λL/2)= 1.6

$$\frac{T}{ø_m} = \frac{2 \times 0.835 \times 6.1}{\left[\frac{(1-1.8933)^2 - 2.53}{1.6} + 0.83 \times 1.5\right]}$$

$$\frac{T}{ø_m} = 71.98\ kNm/rad$$

Computation of the translational stiffness K_H of the beam:

The Translational stiffness of the beam was computed from the rotational stiffness as follows:

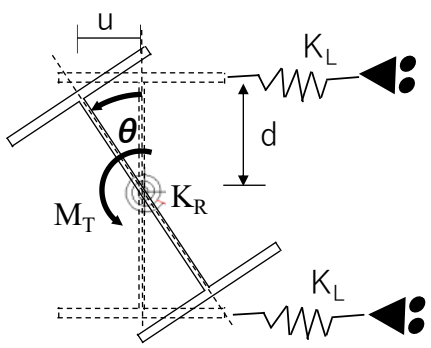

$K_R = \frac{KN.m}{rad}$ $K_H = \frac{KN}{m}$

$M_T=K_R\times\theta=2F\times d$

$F= K_H\times u$

$u=d\times\theta$

$2\times K_L\times u\times d =K_R\times u/d$

$K_H=\frac{K_R}{2\times d^2}$

$K_L = 2478.6\frac{KN}{m}$(assuming d=120.5 mm)

Appendix B: Design of the Braced Frame Models

The members cross-section proportions for the 4-story systems are shown bellow:

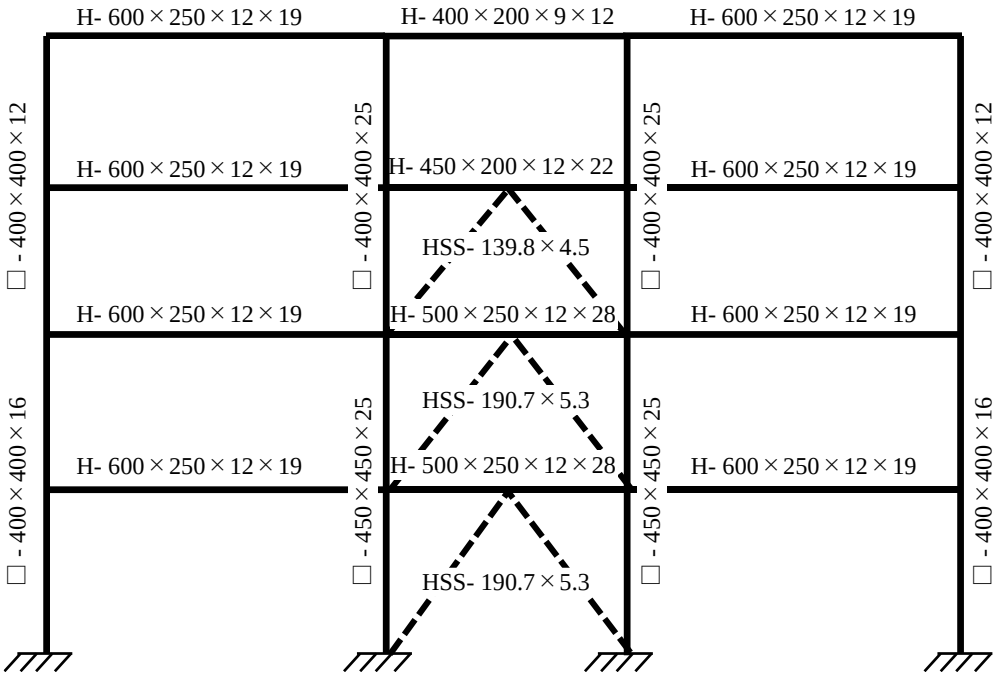

Figure B. 1: Cross-Section Properties Model A with r_0 = 2.0

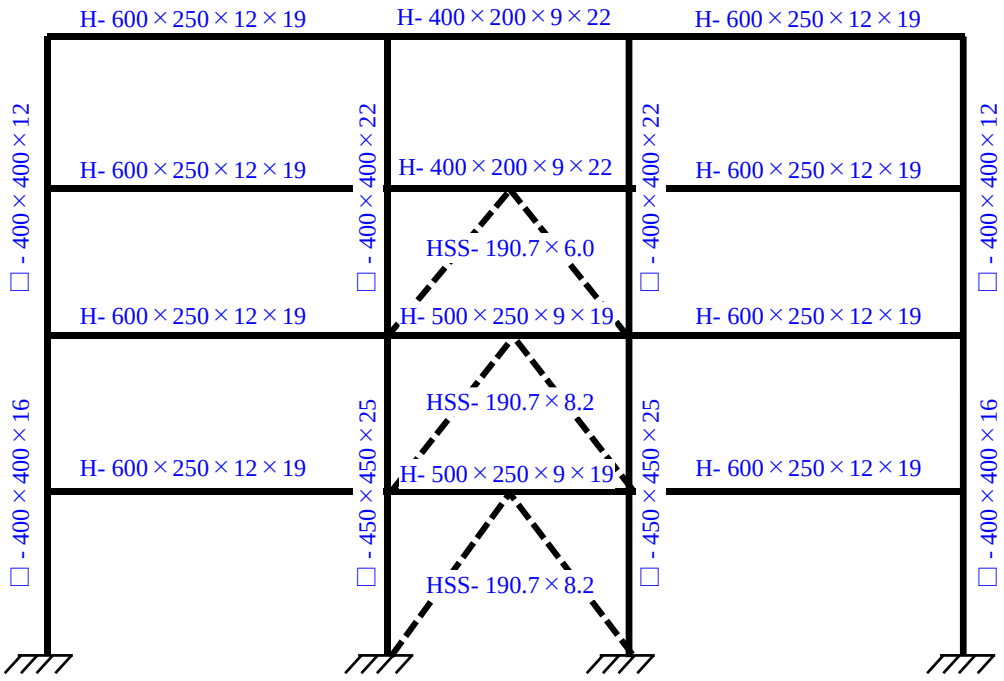

Figure B. 2: Cross-Section Properties Model A with r_0 = 4.0

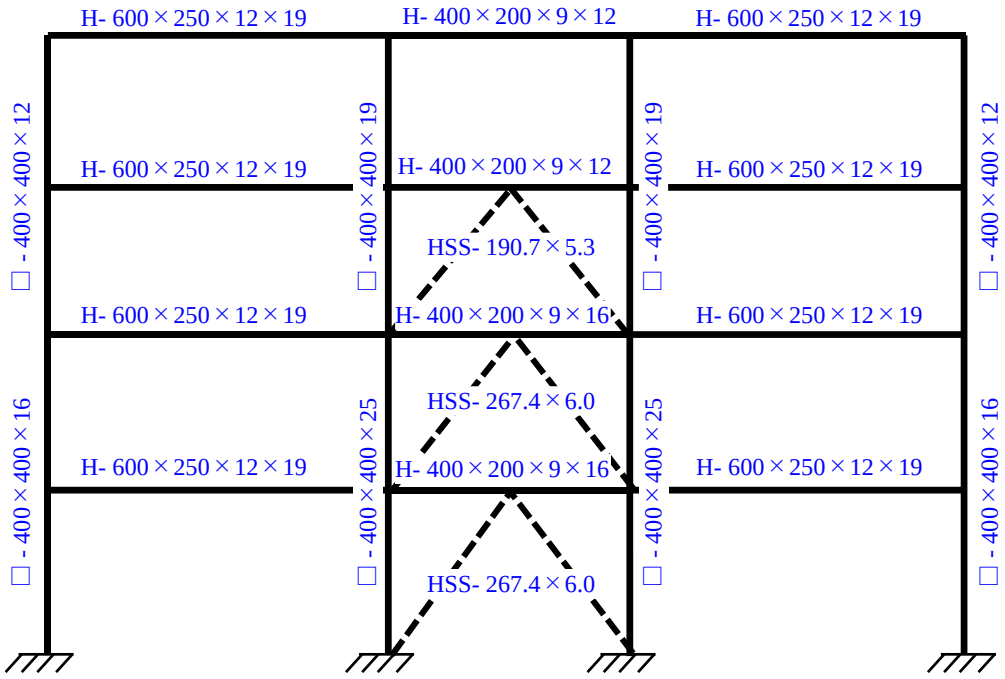

Figure B. 3: Cross-Section Properties Model A with r_0 = 8.0

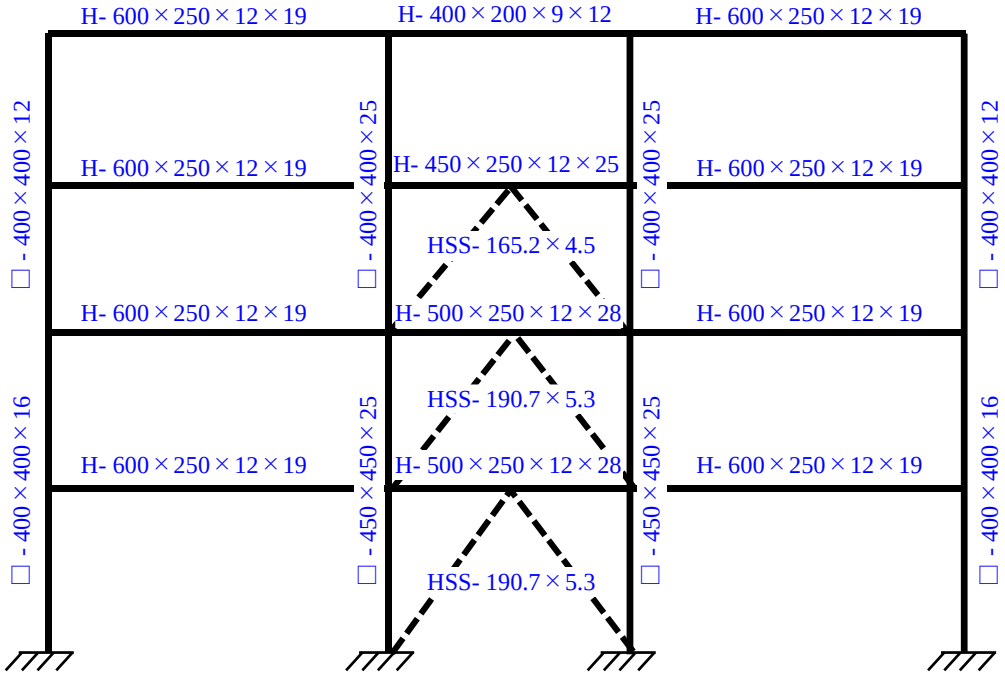

Figure B. 4: Cross-Section Properties Model B with r_0 = 2.0

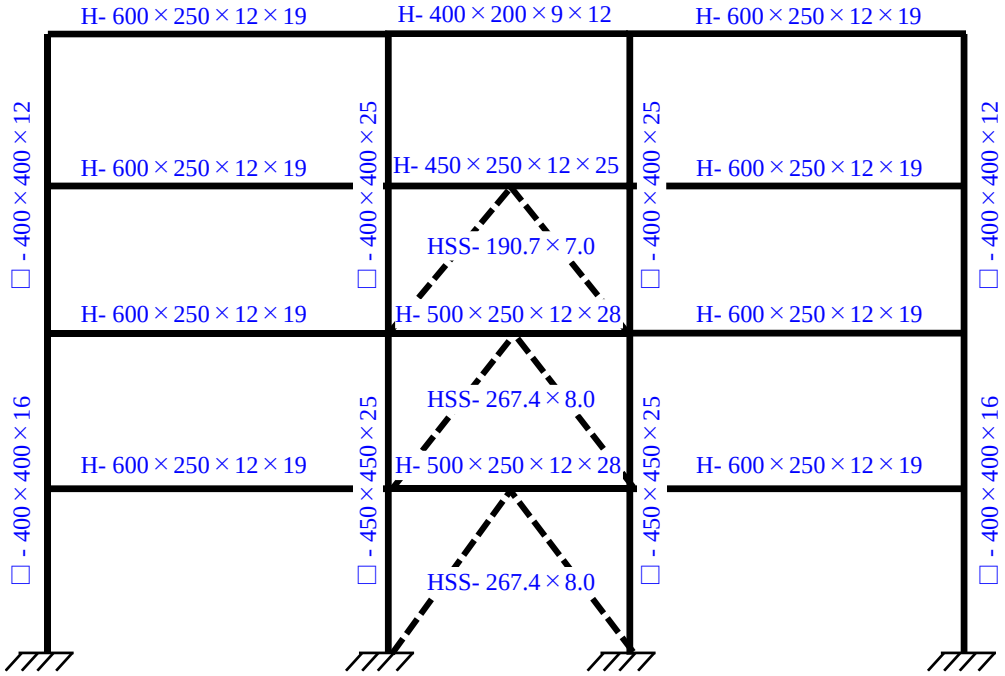

Figure B. 6: Cross-Section Properties Model B with r_0 = 4.0

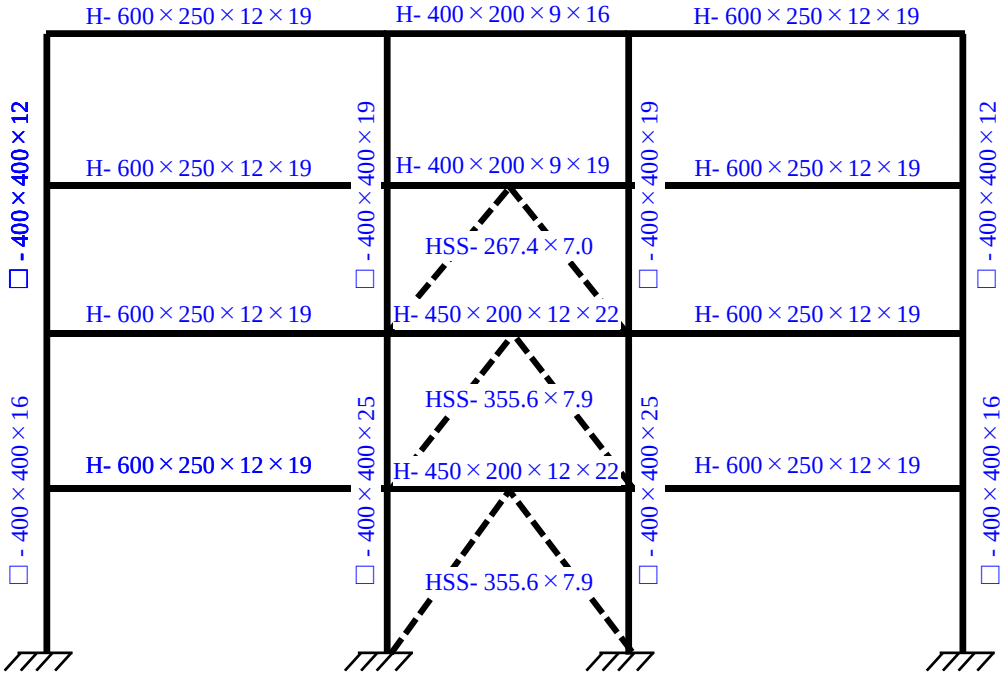

Figure B. 5: Cross-Section Properties Model B with r_0 = 8.0

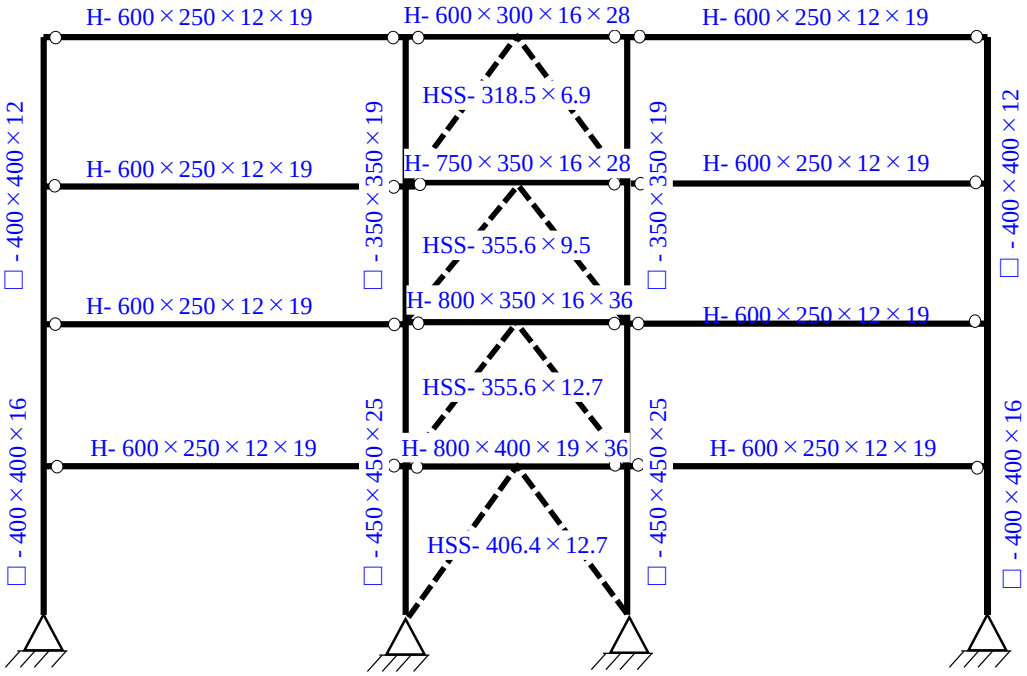

Figure B. 7: Cross-Section Properties Model C

The members cross-section proportions for the 8-story systems are shown below:

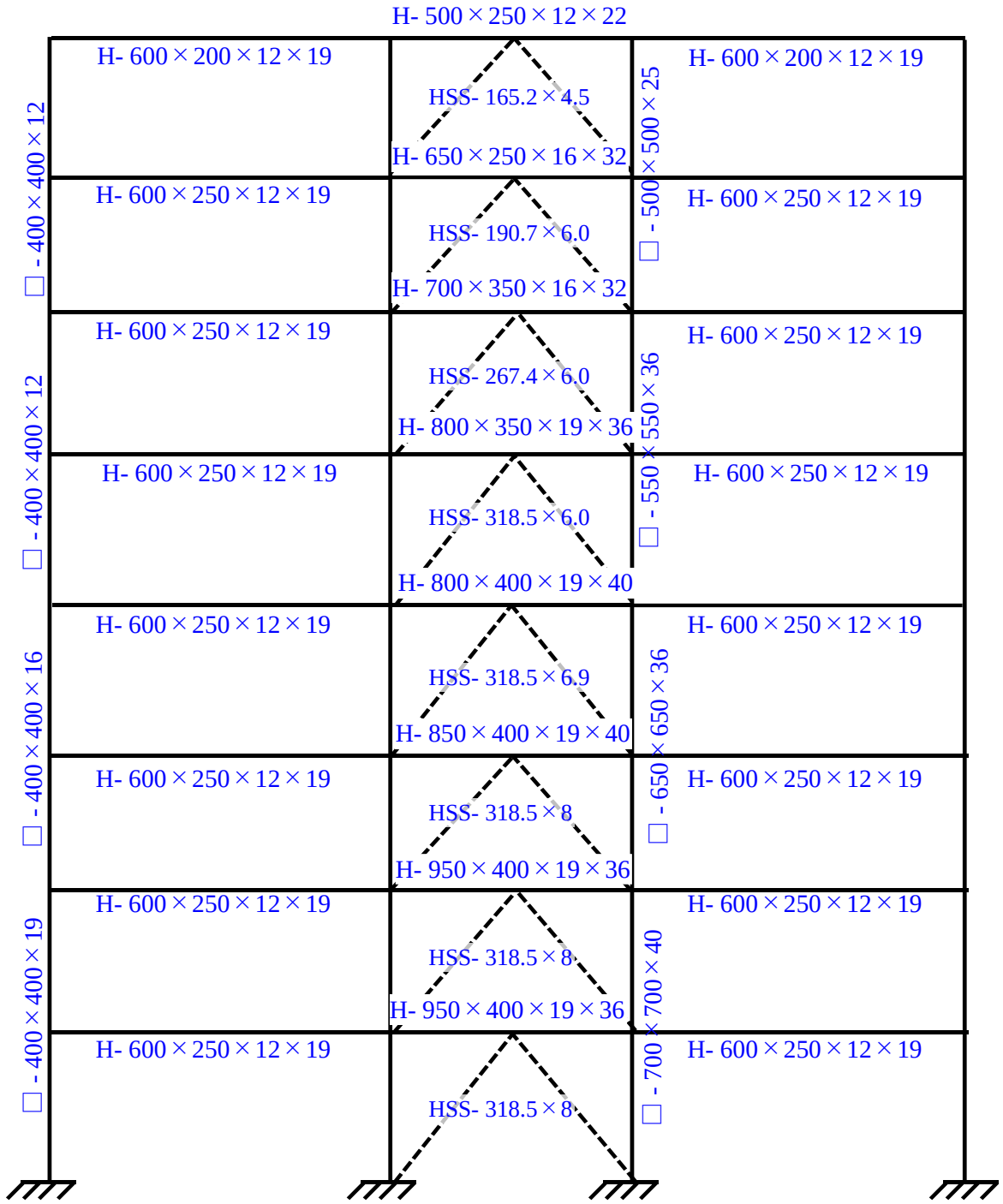

Figure B. 8: Cross-Section Properties for Model A with r_0=2.0.

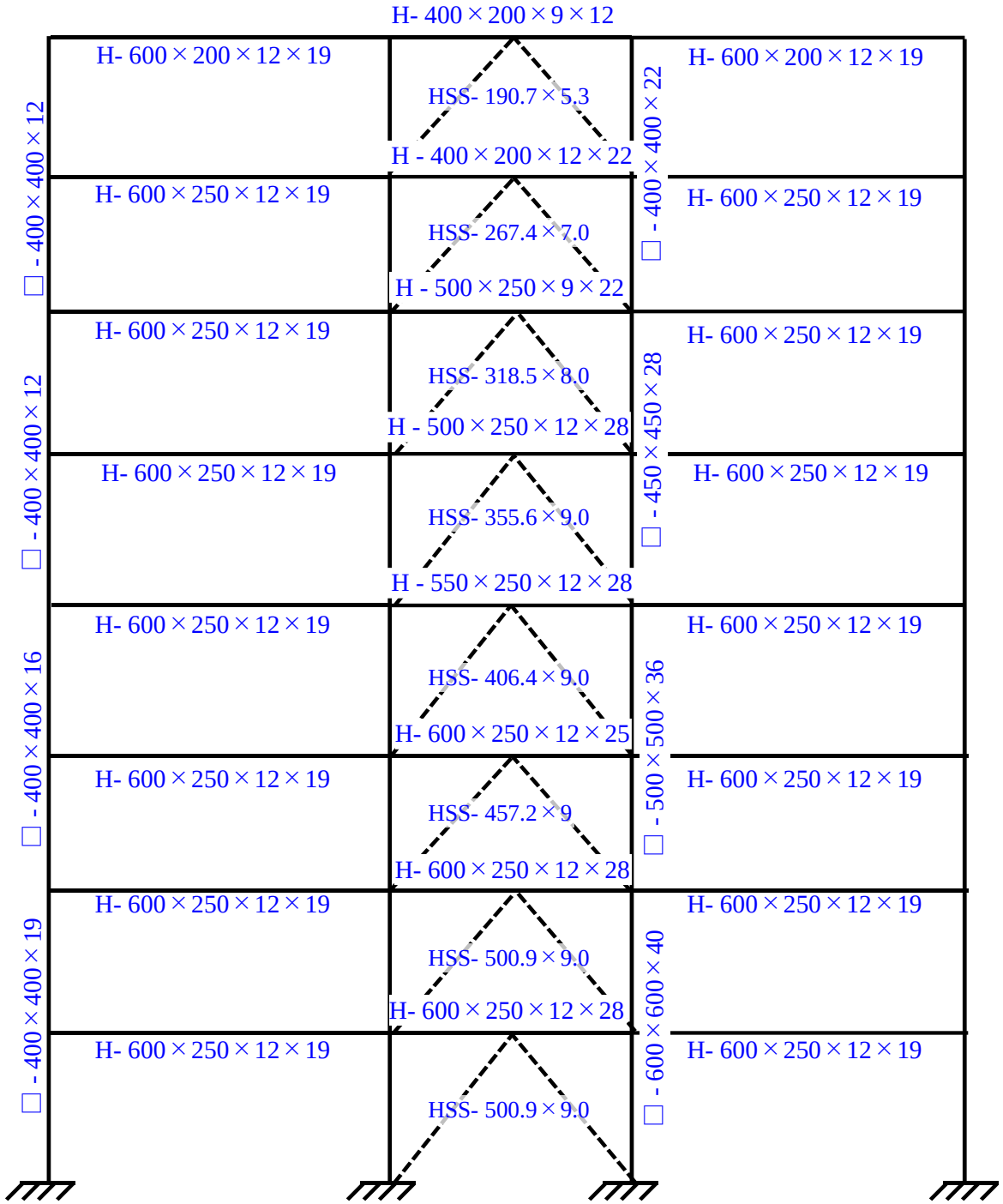

Figure B. 9: Cross-Section Properties Model A with r_0=8.0

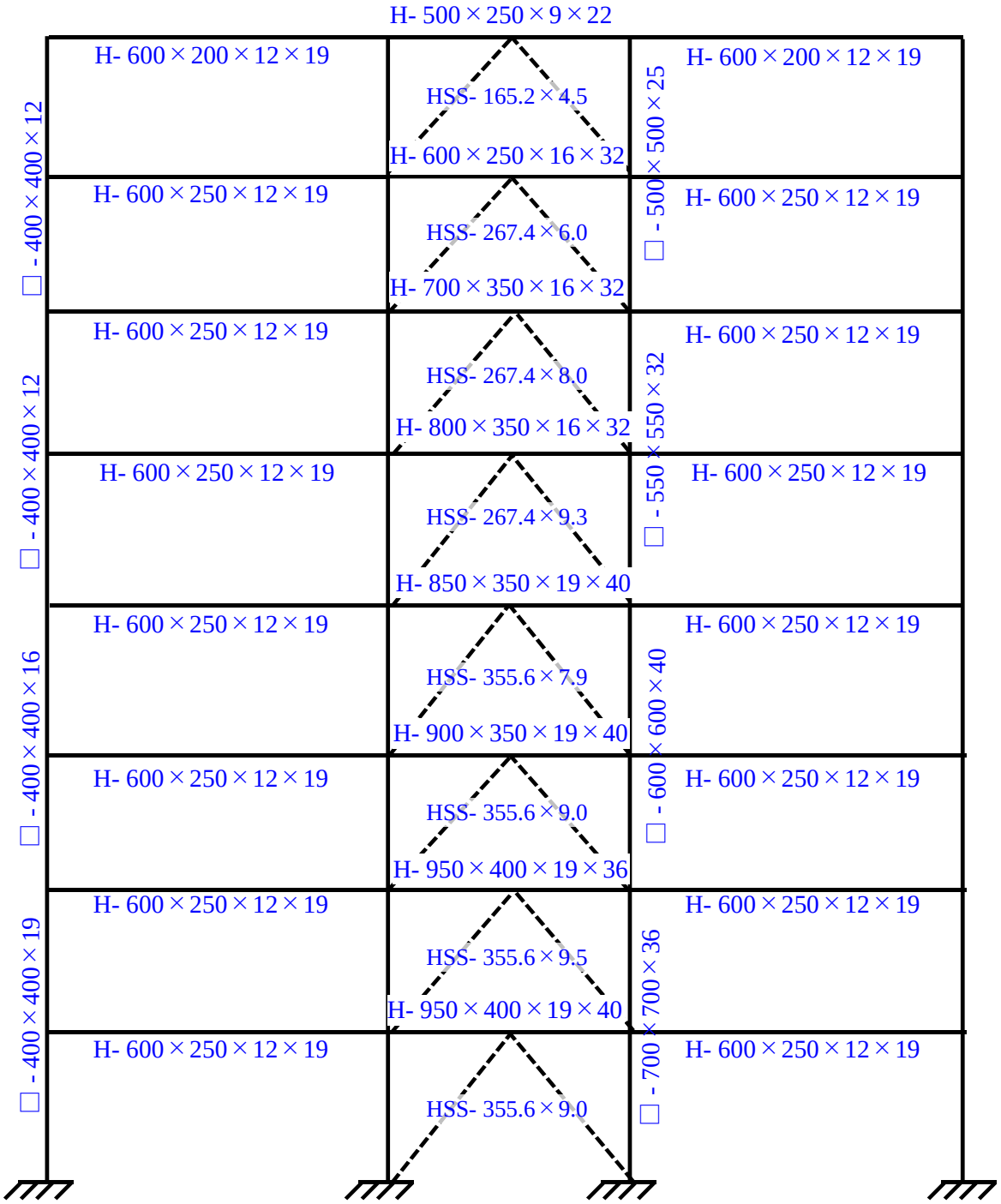

Figure B. 10: Cross-Section Properties Model B with r_0= 2.0

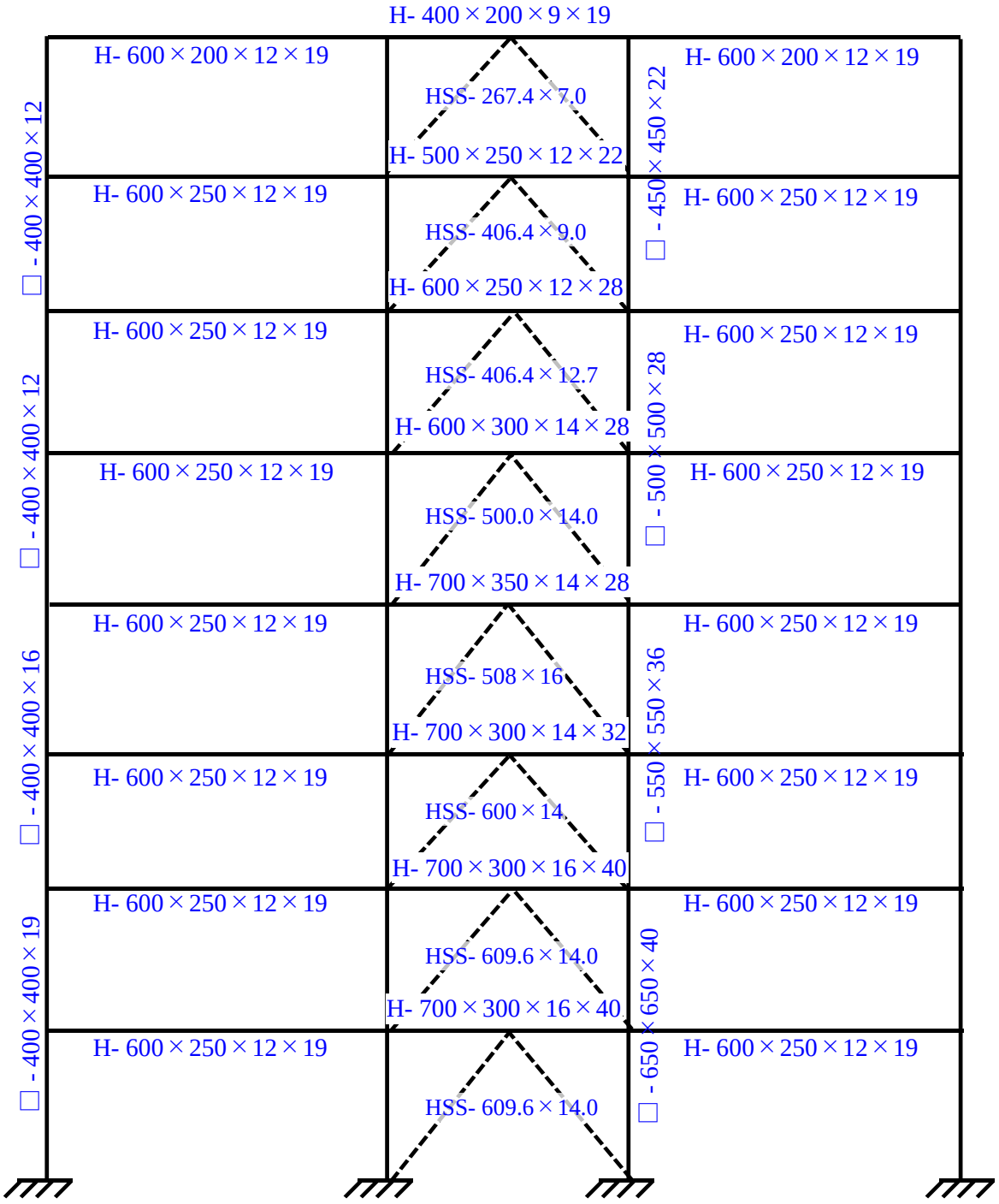

Figure B. 11: Cross-Section Properties Model B with r_0=8.0

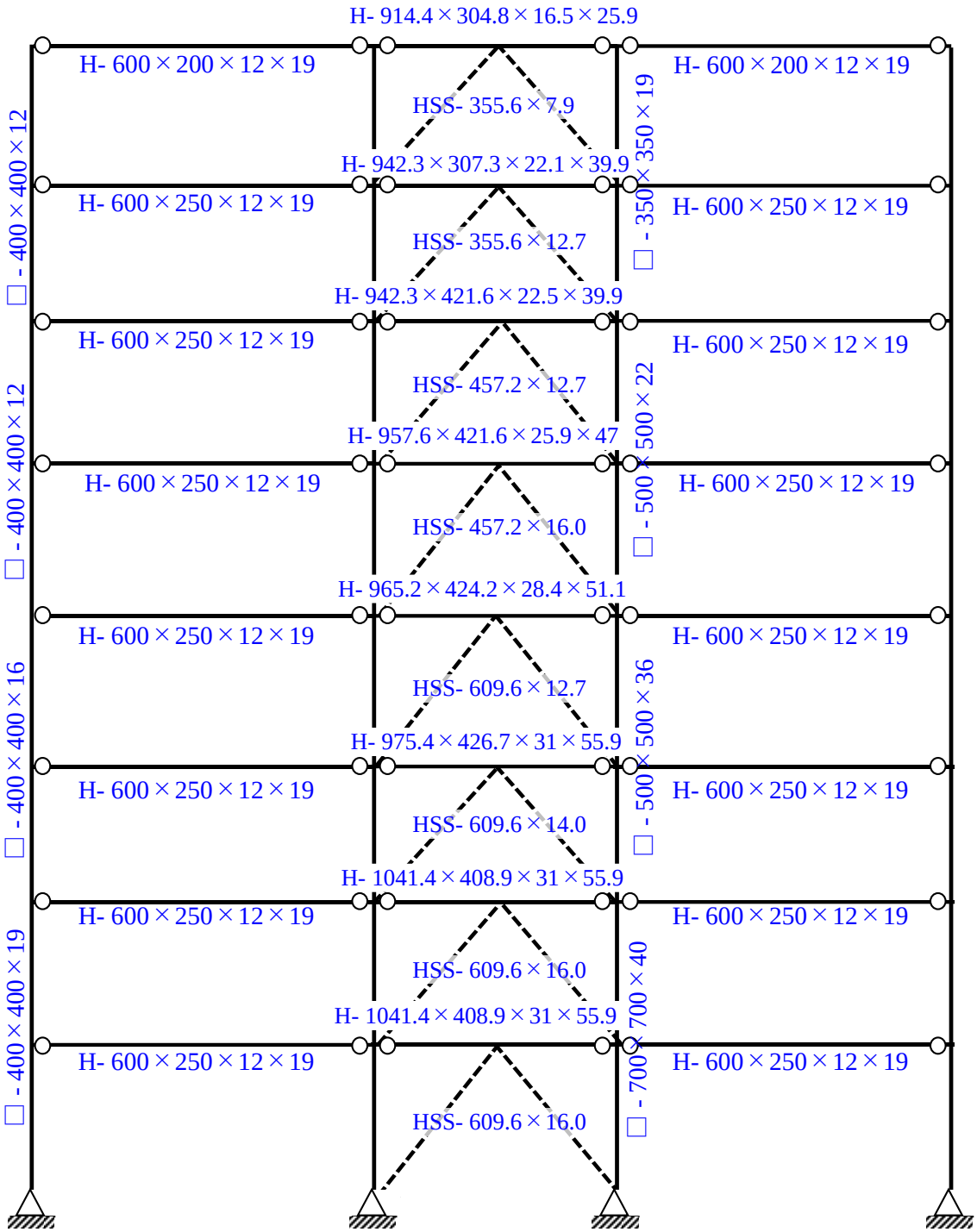

Figure B. 12: Cross-Section Properties for Model C

The members cross-section proportions for the 12-story systems are shown below:

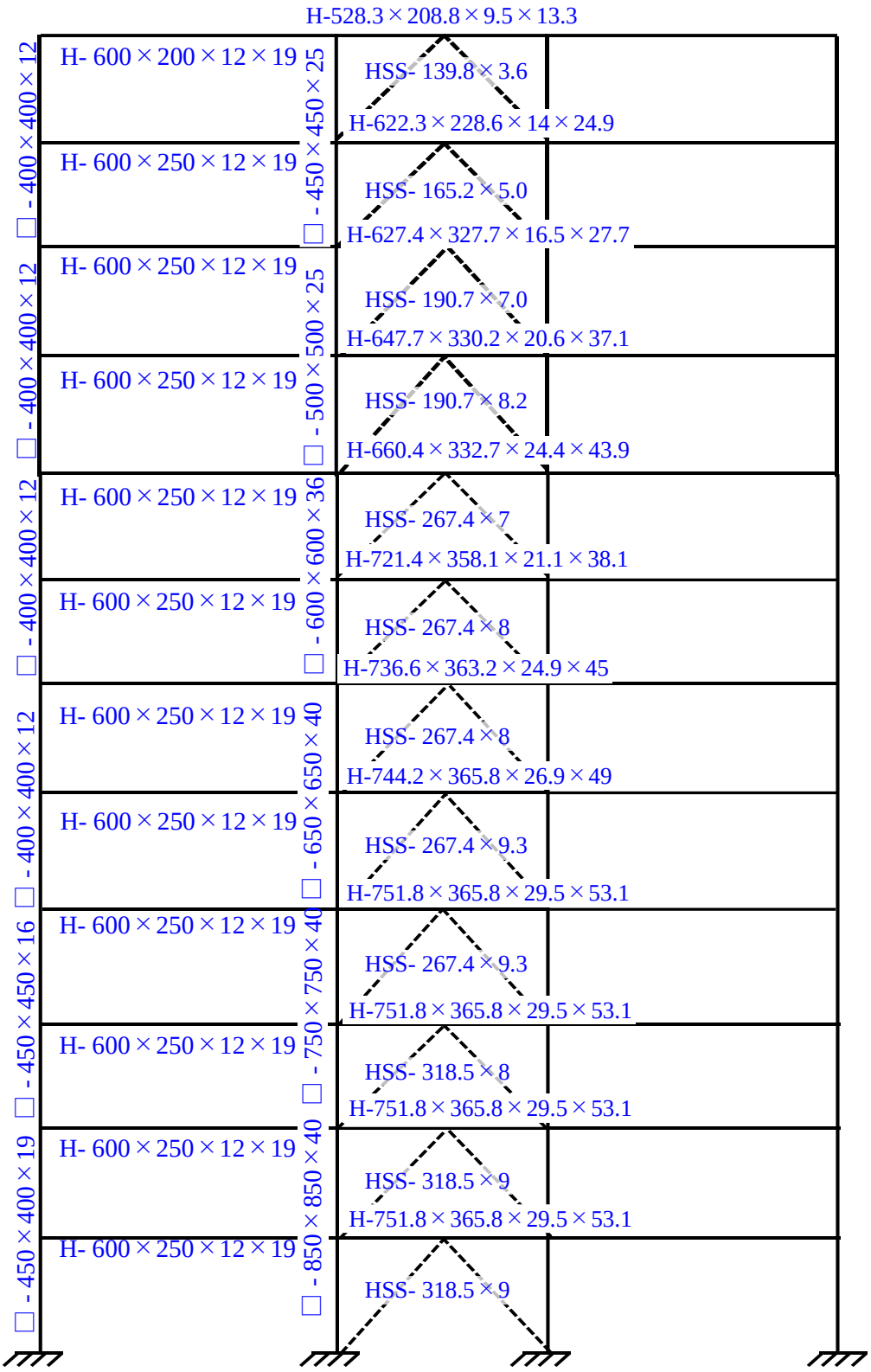

Figure B. 13: Cross-Section Properties for Model A_r_0= 2.0

s

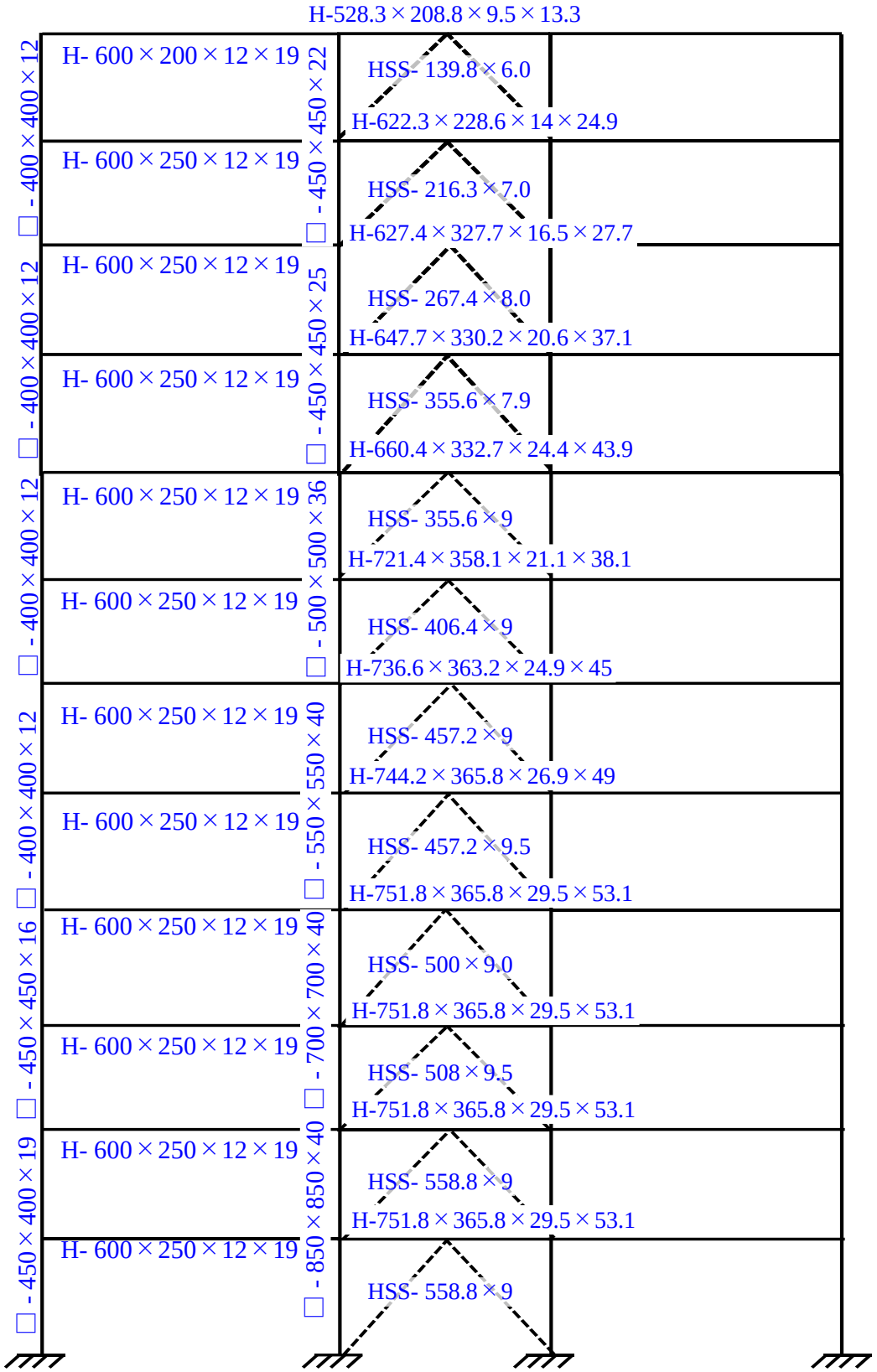

Figure B. 14: Cross-Section Properties for Model A with r_0= 8.0

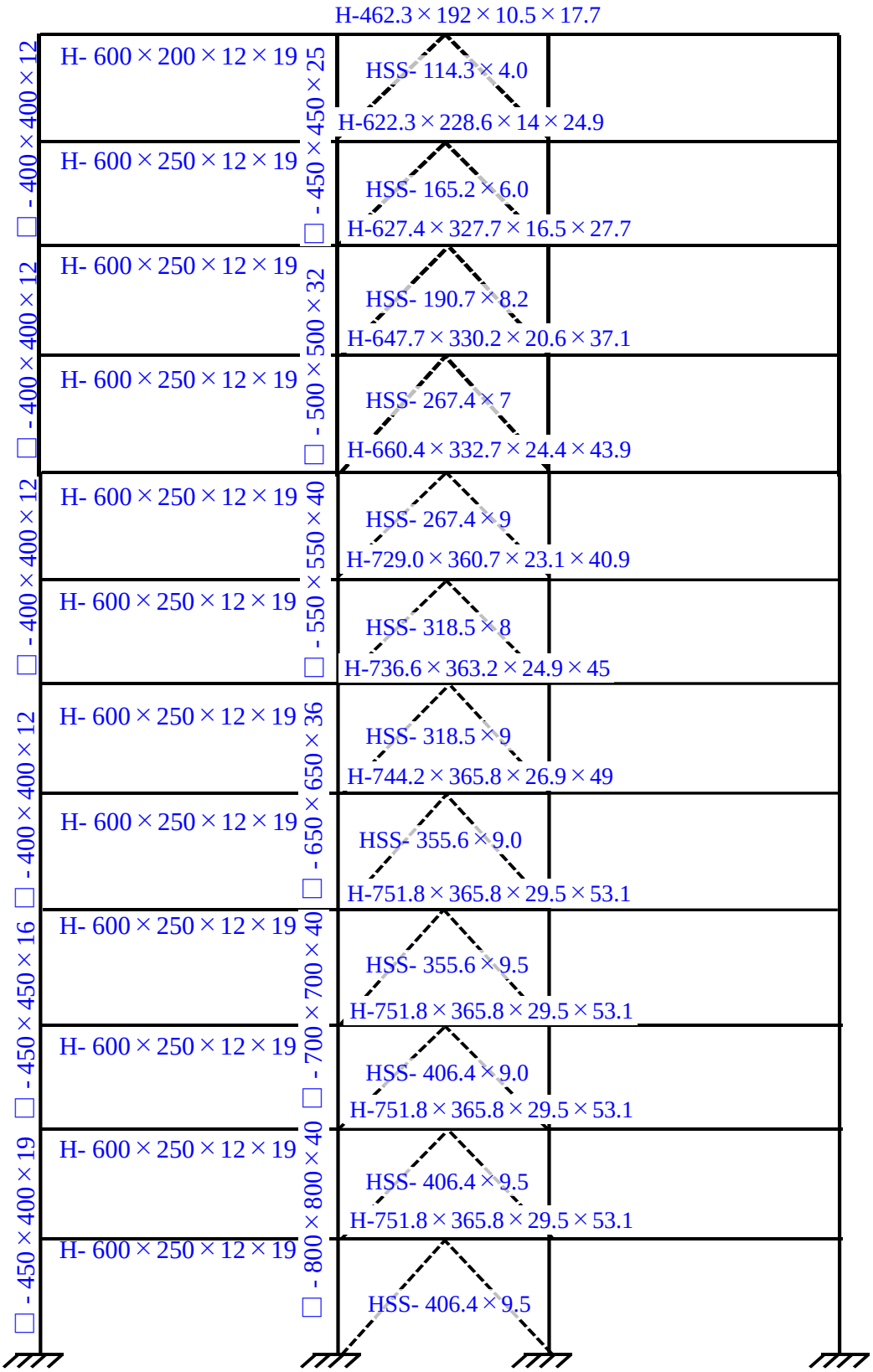

Figure B. 15: Cross-Section Properties for Model B with r_0 = 2.0

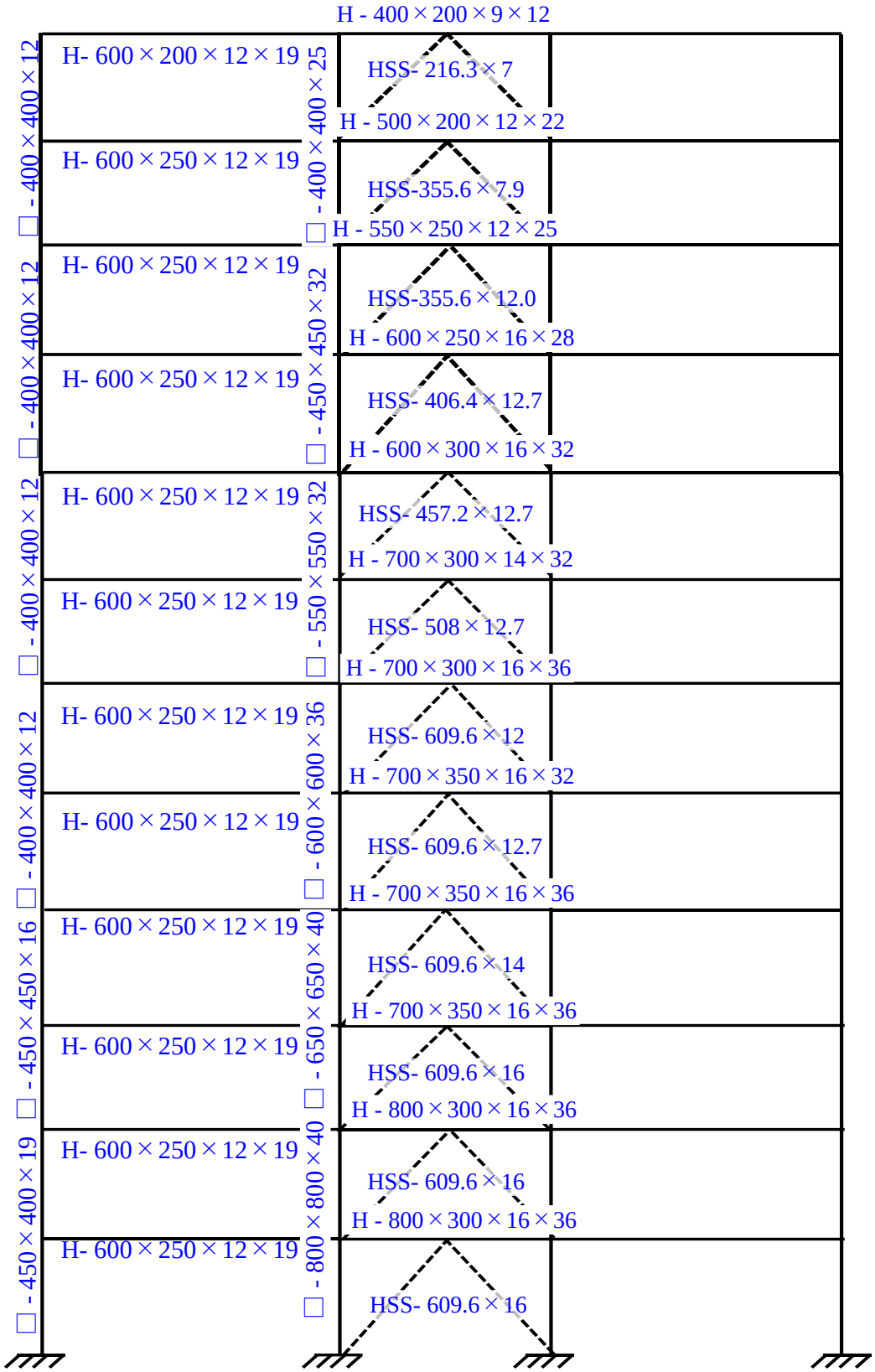

Figure B. 16: Cross-Section Properties for Model B with r_0 = 8.0

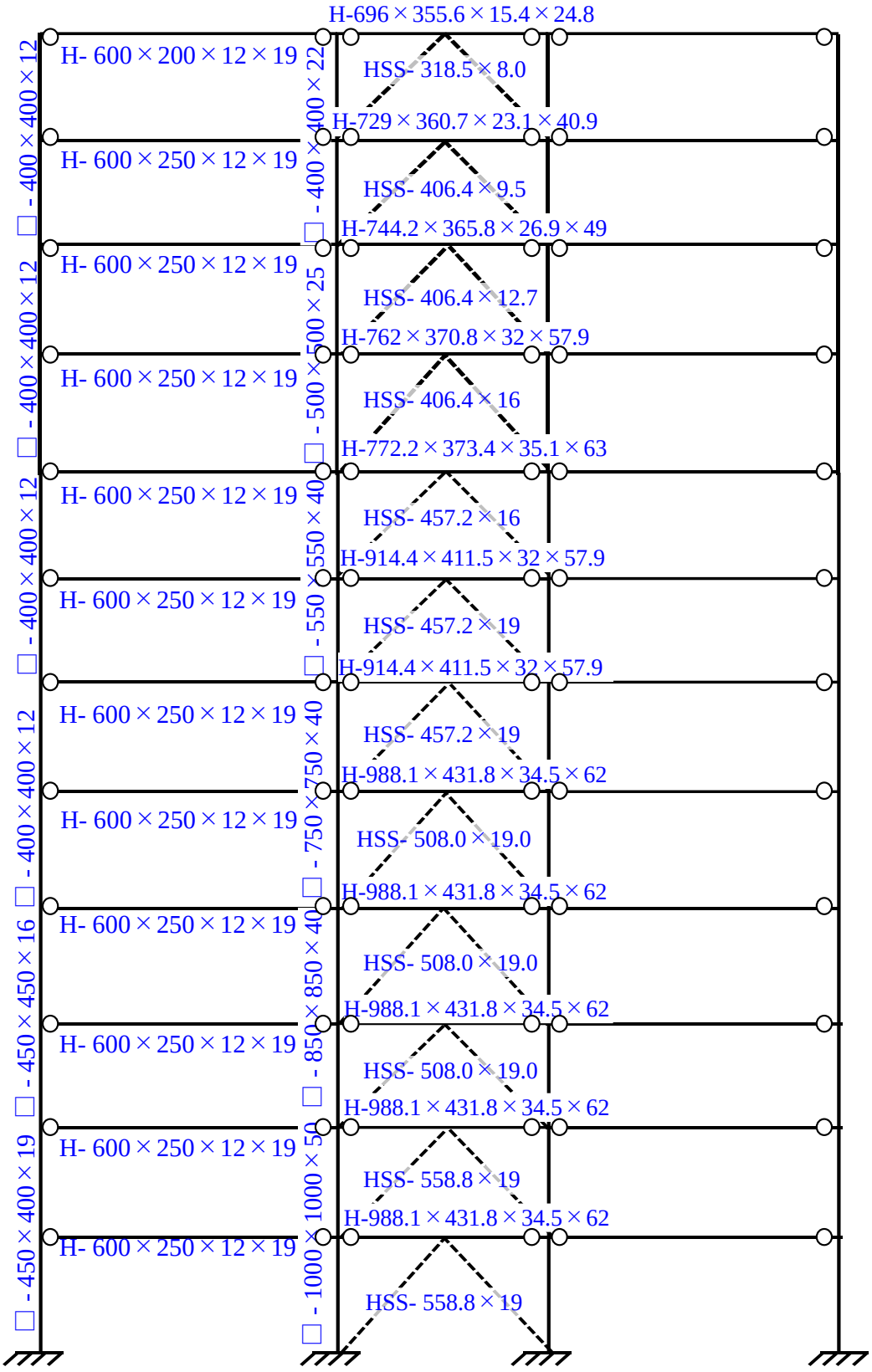

Figure B. 17: Cross-Section Properties for Model C.

Appendix C: Computation of the Plastic Capacity

Plastic capacity of Model 4A_2.0

Floors	$H_{Ext.MRF}$	$H_{Int.MRF}$	H_{CBF} H_{braces}	H_{CBF}	Q_i	Q_i/Q_{un}
4	881	150	0	150	1031	1.1
3	881	279	317	597	1478	1.0
2	881	458	656	1114	1995	1.1
1	1486	1150	656	1806	3292	1.5

Plastic capacity of Model 4A_8.0

Floors	$H_{Ext.MRF}$	$H_{Int.MRF}$	H_{CBF} H_{braces}	H_{CBF}	Q_i	Q_i/Q_{un}
4	881	192.0	0.0	192	1073	1.01
3	881	192	656	848	1730	1.01
2	881	205	1205	1410	2291	1.05
1	1486	897	1205	2102	3587	1.42

Plastic capacity of Model 4B_2.0

Floors	$H_{Ext.MRF}$	$H_{Int.MRF}$	H_{CBF} H_{braces}	H_{CBF}	Q_i	Q_i/Q_{un}
4	881	150	0	150	1031	1.13
3	881	372	386	757	1638	1.12
2	881	458	533	991	1872	1.00
1	1486	1192	533	1725	3211	1.49

Plastic capacity of Model 4B_8.0

Floors	$H_{Ext.MRF}$	$H_{Int.MRF}$	H_{CBF} H_{braces}	H_{CBF}	Q_i	Q_i/Q_{un}
4	881	195	0	195	1076	1.01
3	881	102	727	829	1711	1.00
2	881	172	1189	1361	2242	1.02
1	1486	1023	1189	2212	3697	1.47

Plastic capacity of Model 4C

Floors	$H_{Ext.MRF}$	$H_{Int.MRF}$	H_{CBF} H_{braces}	H_{CBF}	Q_i	Q_i/Q_{un}
4	0	0	1240	1240	1240	1.02
3	0	0	1892	1892	1892	0.97
2	0	0	2521	2521	2521	1.01
1	0	0	2908	2908	2908	1.01

Plastic capacity of Model 8A_2.0

Floors	$H_{Ext.MRF}$	H_{CBF}		Q_i	Q_i/Q_{un}
		$H_{Int.MRF}$	H_{braces}	H_{CBF}		
8	752	382	440	822	1574	1.1
7	881	742	739	1481	2362	1.1
6	881	1069	1205	2274	3155	1.1
5	881	1434	1504	2937	3818	1.1
4	881	1728	1723	3451	4332	1.1
3	881	1869	1990	3858	4739	1.1
2	881	1986	1990	3976	4857	1.1
1	1159	4264	1990	6253	7412	1.6

Plastic capacity of Model 8A_8.0

Floors	$H_{Ext.MRF}$	H_{CBF}		Q_i	Q_i/Q_{un}
		$H_{Int.MRF}$	H_{braces}	H_{CBF}		
8	752	150	656	806	1558	1.0
7	881	240	1399	1639	2520	1.0
6	881	364	1990	2353	3234	1.0
5	881	458	2549	3006	3887	1.0
4	881	515	2979	3495	4376	1.0
3	881	529	3405	3934	4815	1.0
2	881	575	3760	4335	5216	1.0
1	1159	1585	3760	5345	6504	1.2

Plastic capacity of Model 8B_2.0

Floors	$H_{Ext.MRF}$	H_{CBF}		Q_i	Q_i/Q_{un}
		$H_{Int.MRF}$	H_{braces}	H_{CBF}		
8	752	364	394	758	1510	1.1
7	881	669	896	1565	2446	1.1
6	881	1069	1184	2253	3134	1.1
5	881	1380	1370	2750	3631	1.1
4	881	1664	1591	3255	4136	1.1
3	881	1790	1807	3597	4478	1.1
2	881	1977	1904	3881	4762	1.1
1	1159	3897	1904	5801	6960	1.5

Plastic capacity of Model 8B_8.0

Floors	$H_{Ext.MRF}$	H_{CBF}			Q_i	Q_i/Q_{un}
		$H_{Int.MRF}$	H_{braces}	H_{CBF}		
8	752	102	727	829	1581	1.0
7	881	191	1467	1658	2539	1.0
6	881	287	2110	2398	3279	1.0
5	881	343	2765	3108	3989	1.0
4	881	472	3426	3899	4780	1.1
3	881	460	3499	3959	4840	1.0
2	881	514	3698	4212	5093	1.0
1	1159	2244	3698	5942	7101	1.3

Plastic capacity of Model C

Floors	$H_{Ext.MRF}$	H_{CBF}			Q_i	Q_i/Q_{un}
		$H_{Int.MRF}$	H_{braces}	H_{CBF}		
8	0	0	1586	1586	1586	1.0
7	0	0	2518	2518	2518	1.0
6	0	0	3293	3293	3293	1.0
5	0	0	4117	4117	4117	1.1
4	0	0	4465	4465	4465	1.0
3	0	0	4888	4888	4888	1.0
2	0	0	5572	5572	5572	1.1
1	0	0	5572	5572	5572	1.0

Plastic capacity of Model 12A_2.0

Floors	$H_{Ext.MRF}$	H_{CBF}			Q_i	Q_i/Q_{un}
		$H_{Int.MRF}$	H_{braces}	H_{CBF}		
12	752	238	257	496	1248	1.0
11	881	534	486	1020	1901	1.0
10	881	798	854	1652	2533	1.0
9	881	1078	991	2069	2950	1.0
8	881	1293	1399	2692	3573	1.1
7	881	1353	1591	2944	3825	1.0
6	881	1634	1591	3225	4106	1.0
5	881	1794	1781	3575	4456	1.0
4	881	1956	1838	3794	4675	1.0
3	881	1956	1990	3945	4826	1.0
2	881	1956	2230	4185	5066	1.0
1	1589	3754	2230	5983	7572	1.5

Plastic capacity of Model 12A_8.0

Floors	$H_{Ext.MRF}$	H_{CBF}			Q_i	Q_i/Q_{un}
		$H_{Int.MRF}$	H_{braces}	H_{CBF}		
12	752	147	414	560	1312	1.0
11	881	192	1040	1232	2113	1.0
10	881	306	1591	1897	2778	1.0
9	881	382	2245	2628	3509	1.0
8	881	431	2549	2980	3861	1.0
7	881	515	2979	3495	4376	1.0
6	881	610	3405	4014	4895	1.0
5	881	610	3590	4199	5080	1.0
4	881	686	3760	4446	5327	1.0
3	881	686	4034	4721	5602	1.0
2	881	742	4245	4987	5868	1.0
1	1589	2044	4245	6289	7878	1.4

Plastic capacity of Model 12B_2.0

Floors	$H_{Ext.MRF}$	H_{CBF}		H_{CBF}	Q_i	Q_i/Q_{un}
		$H_{Int.MRF}$	H_{braces}	H_{CBF}		
12	752	234	225	458	1210	1.0
11	881	534	519	1053	1934	1.0
10	881	798	825	1623	2504	1.0
9	881	1078	1041	2119	3000	1.0
8	881	1293	1327	2620	3501	1.0
7	881	1477	1432	2909	3790	1.0
6	881	1634	1602	3236	4117	1.0
5	881	1794	1805	3599	4480	1.0
4	881	1956	1904	3859	4740	1.0
3	881	1955	2081	4036	4917	1.0
2	881	1956	2194	4149	5030	1.0
1	1589	4120	2194	6314	7903	1.6

Plastic capacity of Model 12B_8.0

Floors	$H_{Ext.MRF}$	H_{CBF}		H_{CBF}	Q_i	Q_i/Q_{un}
		$H_{Int.MRF}$	H_{braces}	H_{CBF}		
12	752	73	532	606	1358	1.0
11	881	160	1154	1314	2195	1.0
10	881	237	1720	1957	2838	1.0
9	881	305	2162	2467	3348	1.0
8	881	388	3215	3603	4484	1.2
7	881	460	2987	3447	4328	1.0
6	881	514	3397	3911	4792	1.0
5	881	535	3564	4099	4980	1.0
4	881	584	3909	4493	5374	1.0
3	881	584	4208	4792	5673	1.0
2	881	609	4283	4893	5774	1.0
1	1589	2366	4283	6649	8238	1.4

Plastic capacity of Model C

Floors	$H_{Ext.MRF}$	$H_{Int.MRF}$	H_{CBF} H_{braces}	H_{CBF}	Q_i	Q_i/Q_{un}
12	0	0	1432	1432	1432	1.1
11	0	0	2193	2193	2193	1.0
10	0	0	2907	2907	2907	1.0
9	0	0	3631	3631	3631	1.1
8	0	0	4118	4118	4118	1.1
7	0	0	4857	4857	4857	1.1
6	0	0	4857	4857	4857	1.0
5	0	0	5429	5429	5429	1.1
4	0	0	5429	5429	5429	1.0
3	0	0	5429	5429	5429	1.0
2	0	0	6007	6007	6007	1.1
1	0	0	6007	6007	6007	1.0